



HAL
open science

Modélisation Musculo-Squelettique Personnalisée du Rachis Cervical

Maxim van den Abbeele

► **To cite this version:**

Maxim van den Abbeele. Modélisation Musculo-Squelettique Personnalisée du Rachis Cervical. Autre [cond-mat.other]. Ecole nationale supérieure d'arts et métiers - ENSAM, 2018. Français. NNT : 2018ENAM0037 . tel-02548372

HAL Id: tel-02548372

<https://pastel.hal.science/tel-02548372>

Submitted on 20 Apr 2020

HAL is a multi-disciplinary open access archive for the deposit and dissemination of scientific research documents, whether they are published or not. The documents may come from teaching and research institutions in France or abroad, or from public or private research centers.

L'archive ouverte pluridisciplinaire **HAL**, est destinée au dépôt et à la diffusion de documents scientifiques de niveau recherche, publiés ou non, émanant des établissements d'enseignement et de recherche français ou étrangers, des laboratoires publics ou privés.

École doctorale n° 432 : Sciences des Métiers de l'ingénieur

Doctorat ParisTech

T H È S E

pour obtenir le grade de docteur délivré par

l'École Nationale Supérieure d'Arts et Métiers

Spécialité " Biomécanique "

présentée et soutenue publiquement par

Maxim VAN DEN ABEELE

le 17 octobre 2018

**MODÉLISATION MUSCULOSQUELETTIQUE
PERSONNALISÉE DU RACHIS CERVICAL**

Directeur de thèse :
Co-encadrement de la thèse :

Wafa SKALLI
Sébastien LAPORTE
Baptiste SANDOZ

Jury

M. Cédric BARREY, Professeur, Service de Neurochirurgie,
CHU de Lyon – Hôpital Pierre Wertheimer
M. Jozef VANDER SLOTEN, Professeur, Biomechanics Section,
Department of Mechanical Engineering, KU Leuven
M. Olivier GILLE, Professeur, Unité d'Orthopédie, CHU de Bordeaux – Hôpital Pellegrin
Mme Mary BOUXSEIN, Professeur Associé, Department of Orthopedic Surgery,
Beth Israel Deaconess Medical Center
Mme Evelyne EMERY, Professeur, Service de Neurochirurgie, CHU de Caen
Mme Wafa SKALLI, Professeur, IBHGC, ENSAM
M. Sébastien LAPORTE, Professeur, IBHGC, ENSAM
M. Baptiste SANDOZ, Maître de Conférences, IBHGC, ENSAM
M. François LAVASTE, Professeur Emérite, IBHGC, ENSAM
M. Dominique BONNEAU, Médecin, Institut Supérieur de Thérapeutique Manuelle

Président

Rapporteur
Rapporteur

Examineur
Examineur
Examineur
Examineur

Invité
Invité

T
H
È
S
E

"Always make a total effort, even when the odds are against you."

Arnold Palmer

Acknowledgements

This PhD is the result of not only my own investment, but also of the contributions of many other actors, without whom this work would probably not have reached its final status. I would like to express my sincere gratitude to all those who directly and indirectly have helped me in completing this project. In particular, I would like to thank:

- Prof. Wafa Skalli, my PhD-director and scientific director of the *Institut de Biomécanique Humaine Georges Charpak*. Prof. Skalli has the exceptional ability to come up with ideas even when the problem seems unsolvable. By sharing her experience in the field of biomedical engineering, i.e. research and industry, and her passion, she ensured an excellent follow-up of this project.
- Prof. Sébastien Laporte, my PhD co-director. The role of Sébastien was invaluable, particularly in the development of the finite element model. Under the guidance of his expertise and exceptional mind, it was possible to make the necessary technical and scientific advancements. Besides that, he kept up the good spirit with some pretty funny jokes (not) about the Belgians.
- Baptiste Sandoz, Assistant Professor, my PhD co-director. Baptiste was very helpful in the development of the muscle regulation model and in the preparation of experiments. Baptiste was always very receptive and responsive and kept the stress at a minimum level.
- The investors of the BiomecAM chair program on subject-specific modeling, i.e. Société Générale, COVEA, Fondation Yves Cotrel and PROTEOR. With their financial aid, I could complete my PhD in the best conditions.
- Dominique Bonneau, MD. When Dominique stopped by, he always offered to share his unique insights in the human anatomy and blocked an hour or two in his schedule. Thanks to his numerous interventions I gained knowledge on the cervical spine musculature and biomechanics, which was particularly helpful for the development of both the finite element and muscle regulation models.
- Prof. François Lavaste. As the co-inventor of the implant that was modeled at the end of this PhD, Prof. Lavaste took the time at a number of occasions, to explain the implant development process, the biomechanics of total disc replacements and the experimental validation.
- The members of the jury for their participation in this jury. I especially thank Prof. Vander Sloten and Prof. Gille for having accepted to report on my PhD manuscript. I also warmly thank Prof. Bouxsein, Prof. Barrey and Prof. Emery for having accepted to participate as examiners.
- Célia Amabile, Fan Li and Vincent Pomero, who all helped me in developing the muscle regulation model. With Célia, I have spent hours and hours on Matlab to go through the code initially developed by Vincent. Without her help and positive vibe, it would have taken a lot longer. The involvement of Vincent and Fan was indispensable,

as through various skype sessions, they helped me understand the technical details of the model.

- Aurélien Laville, who, thanks to his outstanding PhD, made it possible for me to advance the development of the cervical spine finite element model. He was always very happy to help me out when I called or emailed him.
- Pierre-Yves Rohan and Claudio Vergari for their help in performing the numerous ultrasound elastography measurements. Pierre-Yves took the time to help me with the acquisitions at 7 am in the morning and Claudio was all too happy to exchange ideas and share his expertise, which was indispensable for the post-processing.
- Thomas Joubert and Sylvain Persohn, who helped me overcome any IT-related or technical issues and shared their experience on spine testing and finite element modeling.
- Mohamed Marhoum, who has the ability to magically let appear scientific articles or books that are virtually unfindable. Mohammed was always very responsive and understanding and ensured that my posters or reports were printed out on time.
- Marine Souq, who, especially at the end of my PhD project, helped me with the administration and the organisation of my PhD defense.
- The other PhD candidates, Alice, Aurélien, Boris, Brahim, Brighu, Cédric, Christophe, Emmanuelle, Louis, Maxime, Nolwen, Pierre-Marc, Saman, Samuel, Thibault and Thomas, for creating the very pleasant work atmosphere at the institute.
- My office mates, François and Nicolas, who had to endure my presence, yet made my working spot a very happy place. A special thanks to François for providing me the tools that I needed to perform the FE mesh deformation and the pre-treatment of the data used in the development of the reduced dataset musculoskeletal model.
- Rotary Club Leuven, especially Prof. Vander Sloten, who supported me during my application for the Rotary District Grant, without which I would not have been able to move to Paris and complete the Bme Paris Master Programme.
- My best friends, Albert-Jan and Simon, who, especially while I was writing my manuscript, always offered me the support and understanding I needed. Each time I was in Belgium, they took the time to go out for dinner, to do some car-spotting or to just spend time together. They even spent the weekend in Paris a few times.

And of course, my parents, who remained positive, understanding and patient, even when I locked myself up in my room for work at the most intense moments of the project. They made me feel like I was on holiday, each time I felt the need to spend the weekend in Belgium. They supported me with every decision I have made and offered me their feedback when I asked for it. These few sentences are just not enough to thank them.

Contents

General Introduction	1
1 Musculoskeletal Cervical Spine Anatomy and Biomechanics	3
1.1 Descriptive Anatomy	4
1.2 Cervical Spine Musculature	7
1.3 Cervical Spine Biomechanics	10
1.4 Clinical Context	11
2 Literature Review	15
2.1 Muscle Force Quantification	16
2.2 Finite Element Modeling of the Cervical Spine	22
2.3 Synthesis and Project Objectives	31
3 Cervical Spine Muscle Force Quantification: Muscle Regulation Model	35
3.1 A Subject-specific Biomechanical Control Model for the Prediction of Cervical Spine Muscle Forces	36
3.2 A Subject-specific Analysis	48
4 Finite Element Modeling of the Lower Cervical Spine	59
4.1 A Framework for the Validation of Cervical Spine FE Models	60
4.2 A Subject-specific Analysis	71
5 Clinical Applications	83
5.1 Muscle Force Quantification based on a Reduced Set of Clinical Data	84
5.2 Finite Element Modeling of the Cervical Spine Instrumented with a Total Disc Replacement	95
General Conclusion and Perspectives	107
References	111
A Cervical Spine Ligamentous and Muscular Anatomy	125
B Literature Review	131
C Muscle Regulation Model	139
(Inter)national Communications	143

List of Figures

1.1	The osseous anatomy of four characteristic cervical <i>vertebrae</i>	5
1.2	The osseo-ligamentous anatomy of the upper cervical spine (adapted from Kamina [2015])	6
1.3	Postero-lateral view of the lower cervical spine (adapted from Kapandji [2002]) [a = superior endplate vertebral body, b = <i>unciform</i> process, e = transverse process, f = articular process (facet joint), j = spinous process, 1 = <i>annulus fibrosus</i> , 2 = <i>nucleus pulposus</i> , 3 = anterior longitudinal ligament, 4 = posterior longitudinal ligament, 5 = facet capsule, 7 = yellow ligament, 8 = interspinous ligament, 9 = supraspinous ligament, 10 = intertransverse ligament]	7
1.4	The deep cervical spine muscles (courtesy of Mathias Bonneau, with permission (Bonneau [2017]))	8
1.5	The superficial cervical spine muscles (courtesy of Mathias Bonneau, with permission (Bonneau [2017]))	9
1.6	Anterior view of the cervical spine, with an indication of the <i>longus capitis</i> (left), the <i>rectus capitis anterior</i> and the <i>rectus capitis lateralis</i> (right) (courtesy of Mathias Bonneau, with permission (Bonneau [2017]))	10
1.7	A schematic representation of the FSU (adapted from Kamina [2015]). The ligaments, together with the IVD and the muscles, stabilise the intervertebral joint and redistribute the charges.	11
1.8	The total disease burden in 2016 in the high income countries across the world. Blue represents the non-communicable diseases, red the communicable diseases and green trauma. The size of the squares indicates the importance of the disorder and its colour shading designates the relative difference with the previous years (Institute for Health Metrics and Evaluation (IHME) [2017])	12
2.1	The proprioception-based muscle regulation model assumes that the spinal muscle act to protect the spinal joints (Pomero <i>et al.</i> [2004])	20
2.2	The parameterisation of the 3D reconstruction obtained from biplanar X-ray data allows the automatic generation of a hexahedral mesh (Laville <i>et al.</i> [2009])	26
3.1	Three different interpretations of the agonist and antagonist activation as function of the input command, i.e. the ratio between the net reaction moment and the maximum moment for flexion (0 to 1) and extension (0 to -1), as adapted from Zhou <i>et al.</i> [1996].	38
3.2	From the MRI and biplanar X-ray data, a 3D reconstruction of the cervical spine, the external envelope and the muscles can be obtained. This enables the calculation of the geometric parameters of the muscles in the plane of the IVD of interest, here C5-C6.	40

3.3	Comparison of the muscle force predictions with two reference studies for a selection of two anterior and two posterior muscle groups in four different configurations. [L: left; R: right, IH: <i>infrahyoid</i> , SCM: <i>sternocleidomastoideus</i> , SS cap: <i>semispinalis capitis</i> , Trap: <i>trapezius</i>]	42
3.4	Effect of the intra-articular load threshold values on the model predictions for three joint load components, as obtained with a full-factorial analysis. The graphs present the results of six series of 20 simulations. In each series, the compression threshold remained constant, while the threshold values of the other load components were varied between 10% and 200% of their initial value. The dotted vertical line, as well as the legend entry marked with '**' refer to the reference threshold values.	44
3.5	Effect of the intra-articular load threshold values on the muscle force prediction, as obtained with a full-factorial analysis. The graphs present the results of the 20 simulations performed with a given compression threshold of 1000N for a selection of ten muscles. The dotted vertical line refers to the reference threshold values. [L: left; R: right, IH: <i>infrahyoid</i> , SCM: <i>sternocleidomastoideus</i> , Scal A: <i>scalenus anterioris</i> , Scal M: <i>scalenus medius</i> , Lev Sc: <i>levator scapulae</i> , SS Cerv: <i>semispinalis cervicis</i> , Sple Cerv: <i>splenius cervicis</i> , Sple cap: <i>splenius capitis</i> , Trap: <i>trapezius</i>]	45
3.6	The predicted muscle force distribution for the erect configuration. The length of the force vectors is proportional to the force magnitude. The color gives an indication of the ratio between the force exerted by the muscle and the force at maximal contraction.	45
3.7	The procedure followed to calculate the muscle geometric input data at the level of the C4-C5 to C6-C7 intervertebral joints	49
3.8	The procedure followed to calculate the external forces generated by the head/neck segment above the spinal joint of interest, i.e. C4-C5, C5-C6 and C6-C7	50
3.9	The 3D musculoskeletal models for the six volunteers, generated from the EOS data fused with the MRI data.	51
3.10	The distribution of the exertion points of the external loads, expressed in the local C6-C7 joint frame, as well as their magnitudes, among the six volunteers.	52
3.11	The C6-C7 joint load before (a & b) and after (c & d) muscular regulation for the six subjects in the neutral configuration. Note that the joint load before regulation is given by the external load, calculated from the mass of the body segment above the C6-C7 joint, expressed in the local joint reference frame.	53
3.12	The estimated muscle forces regulating the C6-C7 joint load for the six subjects and a 3D representation for three subjects.	54
3.13	The C6-C7 joint load before (a & b) and after (c & d) muscular regulation for the six subjects in the 20° flexed configuration	54
3.14	The estimated muscle forces regulating the C6-C7 joint load in the neutral and the flexed configuration	55
3.15	The C4-C5 joint load before (a & b) and after (c & d) muscular regulation for the six subjects in the neutral configuration	56
3.16	The C5-C6 joint load before (a & b) and after (c & d) muscular regulation for the six subjects in the neutral configuration	56
3.17	The muscle force predictions regulating the joint load at the C4-C5, C5-C6 and C6-C7 intervertebral levels in the neutral configuration	57

4.1	Sample preparation and experimental boundary and loading conditions . . .	61
4.2	The generic FE mesh of the C4-C7 spinal segment	63
4.3	Experimental flexion/extension behaviour and associated coupled lateral bending and axial rotation. The experimental mean is indicated in red and the experimental corridor in grey.	66
4.4	The RoM as measured in the current study for a) lateral bending, b) flexion/extension and c) axial rotation, compared to the in-vitro data available in the literature.	67
4.5	Numerical vs. experimental flexion/extension behaviour with the associated coupled motions. The numerical curves obtained with the simplified and morphorealistic FE models are depicted in red and green, respectively. The experimental corridors are rendered in blue and orange for respectively the population tested by Coloma <i>et al.</i> [2016] (unpublished data) and Barrey <i>et al.</i> [2015].	68
4.6	Numerical vs. experimental axial rotation behaviour with the associated coupled motions. The numerical curves obtained with the simplified and morphorealistic FE models are depicted in red and green, respectively. The experimental corridors are rendered in blue and orange for respectively the population tested by Coloma <i>et al.</i> [2016] (unpublished data) and Barrey <i>et al.</i> [2015]	68
4.7	The orientation of the predicted helical axes (in blue) for each of the simulated configurations and spinal levels, compared to those observed <i>in-vitro</i> (red).	69
4.8	For each of the five samples, a regular FE mesh was generated from the biplanar X-ray data and from the corresponding CT data.	73
4.9	The point-to-surface distance between the EOS- (a) and CT-based (b) mesh and the corresponding CT-based reconstruction	74
4.10	The numerical moment load vs. angular displacement behaviour, as observed with the EOS- and CT-based FE models, in comparison with the experimental corridor for flexion/extension.	75
4.11	The numerical moment load vs. angular displacement behaviour, as observed with the EOS- and CT-based FE models, in comparison with the experimental corridor for axial rotation.	76
4.12	The experimental (dotted line) moment load vs. angular displacement behaviour in comparison with the corresponding numerical (full line) curves, obtained with both the EOS- (a) and CT-based (b) meshes, for flexion/extension.	77
4.13	The experimental vs. numerical range of motion, as predicted by both the EOS- (a) and CT-based (b) meshes, in flexion/extension (FE), lateral bending (IL) and axial torsion (TO).	78
4.14	The location of the mean centre of rotation (MCR), determined from the experimental load-displacement data under flexion/extension compared to the one predicted by the EOS- (a & b) and CT-based (c & d) FE models.	79
5.1	A template <i>Full DataSet</i> (FDS) musculoskeletal model was deformed onto the 3D reconstruction of the external envelope and the spine, based on a set of control points, common to both the starting and target objects, yielding a subject-specific <i>Reduced DataSet</i> (RDS) musculoskeletal model.	86

5.2	The subject-specific <i>Reduced DataSet</i> (RDS) model, built from an average musculoskeletal model, is adjusted to match the muscle contours manually indicated on one or two MRI slices, yielding the subject-specific <i>Partially Reduced DataSet</i> (PRDS-1 & PRDS-2) models. The figure presents the procedure for one MRI slice, but the same workflow is followed when considering two MRI slices. The only difference being the number of contours considered in the computation of the elastic transformation.	88
5.3	Example of the joint load (a) and muscle force (b, c) predictions for subject S4, obtained with the <i>Full DataSet</i> (FDS) model and the subject-specific <i>Reduced DataSet</i> (RDS) models based on the S2 template, the S1 template and the average template	90
5.4	The mean absolute differences in terms of intervertebral joint loads (a) and muscle forces (b), between the predictions obtained with the RDS, PRDS-1 and PRDS-2 models and those obtained with the corresponding FDS models. The black lines indicate the range between the minimal and maximal difference.	91
5.5	Example of the joint load (a) and muscle force (b, c) predictions for subject S4, obtained with <i>Full DataSet</i> (FDS) model, the subject-specific <i>Reduced DataSet</i> (RDS) model based on the average template, the subject-specific <i>Partially Reduced DataSet</i> model based on the average template and one MRI slice (PRDS-1) and the subject-specific <i>Partially Reduced DataSet</i> model based on the average template and two MRI slices (PRDS-2)	92
5.6	A schematic cross-sectional view of the IVD implant in the sagittal plane. Since the convex and concave surfaces of the central core have different radii of curvature, both rotation and translation are possible.	96
5.7	From the patent and the biplanar X-ray images, a 3D model of the implant was designed, assembled and meshed with hexahedral elements.	97
5.8	Parameterising the EOS-based reconstruction automatically results in a simplified FE mesh. After densification and iterative deformation, a morphorealistic hexahedral mesh is obtained. Based on the biplanar X-ray data, the implant could be virtually inserted.	99
5.9	The experimental load vs. displacement curves for the intact (dotted lines) and instrumented (full lines) configuration under flexion/extension. The red box indicated the instrumented level.	100
5.10	The experimental load vs. displacement curves for the intact (dotted lines) and instrumented (full lines) configuration under axial torsion. The red box indicates the instrumented level.	100
5.11	For each of the five samples, a regular FE mesh of the instrumented configuration was generated from the biplanar X-ray data and from the corresponding CT data.	101
5.12	The retro-projected contours of the FE model generated for sample S1 are consistent with the EOS data.	101
5.13	The numerical load-displacement curves vs. the experimental corridor for flexion/extension, lateral bending and axial rotation, as observed for the instrumented C5-C6 vertebral level.	102
5.14	The numerical moment load vs. angular displacement behaviour in comparison with the experimental corridor for flexion/extension. The instrumented level is indicated in red.	102
5.15	The numerical moment load vs. angular displacement behaviour in comparison with the experimental corridor for axial torsion. The instrumented level is indicated in red.	103

5.16	The experimental (full lines) vs. numerical (dotted lines) load-displacement curves representing the instrumented configuration under flexion/extension. The instrumented level is indicated in red.	104
5.17	The experimental (full lines) vs. numerical (dotted lines) load-displacement curves representing the instrumented configuration under axial torsion. The instrumented level is indicated in red.	104
5.18	The location of the experimentally determined vs. numerically predicted mean centre of rotation (MCR).	105
C.1	The elastic registration procedure to transfer the 3D reconstruction of the muscles from the MRI to the EOS reference system.	140
C.2	Comparison of the muscle force predictions with two reference studies for all muscles/muscle groups that were considered in the analysis for the four configurations. [L: left; R: right, A: anterior, P: posterior, Plat: <i>Platysma</i> , IH: <i>infrahyoid</i> , SCM: <i>sternocleidomastoideus</i> , LCC: <i>longus colli & longus cervicis</i> , Scal: <i>scalenus</i> , Long: <i>longissimus</i> , Lev Scap: <i>levator scapulae</i> , Mult: <i>multifidus</i> , SS Cerv: <i>semispinalis cervicis</i> , SS Cap: <i>semispinalis capitis</i> , Sple Cerv: <i>splenius cervicis</i> , Sple Cap: <i>splenius capitis</i> , Trap: <i>trapezius</i>]	142

List of Tables

2.1	Non-exhaustive overview of the frequently cited models for muscle force quantification [CSA: cross-sectional surface area, FBD: free-body diagram, Min.: minimisation]	17
2.2	Non-exhaustive overview of the frequently cited cervical spine FE models (Part 1) [compr.: compression, conv.: convergence, DM: textitdura mater, DOF: degree of freedom, elas.: elastic, hexa: hexahedral element, hyperel.: hyperelastic, inf.: inferior, iso: isotropic, lin.: linear, lit.: literature, ortho: orthotropic, SC: spinal cord, tetra: tetrahedral element]	23
2.3	Non-exhaustive overview of the frequently cited cervical spine FE models (Part 2) [compr.: compression, conv.: convergence, DM: textitdura mater, DOF: degree of freedom, elas.: elastic, hexa: hexahedral element, hyperel.: hyperelastic, inf.: inferior, iso: isotropic, lin.: linear, lit.: literature, ortho: orthotropic, SC: spinal cord, tetra: tetrahedral element]	24
2.4	Overview of FE models developed for the study of surgical interventions. The column entitled 'Reference FE model' contains the reference towards the FE model used for the study and listed in Tables 2.2 and 2.3 [config.: configuration, compr.: compression, TDR: total disc replacement]	29
3.1	The numerical intervertebral joint forces in each of the four modeled configurations. (PA stands for <i>postero-anterior</i> , ML for <i>medio-lateral</i> and NA for <i>not available</i>)	41
3.2	Results of the Monte Carlo analysis allowing the assessment of the model robustness. (PA stands for <i>postero-anterior</i> , ML for <i>medio-lateral</i> and NA for <i>not available</i>)	43
3.3	Results of the correlation analysis of the parameters defining the antagonist law on the C4-C5 joint load.	43
4.1	Material and element properties of the different model aspects. [AP: antero-posterior, ML: Medio-lateral, ALL: anterior longitudinal ligament, PLL: posterior longitudinal ligament, LF: ligament <i>flavum</i> , ISL: interspinous ligament, Hexa: hexahedral].	64
5.1	Summary of the different template musculoskeletal models used to build the subject-specific <i>Reduced DataSet</i> (RDS) models for each individual subject.	86
A.1	Insertion and termination of the ligaments of the upper cervical spine	126
A.2	Insertion and termination of the ligaments of the lower cervical spine	127
A.3	Insertion, termination and function of the deep cervical spine muscles	128
A.4	Insertion, termination and function of the intermediate cervical spine muscles	128
A.5	Insertion, termination and function of the superficial cervical spine muscles	129
A.6	Insertion, termination and function of the suboccipital cervical spine muscles	129

B.1	The vertebra mechanical properties as described in the commonly cited <i>in-silico</i> studies.	132
B.2	The <i>in-vitro</i> experimental literature on cortical and cortico-spongius bone mechanical properties.	132
B.3	The <i>in-vitro</i> experimental literature on spongius bone mechanical properties.	133
B.4	The IVD mechanical properties as described in the commonly cited <i>in-silico</i> studies.	134
B.5	The <i>in-vitro</i> experimental literature on ligament mechanical properties. . .	135
B.6	The ligament mechanical properties as described in the commonly cited <i>in-silico</i> studies [ALL = Anterior Longitudinal Ligament, PLL = Posterior Longitudinal Ligament, ISL = Interspinous Ligament, LF = <i>Ligamentum Flavum</i> , FC = Facet Capsule, CSA = Cross-sectional Surface Area].	136
B.7	The <i>in-vitro</i> experimental literature on ligament mechanical properties [ALL = Anterior Longitudinal Ligament, PLL = Posterior Longitudinal Ligament, ISL = Interspinous Ligament, LF = <i>Ligamentum Flavum</i> , FC = Facet Capsule, CSA = Cross-sectional Surface Area].	137

List of Abbreviations

ALL	Anterior Longitudinal Ligament
ASD	Adjacent Segment Disease
ASME	American Society of Mechanical Engineers
BMI	Body Mass Index
CoCr	Cobalt Chromium
CSA	Cross-sectional Surface Area
CT	Computed Tomography
CV	Coefficient of Variation
DALY	Disability Adjusted Life Year
DoF	Degrees of Freedom
EMG	Electromyogram
EZ	Elastic Zone
FC	Facet Capsule
FDA	Food & Drug Administration
FDS	Full DataSet
FE	Finite Element(s)
FEA	Finite Element analysis
FSU	Functional Spinal Unit
HFS	Head First - Supine
HU	Hounsfield Unit
ISL	Interspinous Ligament
IVD	Intervertebral disc
LF	<i>Ligamentum Flavum</i> (Yellow Ligament)
LOS	Length of Stay
NZ	Neutral Zone
MCR	Mean Centre of Rotation
MRI	Magnetic Resonance Imaging
PJK	Proximal Junctional Kyphosis
PLL	Posterior Longitudinal Ligament
PMMA	PolyMethyl Methacrylate
PRDS	Partially Reduced DataSet
RMSE	Root Mean Squared Error
RoM	Range of Motion
RDS	Reduced DataSet
SWE	Shear Wave Elastography
SWS	Shear Wave Propagation Speed
UHMWPE	Ultra-High-Molecular-Weight Polyethylene
US	Ultrasound

General Introduction

The cervical spine is a complex and highly mobile structure. It accurately orientates the head to maintain the ocular system on a horizontal plane, regardless of the configuration of the more caudal spinal structures and the lower limbs, while protecting the spinal chord. With knowledge of the important load exerted on the cervical spine on a daily basis (the head weighs on average 4.5 kg (Yoganandan *et al.* [2009])), it is not surprising that neck pain, together with lower back pain, is the second most important cause of invalidity in the developed world (Institute for Health Metrics and Evaluation (IHME) [2017]). As a matter of fact, it is estimated that at least 50% of the population aged over 55 years encounters some form of cervical spine degeneration (Malcolm [2002]; Wang *et al.* [2009]). Spinal surgery, e.g. anterior cervical discectomy combined with fusion or total disc replacement, is very effective for pain relief. This partially explains why the surgery rate continuously increased over the last three decades and still does (Wang *et al.* [2009]; Marquez-Lara *et al.* [2014]; Liu *et al.* [2016]). However, mechanical complications, such as screw loosening and implant subsidence, and clinical complications, such as *pseudarthrosis* and adjacent segment disease, are still frequently reported.

The developmental mechanisms of cervical spine degeneration and surgical complications are still not fully understood. The medical and scientific community agree that spinal overloading, postural abnormalities and muscular dysfunction play an important role. It is also acknowledged that a patient-centered approach, when planning surgery and post-operative care, is fundamental (Abumi *et al.* [2000]; Rousseau *et al.* [2008a]; Kasimatis *et al.* [2009]; Laville *et al.* [2009]; Belin *et al.* [2014]).

It is in this context that the scientific program chaired by BiomecAM concentrates on subject-specific musculoskeletal modeling of the cervical spine, thorax, lower back and larger articulations, such as the knee and shoulder joints. It thereby contributes to the global understanding of human biomechanics, to increasing the efficiency level of pathology prevention and to the design of new medical devices. Regarding the cervical spine, strong advancements have been made during the recent past years at the *Institut de Biomécanique Humaine Georges Charpak*. Innovative finite element mesh generation techniques have been developed, enabling the rapid and automatic generation of hexahedral meshes from a set of biplanar X-rays or CT-scans (Lavaste *et al.* [1992]; Maurel *et al.* [1997]; Laville *et al.* [2009]; Travert [2013]). Quantitative analysis techniques enabling the assignment of subject-specific material properties to the vertebral bone (Sapin de Brosses *et al.* [2010]; El Masri *et al.* [2012]; Choisne *et al.* [2017]) and the intervertebral disc (Vergari *et al.* [2014a,b, 2015]) based on *in-vivo* data have been explored as well. Lastly, the spinal neuromuscular system has been studied and preliminary models for the prediction of muscle activation from medical imaging data have been developed, evaluated and applied (Pomero *et al.* [2004]; Amabile [2016]).

The global objective of this PhD is to exploit these scientific advancements to evolve towards a subject-specific musculoskeletal model of the intact, degenerated and instrumented cervical spine. With this complete model, one aims to contribute to the understanding of the cervical spine degeneration mechanisms and the development of a means of orthopaedic and surgical treatment planning.

To achieve this goal, the project is decomposed in two phases, each treating a different scientific question. In the first phase, the proprioception-based biomechanical control model, developed initially to estimate lumbar spine muscle forces (Pomero *et al.* [2004]), was adapted to the cervical spine, evaluated and validated with EMG recordings extracted from the literature. First, a complex procedure, involving the recording of biplanar X-rays and a stack of high-resolution MRI scans, was followed to generate the subject-specific input data, i.e. muscle geometry, posture and body segment masses. The muscle force predictions obtained as such, were treated as the reference values. In the next step, it was investigated to what extent MRI data, costly and time-consuming to obtain, is necessary to estimate the muscle forces and the associated intervertebral joint load. A unique method was proposed to compute the model input data merely from biplanar X-ray data or from biplanar X-ray data combined with one or two MRI slices. This would significantly accelerate the process and make it possible to build such a model from medical imaging data readily available at the hospital.

In the second phase of this study, a morphorealistic and subject-specific finite element model of the intact cervical spine was developed, based on the parametric finite element model described previously (Laville *et al.* [2009]), and validated with *in-vitro* experimental data. In the process, two models were generated: one from biplanar X-ray data and one from the combined X-ray and CT data. By doing so, the impact of the geometric accuracy on the model behaviour and by extent on a potential use in the clinic could be investigated. Is a CT-scan necessary to investigate internal stresses and deformations or is a rapid and significantly less irradiant biplanar X-ray scan sufficient?

Chapter 1 briefly reminds the cervical spine osseo-ligamentous, muscular and functional anatomy. First, the characteristic features of the main *vertebrae*, muscles and ligaments are presented. In the second section, the functional role of the cervical spine joints is detailed. The third and last section overviews the broader clinical context. The most frequently encountered pathologies and proposed surgical interventions are listed, as well as the main mechanical and clinical post-operative complications, thus highlighting the clinical needs.

Chapter 2 overviews the current *state-of-the-art* regarding subject-specific cervical spine modeling. This bibliographic review is divided into two parts. The first part treats the most common models developed for the quantification of spine muscle forces. In the second part, the main cervical spine finite element models are discussed. The synthesis identifies potential improvements and defines the objectives of this PhD.

In Chapter 3, the adaptation of the proprioception-based muscle regulation model to the cervical spine is explained. A first, rather theoretical, section overviews the main technical features of the model and details the results of the robustness and sensitivity studies, the model validation and the feasibility study. The second section is dedicated to a subject-specific analysis, reinforcing the feasibility study and confirming the need for a subject-specific approach.

Chapter 4 treats the development of the morphorealistic and subject-specific cervical spine FE model. In the first section the mesh generation procedure is explained with the example of a generic FE model. Recommendations regarding model verification and validation are given as well. The second section discusses the in-depth validation of the subject-specific FE model in a *one-to-one* comparison with *in-vitro* experimental behaviour. The differences in terms of performance and predictive power between the FE model based on biplanar X-ray data and the one based on CT-data are discussed as well.

Chapter 5 provides a clinical and industrial application of respectively the muscle regulation model and the FE model. The first section provides the results of the investigation into whether or not MRI-acquisitions are necessary to provide a feasible estimation of the muscle

forces and associated intervertebral joint load. The second section treats the application of the proposed FE model to the cervical spine instrumented with a total disc replacement.

Finally, the general conclusion summarises the main findings of this PhD, lists the long-term perspectives and introduces future work.

Chapter 1

Musculoskeletal Cervical Spine Anatomy and Biomechanics

To fully apprehend the geometrical and biomechanical complexity of the cervical spine, a thorough understanding of the musculoskeletal anatomy is primordial. Moreover, it is imperative to overview the current treatment options and associated mechanical and clinical complications to understand the clinical needs. This chapter briefly overviews the descriptive, muscular and functional anatomy. Also the global clinical context of this PhD-project is sketched.

The description of the cervical spine anatomy and biomechanics was mainly based on the work of Kapandji [2002], Kamina [2015] and Bonneau [2017].

Contents

1.1	Descriptive Anatomy	4
1.1.1	Global Structure and Function of the Spine	4
1.1.2	Osseous Components of the Cervical Spine	4
1.1.3	Cervical Intervertebral Joints and Connective Elements	5
1.2	Cervical Spine Musculature	7
1.2.1	Deep Muscles	8
1.2.2	Intermediate Muscles	8
1.2.3	Superficial Muscles	9
1.2.4	Suboccipital Muscles	9
1.3	Cervical Spine Biomechanics	10
1.4	Clinical Context	11

1.1 Descriptive Anatomy

1.1.1 Global Structure and Function of the Spine

Above the *sacrum*, the mobile vertebral column is a stack of twenty-four osseous structures, the *vertebrae*, separated by fibrocartilaginous shock absorbers, the intervertebral discs (IVD), connecting the head to the *pelvic* girdle. It supports and orients the head, always maintaining the two eyes on a horizontal line, regardless of the configuration and condition of the lower limbs. This flexible, yet rigid, structure ensures a stable posture and high mobility, whilst preserving the integrity of the spinal chord, through the interplay between the *vertebrae*, the associated IVDs, the ligaments and the muscles. Based on functional differences, the spine can be divided into three zones. From cranial to caudal, one distinguishes the cervical, thoracic and lumbar spine. The *sacrum* forms the connection with the *pelvic* girdle and consists of five fused *vertebrae*. At the most caudal end of the vertebral column, one finds the *coccyx*, a fusion of four to five *vertebrae* (Platzer [2012]; Kamina [2015]; Bonneau [2017]).

1.1.2 Osseous Components of the Cervical Spine

The cervical spine is composed of seven small *vertebrae*, eight when counting the *occiput* (C0). It constitutes the most cranial compensation system to keep the head on a horizontal plane above the *pelvis*. Functional and morphological differences necessitate a differentiation between the upper (C1-C2) and the lower (C3-C7) cervical spine (Kapandji [2002]; Rousseau *et al.* [2008b]; Ombregt [2013]; Kamina [2015]; Bonneau [2017]).

The two *vertebrae* of the upper cervical spine, i.e. *atlas* (C1) and *axis* (C2), are completely different in terms of geometry from each other and from the other cervical *vertebrae*. The *atlas* (Figure 1.1a) consists of two lateral masses interconnected with an anterior and posterior arch. The two *fossa* on the superior surface of the lateral masses articulate with the *occipital condyles*, while those on the inferior surface articulate with the articular processes of the *axis*. The lateral masses and the two arches encircle the vertebral *foramen*, which is subdivided into two regions by the transverse ligament. The anterior space is taken in by the *odontoid* process of the *axis*, in contact with the *odontoid fossa* on the internal face of the anterior arch. The posterior space is reserved for the spinal chord. The *axis* (Figure 1.1b) is characterised by the *odontoid* process or *dens axis*, around which the *atlas* rotates, on top of a vertebral body. Two small *pedicles* connect the posterior arch, formed by thick *lamina* and a bifid spinous process, with the vertebral body, thus defining the vertebral *foramen*. Infero-laterally, articular processes form the connection with the subjacent C3-*vertebra* (Kapandji [2002]; Rousseau *et al.* [2008b]; Ombregt [2013]; Kamina [2015]).

The C3 and the other four *vertebrae* of the lower cervical spine have a very similar architecture (Figure 1.1c). The vertebral body is small, but wide, and has saddle-shaped endplates. The superior one is delimited laterally by the so-called *unci* or *unciform* processes. The articular processes with their superior *facet* surfaces oriented upwards and outwards and their inferior surfaces inversely oriented, form the connection between the *vertebra* above and the subjacent one. The thin *lamina* attach the bifid spinous process to the vertebral body with flat *pedicles* (Kapandji [2002]; Rousseau *et al.* [2008b]; Ombregt [2013]; Kamina [2015]).

Apart from the *unci* and the bifid spinous processes, the *vertebrae* of the lower cervical

spine share a third unique feature, i.e. a transverse *foramen*, guiding the vertebral artery and vein. The C7 *vertebra* (Figure 1.1d) is an exception, as it has a long spinous process terminating at a single *tubercle*. Although a small transverse *foramen* is present, the vertebral artery and vein do not pass through, but rather in front of it. As such, the C7 *vertebra* forms the transition between the cervical and thoracic spine (Ombregt [2013]; Kamina [2015]).

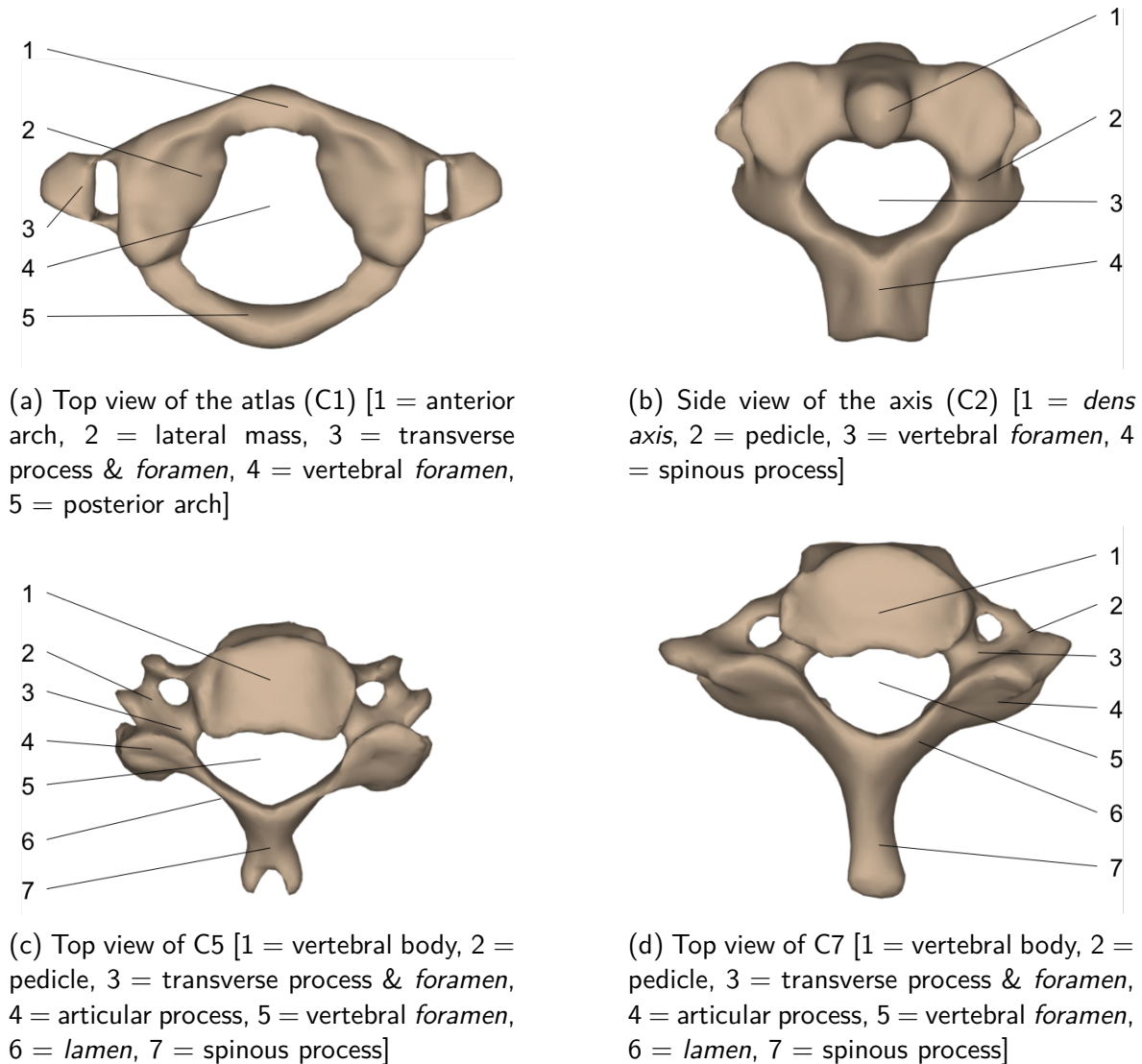


Figure 1.1: The osseous anatomy of four characteristic cervical *vertebrae*.

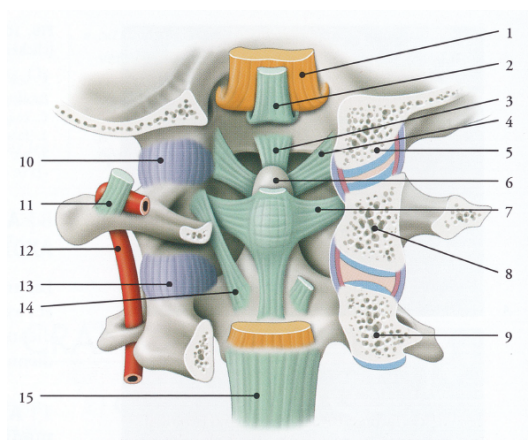
1.1.3 Cervical Intervertebral Joints and Connective Elements

The skull, with its *occipital condyles*, articulates with the corresponding *fossa* on the lateral masses of the *atlas* to form the *atlanto-occipital* joint. This spherical synovial joint allows flexion/extension and lateral inclination. Stability, in the clinical sense of the word, is provided by the joint capsule, the anterior and posterior *atlanto-occipital* membranes connecting the *foramen magnum* with the arches of the *atlas* and the *atlanto-occipital* ligament between the *jugular* and the transverse processes (Figure 1.2).

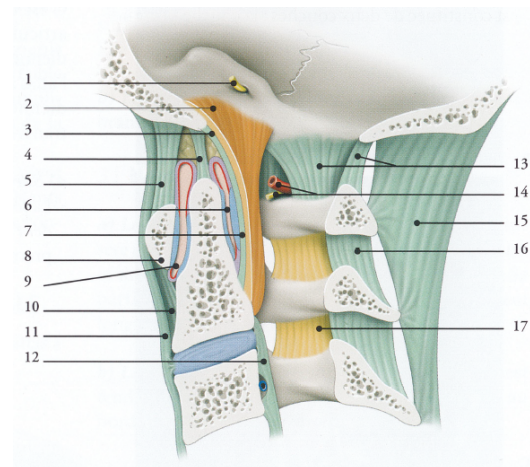
The cylindrical articulation between the *atlas* and the *odontoid* process is called the *atlanto-odontoid* joint and allows primarily rotation and a limited amount of flexion/extension and lateral inclination. The synovial contact between the *dens axis* and the anterior arch

of the *atlas* is maintained by the cruciform ligament, composed of the transverse ligament and a longitudinal section between the *foramen magnum* and the vertebral body of the *axis*, and the *ligamentum apicis dentis* between the *foramen magnum* and the apex of the *odontoid* process (Figure 1.2).

The convex inferior surfaces of the lateral masses of the *atlas* slide and roll over the convex superior surfaces of the articular processes of the *axis*, thus constituting the ovoid shaped *synovial atlanto-axoidal* joint. The joint capsules, together with the anterior *atlanto-axoidal* ligament between the anterior arch of the *atlas* and the vertebral body of the *axis* and the posterior *atlanto-axoidal* ligament between the posterior arch of the *atlas* and the *lamen* of the *axis* maintain joint stability (Figure 1.2). One could state that the combination of the C0-C1 and C1-C2 joints fulfils the same mechanical function as a universal joint (Kapandji [2002]; Swartz *et al.* [2005]; Ombregt [2013]; Kamina [2015]).



(a) Postero-anterior view of a frontal section of the upper cervical spine [3 = *ligamentum apicis dentis*, 4 = alar ligament, 5 = *occipital condyle*, 7 = transverse ligament (transverse section cruciform ligament), 8 = lateral mass *atlas*, 9 = articular process *axis*, 10 = capsule *atlanto-occipital* joint, 11 = *atlanto-occipital* ligament, 13 = capsule *atlanto-axoidal* joint]



(b) Medio-lateral view of a sagittal section of the upper cervical spine [3 = longitudinal section cruciform ligament, 5 = anterior *atlanto-occipital* membrane, 10 = anterior *atlanto-axoidal* ligament, 13 = posterior *atlanto-occipital* membrane]

Figure 1.2: The osseo-ligamentous anatomy of the upper cervical spine (adapted from Kamina [2015])

The intervertebral joints of the lower cervical spine are very similar to those in the other spinal segments and are composed of an intervertebral *symphysis*, characterised by the IVD, anteriorly and the *zygapophysial* or facet joints postero-laterally.

The IVD functions as a shock absorber, but also provides flexibility to the spine in flexion/extension, lateral inclination and to a lesser extent axial rotation. It consists of a highly hydrated gel-like substance (70% to 80% water), the *nucleus pulposus*, surrounded by several layers of fibrous tissue, the *annulus fibrosus*. The anterior and posterior longitudinal ligaments joining the adjacent vertebral bodies anteriorly and posteriorly, contribute to the joint stability (Figure 1.3).

The facet joints are composed of the superior facet surface of the *vertebra* below and the corresponding inferior facet surface of the *vertebra* above and are essentially planar *synovial* joints allowing sliding movements. Five ligaments provide stability, i.e. the joint

capsule, the yellow ligament between the *lamina*, the intertransverse ligament between the transverse processes, the interspinous ligament joining the spinous processes and the supraspinous ligament on the tubercles of the spinous processes (Figure 1.3).

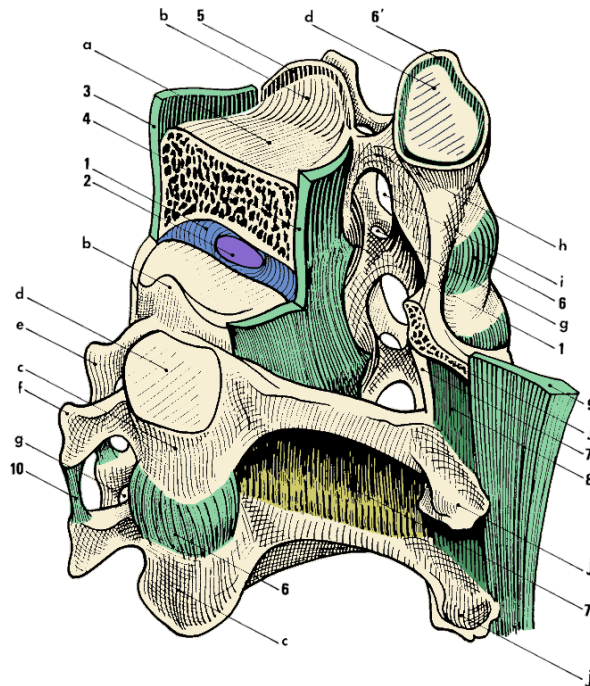


Figure 1.3: Postero-lateral view of the lower cervical spine (adapted from Kapandji [2002]) [a = superior endplate vertebral body, b = *unciform* process, e = transverse process, f = articular process (facet joint), j = spinous process, 1 = *annulus fibrosus*, 2 = *nucleus pulposus*, 3 = anterior longitudinal ligament, 4 = posterior longitudinal ligament, 5 = facet capsule, 7 = yellow ligament, 8 = interspinous ligament, 9 = supraspinous ligament, 10 = intertransverse ligament]

Particular for the cervical spine, is the presence of the *uncovertebral* joint, resulting from an oblique cleft in the lateral part of the IVD, limited by the *unci* and the uncovertebral ligament. However, some authors considered these as pseudo joints, as they lack articular cartilage and *synovial* fluid (Kapandji [2002]; Swartz *et al.* [2005]; Ombregt [2013]; Kamina [2015]).

A more complete description of the insertion and origin of the cervical spine ligaments can be found in Appendix A.

1.2 Cervical Spine Musculature

The spinal musculature is a redundant system, where each muscle has several functions and where for each loading configuration various muscle activation patterns are possible. Muscles with a short lever arm are activated for precise low-amplitude movements, while those with a longer lever arm are recruited for larger movements. Certain muscles are directed obliquely downwards and away from the spine, others are directed towards the spine. There are mono-articular muscles, covering merely one intervertebral joint, while others are pluri-articular (Bernstein [1967]; Kapandji [2002]; Pomero *et al.* [2004]; Platzer [2012]; Kamina [2015]; Bonneau [2017]).

Generally, the spinal musculature is subdivided into four groups, based on their location with respect to the spine. One distinguishes the deep muscles lying closest to the spinal

joint and having the shortest lever arm, the intermediate and the superficial muscles. The fourth group is composed of the suboccipital muscles, responsible for the small movements of the C0-C2 universal joint. The following provides an overview of the main muscles. A more precise description of these muscles, i.e. insertion, termination and function, is given in Appendix A.

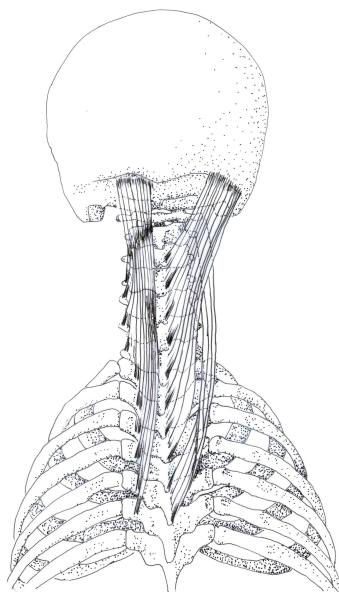
1.2.1 Deep Muscles

Located posteriorly on both sides of the cervical spine, one finds the extensor muscles, with insertion on the skull, i.e. *splenius capitis*, *longissimus capitis* and *semispinalis capitis*, or with insertion on the cervical spine, i.e. *splenius cervicis*, *longissimus cervicis* and *semispinalis cervicis* (Figure 1.4a).

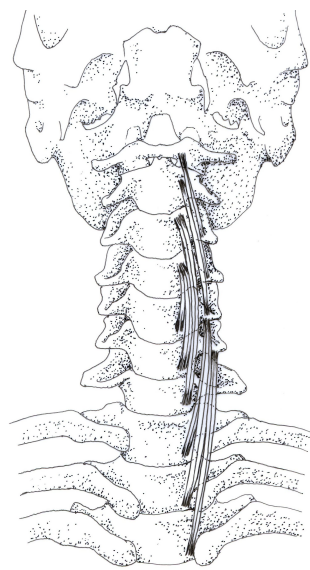
The *longus colli* and *longus capitis* are located anteriorly with insertions on the cervical spine and skull, respectively, and flex the cervical spine and the head. Unilateral contraction leads to ipsilateral rotation or inclination (Figures 1.4b and 1.6).

The *scalenus* muscles, i.e. *scalenus anterior*, *scalenus medialis* and *scalenus posterior*, connect the cervical spine to the first and second ribs of the thorax. As such, they can be recruited as accessory inspiratory muscles, as well as frontal and lateral flexors (Figure 1.4c).

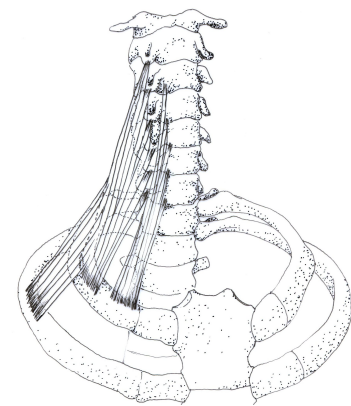
The *levator scapula* joins the cervical spine and the scapula. This muscle lifts the scapula when its exertion point lies at its insertion. In case its exertion point lies at its termination, it extends the cervical spine under bilateral contraction or inclines it under unilateral contraction.



(a) Posterior view of the cervical spine, with a schematic representation of the *semispinalis capitis* and *cervicis* (left) and the *splenius capitis* and *cervicis* (right)



(b) Anterior view of the cervical spine, with an indication of the *longus colli*



(c) Antero-superior view of the cervical spine with the anterior, medial and posterior *scalenus muscles* schematically represented

Figure 1.4: The deep cervical spine muscles (courtesy of Mathias Bonneau, with permission (Bonneau [2017]))

1.2.2 Intermediate Muscles

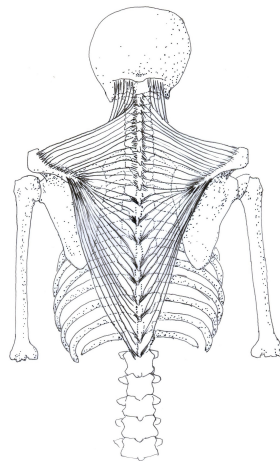
The *suprahyoideus* and *infrahyoideus* are located anteriorly and connect the *hyoid* bone to the *mandible* and to the *sternum*, respectively. Although their primary function is to move the *hyoid* bone, they can induce head and cervical spine flexion with the mastication muscles keeping the mouth closed

1.2.3 Superficial Muscles

Closest to the skin and covering multiple joints, one find the *sterno-cleido-mastoideus* and the *trapezius*.

The *trapezius* covers a large part of the dorsal side of the neck. Bilateral contraction extends the cervical spine, while unilateral contraction rotates and inclines it ipsilaterally (Figure 1.5a).

The *sterno-cleido-mastoideus* crosses the neck on both sides diagonally. A unilateral contraction leads to a contralateral rotation and an ipsilateral inclination of the head. Under bilateral contraction, this muscle is able to flex or extend the head and cervical spine, depending on whether or not the other muscles rigidified the spine. Incidentally, it can also function as an inspiratory muscle when its exertion point coincides with its insertion (Figure 1.5b).



(a) Posterior view of the back, with an indication of the *trapezius*



(b) Lateral view of the cervical spine and the *sterno-cleido-mastoideus*

Figure 1.5: The superficial cervical spine muscles (courtesy of Mathias Bonneau, with permission (Bonneau [2017]))

1.2.4 Suboccipital Muscles

Small muscles with a relatively short lever arm operate the universal C0-C2 joint, inducing precise low-amplitude movements.

Antero-laterally, one finds the *rectus capitis anterior* and the *rectus capitis lateralis*, that flex the head when the muscles on both sides contract, or incline the head ipsilaterally under unilateral contraction.

The *rectus capitis posterior major* and *minor* and the inferior and superior *obliquus*, are located posteriorly. Bilateral contraction of these muscles extends the head and the upper

cervical spine, while unilateral contraction inclines and rotates the head ipsilaterally (Figure 1.6).

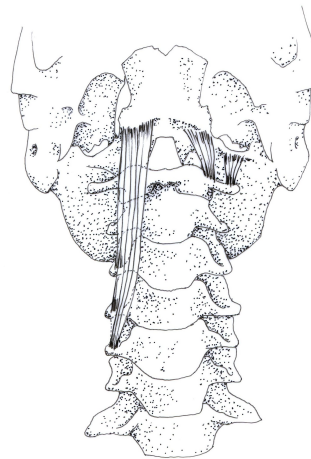


Figure 1.6: Anterior view of the cervical spine, with an indication of the *longus capitis* (left), the *rectus capitis anterior* and the *rectus capitis lateralis* (right) (courtesy of Mathias Bonneau, with permission (Bonneau [2017]))

1.3 Cervical Spine Biomechanics

The decreasing obliquity of the facet surfaces from cranial to caudal and the antero-posterior IVD height difference ¹ is responsible for the physiological lordosis (ventrally convex spinal curvature) of the cervical spine in the sagittal plane. Asymptomatic straight, sigmoid-shaped and kyphotic curvatures are also prevalent (Ombregt [2013]). The curvature becomes kyphotic (dorsally convex) in the thoracic and lordotic again in the lumbar spine. It has been shown that these curvatures improve the resistance of the spine to axial compression (Kapandji [2002]; Bonneau [2017]). In the frontal plane, the spine is straight, although slight asymptomatic deviations are common (Kamina [2015]).

The spinal functional architecture can be compared to a ship's mast: the stacking of the vertebral bodies anteriorly and the facet joints posteriorly connects the head with the pelvic girdle. Ligamentous and muscular connections exist between each pair of *vertebrae*, linking the spine to its basis. As such, a highly flexible structure is obtained, which can be rigidified when a mechanically stable configuration is required (Panjabi [1992a]; Kapandji [2002]; Bonneau [2017]).

A schematic representation of the cervical functional spinal unit (FSU) ², is given in figure 1.7. The FSU is surrounded by muscular and ligamentous tissue. External forces and internal loads due to muscular contraction are transferred to the adjacent levels through the IVD and the facet joints.

The ligaments not only stabilise the intervertebral joints, but also function as displacement sensors prompting the muscles to act (Panjabi [1992a]). The role of the spinal musculature is twofold: on the one hand they act as motion actuators and on the other hand they stabilise the spine by exerting axial forces on the spine during co-contraction. A muscle globulises when it contracts, thus inducing transverse forces limiting inter-vertebral movement, a secondary source of stability (Kapandji [2002]; Bonneau [2017]; Lecompte *et al.*).

¹The IVD is thicker anteriorly than posteriorly (Ombregt [2013])

²The ensemble of two *vertebrae* and the IVD in between them, is defined a functional spinal unit (FSU)

With its self-regulating functioning, the IVD contributes as well to the stability of the spine. Indeed, under asymmetric loadings, the fibres in the *annulus* contralateral to the load are tensioned. The *nucleus* gets pressurised and pushes against the *annulus* ipsilaterally to the load. This induces a restoring moment which limits the range of motion (RoM) (Ombregt [2013]; Kapandji [2002]).

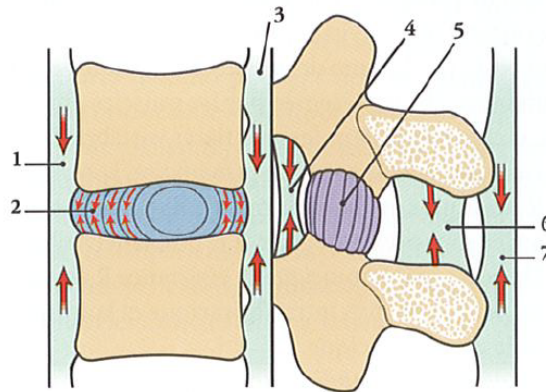


Figure 1.7: A schematic representation of the FSU (adapted from Kamina [2015]). The ligaments, together with the IVD and the muscles, stabilise the intervertebral joint and redistribute the charges.

Due to the architecture of the *vertebra*, i.e. the presence of the *unci* and the facet orientation, the functioning of the IVD and ligament tensioning, pure motion is not possible in the cervical spine: lateral inclination is always combined with ipsilateral rotation and vice-versa. One speaks of movement coupling (Ombregt [2013]; Kapandji [2002]).

1.4 Clinical Context

According to the Institute for Health Metrics and Evaluation (IHME), in 2016 the second most important cause of disease burden, expressed in disability-adjusted life years (DALY)³, was lower back and neck pain. Figure 1.8 visualises to what extent each type of disorder contributed to the total disease burden in high income countries. Lower back and neck pain represent more than 7% of the DALYs and gain importance each year at a rate of 0.4% (Institute for Health Metrics and Evaluation (IHME) [2017]). As a matter of fact, more than 50% of the population aged over 55 years encounters degenerative changes of the cervical spine (Malcolm [2002]; Wang *et al.* [2009]). The prevalence of neck pain increases with age, but also gender, race and geographical factors seem to be correlated (Fejer *et al.* [2006]). In middle-income countries the same trends are visible, albeit with a greater relative importance of cardiovascular diseases (Institute for Health Metrics and Evaluation (IHME) [2017]).

Numerous retrospective database analyses, having covered altogether the period between 1990 and 2013, revealed a clear increasing trend in utilisation and rates of cervical spine surgery and in related hospital charges. The age at surgery also increased over time, but length of stay (LOS), mortality rate and the number of complications did not change much (Patil *et al.* [2005]; Wang *et al.* [2007, 2009]; Marawar *et al.* [2010]; Marquez-Lara *et al.*

³DALY is a metric for disease burden and is defined as the number of life years lost due to disability (World Health Organisation [2016])

[2014]; Alosch *et al.* [2015]; Liu *et al.* [2016]). The explanation for these trends is multifold. Although stagnation is near, the population is constantly ageing. Improved diagnostics, more efficient imaging technology and the increasing number of surgeons, made it possible for more patients to gain access to primary health care. Also the growing awareness and evidence of the cost-efficiency and effectiveness of spinal surgery, have had an important influence (Patil *et al.* [2005]; Marawar *et al.* [2010]; Baaj [2017]).

In general, three types of neck pain are differentiated: axial neck pain, *radiculopathy* and *myelopathy* (Todd [2011]). Axial neck pain is described as pain sensed along the spinal column, often with a mechanical nature, while *radiculopathy* and *myelopathy* are due to irritation of the nerve roots and spinal chord, respectively.

The most common diagnosis is cervical *spondylosis*⁴, characterised by IVD degeneration⁵ and by the formation of *osteophytes*⁶. Facet joint cartilage degeneration, i.e. *osteoarthritis*, might occur as well. When this leads to nerve root or spinal chord impingement, *radiculopathy* or *myelopathy* might appear. Disc herniation, mostly affecting the lower cervical spine, is the second most common diagnosis. The *nucleus* prolapses through a tear in the *annulus fibrosus* and may compress the nerve roots or spinal chord, leading once again to *radiculopathy* or *myelopathy*. The third most common diagnosis is cervical *stenosis*, i.e. the narrowing of the intramedullary canal. This can be caused by disc bulging, *osteoarthritis*, tumours or thickened ligaments, and might lead to spinal chord pinching, possible inducing *myelopathy* (McClure [2000]; Malcolm [2002]; Wang *et al.* [2007]; Korinth [2008]; Wang *et al.* [2009]; Bible and Kang [2016]; Shim [2016]).

Radiculopathy and axial neck pain can be treated with conservative therapy, i.e. with anti-inflammatory medication, bed rest, neck immobilisation, muscle strengthening exercises or traction (McClure [2000]; Korinth [2008]; Todd [2011]). When such an approach does not lead to complete pain relief, surgery is necessary. *Myelopathy* on the other hand, almost always necessitates a surgical intervention.

Depending on the clinical evaluation of the patient, the surgeon might opt for decompression surgery, *discectomy*⁷ with or without *arthrodesis*⁸ or total disc replacement (TDR). The cervical spine can be approached anteriorly or posteriorly through a large incision or by using minimally invasive methods (Patil *et al.* [2005]; Wang *et al.* [2007]; Korinth [2008]; Wang *et al.* [2009]; Goel *et al.* [2012]; Liu *et al.* [2016]).

Regarding decompression surgery, there are generally two options: *foraminotomy* and *laminectomy*. *Foraminotomy* involves relieving the pressure on nerve roots or spinal chord by removing bony protrusions or the prolapsed part of the IVD. During *laminectomy*, the *lamina* and spinous processes are removed. In some cases, both techniques are combined. The use of posterior or anterior instrumentation (screw-rod or screw-plate systems) is not always necessary. Even after *laminectomy*, the facet joints and IVD maintain spinal stability (unless the IVD is degenerated). In case of multilevel *laminectomy*, instrumentation is used to prevent sagittal deformation (Korinth [2008]).

In about 80% of the cases, anterior cervical fusion (ACF) following a complete or partial

⁴*Spondylosis* refers to wear and tear of the *vertebra* and IVD (McClure [2000])

⁵Disc dehydration, which is part of the normal ageing process, can lead to a decreased IVD thickness, a phenomenon commonly known as degenerative disc disease

⁶*Osteophytes* are bony protrusions formed at the edges of the facet joint surfaces and vertebral endplates, in an attempt to restore spinal stability and to unload the facet joints

⁷The removal of the IVD is called *discectomy*

⁸*Arthrodesis* refers to the fusion of two or more vertebral levels using bone grafts

discectomy is performed (Marquez-Lara *et al.* [2014]; Tasiou *et al.* [2017]; Liu *et al.* [2016]). It consists of the removal of the IVD and inserting interbody cages, filled with bone grafts, in the disc space. Stability is provided with screw-plate systems fixed to the adjacent *vertebrae*. A posterior approach (posterior cervical fusion, PCF) might be used as an alternative or combined with the anterior approach (Patil *et al.* [2005]; Wang *et al.* [2007]; Korinth [2008]; Wang *et al.* [2009]; Marquez-Lara *et al.* [2014]; Liu *et al.* [2016]). However, as it comes with a higher incidence of complications (10.8% vs. 9%) (Nasser *et al.* [2010]; Bydon and Gokaslan [2015]), a higher mortality rate (12.6% vs. 2.9%) (Marquez-Lara *et al.* [2014]) and a longer LOS (7.5 days vs. 2 days) (Liu *et al.* [2016]; Marquez-Lara *et al.* [2014]), it is a less popular choice. In case one aims for *arthrodesis* at multiple levels, the *vertebrae* in between the IVDs to be resected might be removed as well, as fusion rates are shown to increase with decreasing number of bony interfaces (Bible and Kang [2016]).

Commonly encountered clinical complications are *dysphagia*⁹ and/or voice problems (1.7% to 10.1%), nerve root and/or spinal chord injuries (0.2% to 2.6%) and vertebral artery injuries (0.3% to 4.0%) (Abumi *et al.* [2000]; Fountas *et al.* [2007]; Wang *et al.* [2007]; Campbell *et al.* [2010]; Nasser *et al.* [2010]; Bible and Lee [2015]; Cheung and Luk [2016]; Tasiou *et al.* [2017]). Frequently reported mechanical complications are screw loosening (0.1% to 1.3%), screw breakage (2.1% to 3.8%), plate fracture (around 1.4%) and implant or graft subsidence (19.3% to 42.5%) (Fountas *et al.* [2007]; Nasser *et al.* [2010]; Okamoto *et al.* [2012]; Belin *et al.* [2014]; Cheung and Luk [2016]; Tasiou *et al.* [2017]). The most pressing complications related to *arthrodesis* are the consequent overloading of the segments adjacent to the fused segments, i.e. adjacent segment disease (ASD) (1% and 15%), and incomplete fusion or *pseudarthrosis* (0% and 50%) (Belin *et al.* [2014]; Bible and Kang [2016]; Bevevino and Hilibrand [2016]; Cheung and Luk [2016]; Tasiou *et al.* [2017]). TDR, a technique in which the native IVD is replaced by a prosthetic one (ball-and-socket, sandwich or elastomer design), aims to conserve the spinal mobility, thus reducing the risk for ASD. Although the reoperation rate for ASD could indeed be reduced significantly, other complications, such as wear debris migration and implant subsidence, might arise (Goel *et al.* [2012]; Blumenthal *et al.* [2013]; Delamarter and Zigler [2013]).

The developmental mechanisms of cervical spine degeneration and the associated surgical complications are not yet fully understood. However, a relationship between these issues and spinal overloading, postural abnormalities and muscular dysfunction has been established (Falla *et al.* [2007]; Fernández-de-las Peñas *et al.* [2008]; Cheng *et al.* [2014]; Alpayci *et al.* [2016]). Spinal surgery is a complex intervention and requires thorough planning and intensive post-operative care to guarantee a satisfactory outcome (Kasimatis *et al.* [2009]; Belin *et al.* [2014]). Important factors to be taken into consideration are the patient's geometry, mechanical properties and posture (Rousseau *et al.* [2008a]; Laville *et al.* [2009]). For example, it has been shown with a generic FE model that the performance of TDR is influenced by the spinal sagittal curvature (Chen *et al.* [2018]) and that decreased bone quality affects the outcome of an *arthrodesis* (Natarajan *et al.* [2000]). Muscle forces and the associated spinal loading should be considered as well. Indeed, through 3D modeling, it has been shown that resection of certain muscles during surgery may lead to an altered muscle activation pattern post-operatively (Bresnahan *et al.* [2010]) and MR imaging has revealed histological changes of the muscles post-operatively (Motosuneya *et al.* [2006]). Considering fat infiltrated muscular tissue and decreased joint resistance, the altered muscle

⁹*Dysphagia* is the difficulty or discomfort in swallowing and might occur after anterior cervical spine surgery as this necessitates retraction of the *oesophagus* and the vocal chord to the side to access the spine

activation pattern might not be able to conserve the spinal integrity after surgery. With the number of cervical spine surgeries increasing yearly and because of the constantly ageing population (although stagnation is almost reached), this topic becomes increasingly important.

Chapter 2

Literature Review

The description of the broader clinical context of this project (see Chapter 1) has shown that a subject-specific modeling approach, considering the morphology, material properties and posture of the subject, as well as the active muscle forces maintaining this posture, is essential to more efficiently plan surgeries and post-operative care and to fully understand spinal biomechanics, the mechanical implications of degeneration and post-operative complications.

This chapter overviews the scientific literature regarding subject-specific finite element modeling and muscle force quantification. One concludes with a synthesis of this literature and an overview of the objectives of this PhD.

Contents

2.1	Muscle Force Quantification	16
2.1.1	EMG-based	16
2.1.2	Optimisation	18
2.1.3	EMG-assisted optimisation	19
2.1.4	Proprioception-based Control Model	20
2.1.5	Input Data	21
2.2	Finite Element Modeling of the Cervical Spine	22
2.2.1	Model Geometry	22
2.2.2	Discretisation	25
2.2.3	Material Properties	26
2.2.4	Boundary and Initial Conditions	28
2.2.5	Verification and Validation	28
2.2.6	FE Modeling of the Instrumented Cervical Spine	28
2.3	Synthesis and Project Objectives	31

2.1 Muscle Force Quantification

Chapter 1 highlighted the importance of the cervical spine musculature in maintaining a stable head and neck posture, in protecting the spinal chord and in properly orienting the ocular system (Rousseau *et al.* [2008a]; Bonneau [2017]; Lecompte *et al.*; Bonneau). Uni- or bi-lateral contraction of the muscles enables the orientation of the head/neck complex, while co-contraction maintains stability. Co-contracting muscles exert compressive forces on the spine, thus rigidifying the system. Because they are isochoric, i.e. they maintain a constant volume when contracting, and contained within an inextensible *fascia*, they simultaneously generate axial forces onto the spine, a secondary stabilisation mechanism. It is therefore not a coincidence that a relationship between abnormal muscle behaviour on the one hand and spinal disorders and neck pain on the other hand could be established (Falla *et al.* [2007]; Fernández-de-las Peñas *et al.* [2008]; Cheng *et al.* [2014]; Alpayci *et al.* [2016]).

Note that, while the implications of the muscle's active roll are rather straightforward, its passive function to maintain spinal stability is subject to debate. The clinical and mechanical interpretations of the term 'stability' are different. From a mechanical point of view, 'stability' refers to an equilibrium state for which the potential energy has reached a minimum. A system is unstable when its potential energy is at a maximum, i.e. a small perturbation suffices to bring the system out of equilibrium. In a clinical context, 'stability' is often linked to rigidity, cohesion of the composing structures or joint displacements. It is frequently described as the occurrence of excessive intervertebral joint displacements, thus inducing spinal chord or nerve root impingement (Panjabi *et al.* [1989]; Panjabi [1992a,b]). The role of the spinal musculature, together with the osseoligamentous components, is to keep these joint displacements within the physiological limits. *In-vitro* experiments with simulated muscle forces, have shown that this hypothesis might indeed be valid *in-vitro* (Panjabi *et al.* [1989]; Wilke *et al.* [1995]; Panjabi *et al.* [2001b]; Kettler *et al.* [2002]).

Quantification of the spinal muscle force distribution and the resulting intra-articular loads in various configurations seems essential, as this could provide valuable information for a biomechanical and clinical evaluation of the patient (Moroney *et al.* [1988a]; Choi [2003]). However, due to the well-known muscle redundancy issue, i.e. multiple muscle force patterns are possible to achieve a certain configuration or different muscles can be recruited to fulfil the same action (Bernstein [1967]), this still proves a technical challenge.

Literature proposes different strategies to approach the muscle redundancy problem, of which the most frequently encountered techniques are listed in Table 2.1. Generally, these can be subdivided into three different groups: the EMG-driven, the optimisation and the EMG-assisted optimisation techniques. In the following, each of these techniques are detailed, with a special attention to the model assumptions, the proposed mathematical tools, the required input data and model evaluation. A fourth strategy that explicitly integrates the hypothesis on the role of spinal muscles in preserving the spinal integrity, developed at our institute, is discussed as well.

Although most of these techniques are applicable for dynamic analyses, the focus is on quasi-static analyses. As a proposed technique might have given rise to multiple publications, only the first one, detailing the procedure, is listed. The procedures themselves did not evolve much, yet the computation of the input data did. Nevertheless, more recent contributions are listed as well.

Method	Spinal Segment	Joints covered	Subject-specific Input	Method	Antagonism	Force Ligaments/ Passive Muscle	Representation Muscles	Muscle Geometry	Calculation External Load	Mechanical Equilibrium	Physiological Validity	Evaluation	Recent Uses
EMG-based	McGill (1992)	Lumbar	Single	EMG, ground reaction forces & 3D digitised landmarks	EMG vs. muscle force & computation common gain	Stress-strain curves from literature	Fascicle + anatomical CSA	Scaled 3D model from literature	Segment mass & kinematics	Yes	Yes	No	Cholewicki et al. (1995) Choi et al. (1999)
	Gramata et al. (1993)	Lumbar	Single	EMG, ground reaction forces & 3D digitised landmarks	EMG-based	No	Fascicle + anatomical CSA	Scaled 3D model from literature	Estimated segment mass + measured forces + kinematics	No	Yes	No	Gagnon et al. (2001)
	Nussbaum et al. (1998)	Lumbar	Single	EMG, ground reaction forces & 3D digitised landmarks	EMG vs. muscle force & call ration	Stress-strain curves from literature	Fascicle + anatomical CSA	Scaled 3D model from literature	Segment mass + ground reaction forces	No	Yes	Comparison with <i>in-vivo</i> measured joint load	Jia et al. (2011)
	Schultz et al. (1983)	Lumbar	Single	EMG & 3D digitised landmarks	Min(muscle stress) & Min(spine compression)	No	Fascicle + anatomical CSA	Cadaver data (literature)	Segment mass + measured forces + kinematics	Yes	No	No	Cholewicki et al. (1995)
	Hellier et al. (1985)	Cervical	Single	No	Min(joint stresses)	Part of objective function	Fascicle + anatomical CSA	Literature	Segment mass + measured forces	Yes	No	Comparison with EMG-data from 5 subjects	
	Bean et al. (1988)	Lumbar	Single	No	Min(muscle force intensity) & min(muscle forces)	No	Fascicle + anatomical CSA	Literature	Segment mass	Yes	No	No	Choi et al. (1999) Gagnon et al. (2001)
	Moroney et al. (1988)	Cervical	Single	Location exertion point forces	Min(muscle force intensity) & Min(joint compression)	No	Fascicle + anatomical CSA	Scaled 3D model from literature	Segment mass + measured forces	Yes	No	Comparison with EMG-data from 14 subjects	
	Goel et al. (1993)	Lumbar	Single	EMG, CT-data & 3D digitised landmarks	Min(muscle force intensity) & Min(muscle stresses - max. stress) ^{1/3}	Based on FE model	Fascicle + anatomical CSA	CT-data	Ground reaction forces + CT-data	Yes	No	No	
	Han et al. (1995)	Lumbar	Single	EMG, CT-data & 3D digitised landmarks	Min(muscle stresses - max. stress) ^{1/3}	No	Fascicle + anatomical CSA	CT-data & literature	Segment mass	Yes	No	Comparison with EMG-data from 5 subjects	
	Stokes et al. (2001)	Lumbar	Multiple	No	Min(muscle stresses) ^{1/3} + Min(muscle displacement) ^{1/3} ; Min(muscle displacement) ^{1/3} ; Min(muscle displacement) ^{1/3}	No	No	Literature	Measured forces	Yes	No	Comparison with EMG-data from 14 subjects	
Optimisation	Chancey et al. (2003)	Cervical	Multiple	3D digitised landmarks from cadaver	Min(ratio muscle force to max force) -> min(muscle fatigue)	Based on FE model + stress-strain curves from literature	Fascicle + anatomical CSA	Cadaver & MRI data (literature)	Segment mass	Yes	No	No	
	Eqzuerro et al. (2004)	Lumbar	Single	Kinematics	Min(muscle stresses) ^{1/3}	Based on FE model	Fascicle + anatomical CSA	Scaled 3D model from literature	Segment mass	Yes	No	No	Arjmand et al. (2006b) Arjmand et al. (2006c) Arjmand et al. (2009) Azari et al. (2017) Ghezalbash et al. (2016a,b, 2018)
	Arjmand et al. (2006)	Lumbar	Multiple	EMG, ground reaction forces & 3D digitised landmarks	Min(muscle stresses) ^{1/3}	Based on FE model + stress-strain curves from literature	Fascicle + anatomical CSA	Literature	Ground reaction forces & kinematics	Yes	No	No	
	Han et al. (2011)	Lumbar	Multiple	No	Muscle forces constituting follower load minimising joint load (stability hypothesis)	No	Fascicle + anatomical CSA	Literature	Literature	Yes	No	No	
	Han et al. (2012)	Lumbar	Multiple	Antropometric data (from other <i>in-vivo</i> study)	Min(muscle activation)	Stress-strain curves from literature	Fascicle + anatomical CSA	Scaled 3D model from literature (AnyBody)	From scaled AnyBody model	Yes	No	Literature (EMG + IVD Implant)	
	Hajhosseini et al. (2014)	Lumbar	Multiple	Antropometric data	Min(muscle stresses) ^{1/3} + second derivatives potential energy > 0 (stability hypothesis)	No	Fascicle + anatomical CSA	Literature	Literature + kinematics	Yes	No	Literature (intradiscal pressure)	Hajhosseini et al. (2015) Mohammadi et al. (2015)
	Cholewicki et al. (1994)	Lumbar	Single	EMG & 3D digitised landmarks	EMG vs. muscle force + computation common gain + Min(muscle force correction coefficients)	Stress-strain curves from literature	Fascicle + anatomical CSA	Cadaver data (literature)	From scaled model	Yes	Yes	No	Cholewicki et al. (1995) Cholewicki et al. (1996) Gagnon et al. (2001) Arjmand et al. (2009) Mohammadi et al. (2015)
	Choi et al. (1999)	Cervical	Single	EMG & ground reaction forces	EMG-based	No	Fascicle + anatomical CSA	Scaled 3D model from literature	Segment mass + force measurements	Yes	Yes	No	Choi (2003)
	Gagnon et al. (2011)	Lumbar	Multiple	EMG, ground reaction forces & 3D digitised landmarks	EMG-based	Stress-strain curves from literature	Fascicle + anatomical CSA	Scaled 3D model from literature	Ground reaction forces	Yes	Yes	No	Mohammadi et al. (2015) Gagnon et al. (2016)

Table 2.1: Non-exhaustive overview of the frequently cited models for muscle force quantification [CSA: cross-sectional surface area, FBD: free-body diagram, Min.: minimisation]

2.1.1 EMG-based

EMG-based techniques integrate a direct relationship between the measured EMG-signal, representing the electrical potential a muscle cell produces when activated by the nervous system, and the muscle contraction force. Usually, the subjects are asked to perform certain tasks, such as resisted flexion, while monitoring their kinematics, i.e. by tracing 3D reflective fiducial markers with an optoelectronic system, and measuring the reaction forces. Surface EMG is recorded with electrodes placed on the skin surface around a specific intervertebral joint of interest. The EMG data is normalised with respect to the data recorded during maximum voluntary contractions.

Both McGill [1992] and Granata and Marras [1993] assumed that the muscle force could be linearly correlated with the corresponding normalised EMG-signal. A common gain, i.e. a global calibration factor, was calculated by matching the measured with the predicted joint moments. A similar strategy was used by Nussbaum and Chaffin [1998] and Jia *et al.* [2011], yet a more complex 4-parameter exponential law was assumed.

In either of these models, the joint moments were calculated from a 3D linked-segment model, the measured (reaction) forces and the recorded kinematics. Muscle cross-sectional geometry was derived from the literature and scaled based on anthropometric data.

McGill [1992] and Nussbaum and Chaffin [1998] differentiated the muscle's active from its passive force components and took into consideration the ligament forces. To determine the part of the joint moment taken up by these passive elements, the literature-based stress-strain curves were evaluated based on the kinematic data. The remaining joint moment was distributed among the muscles, based on the EMG data.

EMG-based techniques generally yield physiologically acceptable muscle force patterns, as the EMG data is directly integrated in the process. However, the solution not necessarily maintains mechanical equilibrium. A clinical implementation is difficult as motion capture data, reaction forces and EMG recordings are to be acquired. Moreover, apart from Choi and Vanderby Jr. [1999], none of the listed studies treated cervical spine muscle force quantification. Most studies focussed on the lumbar spine.

2.1.2 Optimisation

The most frequently described technique is the mathematical optimisation of an objective function incorporating certain physiological principles. A wide variety of approaches have been described. After determining the joint load from the estimated body segment mass, the measured external forces and the kinematic data, Schultz *et al.* [1983] estimated the muscle forces in an iterative optimisation scheme: the maximal muscle contraction stress was iteratively adjusted while minimising the joint compression force. The objective was to minimise both the contraction intensity and joint compression. Bean *et al.* [1988] adjusted this strategy by sequentially solving two optimisation problems. Instead of iteratively adjusting the muscle contraction intensity, the authors first looked for the optimal contraction stress, which was then used as an upper bound in the second optimisation, aiming to minimise the joint compression. The resulting muscle forces balanced the external loads, estimated from the body segment mass. Moroney *et al.* [1988a] correlated the predicted muscle forces, obtained with this technique, with EMG-recordings for different modeled configurations. The authors observed a high positive correlation for the anterior muscles and a weak one for the posterior muscles. In these three studies, a single joint was considered and muscle geometry was obtained from the literature. Helleur *et al.* [1985] proposed a

similar procedure, yet the contributions of the passive elements, such as the ligaments, were integrated in the objective function. However, the optimisation was merely based on joint stress minimisation and piloted by the estimated body segment mass and measured external forces.

Goel *et al.* [1993] and Han *et al.* [1995] used a different approach to estimate the muscle forces, based on subject-specific muscle geometric data obtained from CT-imaging. From the kinematics data, the measured external forces and the body segment mass, estimated from regression models described in the literature, the external joint load could be determined. Based on the minimisation of the cubed difference between the muscle stress and the corresponding maximal allowable muscle stress, the joint moments were redistributed among the muscles. Contrary to Han *et al.* [1995], Goel *et al.* [1993] also quantified the contribution of the ligament forces with an FE model, which was subjected to the same angular displacements as recorded experimentally. Han *et al.* [1995] could establish, as did Moroney *et al.* [1988a], a linear correlation between the predicted forces and the recorded EMG-signals.

Ezquerro *et al.* [2004] and Arjmand and Shirazi-Adl [2006] also combined optimisation with FE modeling to estimate the joint load and associated muscle forces. Two major differences were noted with Goel *et al.* [1993]. Firstly, the authors minimised the sum of cubed muscle stresses, instead of the cubed difference between the muscle stress and maximal allowable muscle stress. Secondly, the FE model was evaluated iteratively to estimate the joint load. In each iteration, the required forces and moments corresponding to the imposed kinematics were re-evaluated with the muscle force predictions and kinematics as boundary conditions. Arjmand and Shirazi-Adl [2006] also partitioned the predicted muscle forces into passive and active components, based on the evaluation of the stress-strain curves extracted from the literature. In these two studies the muscle geometry data was obtained from the literature. Apart from the kinematics and external force data, the model input was thus not subject-specific. Ghezalbash *et al.* [2016] dealt with this issue by adjusting both the muscle geometry and the FE model to the subject under study, based on gender, age, height and weight.

Hajihosseinali *et al.* [2014] expanded the method proposed by Arjmand and Shirazi-Adl [2006], by integrating the concept of spinal stability in the optimisation process. The joint load was again distributed among the muscles by minimising the sum of cubed muscle stresses, but this time, the second derivative of the potential energy was forced to remain positive. Without using FE modeling, Stokes and Gardner-Morse [2001] also attempted to include spinal stability. A multi-criteria cost function was proposed, minimising simultaneously the sum of squared global and local intervertebral joint displacements, the sum of squared intervertebral forces, the sum of cubed muscle stresses and the eigenvalues of the trunk buckling modes.

A different method, more appropriate for dynamic analyses, was developed by Chancey *et al.* [2003]. The authors developed an FE model, based on data (geometry and segment masses) harvested from dissections combined with MRI data. A compression impact on the skull was simulated with and without muscle pre-contraction. In any case, the muscle forces counteracting the head-neck mass were quantified by minimising muscle fatigue.

Contrary to the EMG-based techniques, optimisation results in muscle forces fulfilling the mechanical equilibrium constraint. However, as illustrated by Moroney *et al.* [1988a]

and Han *et al.* [1995], the predicted muscle force pattern is not always fully consistent with EMG-recordings. Because in most cases, kinematics and reaction forces are necessary, a use in a hospital environment is difficult. Again, most studies concentrated on the lumbar spine. Only Helleur *et al.* [1985], Moroney *et al.* [1988a], Choi and Vanderby Jr. [1999] and Chancey *et al.* [2003] applied the optimisation technique to the cervical spine.

2.1.3 EMG-assisted optimisation

The so-called hybrid models combine the advantages of EMG-driven and optimisation-based techniques. The EMG signals are treated as a first estimation of the muscle forces, which is then further optimised to ensure the equilibrium constraints are met. Cholewicki *et al.* [1995] describes this procedure as follows. As did McGill [1992], the force generated by the muscle was assumed linearly correlated with the corresponding normalised EMG-signal. For each individual muscle the smallest possible correction factor is calculated such that the joint moments can be fully balanced. Choi and Vanderby Jr. [1999] used the same method for the cervical spine, but first calculated the common gain, as prescribed by McGill [1992], before calculating the individual correction factors.

Gagnon *et al.* [2011] improved the method by writing the mechanical equilibrium constraints for each individual intervertebral joint. As such, the muscle force predictions, corresponding to the recorded EMG signals, balance the joint moments not only at a single, but at multiple intervertebral levels.

Several comparative studies have pointed out important differences between the EMG-driven and optimisation-based techniques (Cholewicki *et al.* [1995]; Choi and Vanderby Jr. [1999]; Gagnon *et al.* [2001]; Arjmand *et al.* [2009]; Mohammadi *et al.* [2015]). The general conclusion is that the EMG-driven methods offer a higher consistency with EMG-recordings as, among other factors, the interplay between agonist and antagonist muscles is considered, albeit implicitly. Moreover, combining with optimisation also allows to deal with mechanical equilibrium. As such, EMG-assisted optimisation is considered to offer the most physiologically relevant predictions. However, the main limitations are the necessity for EMG recordings, motion capture data and knowledge about the reaction forces, information that is difficult to obtain in a clinical context. Furthermore, apart from Choi and Vanderby Jr. [1999], none of the listed studies explored the application of this technique to the cervical spine.

2.1.4 Proprioception-based Control Model

Different from the above described techniques, the proprioception-based control strategy aims to predict physiologically acceptable muscle forces, fulfilling the mechanical equilibrium constraints, independently from EMG and motion capture data, but entirely based on medical imaging data (Pomero *et al.* [2004]). It changes the paradigm by assuming that muscles are recruited merely to protect the spine from overloading. The muscle activation pattern is determined in an iterative process aiming to minimise the difference between the joint load and the physiological joint load limits. By controlling intervertebral forces and moments, intervertebral displacements can be limited, thus protecting the spinal joint. Figure 2.1 visually explains the model hypothesis.

The technique was initially developed for the lumbar spine and necessitates adjustments for it to be applicable to the cervical spine. Although a direct use in the clinic seems feasible, the method requires both biplanar X-ray and MRI data. A biplanar X-ray acquisition

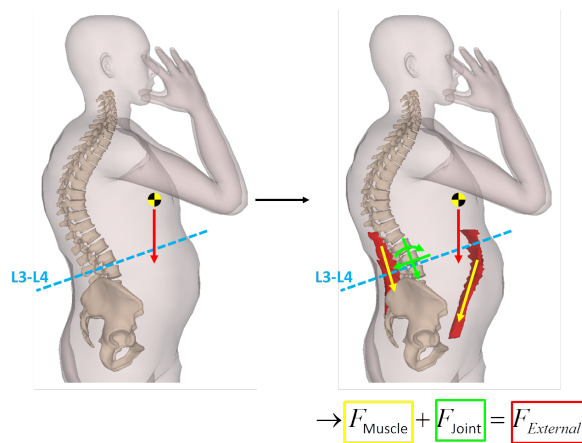


Figure 2.1: The proprioception-based muscle regulation model assumes that the spinal muscle act to protect the spinal joints (Pomero *et al.* [2004])

requires only a few minutes and the associated 3D reconstruction of the spine and the external envelope can be obtained semi-automatically. However, a high resolution MRI scan is necessary to reconstruct the muscle geometry in 3D. Not only the actual acquisition is time-consuming, the post-treatment (segmentation and 3D reconstruction) requires at least 1.5 hours. For it to be implemented in the clinic, modifications to the pre-processing are necessary.

2.1.5 Input Data

As shown in the above, for each technique specific input data is required. Apart from the proprioception-based model, the EMG-based, optimisation and EMG-assisted optimisation techniques require motion capture data, combined with reaction force measurements, estimated body segment masses and an indication of the muscle geometry. In most cases the intervertebral joint load is calculated through inverse dynamics, i.e. the forces required to achieve the configuration measured from the kinematics are calculated. The body segment mass is usually estimated using regression models described in the literature. To run the EMG-based and EMG-assisted optimisation models, EMG data is required as well. Muscular geometry is generally obtained from the literature, i.e. from dissections or medical imaging, and scaled with morphometric measurements. Besides the uncertainty on the kinematic recordings and on the calculations made with inverse dynamics, there is no guarantee that scaled muscle geometry correctly represents the subject-specific data. The proprioception-based control model on the other hand is entirely based on medical imaging data. The 3D geometry of the spine, the external envelope and the muscles are derived from the biplanar X-ray fused with the MRI data. The body segment masses are calculated from the corresponding volume calculated from the 3D reconstruction of the external envelope, combined with density models described in the literature.

2.2 Finite Element Modeling of the Cervical Spine

Finite element (FE) modeling consists of discretising a complex two- or three-dimensional geometry, using a finite number of elements with a simple and well-defined geometry, interconnected at their nodes. Forces and displacements are calculated at the level of these nodes, using the principle of virtual work. By interpolation of the nodal values, the deformations and stresses at the element level can be evaluated. As such, the strain and stress fields for the entire object can be approximated. This modeling technique is considered the golden standard in automotive and aerospace engineering and becomes increasingly popular in the biomedical engineering field, with applications in research and industry and strong perspectives for a use in the clinic. In research, these models are used for the detailed study of joint biomechanics and degeneration mechanisms. In the biomedical industry, they are used to evaluate implant designs and to more efficiently plan *in-vitro* validation experiments and even clinical trials. On the longer term, FE models could also be introduced in the hospital environment to plan or simulate surgeries. With FE modeling, one gains access to stresses and strains inside the bone, the surrounding soft tissue or the implant, data that cannot be recorded *in-vitro*. It is also possible to study the influence of geometry, material properties and boundary conditions, which would be very time-consuming and expensive to achieve *in-vitro*.

As these models become part of the implant development process and are used in surgery planning, the scientific community and regulatory agencies, such as the Food and Drug Administration (FDA) and the American Society of Mechanical Engineers (ASME), proposed recommendations aiming to standardise the development, verification and validation processes. The FE model behaviour is determined by essentially three parameters: the model geometry, the material properties and the boundary conditions. An FE model is a discretisation of the real geometry. The predictions are thus mere approximations. Increasing the number of elements, i.e. densifying the mesh, while correctly positioning the nodes to fully grasp the real geometry, might yield more accurate results. Besides an accurate model geometry and appropriate mesh density, a correct estimation of the material properties and boundary conditions is essential. Having verified these three parameters, it is vital to confirm the biofidelity of the model predictions. This is achieved by comparing the model behaviour with the literature and/or with experimental observations while reproducing the boundary and loading conditions (Viceconti *et al.* [2005]; American Society of Mechanical Engineers [2006]; Jones and Wilcox [2008]; Anderson *et al.* [2012]; Erdemir *et al.* [2012]; Noailly and Lacroix [2012]; US Food and Drug Administration - Center for Devices and Radiological Health [2016]).

In agreement with the subject of this PhD-project, this section focusses on the *state-of-the-art* in cervical spine FE modeling for quasi-static analyses. FE models for dynamic configurations were considered out of scope. However, an extensive review of the relevant literature can be found in the PhD-manuscript of Aurélien Laville (Laville [2011]). Tables 2.2 and 2.3 present the most common FE models intended for quasi-static analyses. The FE models are listed chronologically and per research team. As one model might have formed the subject of multiple publications, only the most recent publications were cited. In the following, the synthesis table is commented based on the above mentioned parameters, i.e. model geometry, meshing, material properties, boundary conditions, verification and validation.

Author (Year)	Segment	Geometry	# Elements	Vertebra		Endplate/Facet Cartilage	Facet Contact	IVD Annulus	Nucleus	Ligaments	Muscles	Spinal Cord	Boundary & Force Conditions	Mesh Conv.	Validation	Related Studies
				Cortical	Spongiosa											
Goel et al. (1998)	C5-C6	CT [1 subject, 68y]	5577 solid & 221 cable	Hexa - iso [E = 10GPa, v = 0.3]	Hexa - iso [E = 450MPa, v = 0.25]	Hexa - iso [E = 3.5GPa, v = 0.25]	Gap	Hexa - iso [E = 4.2MPa, v = 0.45]	Fluid	Cable - Bilinear iso.	-	-	-	In-vitro literature - Curve	Clausen et al. (1997)	
Natarajan et al. (2000)	C5-C6	CT [1 subject, 38y]	2223	Hexa - iso [E = 10GPa, v = 0.3]	Hexa - iso [E = 450MPa, v = 0.25]	Hexa - iso [E = 3.5GPa, v = 0.25]	Surf.-to-surf.	Hexa - iso [E = 4.2MPa, v = 0.45] + cable	Fluid	Cable - Bilinear iso.	-	-	-	-	In-vitro literature - RoM	-
Ng et al. (2003)	C4-C6	3D Digitizer [1 subject, 68y]	7730	Hexa - iso [E = 10GPa, v = 0.29]	Hexa - iso [E = 100MPa, v = 0.29]	Hexa - iso [E = 3.5GPa, v = 0.29]	Surf.-to-surf.	Hexa - iso [E = 3.4MPa, v = 0.4]	Hexa - iso [E = 1MPa, v = 0.49]	Cable - Linear iso.	-	-	-	-	In-vitro literature - RoM & Curve	Ng et al. (2001), Teo et al. (2001)
Zhang et al. (2006)	C6-C7	3D digitizer [1 subject, 68y] + literature	22094	Hexa - iso [E = 12GPa, v = 0.29]	Hexa - iso [E = 450MPa, v = 0.29]	Hexa - iso [E = 3.5GPa, v = 0.29]	Surf.-to-surf.	Hexa - iso [E = 3.4MPa, v = 0.4]	Hexa - iso [E = 1MPa, v = 0.49]	Cable - Linear iso.	-	-	-	-	In-vitro literature - RoM	Zhang et al. (2005)
Ha (2006)	C3-C6	CT [1 subject, 69y]	38718	Hexa - iso [E = 10GPa, v = 0.29]	Hexa - iso [E = 100MPa, v = 0.29]	Hexa - iso [E = 3.5GPa, v = 0.29]	Surf.-to-surf.	Hexa - iso [E = 4.2MPa, v = 0.45] + cable	Hexa - iso [E = 1MPa, v = 0.499]	Cable - Linear iso.	-	-	-	-	In-vitro & In-silico literature - RoM & Curve	-
Delfalamar et al. (2008)	C6-C7	CT [1 subject, 48y]	-	Shell [rigid body]		-	Surf.-to-surf.	Tetra - hyperel.	-	Cable - Multilinear iso.	-	-	-	-	In-vitro & In-silico literature - RoM & Curve	-
Greaves et al. (2008)	C4-C6	Visible Human & cryomicrotome	8662	Hexa [E = 10GPa, v = 0.29]		-	Surf.-to-surf.	Spring [E = 3.4 MPa]	-	Cable - Linear iso.	-	SC: Hexa - iso [E = 0.25 MPa, v = 0.49]; DM: Shell [E = 5 MPa, v = 0.45]	-	-	In-vitro literature - Curve	-
Wheeldon et al. (2008)	C4-C6	CT & cryomicrotome [1 subject, 33y]	10371 solid & 595 cable	Hexa - iso [E = 10GPa, v = 0.29]	Hexa - iso [E = 100MPa, v = 0.29]	Hexa - iso [E = 3.5GPa, v = 0.29]	Surf.-to-surf.	Hexa - iso [E = 3.4MPa, v = 0.4]	Hexa - iso [E = 3.4MPa, v = 0.49]	Cable - Linear iso.	-	-	-	-	In-vitro literature - Curve	Voo et al. (1997); Yoganandan et al. (1996, 1997); Kumarasan et al. (1997, 1999a, 1999b, 2000)
Lin et al. (2009) [University of Michigan]	C5-C6	CT [1 subject, -]	> 3·10 ⁶	Hexa - iso [E = 12GPa, v = 0.3]	Hexa - iso [E = 100MPa, v = 0.3]	-	Surf.-to-surf.	-	-	-	-	-	-	-	-	-
Laville et al. (2009)	C3-C7	3D digitizer & Biplanar X-rays [69 subjects]	4142 solid & 952 cable	Hexa - iso [E = 12GPa, v = 0.3]	Hexa - iso [E = 100MPa, v = 0.2]	Hexa - iso [E = 6GPa, v = 0.3]	Surf.-to-surf.	Hexa - iso [E = 2.5MPa, v = 0.45] + cable	Hexa - iso [E = 2.5MPa, v = 0.45]	Cable - Bilinear iso.	-	-	-	-	In-vitro experiment & In-vitro literature - RoM & Curve	Maurel et al. (1997); Rousseau et al. (2008); Barrey et al. (2015)
Kalleneyn et al. (2010)	C2-C7	CT [1 subject, 74y]	-	Hexa - iso [E = 10GPa, v = 0.3]	Hexa - iso [E = 450MPa, v = 0.25]	Hexa - iso [E = 3.5GPa, v = 0.25]	Surf.-to-surf.	Hexa - iso [E = 4.2MPa, v = 0.45] + cable	Fluid	Cable - Multilinear iso.	-	-	-	Yes	In-vitro experiment - RoM & Curve	Kalleneyn et al. (2009)
Toosizadeh et al. (2011)	C6-C7	CT [1 subject, 26y]	-	Tetra - ortho [Ezz = 11.3GPa, Ezz = 22MPa, vxy = 0.48, vyz = 0.2]	Tetra - ortho [Ezz = 11.3GPa, Ezz = 22MPa, vxy = 0.48, vyz = 0.2]	Tetra - iso [E = 3.5GPa, v = 0.4]	Surf.-to-surf.	Tetra - hyperel. + cable	Tetra - hyperel.	Cable - Multilinear iso.	-	-	-	-	In-vitro & In-silico literature - RoM	-

Table 2.2: Non-exhaustive overview of the frequently cited cervical spine FE models (Part 1) [compr.: compression, conv.: convergence, DM: textitadura mater, DOF: degree of freedom, elas.: elastic, hexa: hexahedral element, hyperel.: hyperelastic, inf.: inferior, iso: isotropic, lin.: linear, lit.: literature, ortho: orthotropic, SC: spinal cord, tetra: tetrahedral element]

Author	Year	Segment	Geometry	# Elements	Vertebra		Posterior Arch	Endplate/Facet	Facet Contact	VD	Nucleus	Ligaments	Muscles	Spinal Cord	Boundary & Force Conditions	Mesh Conv.	Validation	Related Studies
					Cortical	Spongious												
DeWit et al.	(2012)	C4-C5	literature	23024	Hexa - iso [E = 16.8GPa, v = 0.3]	Hexa - ortho [Ex = 100MPa, Ey = 300MPa, vx = 0.3, vxz = 0.1]	Hexa - iso [E = 16.8GPa, v = 0.3]	Hexa - iso [E = 5.6Pa, v = 0.4]	Surf.-to-surf.	Hexa - hyperel. + ortho. fibres	Fluid	Cable - Multilinear iso.	-	-	DOF inf. surface inf. vertebra fixed + Pure Moment	Yes	In-vitro literature - ROM & Curve	Parzer et al. (2009)
Falzan et al.	(2012a)	C3-C7	-	21895	Hexa - iso [E = 10GPa, v = 0.3]	Hexa - iso [E = 450MPa, v = 0.25]	Hexa - iso [E = 3.5GPa, v = 0.25]	-	Surf.-to-surf.	Hexa - iso [E = 4.2MPa, v = 0.25] + cable	Fluid	Cable - Bilinear iso.	-	-	DOF inf. vertebra fixed + Pure Moment	-	In-vitro experiment & In-vitro literature - ROM	Falzan et al. (2012b)
Hussain et al.	(2013)	C3-T1	CT [1 subject, 38V]	-	Tetra - iso [E = 10GPa, v = 0.29]	Tetra - iso [E = 100MPa, v = 0.29]	Tetra - iso [E = 3.5GPa, v = 0.29]	Tetra - iso [E = 500MPa, v = 0.4]	-	Tetra - iso [E = 2.5MPa, v = 0.4]	Tetra - iso [E = 1.5MPa, v = 0.49]	Cable - Bilinear iso.	-	-	DOF inf. surface inf. vertebra fixed + Pure Moment	-	In-vitro literature - ROM	Hussain et al. (2009)
Erbulur et al.	(2014)	C2-T1	CT [1 subject, 35V]	106547	Hexa - iso [E = 10GPa, v = 0.3]	Hexa - iso [E = 450MPa, v = 0.25]	Hexa - iso [E = 3.5GPa, v = 0.25]	Hexa -	Gap	Hexa - hyperel. + lin. elas. fibres	Fluid [E = 1 MPa, v = 0.499]	Cable - Bilinear iso.	-	-	DOF inf. surface inf. vertebra fixed + Pure Moment	-	In-silico literature - Curve	Zafarparandeh et al. (2016)
Lin et al. (National Taipei University of Technology)	(2014)	C3-C7	CT [1 subject, 55V]	93646	Tetra - iso [E = 10GPa, v = 0.29]	Tetra - iso [E = 10MPa, v = 0.29]	Tetra - iso [E = 3.5GPa, v = 0.29]	Tetra - iso [E = 500MPa, v = 0.4]	Fractional Surf.-to-surf.	Tetra - iso [E = 4.2MPa, v = 0.45] + cable	Tetra - iso [E = 1MPa, v = 0.499]	Cable - Multilinear iso.	-	-	DOF inf. surface inf. vertebra fixed + Pure Moment	Yes	In-vitro literature - ROM	-
Mo et al.	(2014)	C3-C7	CT [1 subject, 32V]	127148	Shell - iso [E = 12GPa, v = 0.29]	Tetra - iso [E = 100MPa, v = 0.29]	Tetra - iso [E = 1.2GPa, v = 0.29]	-	Surf.-to-surf.	Hexa - iso [E = 3.4MPa, v = 0.40] + cable	Hexa - iso [E = 1MPa, v = 0.49]	Cable - Multilinear iso.	-	-	DOF inf. surface inf. vertebra fixed + Pure Moment	Yes	In-vitro literature - ROM	-
Completto et al.	(2015)	C4-C6	CT [1 subject, 42V]	226367	Tetra - iso [CT-based properties]	Tetra - iso [CT-based properties]	-	-	Surf.-to-surf.	Hexa - iso [E = 4.2MPa, v = 0.45]	Hexa - iso [E = 0.1MPa, v = 0.499]	Cable - Bilinear iso.	-	-	DOF inf. vertebra fixed + Comp. & Traction	-	-	-
Duan et al.	(2015)	C3-C7	CT [1 subject, 32V]	130748	Tetra - iso [E = 12GPa, v = 0.3]	Tetra - iso [E = 100MPa, v = 0.25]	Tetra - iso [E = 3.5GPa, v = 0.4]	-	Surf.-to-surf.	Hexa - iso [E = 3.4MPa, v = 0.4]	Hexa - iso [E = 1MPa, v = 0.49]	Cable - Multilinear iso.	-	-	DOF inf. surface inf. vertebra fixed + Pure Moment	-	In-vitro literature - ROM	Duan et al. (2011)
Osh et al.	(2016a)	C0-T1	CT [1 subject, 26V]	-	Shell - iso [E = 17.1GPa, v = 0.3]	Tetra - iso [E = 327.495MPa, v = 0.3]	-	-	Surf.-to-surf.	Hexa - hyperel. + ortho. fibrous lamina	Hexa - visco-elastic [K = 1.220 MPa]	Cable - Multilinear iso.	-	-	DOF inf. surface inf. vertebra fixed + Pure Moment	Yes	In-vitro literature - Curve	Osh et al. (2016b)
Yu et al.	(2016)	C3-C7	CT [1 subject, 26V]	330648	Tetra - iso [E = 12GPa, v = 0.3]	Tetra - iso [E = 450MPa, v = 0.25]	-	Tetra - iso [E = 500MPa, v = 0.4]	Surf.-to-surf.	Hexa - iso [E = 3.4MPa, v = 0.4]	Hexa - iso [E = 1MPa, v = 0.49]	Cable - Linear iso.	-	-	DOF inf. surface inf. vertebra fixed + Pure Moment	-	In-vitro & In-silico literature - ROM	-
Wang et al.	(2017)	C0-T1	CT [1 subject, 30V]	255401	Tetra - iso [E = 10GPa, v = 0.3]	Tetra - iso [E = 450MPa, v = 0.25]	-	Tetra - iso [E = 16Pa, v = 0.3]	Surf.-to-surf.	Hexa - hyperel. + lin. elas. fibres	-	Cable - Bilinear iso.	-	-	DOF inf. surface inf. vertebra fixed + Pure Moment & Traction	-	In-vitro & In-silico literature - ROM	-
Chen et al.	(2018)	C3-C7	CT [-]	55022	Hexa - iso [E = 10GPa, v = 0.3]	Hexa - iso [E = 450MPa, v = 0.23]	Hexa - iso [E = 3.5GPa, v = 0.23]	-	Surf.-to-surf.	Hexa - iso [E = 4.2MPa, v = 0.45]	Hexa - iso [E = 1MPa, v = 0.499]	Cable - Multilinear iso.	-	-	DOF inf. surface inf. vertebra fixed + Pure Moment	Yes	In-vitro & In-silico literature - ROM	Jung et al. (2013)
Yuan et al.	(2018)	C3-C7	CT [1 subject, 38V]	286382	Tetra - iso [E = 12GPa, v = 0.29]	Tetra - iso [E = 450MPa, v = 0.29]	-	Tetra - iso [E = 500MPa, v = 0.4]	Surf.-to-surf.	Tetra - iso [E = 3.4MPa, v = 0.4]	Tetra - iso [E = 1MPa, v = 0.499]	Cable - Multilinear iso.	-	-	DOF inf. surface inf. vertebra fixed + Pure Moment	Yes	In-vitro & In-silico literature - ROM	Wu et al. (2017)

Table 2.3: Non-exhaustive overview of the frequently cited cervical spine FE models (Part 2) [compr.: compression, conv.: convergence, DM: textidura mater, DOF: degree of freedom, elas.: elastic, hexa: hexahedral element, hyperel.: hyperelastic, inf.: inferior, iso: isotropic, lin.: linear, lit.: literature, ortho: orthotropic, SC: spinal cord, tetra: tetrahedral element]

2.2.1 Model Geometry

In most studies, the model geometry for the osseous components was obtained from the segmentation and subsequent 3D reconstruction of a CT scan of one subject, acquired either *in-vivo* (Natarajan *et al.* [2000]; Ha [2006]; Hussain *et al.* [2009]; Duan *et al.* [2011]; Toosizadeh and Haghpanahi [2011]; Hussain *et al.* [2013]; Erbulut *et al.* [2014]; Duan *et al.* [2015]) or *in-vitro* (Yoganandan *et al.* [1996]; Clausen *et al.* [1997]; Yoganandan *et al.* [1997]; Pérez del Palomar *et al.* [2008]; Kallemeyn *et al.* [2009, 2010]). Some authors combined the CT-based geometry with *cryomicrotome* images (Kumaresan *et al.* [1997]; Voo *et al.* [1997]; Kumaresan *et al.* [1999b, 2000]; Wheeldon *et al.* [2008]), with radiographs (Goel and Clausen [1998]), with measurement data obtained from dissections (Faizan *et al.* [2012b]) and/or with information obtained from the literature (Ng and Teo [2001]; Teo and Ng [2001]; Ng *et al.* [2003]; Zhang *et al.* [2005, 2006]; Pérez del Palomar *et al.* [2008]; Hussain *et al.* [2009]; Duan *et al.* [2011]; Hussain *et al.* [2013]; Erbulut *et al.* [2014]; Duan *et al.* [2015]) to correctly orient the *vertebrae*, to accurately represent the IVD and joint cartilage and to obtain an indication of the ligament insertion sites. The model geometry was not always extracted from medical imaging data. Other potential sources were the literature (Panzer and Cronin [2009]; Panzer *et al.* [2011]; DeWit and Cronin [2012]), 3D digitised anatomical landmarks indicated on cadaveric samples (Maurel *et al.* [1997]; Ng and Teo [2001]; Teo and Ng [2001]; Ng *et al.* [2003]; Zhang *et al.* [2005, 2006]) and *cryomicrotome* images (Greaves *et al.* [2008]).

In general, the FE model represents one particular subject in one configuration. Only one study, published by our research group, describes the development of a subject-specific FE model (Laville *et al.* [2009]). Low-dose biplanar X-ray images were acquired with the sample in the upright configuration, from which a set of geometric primitives was calculated. Based on these geometric primitives, a parametric subject-specific FE mesh could be generated automatically. IVD geometry was generated from the interpolation of the adjacent vertebral endplates, as the 3D reconstruction on which the model geometry was based, reflects the natural posture of the sample. This procedure was initially developed for the lumbar spine (Lavaste *et al.* [1992]) and adapted to the cervical spine based on 3D digitised landmarks obtained from a significant number of cadaveric samples (Maurel *et al.* [1997]). Besides the generation of subject-specific models, the parametric modeling approach makes it possible to study the influence of certain geometric parameters. However, because the model is parameterised, it is a simplification of reality. The effect of geometric accuracy has not yet been analysed.

2.2.2 Discretisation

For volumetric representations, the hexahedral element is considered the golden standard in FE modeling, as it does not suffer from shear or volume locking and thus has a better performance than its tetrahedral alternative of similar size. Most of the cervical spine FE models are meshed with 8-node hexahedral elements with 3 degrees of freedom (DoF) per node. However, the adopted meshing technique is rarely described. Using edge-detection, Yoganandan *et al.* [1997] and Ha [2006] segmented the CT scans, yielding a stack of vertebral contours. The 3D surface, obtained as such, was described with 3D splines, thus yielding NURBS patches. From these NURBS patches, a hexahedral mesh could be generated using the *mapped mesh* technique. Ng and Teo [2001] adopted a similar meshing technique, yet based on 3D digitised data from a cadaver sample.

At our research institute, the first *multiblock meshing* technique was developed, initially for the lumbar spine (Lavaste, Skalli *et al.* [1992]) and later on adapted to the cervical spine

(Maurel *et al.* [1997]; Laville *et al.* [2009]). As discussed in the above, the 3D reconstruction data obtained from biplanar X-ray images was parameterised, i.e. the geometry of each anatomical zone was approximated with geometric primitives, such as circles, cylinders and planes. As these primitives could be discretised fairly easily, a hexahedral, yet simplified, mesh could be obtained automatically. Figure 2.2 illustrates the procedure for the vertebral body of a C4 *vertebra*. Recently, an algorithm was developed to optimise the mesh element quality, yielding a robust and high-quality hexahedral mesh, even when the initial mesh contained highly distorted elements (Travert [2013]). Kallemeyn *et al.* [2009] described a similar approach to obtain a morphorealistic hexahedral mesh of the C4-C5 FSU. Once again, the vertebral geometry was subdivided into anatomical zones, e.g. the vertebral body, the spinous process, *etc.*. Interactively, premeshed building blocks were placed around each of these zones. By projecting the external nodes of these building blocks onto the target surface, obtained from CT data, and interpolating the internal nodes, a hexahedral and geometrically accurate mesh could be obtained. This *multiblock meshing* technique was also used by Erbulut *et al.* [2014] to generate a hexahedral mesh of the C2-T1 segment.

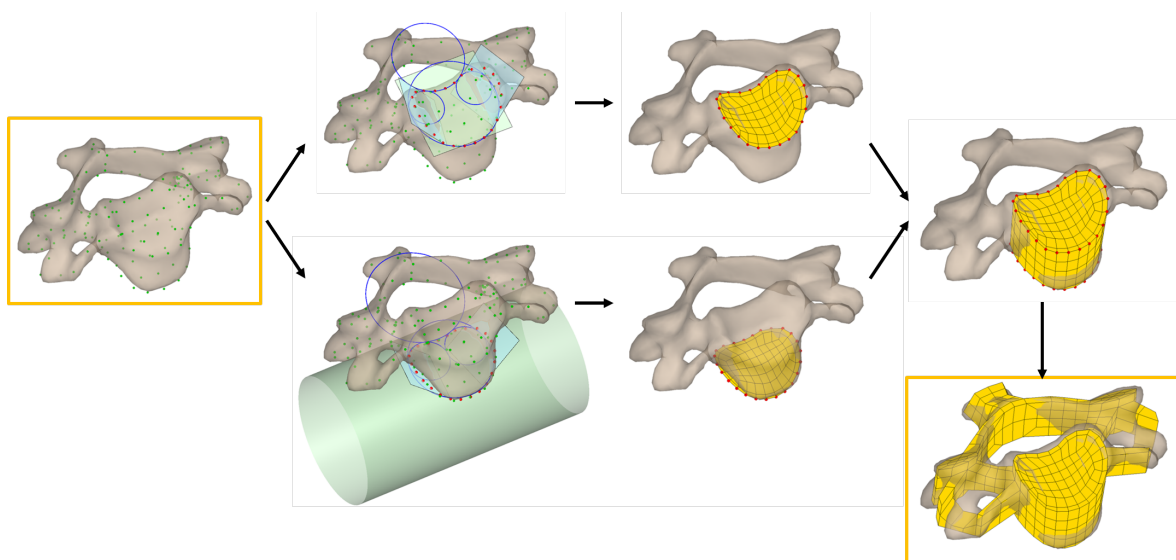


Figure 2.2: The parameterisation of the 3D reconstruction obtained from biplanar X-ray data allows the automatic generation of a hexahedral mesh (Laville *et al.* [2009])

Some authors also used tetrahedral meshes (Toosizadeh and Haghpanahi [2011]; Hussain *et al.* [2009, 2013]; Wang *et al.* [2017]), as well as a combination of hexahedral and tetrahedral elements (Duan *et al.* [2011, 2015]). In case mixed meshes were used, the complex vertebral geometry was usually *freemeshed* with tetrahedral elements, while a hexahedral mesh was generated for the IVD. Pérez del Palomar *et al.* [2008] treated the *vertebrae* as rigid bodies and thus generated surface meshes for the osseous components, using both triangular and quadrilateral elements. However, a volumetric tetrahedral mesh was defined for the IVD.

The volumetric soft tissue components were generally meshed by extruding the adjacent bony surfaces and spinal ligaments were consistently represented by cable elements.

Some studies focussed on one FSU (Clausen *et al.* [1997]; Goel and Clausen [1998]; Panzer and Cronin [2009]; Panzer *et al.* [2011]; DeWit and Cronin [2012]), while others concentrated on the lower cervical spine (Laville *et al.* [2009]; Wheeldon *et al.* [2008]; Hussain *et al.* [2009]; Duan *et al.* [2011]; Hussain *et al.* [2013]; Duan *et al.* [2015]). In a few cases the upper cervical spine was considered partially, merely including the C2-*vertebra* (Kallemeyn *et al.* [2010]), or entirely, i.e. including the *occiput* (Zhang *et al.*

[2005, 2006]; Pérez del Palomar *et al.* [2008]). Even after correcting for the number of *vertebrae* represented in the model, a high variability in terms of mesh density was observed, with the number of elements ranging from 7730 to 130748 for the models representing a stacking of at least three *vertebrae*.

2.2.3 Material Properties

The literature seemed to have reached consensus regarding the assignment of material properties to the osseous components. Most authors differentiated between the cortical bone, the spongy bone and the posterior aspect and assumed a linear elastic and isotropic material behaviour. The elastic modulus of the cortical bone was either 10 GPa, 12 GPa or 16.8 GPa, with the Poisson's ratio ranging between 0.29 and 0.30. An elastic modulus of 100 MPa or 450 MPa and a Poisson's ratio of 0.25 to 0.29 were usually assigned to the spongy bone. The posterior arch was almost always assigned a Young's modulus of 3.5 GPa, while the Poisson's ratio could vary between 0.25 and 0.30. As mentioned before, in one study the *vertebrae* were considered undeformable (Pérez del Palomar *et al.* [2008]). Two other teams assumed a linear elastic, orthotropic material model for the spongy bone (Panzer and Cronin [2009]; Panzer *et al.* [2011]; DeWit and Cronin [2012]) or for both the cortical and cancellous bone (Toosizadeh and Haghpanahi [2011]). However, the selected Young's moduli matched the above mentioned ranges.

Regarding the endplate cartilage, a larger variation was to be noted. Mostly assumed linear elastic and isotropic, the values for the elastic modulus could be as low as 100 MPa or as high as 5.6 GPa, while the Poisson's ratio varied between 0.2 and 0.4.

Various constitutive models were considered for the soft tissue components, particularly for the ligaments. The IVD is usually modeled as a fibre-reinforced *annulus*, surrounding an incompressible low-stiffness *nucleus*. The *annulus*-matrix is often considered linear elastic and isotropic. The elastic modulus varied between 2.5 MPa and 40 MPa and the Poisson's ratio between 0.4 and 0.49. The linear elastic fibres are often assigned elastic moduli of 450 MPa. Toosizadeh and Haghpanahi [2011] differentiated between the anterior, posterior and lateral fibres. In the model developed at our laboratory, different properties were also chosen for the anterior and posterior fibres (Maurel *et al.* [1997]; Laville *et al.* [2009]). Sometimes, the presence of the fibres was considered only mathematically with hyperelastic formulations, based on the Mooney-Rivlin (Toosizadeh and Haghpanahi [2011]), the Hill (Panzer and Cronin [2009]; Panzer *et al.* [2011]; DeWit and Cronin [2012]) or the Holzapfel (Pérez del Palomar *et al.* [2008]) model. In that case the *annulus* mesh was homogeneous.

The *nucleus* was in most cases assumed linear elastic and isotropic. The Poisson's ratio was set equal to 0.49, while the Young's modulus varied between 1 MPa and 3.4 MPa. Other studies prescribed the use of incompressible fluid elements (Faizan *et al.* [2012b,a]; Kallemeyn *et al.* [2010]).

Although it is not apparent from Tables 2.2 and 2.3, an even higher variability was observed when looking into the material properties of the ligaments. Most authors approximate the typical sigmoid-shaped stress-strain behaviour with a linear or bilinear curve, characterised by one or two elastic moduli, respectively. Some authors explicitly incorporated the weak resistance under low forces, i.e. the so-called *slack length*, in the linear or bilinear description of the ligaments (Maurel *et al.* [1997]; Goel and Clausen [1998]; Laville *et al.* [2009]; Faizan *et al.* [2012b]; Erbulut *et al.* [2014]), while others attempted to approach as close as possible the actual sigmoid-shaped curve (Kumaresan *et al.* [1998, 1999b];

Wheeldon *et al.* [2008]; Panzer and Cronin [2009]; Kallemeyn *et al.* [2010]; Duan *et al.* [2011]; Panzer *et al.* [2011]; Toosizadeh and Haghpanahi [2011]; DeWit and Cronin [2012]; Jung *et al.* [2013]; Duan *et al.* [2015]). The observed ranges for the maximal Young's modulus for the anterior longitudinal ligament, the posterior longitudinal ligament, the yellow ligament, the interspinous ligament and the facet capsules were 11.9 MPa to 54.4 MPa, 10 MPa to 40.9 MPa, 1.5 MPa to 31 MPa, 1.5 MPa to 10 MPa and 4.9 to 33.3 MPa, respectively.

When verifying which articles were cited by these authors to justify the choice of material properties, it was noted that in most cases the *in-silico* literature was cited, describing not only cervical spine (Saito *et al.* [1991]; Kleinberger [1993]; Yoganandan *et al.* [1996]; Clausen *et al.* [1997]; Maurel *et al.* [1997]), but also lumbar spine FE models (Shirazi-Adl *et al.* [1984]; Ueno and Liu [1987]; Lavaste *et al.* [1992]; Goel *et al.* [1995]; Sharma *et al.* [1995]). On their turn, these authors very often refer to the same *in-vitro* (review) studies as well: Yamada [1970], Evans [1973], Bernstein *et al.* [1976] and Clausen [1996].

Several studies have illustrated the importance of assigning appropriate mechanical properties to the soft tissue elements, as they can significantly alter the load-displacement behaviour under pure moment (Kumaresan *et al.* [1999a]; Brolin and Halldin [2004]; Naserkhaki *et al.* [2017]), compression (Espino *et al.* [2003]; Travert *et al.* [2011]; Yang *et al.* [2016]) and tension (Brolin and Halldin [2004]) loading, as well as the internal stress distribution. Moreover, compared to the bone tissue material properties, the soft tissue mechanical behaviour seemed to have a more significant effect (Kumaresan *et al.* [1999a]). Contrary to bone tissue, for which CT-based (Kopperdahl *et al.* [2002]; Rho *et al.* [1995]) and X-ray-based (Sapin de Broses *et al.* [2010]) techniques are available, few non-destructive techniques quantifying soft tissue mechanical properties exist. Assigning subject-specific soft tissue material properties thus remains a challenge. The most reliable method to quantify the ligament mechanical properties is the *ex-vivo* uniaxial tension test to assess stiffness, elastic modulus and ultimate tensile strength (Chazal *et al.* [1985]; Maurel *et al.* [1997]; Yoganandan *et al.* [2000]; Mattucci *et al.* [2012]). All of them reflect a high inter-subject variability, which partly explains the important variability observed *in-silico*.

Appendix B provides an overview of the first level reference articles and compares the proposed material properties with those listed in the most commonly cited *in-vitro* literature.

2.2.4 Boundary and Initial Conditions

The boundary conditions were very similar among the different studies. Depending on the envisaged loading configuration, all DoF of the external nodes of the most caudal *vertebra* were blocked, while a pure moment (e.g. Natarajan *et al.* [2000]; Laville *et al.* [2009]; Kallemeyn *et al.* [2010]), tensile (e.g. Greaves *et al.* [2008]) or compression (e.g. Wang *et al.* [2017]) loading was applied to the most cranial one.

The initial conditions were scarcely detailed. One might assume that these were determined from the geometric input data (see the above). For example, Laville *et al.* [2009] automatically obtained the subject-specific FE mesh from a set of biplanar X-ray images, acquired in the upright configuration. The initial conditions were thus given by the configuration in which the sample was X-rayed. Goel and Clausen [1998] also used radiographs to define the relative orientation of the stacked *vertebrae*, while other studies used information on the normal lordotic curve described in the literature (Ng and Teo [2001]; Teo and Ng [2001]; Ng *et al.* [2003]; Zhang *et al.* [2005, 2006]; Pérez del Palomar *et al.* [2008]; Erbulut *et al.* [2014]).

The facet joints and in some cases the interaction between the spinous processes were often modeled with frictionless surface-to-surface contact elements (e.g. Natarajan *et al.* [2000]; Laville *et al.* [2009]; Kallemeyn *et al.* [2010]).

2.2.5 Verification and Validation

To the best of our knowledge, apart from three studies (Panzer and Cronin [2009]; Kallemeyn *et al.* [2010]; Chen *et al.* [2018]), none of the listed FE models built with hexahedral elements underwent a mesh convergence analysis to determine an appropriate element size. Due to the complex vertebral geometry and the high inter-subject variability, generating a hexahedral mesh is difficult, let alone performing a mesh convergence analysis.

To validate the model behaviour, one generally compares the predicted range of motion (RoM) or local stiffness, calculated from the load-displacement curves, with the corresponding measures obtained from experimental data. Few studies included a direct validation step in the model development process, in which the actual load-displacement curves would be compared directly to those observed in dedicated experiments (Clausen *et al.* [1997]; Goel and Clausen [1998]; Kumaresan *et al.* [1999b]; Wheeldon *et al.* [2008]; Laville *et al.* [2009]; Faizan *et al.* [2012a]; Barrey *et al.* [2015]) or those extracted from the literature (Teo and Ng [2001]; Ha [2006]; Pérez del Palomar *et al.* [2008]; Greaves *et al.* [2008]; Panzer and Cronin [2009]; Toosizadeh and Haghpanahi [2011]; Panzer *et al.* [2011]; DeWit and Cronin [2012]; Erbulut *et al.* [2014]). Kallemeyn *et al.* [2010] performed a more extensive validation by comparing the numerical with the experimental curve for different mechanical configurations of the sample. In an *in-vitro* experimental analysis, the ligaments were sequentially removed until only the *vertebrae* and the IVDs remained. At each step, the load-displacement behaviour under pure moment loading was recorded. This analysis was mimicked numerically in reverse order and at each step the model behaviour was evaluated against the corresponding experimental behaviour. By doing so, the authors were able to adjust the material properties for the IVD and each ligament individually, starting from values described in the literature. After verification with the literature, the authors were thus able to increase the predictive power of the model. A similar investigation was performed at our institute by Tonetti *et al.* [1995] (unpublished data) and Maurel *et al.* [1997].

2.2.6 FE Modeling of the Instrumented Cervical Spine

The above described FE models were used for the study of spinal biomechanics, to assess the influence of certain geometric parameters or to evaluate the role of the spinal ligaments. Some were also used to evaluate different types of surgical instrumentation. Table 2.4 provides a broad overview of the main studies with reference towards Tables 2.2 and 2.3.

A number of studies focussed on anterior or posterior fusion. Natarajan *et al.* [2000] assessed the influence of *osteoporosis* and the bone graft tightness on the outcome of anterior fixation. Hussain *et al.* [2009] attempted to quantify the effect of screw angulation on bone graft and bone-screw stresses after *corpectomy* combined with anterior fusion. Duan *et al.* [2011] also analysed different screw orientations, yet for posterior fixation after *laminectomy*. Wu *et al.* [2017] compared two different anterior fixation techniques for the stabilisation of a *corpectomy*.

A larger number of the listed studies analysed the performance of different total disc replacements and the effect of various geometrical parameters. Ha [2006], Faizan *et al.* [2012a], Mo *et al.* [2014] and Completo *et al.* [2015] compared various types of TDR with anterior or posterior fusion, with a special attention to adjacent segment overloading. Other

	Segment	Geometry	Analysis	Loading	Muscles	Validation		Reference FE model	Similar Studies
						Intact	Instrumented		
Natarajan <i>et al.</i> (2000)	C5-C6	CT [1 subject]	Discectomy & Anterior fixation	Pure 0.5 Nm moment + Compr. preload	-	In-vitro literature - RoM	-	Natarajan <i>et al.</i> (2000)	-
Ha (2006)	C3-C6	CT [1 subject]	Elastomer-type TDR	Pure 1 Nm to 1.8 Nm moment + Compr. Preload	-	In-vitro & In-silico literature - RoM & Curves	-	Ha (2006)	-
Rousseau <i>et al.</i> (2008)	C5-C6	3D digitiser & Biplanar X-rays [69 subjects]	Ball-and-socket TDR	Pure 1.6 Nm moment + Compr. preload	-	In-vitro literature & In-vitro experiments - Curves	-	Laville <i>et al.</i> (2009)	-
Hussain <i>et al.</i> (2009)	C3-T1	CT [1 subject]	Corpectomy & Anterior fixation	Pure moment + Follower load	-	In-vitro literature - RoM	In-vitro literature - RoM	Hussain <i>et al.</i> (2013)	Hussain <i>et al.</i> (2013)
Lin <i>et al.</i> (2009) [University of Michigan]	C3-C7	CT [1 subject]	Different types of TDR	Pure 1.8 Nm moment + Compr. Preload	-	-	-	Lin <i>et al.</i> (2009)	-
Duan <i>et al.</i> (2011)	C3-C7	CT [1 subject]	Laminectomy & Posterior fixation	Pure 1 Nm moment + Follower load	-	In-vitro literature - RoM	-	Duan <i>et al.</i> (2015)	Duan <i>et al.</i> (2015)
Faizan <i>et al.</i> (2012,a)	C3-C7	CT [1 subject]	TDR vs. Posterior fusion vs. TDR + Posterior fusion	Pure 2 Nm moment + Follower load	-	In-vitro experiments - RoM	In-vitro experiments - RoM	Faizan <i>et al.</i> (2012,a)	Faizan <i>et al.</i> (2012,b)
Jung <i>et al.</i> (2013)	C3-C6	CT [-]	Different types of TDR	Pure 1 Nm moment + Follower load	-	In-vitro & In-silico literature - RoM	-	Chen <i>et al.</i> (2018)	Chen <i>et al.</i> (2018)
Lin <i>et al.</i> (2014) [National Taipei University of Technology]	C3-C7	CT [1 subject]	Different types of TDR	Displacement controlled	-	In-vitro literature - RoM	-	Lin <i>et al.</i> (2014)	-
Mo <i>et al.</i> (2014)	C3-C7	CT [1 subject]	Two types of TDR vs. Anterior Fusion	Displacement controlled	-	In-vitro literature - RoM	-	Mo <i>et al.</i> (2014)	-
Completo <i>et al.</i> (2015)	C4-C6	CT [1 subject]	Unilevel TDR vs. Bilevel TDR vs. TDR + Fusion cage	Compression	-	-	-	Completo <i>et al.</i> (2015)	-
Yu <i>et al.</i> (2016)	C3-C7	CT [1 subject]	Two types of TDR	Pure 1 Nm moment + Follower load	-	In-vitro & In-silico literature - RoM	-	Yu <i>et al.</i> (2016)	-
Wu <i>et al.</i> (2017)	C3-C7	CT [1 subject]	Two types of anterior fusion	Pure 1 Nm moment	-	In-vitro & In-silico literature - RoM	-	Wu <i>et al.</i> (2017)	-
Yuan <i>et al.</i> (2018)	C3-C7	CT [1 subject]	Ball-and-socket TDR	Pure 1 Nm moment + Follower load	-	In-vitro & In-silico literature - RoM	-		

Table 2.4: Overview of FE models developed for the study of surgical interventions. The column entitled 'Reference FE model' contains the reference towards the FE model used for the study and listed in Tables 2.2 and 2.3 [config.: configuration, compr.: compression, TDR: total disc replacement]

groups, such as Lin *et al.* [2009], Jung *et al.* [2013], Lin *et al.* [2014] and Yu *et al.* [2016], compared the behaviour of different commercially available disc implants. Rousseau *et al.* [2008a] evaluated the influence of the radius of the ball component and the position of the centre of rotation of a ball-and-socket IVD prosthesis. In a similar study, Faizan *et al.* [2012b] analysed the sensitivity of two other geometrical parameters, i.e. the ball shape and its position relative to the adjacent implant components. The influence of a fifth geometrical parameter, i.e. the prosthesis height, was studied by Yuan *et al.* [2018].

Most of the authors developed the FE model using CT-scans acquired from only one subject. Generally, the model was not easily adaptable to the CT-data of another subject. A subject-specific analysis of the instrumented spine has not yet been attempted.

Usually, only the intact configuration was imaged. The instrumented configuration was obtained by mimicking the relevant surgical intervention. The IVD, the vertebral body and/or the ligaments were removed and the FE model of the instrumentation was put in place. However, none of the studies modeled the actual implantation, which locally changes the mechanical status or geometry of the subject. Indeed, during TDR, the adjacent *vertebrae* are moved apart, thus increasing ligament tensioning and prestressing the implant. During anterior or posterior fixation, on the other hand, the relative orientation of the involved *vertebrae* is adjusted.

Most of the authors studied the model behaviour under a pure moment loading. In two studies, a displacement controlled simulation was performed for the instrumented configuration (Lin *et al.* [2014]; Mo *et al.* [2014]). The imposed angular displacement corresponded to the angular displacement recorded during a pure moment loading in the intact configuration. In most cases, the moment loading was combined with a follower load or a compressive preload, simulating the weight of the head and the muscle load. The actual muscle forces, however, were not modeled.

In almost all of these studies, the FE model behaviour was evaluated against the literature. Usually, this was performed only for the intact configuration with RoM as the determinative factor. Both the *in-silico* and *in-vitro* literature was considered. Two studies not only compared the RoM, but also the actual load-displacement curves (Ha [2006]; Rousseau *et al.* [2008a]). In merely two studies, the behaviour of the model representing the instrumented configuration was evaluated as well. Hussain *et al.* [2009] compared the numerically observed RoM with the *in-vitro* literature. Faizan *et al.* [2012a] performed dedicated *in-vitro* experiments on six cadaveric samples for model validation purposes. Both the intact and the instrumented spinal segment were tested. Yet, only the RoM was recorded.

2.3 Synthesis and Project Objectives

The scientific community acknowledges the necessity for a patient-specific approach, integrating subject-specific geometry, posture, material properties and muscle forces, to fully understand spinal biomechanics, to enable an efficient surgery planning and to profoundly evaluate implants (Rousseau *et al.* [2008a]; Laville *et al.* [2009]; Dreischarf *et al.* [2014]). As can be appreciated from the above, the literature records already a large part of the required building blocks. Yet, certain important shortcomings are to be noted.

To quantify the spinal muscle forces, generally three different techniques are proposed: optimisation, EMG-assisted methods or techniques combining EMG with optimisation, the so-called hybrid approach. The advantage of this hybrid approach is its ability to predict a muscle force pattern that is consistent with the EMG recordings, while maintaining mechanical equilibrium. However, implementation in a clinical context is difficult, since it is necessary to measure kinematics, reaction forces and EMG. Furthermore, as only the superficial muscles can be accessed, unless invasive techniques are adopted, the activity of the inaccessible muscles has to be considered similar to that of the measured muscles (Cholewicki *et al.* [1995]; McGill [1992]). Besides, the relationship between the EMG signal and the generated force should be treated with caution (Hof [1997, 1984]). The so-called 'cross-talk effect', i.e. one electrode captures the electrical activity of all muscles in its vicinity, should be considered as well.

The optimisation-based approaches yield muscle and joint force predictions that satisfy mechanical equilibrium. However, the predictions might be questionable from a physiological point of view, since a positive correlation with EMG recordings could be established only in certain configurations (Hughes *et al.* [1994]; McMulkin *et al.* [2003]). The proposed objective functions, e.g. the sum of cubed muscle stresses, may be more useful for dynamic analyses. Indeed, when the most probable muscle force pattern inducing a certain joint motion is to be found, it might be relevant to minimise muscle load, i.e. preventing muscle fatigue (Chancey *et al.* [2003]; Seth *et al.* [2011]). Furthermore, although the method is independent from EMG data, it is necessary to acquire motion capture data and to measure (ground) reaction forces, which is not available in the clinic.

Using a different approach, based on the hypothesis that spinal muscles are activated to protect the intervertebral joint from overloading, the proprioception-based control model aims to predict physiologically relevant muscle forces and associated joint loads from biplanar X-ray and MRI data, independently from EMG. Although this procedure does not require EMG nor motion capture data, a high-resolution MRI scan is necessary to accurately reconstruct the muscle geometry. Because an MRI acquisition is time-consuming and can be uncomfortable for patients suffering from spinal disorders, a direct use in the hospital is not yet feasible.

Apart from a few studies (Goel *et al.* [1993]; Han *et al.* [1995]; Pomero *et al.* [2004]), subject-specific input data is rarely used. The external load is usually determined from the measured (ground) reaction forces combined with an estimation of the body segment mass. However, muscle geometry was in most cases derived from the literature and scaled based on morphometric measurements or on kinematics data. Moreover, most authors concentrated on the lumbar spine. In only four of the listed publications (Helleur *et al.* [1985]; Moroney *et al.* [1988a]; Chancey *et al.* [2003]; Choi and Vanderby Jr. [1999]) the particularities of the cervical spine were studied.

Regarding the finite element modeling, the following remarks can be made. Most studies obtained the model geometry from CT data or the 3D digitalisation of merely one subject,

acquired *in-vivo* or *in-vitro*. The hexahedral element, considered the golden standard in FE modeling, is the element of preference. However, the adopted meshing technique was rarely discussed. The largely described high inter- and intra-subject variability, as well as the complex vertebral morphology, turn the generation of a hexahedral mesh into a difficult task. Only one study developed a technique to generate a hexahedral mesh from a random set of biplanar X-ray images, making it possible to automatically generate subject-specific FE models (Laville *et al.* [2009]).

In almost all cases, the material properties of both the bone and soft tissue components were obtained from the literature and assumed linear elastic and isotropic. Considering that the deformations are mostly concentrated in the IVD, although important deformations at the pedicle level have been recorded, this assumption might be acceptable for the *vertebrae*, but not for the IVD. Furthermore, an important variability in terms of soft tissue material properties could be noted. This was to be expected, as *in-vitro* experiments exposed an important inter-subject variability. Moreover, various references were used by these authors to justify their choice of material properties.

Because of the high complexity of the FE model and despite the recommendations of both the regulatory agencies and the scientific community, few studies attempted a mesh convergence analysis to define the correct element size (Panzer and Cronin [2009]; Erbulut *et al.* [2014]), although it is an important step in the verification process. This explains the high variability in terms of mesh density, which was observed even after having corrected for the number of modeled vertebral levels. Indeed, the lower cervical spine was not always fully represented, neither was the combined upper and lower cervical spine.

To validate the model behaviour, one often compared the predicted range of motion (RoM) or local stiffness with those reported in the literature (Duan *et al.* [2011]; Faizan *et al.* [2012a]; Hussain *et al.* [2009]; Kumaresan *et al.* [1997]; Zhang *et al.* [2005]). This so-called indirect validation might mask important differences between the experimental and numerical load-displacement curves. In few cases, direct validation was performed with dedicated experimental data (Clausen *et al.* [1997]; Natarajan *et al.* [2000]; Teo and Ng [2001]; Ha [2006]; Laville *et al.* [2009]; Pérez del Palomar *et al.* [2008]; Panzer and Cronin [2009]), considering not only the RoM but the complete load-displacement curve. Maurel *et al.* [1997] and Kallemeyn *et al.* [2010] not only compared the numerical with the experimental curve for the intact sample, but also sequentially removed the ligaments and repeated this comparison at each step until only the *vertebrae* and the IVDs remained. This allowed them to adjust the material properties of the IVD and the individual ligaments when necessary.

Most of the listed models were developed for the study of cervical spine biomechanics or for implant testing, but none of these models considered the muscles. FE models developed for dynamic analyses, on the other hand, did indeed integrate muscles and some of the optimisation-based muscle regulation models, described in the above, integrated FE modeling. However, a volumetric representation was only scarcely used, as the muscles were modeled with membrane (Frechede *et al.* [2006]) or cable elements (Goel *et al.* [1993]; Chancey *et al.* [2003]; Ezquerro *et al.* [2004]; Brodin *et al.* [2005]; Arjmand and Shirazi-Adl [2006]).

Based on these comments, the objectives of this PhD-project were defined as follows. The global aim is to develop a subject-specific musculoskeletal model of the cervical spine that can be used for surgery planning in a clinical context and for implant evaluation in an industrial context. The model incorporates subject-specific geometry, posture, material behaviour and boundary conditions. Concerning the boundary conditions, the active muscle forces counterbalancing the body segment mass and potential external forces are to be

considered.

In the first phase of this PhD, the development of a subject-specific muscle regulation model, using the proprioception-based control model proposed by Pomeroy *et al.* [2004], will be treated. A method for the generation of subject-specific input data, i.e. muscle geometry and external loading, will be developed. After a subject-specific analysis determining the feasibility of this model, it will be investigated to what extent the calculation of the model input data can be simplified and accelerated, thus preparing the model for integration in the hospital environment.

In the second phase, a morphorealistic and subject-specific finite element model of the lower cervical spine will be developed, building further upon the work of Maurel *et al.* [1997] and Laville *et al.* [2009]. Extensive modifications of the model geometry and material behaviour will be practiced to ensure the predictive power. The importance of geometric accuracy will be investigated by generating a model from both biplanar X-ray and CT data and comparing the behaviour of both models with *in-vitro* experimental data in a *one-to-one* fashion. To illustrate the power and feasibility of the model, not only the intact, but also the surgically restored cervical spine will be modeled.

Chapter 3

Cervical Spine Muscle Force Quantification: Muscle Regulation Model

As mentioned in Chapters 1 and 2, the cervical spine muscles precisely orient the head, while stabilising the individual intervertebral joints and protecting the spinal chord. As muscular degeneration or malfunctioning explains a large range of cervical spine pathologies, patient-specific muscle force quantification might be necessary to aid surgical planning.

This chapter overviews the functioning, evaluation and application of the muscle regulation model developed in the context of this PhD project. The following has been published in *Clinical Biomechanics*, under the title 'A Subject-specific Biomechanical Control Model for the Prediction of Cervical Spine Muscle Forces' (Van den Abbeele *et al.* [2018])¹. As this article focussed on the feasibility of this model, a supplementary section discussing a subject-specific analysis was added as well.

Contents

3.1	A Subject-specific Biomechanical Control Model for the Prediction of Cervical Spine Muscle Forces	36
3.1.1	Introduction	36
3.1.2	Materials & Methods	36
3.1.3	Results	40
3.1.4	Discussion	45
3.2	A Subject-specific Analysis	48
3.2.1	Introduction	48
3.2.2	Materials & Methods	48
3.2.3	Results	51
3.2.4	Discussion	55

¹Potential copyright issues regarding the reuse of this article, including the figures and tables, have been cleared with the publisher, *Clinical Biomechanics*

3.1 A Subject-specific Biomechanical Control Model for the Prediction of Cervical Spine Muscle Forces

3.1.1 Introduction

Cervical spine musculature plays an important role in maintaining head-neck equilibrium and stability and in preventing intervertebral joint lesions (Panjabi *et al.* [1998]; Rousseau *et al.* [2008a]; Lecompte *et al.*). Indeed, spinal instability is related to excessive intervertebral displacements, which induces pain. To limit these displacements, the nervous system controls the spinal musculature (Panjabi *et al.* [1989]; Panjabi [1992a,b]). Thus, abnormal muscle behaviour may be an explanatory factor of the aetiology of neck pain and cervical spine disorders (Falla *et al.* [2007]; Fernández-de-las Peñas *et al.* [2008]; Cheng *et al.* [2014]; Alpayci *et al.* [2016]). Furthermore, the developmental mechanisms of surgical complications are not yet fully understood, particularly adjacent segment disease (ASD) and proximal junctional kyphosis (PJK), which might induce a secondary compensation at the level of the cervical spine. Abnormal spine loading and muscular dysfunction could be an issue. Therefore, quantifying the spinal muscle force distribution and the corresponding intervertebral joint load in different configurations could provide valuable information for a biomechanical and clinical evaluation of the patient (Moroney *et al.* [1988a]; Choi [2003]). However, multiple muscle systems are difficult to model because of the well-known redundancy problem, i.e. for any given configuration a multitude of muscles can be recruited (Bernstein [1967]), and because of the limitations of the available measurement techniques.

Various models have been developed to face this issue, including mechanistic models using rigid cables simulating the muscles (Kettler *et al.* [2002]), optimisation models based on the mathematical optimisation of a cost function considering muscle stresses or energy expenditure (Moroney *et al.* [1988a]; Han *et al.* [1995]; Stokes and Gardner-Morse [1995]; Chancey *et al.* [2003]) and EMG-assisted optimisation models adopting a direct relationship between muscle or joint forces and EMG data (Cholewicki *et al.* [1995]; Lo Martire *et al.* [2017]). The proprioception-based regulation model, originally developed for the lumbar spine, with the assumption on the core control strategy that muscles prevent spinal joint overloading and limit intervertebral displacement to protect spine and spinal cord (Panjabi *et al.* [1989]; Panjabi [1992a]), yields physiologically and mechanically consistent results, independently from EMG measurements. This promotes building such a model from clinical image data (Pomero *et al.* [2004]).

The aim of the present study was to propose a subject-specific proprioception-based biomechanical control model to estimate the cervical spine muscle forces. The results reported in two reference studies were used to evaluate the consistency of the model predictions. In order to progress towards the use of this model in a clinical context, the robustness of the model against the uncertainty on the main model parameters was quantified and the feasibility of generating this subject-specific model was assessed with a case study based on one subject.

3.1.2 Materials & Methods

The proprioception-based muscle regulation model

The biomechanical muscle control model for the lumbar spine described earlier (Pomero *et al.* [2004]), was adapted to the cervical spine. The model assumes that the spinal

musculature protects the spine and the spinal cord by maintaining the intervertebral joint load below the physiological limit, thus preventing the excessive displacement of a *vertebra* with respect to the subjacent one (Panjabi *et al.* [1989]; Panjabi [1992a]).

The most important model features are detailed hereafter. Let the six-component wrench (generalised forces and moments (Dumas *et al.* [2004])) JL represent the intra-articular load, i.e. postero-anterior shear, medio-lateral shear, compression, lateral bending moment, flexion moment and torsion moment. The six-component wrench TH describes the corresponding physiological joint load thresholds and F_M the resultant load generated by the muscles, which also contains six components. The six-component wrench $NetFM$ represents the net reaction load. From the free-body diagram, the following equation describing mechanical equilibrium can be derived:

$$F_M + JL = NetFM \quad (3.1.1)$$

In case JL remains below TH , the need for muscular activity is limited and an energetically economical equilibrium is installed. However, when $\frac{JL_i}{TH_i} > 1$ for a given load component i , spinal overloading is imminent. Muscles are to be activated ($F_M \gg 0$) to ensure mechanical equilibrium and to lower the intervertebral load to physiologically acceptable levels.

This activation strategy is defined in a closed-loop control process. At each iteration, a *regulation request*, determined by the $\frac{JL}{TH}$ ratio, is evaluated. Based on this regulation request, the excitation and activation levels of the agonist and antagonist muscles are calculated, from which F_M can be derived. JL can then be updated and compared again with TH . The control loop is ended as soon as JL drops below TH or a minimum is reached.

Muscle Regulation Request Function

The regulation request grossly mimics the functioning of the neuromuscular system, i.e. progressively prompting the muscles to act when the intervertebral joint load JL approaches the physiological limits TH . It is represented by a six-component vector Y . For each joint load component i , Y_i is given as follows:

$$Y_i = \alpha \cdot \left(\frac{JL_i}{TH_i} \right)^3 \quad (3.1.2)$$

where α is an arbitrarily defined amplification constant.

Agonist Muscle Activation

MRC_{ij} represents the capacity of the j 'th muscle to regulate the i 'th joint load component and is determined by the muscle's line of action and moment arm. This 6 by N matrix, with N the number of muscles, is multiplied with Y_i to obtain the excitation level of the agonist muscles. Passing this value through a positive sigmoid function yields the agonist muscle's activation MA_j^{Ag} , with values ranging from 0 (not activated) to 1 (fully activated).

Antagonist Muscle Activation

For a given external load component, muscle pairs are considered agonist-antagonist when their lines of action are opposed, with a sensitivity S . For each muscle j , the antagonist muscle activation MA_j^{Antag} can then be calculated from the corresponding agonist muscle

activation MA_j^{Ag} , considering a certain level of coactivation G^{coact} and a general antagonist law adopted from Zhou *et al.* [1996], fully determined by two parameters *overlap* and *gain* (see also Figure 3.1).

Muscle Force Computation

The agonist and antagonist activations are calculated in parallel and are summed to form the global activation matrix MA . To calculate the individual muscle forces, MA_j is multiplied with the muscle's maximal admissible stress σ_j^{muscle} and its cross-sectional surface area CSA_j :

$$F_M = MA \cdot \sigma^{muscle} \cdot CSA \quad (3.1.3)$$

By inserting F_M into Equation 3.1.1, JL can be updated.

The above described routine was programmed in Simulink R2014b (The Mathworks Inc., Natick, MA, USA).

Synthesis

This proprioception-based model is able to estimate, independently from EMG recordings, the muscle force distribution and the corresponding joint load at a certain vertebral level. As an input, the following mechanical and geometrical information on the intervertebral joint and the surrounding muscles are required. For each muscle, the cross-sectional surface area, the moment arm with respect to the joint centre, the direction vector and the maximal admissible stress are to be obtained. The external load expressed in the local reference frame of the intervertebral joint is also a necessary input, as well as the corresponding physiological load threshold.

Model evaluation

To evaluate the model consistency, the predictions were compared with the results described by Moroney *et al.* [1988a] and Choi [2003]. Moroney *et al.* [1988a] choose an optimisation strategy to estimate the muscle activation pattern and correlated their results with *in-vivo* acquired EMG data. Choi [2003] used an EMG-based hybrid model. The estimated muscle forces were compared in left twist, left bending, extension and flexion with the same input parameters as used in these studies.

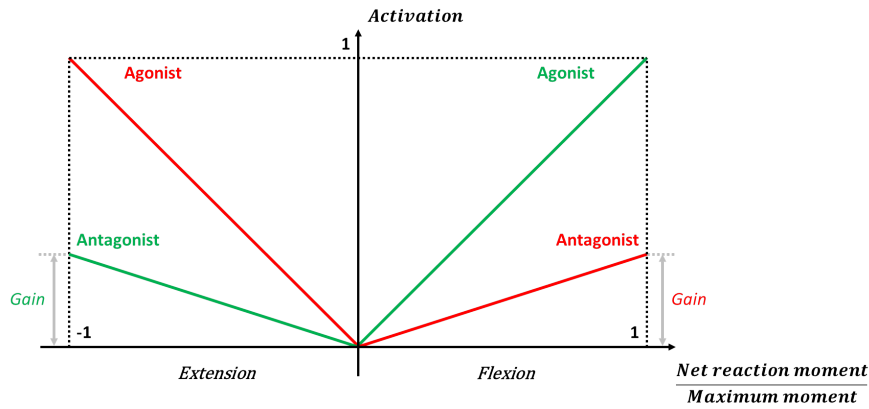
Model robustness and sensitivity study

To progress towards a subject-specific model, built from medical image data, the propagation of the uncertainty on the model input data through the model was quantified.

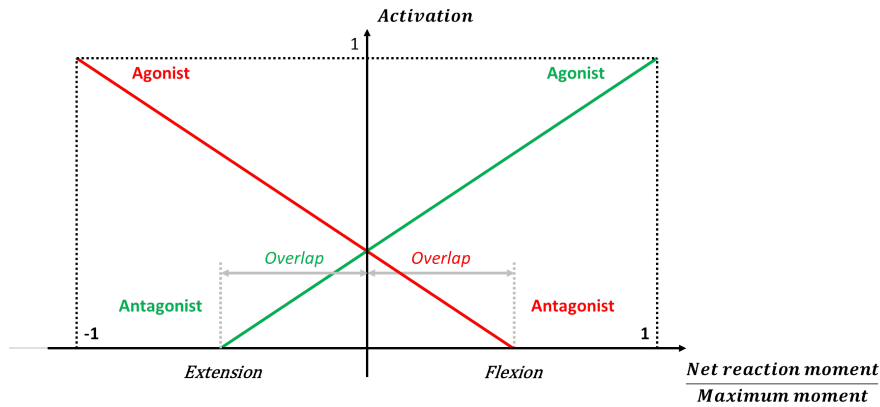
The muscle's geometrical characteristics, its centroid location, its line of action and its CSA, are obtained from MRI and biplanar X-ray data. With few available slices, the calculation of the muscle's line of action might be inaccurate. In a Monte Carlo analysis, a random error of maximally $\pm 7.5^\circ$ was added to the direction cosines, the propagation of which was monitored throughout 1500 simulations.

The influence of the antagonist law parameters (S , G^{coact} , *gain* and *overlap*) and the physiological intra-articular load thresholds (TH), on the muscle force estimation was assessed in a correlation analysis and a full factorial study. Random pseudo-normal distributions were defined for the antagonism sensitivity S (ranging from 0 to 0.3), the antagonist coactivation G^{coact} (with values between 0 and 0.4), the co-contraction *gain*

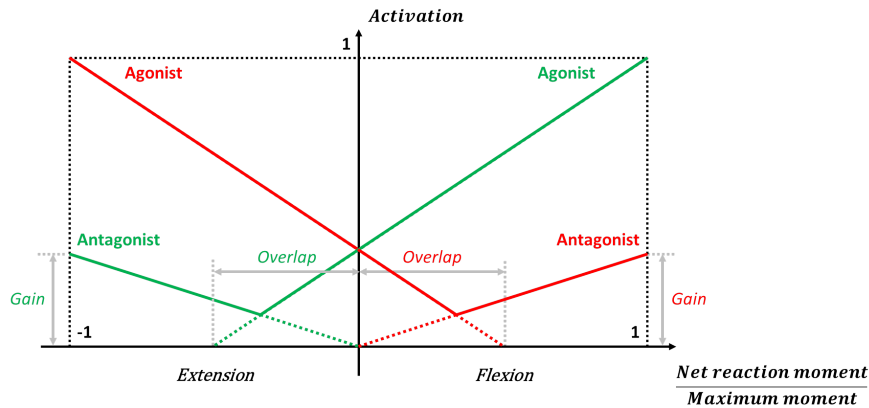
3.1. A SUBJECT-SPECIFIC BIOMECHANICAL CONTROL MODEL FOR THE PREDICTION OF CERVICAL SPINE MUSCLE FORCES



(a) In this configuration, the antagonist vs. agonist behaviour can be described by a single parameter *gain*, representing the ratio between the antagonist and agonist activation.



(b) In this configuration, the parameter 'overlap' determines the antagonist vs. agonist behaviour. *Overlap* represents the percentage of the net reaction to maximum moment ratio at which the agonist and antagonist muscle are both active. In flexion, for instance, the antagonist muscle stays active up to *overlap*, where it reaches zero activity. In full flexion, the only active muscle is the agonist muscle.



(c) This is essentially a combination of configurations a and b. The agonist and antagonist muscles are both active in full flexion (or full extension). The ratio of their activities is given by *gain*. Because of the *overlap*, the activity of the antagonist muscle never reaches zero, even at low agonist input commands. This configuration was chosen for this study. The two other parameters *S* and *Gcoact* are used internally in the closed-loop control process and cannot be visually represented. *S* defines the antagonist sensitivity, i.e. the value above which a muscle is considered antagonist and *Gcoact* is a coefficient defining the relative level of agonist-antagonist coactivation.

Figure 3.1: Three different interpretations of the agonist and antagonist activation as function of the input command, i.e. the ratio between the net reaction moment and the maximum moment for flexion (0 to 1) and extension (0 to -1), as adapted from Zhou *et al.* [1996].

(limited between 0 and 0.4) and the *overlap* (in the range of 0 and 1). In each of the 2000 simulations, each parameter was randomly sampled from their respective populations.

In accordance with the literature, the joint load threshold values TH_i for postero-anterior shear, medio-lateral shear, compression, flexion/extension moment, lateral bending moment and axial rotation moment were set respectively to 50 N, 50 N, 1000 N, 3 Nm, 3 Nm and 3 Nm (Panjabi *et al.* [1986]; Moroney *et al.* [1988b]; Voo *et al.* [1998]; Yoganandan *et al.* [2001]). To assess the effect of the load threshold values on the model outcome, six series of 20 simulations were performed with six different values for the compressive load threshold, i.e. 200 N, 500 N, 1000 N, 1500 N, 2000 N and 2500 N. In each series, the threshold values for the other five load components were varied from 10% to 200% of their initial values.

The geometrical data and the data regarding the external load were obtained from Moroney *et al.* [1988a]. A resisted left twist was modeled with a focus on the C4/C5 intervertebral joint.

Model feasibility: a case study

The feasibility of building the subject-specific model is assessed with a case study based on MRI and biplanar X-ray data of one asymptomatic patient (male, 26 years, 65 kg, 1.77 m, BMI 20.8).

The MRI data was recorded with a 1.5 T Philips Achieva MRI system (Philips Medical Systems, Koninklijke Philips N.V, Amsterdam, The Netherlands) with the patient lying down in the head first - supine (HFS) position. Biplanar sagittal and frontal X-rays were taken with an EOS-system (EOS imaging SA., Paris, France) with the patient standing upright.

The 3D geometry of 19 cervical spine muscles was reconstructed semi-automatically from the MRI data (Jolivet *et al.* [2008]; Li *et al.* [2014]). The muscle geometry was transferred from the lying to the erect posture via the Kriging method (Trochu [1993]), as described earlier for the lower limb (Hausselle *et al.* [2012]). The muscle CSAs, lever arms and direction cosines were calculated at the level of the C5/C6 intervertebral disc (IVD) plane. The process is visually represented in Figure 3.2 (More details can be found in Appendix C).

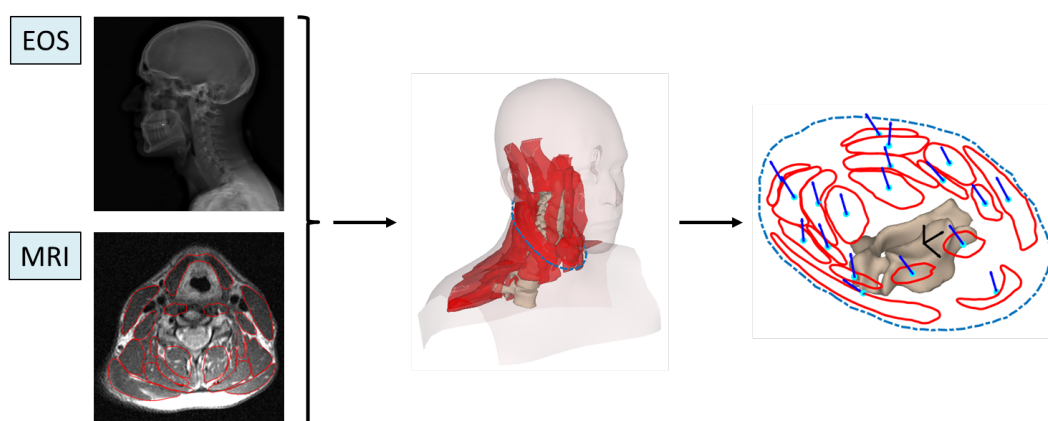


Figure 3.2: From the MRI and biplanar X-ray data, a 3D reconstruction of the cervical spine, the external envelope and the muscles can be obtained. This enables the calculation of the geometric parameters of the muscles in the plane of the IVD of interest, here C5-C6.

The erect posture was modeled considering the mass of the head and the neck segment superior to the C5/C6 IVD plane. These body segment masses were calculated using barycentremetry based on subject-specific volume data and generic density data (Dempster [1955]). The resultant load was expressed in the reference frame of the C5/C6 IVD plane.

3.1.3 Results

For the 3625 simulations performed during this study, the model always fully converged towards a solution, which was obtained in less than five seconds on a regular desktop computer (3.4 GHz i5 CPU and 4Gb RAM).

Model Evaluation

The numerical intervertebral joint load in relation to the physiologically acceptable threshold values and the results published in Moroney *et al.* [1988a] are listed in Table 3.1, for each of the four evaluated configurations (left twist, left bending, flexion and extension). The predicted joint loads remained below the threshold values, except for the postero-anterior shear component in left twist and the postero-anterior shear as well as compression components in extension. The joint force amplitudes presented in this study were generally lower than or equal to the values reported by Moroney *et al.* [1988a], with differences ranging from -70% to 0%. The model predicted higher force amplitudes in extension and to a lesser extent flexion.

		PA	ML	Compression	Lateral	Flexion/	Torsion
		Shear [N]	Shear [N]	[N]	Bending [Nm]	Extension [Nm]	[Nm]
Threshold		50	50	1000	3	3	3
Left twist	Current Study	62.5	-29.2	757.1	1.6	1.6	1.6
	Moroney et al. (1988)	70	33	778	NA	NA	NA
Left bending	Current Study	25	-47.9	759.9	2.2	-2.2	-0.9
	Moroney et al. (1988)	93	125	758	NA	NA	NA
Extension	Current Study	196.8	0	1211.4	0	2.9	0
	Moroney et al. (1988)	135	0	1164	NA	NA	NA
Flexion	Current Study	32.2	0	629.4	0	-2.9	0
	Moroney et al. (1988)	31	0	558	NA	NA	NA

Table 3.1: The numerical intervertebral joint forces in each of the four modeled configurations. (PA stands for *postero-anterior*, ML for *medio-lateral* and NA for *not available*)

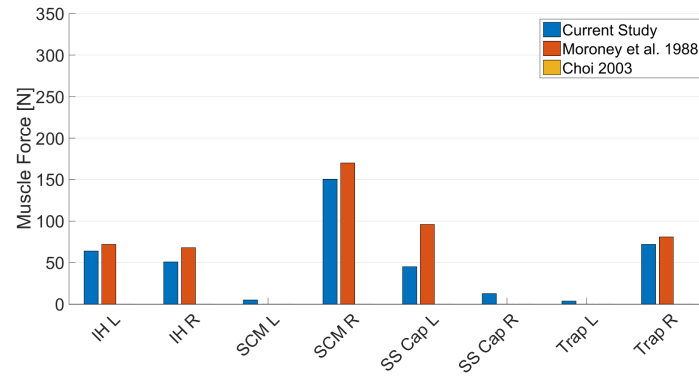
The predicted forces for a selection of four anterior and four posterior muscles in each of the four configurations in relation to those reported by Moroney *et al.* [1988a] and Choi [2003] are shown in Figure 3.3. Globally, the muscle forces predicted by the current model were lower than or equal to the muscle forces obtained by these authors (The comparison for the complete set of muscles can be found in Appendix C).

Relative comparison with the results reported by Moroney *et al.* [1988a] shows that the differences do not exceed 15%, except for five out of the 28 considered muscles in the left twisted configuration (i.e. the right *infrahyoid*, the left and right *levator scapulae* muscles and both the *semispinalis capitis* and *semispinalis cervicis* muscles) and for seven muscles in the left inclined configuration (i.e. the right *infrahyoid*, both *sternocleidomastoideus* muscles, the two *semispinalis capitis* muscles and the left and right *trapezius* muscles).

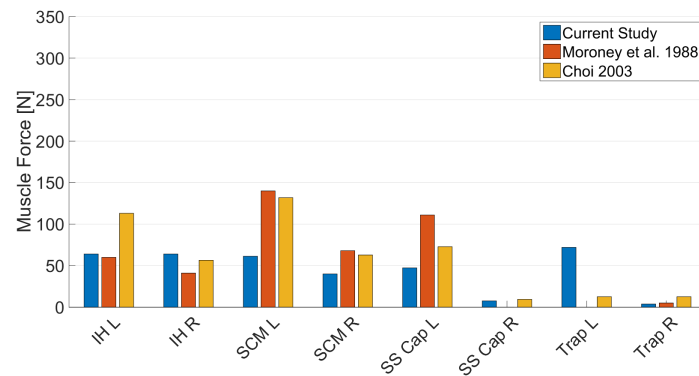
The muscle activation pattern reported in this study agreed with the one Choi [2003] obtained with an EMG-based hybrid model. Moreover, the predicted force amplitudes were lower in left bending and flexion and similar in extension.

Robustness study

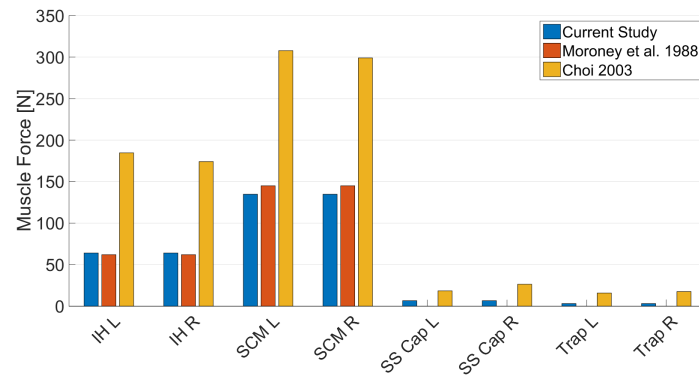
The mean value and the standard deviation for each intervertebral joint load component, predicted by the model in the 1500 simulations considering a random error on the muscle's



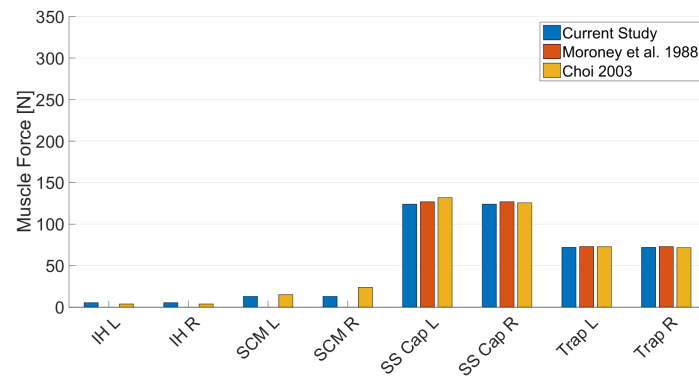
(a) Left twist



(b) Left bending



(c) Flexion



(d) Extension

Figure 3.3: Comparison of the muscle force predictions with two reference studies for a selection of two anterior and two posterior muscle groups in four different configurations. [L: left; R: right, IH: *infrahyoid*, SCM: *sternocleidomastoideus*, SS cap: *semispinalis capitis*, Trap: *trapezius*]

direction cosines, are presented in Table 3.2. The maximum coefficient of variation (CV) was obtained for the medio-lateral shear force (-10%) and the lateral bending moment (8.9%).

	PA Shear [N]	ML Shear [N]	Compression [N]	Lateral Bending [Nm]	Flexion/ Extension [Nm]	Torsion [Nm]
mean	22.3	-12.8	-306.5	0.5	-0.6	-0.6
SD	1.3	1.3	9.1	0.04	0.04	0.02
CV	5.6%	-10%	-3%	8.9%	-7%	-3.1%

Table 3.2: Results of the Monte Carlo analysis allowing the assessment of the model robustness. (PA stands for *postero-anterior*, ML for *medio-lateral* and NA for *not available*)

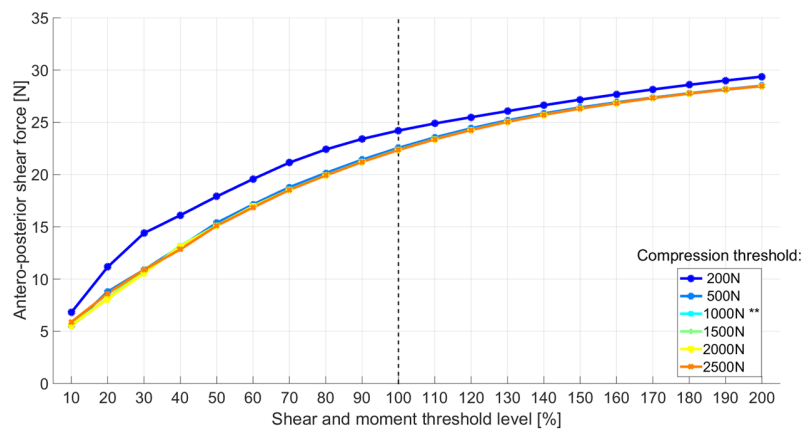
Sensitivity study

The results of the correlation analysis between the parameters defining the antagonist law and each of the predicted intervertebral load components are summarised in Table 3.3. The highest correlation coefficients were found for G^{coact} ($\rho \geq 0.43$), while the lowest were noted for *gain* ($\rho \leq 0.13$).

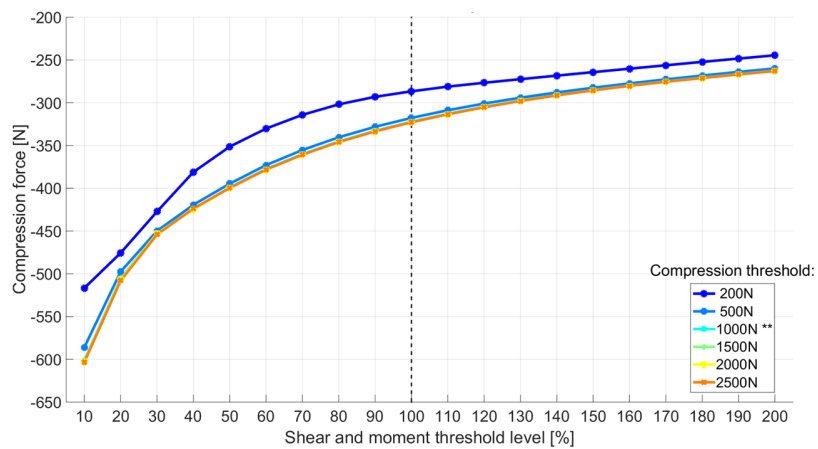
Spearman Correlation Coefficient	S	G^{coact}	Gain	Overlap
Antero-posterior shear	-0.54	-0.43	0.13	-0.36
Medio-lateral shear	-0.39	0.70	-0.0059	0.53
Compression	0.38	-0.73	-0.037	-0.50
Lateral bending moment	-0.16	0.78	-0.0050	0.54
Flexion/Extension moment	0.50	-0.69	-0.043	-0.47
Axial torsion moment	0.59	-0.62	-0.12	-0.37

Table 3.3: Results of the correlation analysis of the parameters defining the antagonist law on the C4-C5 joint load.

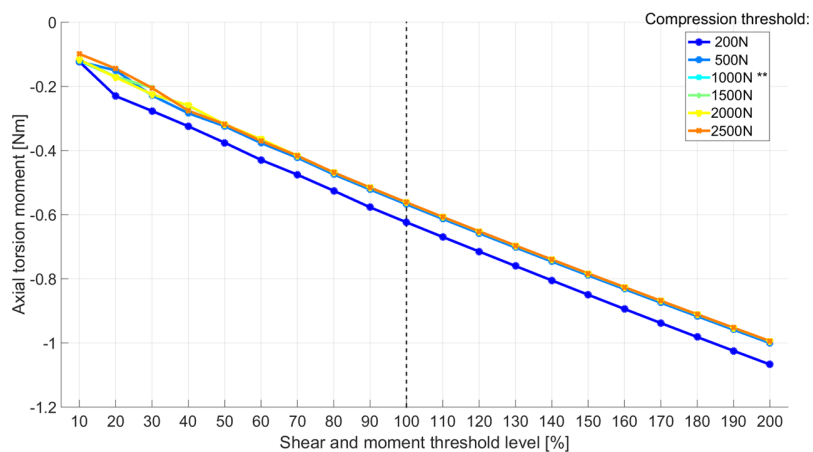
The effect of varying the intervertebral joint load threshold values on the predicted postero-anterior shear forces, compression forces and axial torsion moments, i.e. the result of the full factorial analysis, is illustrated in Figure 3.4. Adjustment of the compression threshold from 200N to 500N impacted all intervertebral joint load components. However, increasing the compression threshold above 500N did not yield a significant change in joint forces. For example, the postero-anterior shear force decreased from 24.2N to 22.5N and from 22.5N to 22.3N, with the compression threshold increasing from 200N to 500N and from 500N to 2500N, respectively. Adjusting the threshold values of the five other load components from 10% to 200% of their initial value, had a more significant effect. For a given compression threshold of 1000N, the postero-anterior shear force, for instance, increased from its initial value of 22.4N to 28.5N when the threshold values were doubled, and decreased to 15.1N when the threshold values were halved. Doubling the threshold values leads to relatively small changes in muscle forces and force distribution, while halving the threshold values yields a different muscle activation pattern and higher muscle forces, as illustrated in Figure 3.5.



(a) Effect on intra-articular postero-anterior shear force



(b) Effect on intra-articular compression force



(c) Effect on intra-articular axial torsion moment

Figure 3.4: Effect of the intra-articular load threshold values on the model predictions for three joint load components, as obtained with a full-factorial analysis. The graphs present the results of six series of 20 simulations. In each series, the compression threshold remained constant, while the threshold values of the other load components were varied between 10% and 200% of their initial value. The dotted vertical line, as well as the legend entry marked with '**' refer to the reference threshold values.

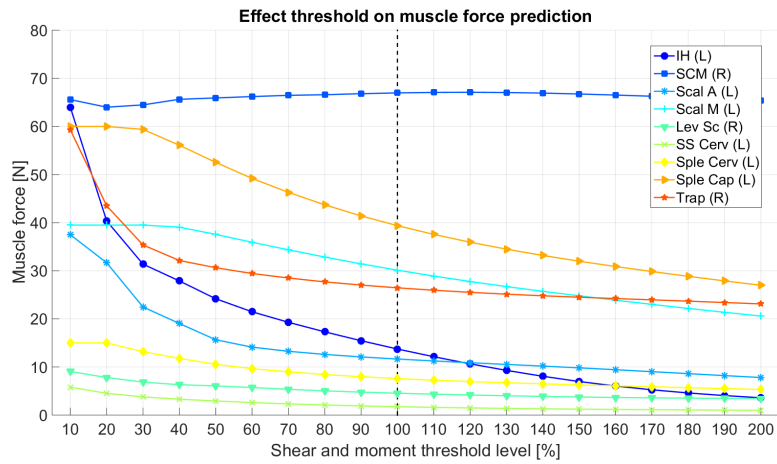


Figure 3.5: Effect of the intra-articular load threshold values on the muscle force prediction, as obtained with a full-factorial analysis. The graphs present the results of the 20 simulations performed with a given compression threshold of 1000N for a selection of ten muscles. The dotted vertical line refers to the reference threshold values. [L: left; R: right, IH: *infrahyoid*, SCM: *sternocleidomastoideus*, Scal A: *scalenus anterioris*, Scal M: *scalenus medius*, Lev Sc: *levator scapulae*, SS Cerv: *semispinalis cervicis*, Sple Cerv: *splenius cervicis*, Sple cap: *splenius capitis*, Trap: *trapezius*]

Model feasibility: a case study

The barycentremetric evaluation of the 26 year old male volunteer yielded the following external load, expressed in the IVD reference frame: [26.10N; -0.15N; -36.50N; 0.07Nm; 0.87Nm; 0.05Nm].

The estimated muscle force distribution is visualised in Figure 3.6. The corresponding load sensed by the intervertebral joint was 29.80N of forward shear, 0.15N of left shear, 47.90N of compression, 0.04Nm of right bending, 0.43Nm of flexion and 0.05Nm of left axial torsion.

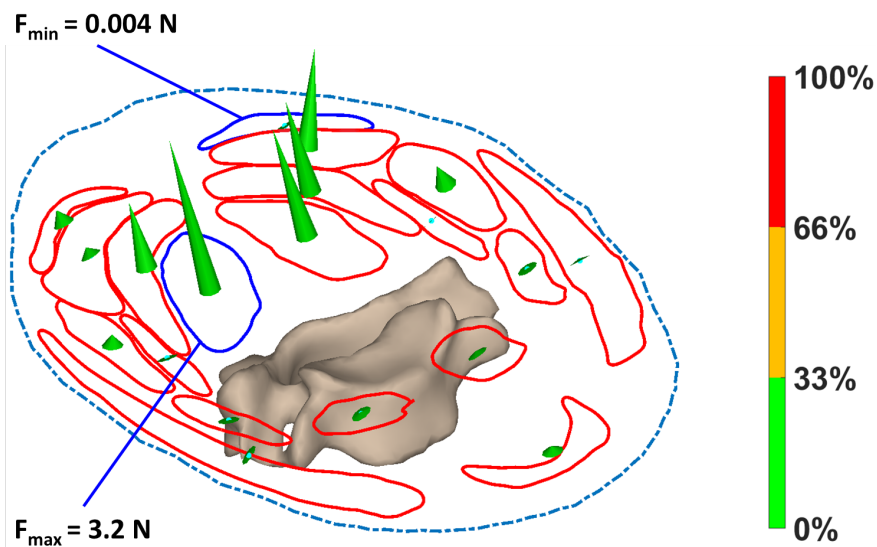


Figure 3.6: The predicted muscle force distribution for the erect configuration. The length of the force vectors is proportional to the force magnitude. The color gives an indication of the ratio between the force exerted by the muscle and the force at maximal contraction.

3.1.4 Discussion

The aim of the present study was to propose a subject-specific proprioception-based control model for the cervical spine. As such, this study provides an alternative methodology to estimate the active muscle forces for a specific configuration and a specific subject, based on biplanar X-ray and MRI data and independently from EMG recordings.

Although the importance of the muscular system in ensuring spinal stability and injury prevention has often been confirmed (Falla *et al.* [2007]; Fernández-de-las Peñas *et al.* [2008]), most studies focused on the lumbar spine. Few authors investigated the behaviour of the cervical spine muscular system (Moroney *et al.* [1988a]; Bernhardt *et al.* [1999]; Kettler *et al.* [2002]; Choi [2003]).

To solve the muscle redundancy problem, optimisation techniques and EMG-driven methods are generally used (Moroney *et al.* [1988a]; Cholewicki *et al.* [1995]; Han *et al.* [1995]; Stokes and Gardner-Morse [1995]). Validation of these numerical strategies remains an issue, since muscle forces cannot be measured *in-vitro* or *in-vivo*. EMG provides a trustworthy indication on the muscle activity of the most superficial muscles, but not necessarily allows the quantification of muscle forces, since the relationship between muscle activity and force should be treated with caution (Hof [1984, 1997]).

The proprioception-based control model changes the paradigm by assuming that the muscular system will act only to protect the spinal joints, i.e. to prevent excessive joint loads and intervertebral displacements, which is naturally a primordial constraint in the cervical spine. This hypothesis on the neuromuscular control, detailed for the first time by Panjabi [1992a], could be confirmed experimentally *in-vitro* (Panjabi *et al.* [1989]; Wilke *et al.* [1995]; Kettler *et al.* [2002]). Its applicability *in-vivo* could be proven as well, based on EMG data (Cholewicki and McGill [1996]). Pomero *et al.* [2004] proposed this control model to predict the muscle force distribution in the lumbar spine. Given the geometrical and functional similarities between the cervical and lumbar spine, the model also applies to the cervical spine, provided that the model parameters are adjusted appropriately.

The comparison with the results obtained with optimisation and EMG-assisted optimisation techniques, showed that this proprioception-based control model generally predicted lower muscle forces and a lower intervertebral joint load for the cervical spine. One could argue that a more efficient configuration is obtained, which might be preferable from a physiological point of view. The same observation was made by Pomero *et al.* [2004] for the lumbar spine. This behaviour can be explained by the fact that the model distributes the regulation request, defined by the external load and the intervertebral joint load threshold, among the different muscles, based on their direction and cross-sectional surface area instead of using a more theoretical and global optimisation technique.

In all four modeled configurations, the predicted muscle forces resembled the estimations reported by Moroney *et al.* [1988a]. For few muscles differences of up to 15% were found. The higher differences noted for, amongst others, the *sternocleidomastoideus* and the *infrahyoid* muscles can be ascribed to the lack of an explicit consideration of antagonist activation in Moroney's optimisation model. Moreover, the predicted activation patterns were very similar to those obtained by Choi [2003] with an EMG-assisted optimisation, thus confirming the plausibility of the current model. On the other hand, the results reported by Choi [2003] in the left bended and flexed configuration were clearly higher than those described here. This might be because Choi [2003] used EMG data to provide a first muscle force estimation, which was then further optimised. In the extended configuration,

the recorded EMG signals are probably more uniformly distributed among the activated muscles, which is not the case for the other two asymmetrical configurations. The effect of the EMG-related coefficients on the optimisation process might thus be less significant.

It should be acknowledged that the current model has its limitations. As in the models described in literature, the influence of the passive elements, i.e. the external envelope, the muscle *fascia* and the ligaments, is not taken into account. This might explain the model behaviour in extension, in which the physiological thresholds were not respected. Supplementary work is in progress to include these passive elements in the analysis.

Muscular activity is primordial to maintain the mechanical stability of the spine (Bergmark [1989]; Panjabi [1992a]; Cholewicki *et al.* [1995]). By explicitly modeling, albeit in a simplified manner, the agonist-antagonist interplay, based on Zhou *et al.* [1996], the concept of mechanical stability was integrated. Furthermore, even in cases where JL remains below TH , certain agonist and antagonist muscles were activated, due to the definition of the antagonist law, which never reaches zero (see also Figure 3.1), and of the regulation request function. However, supplementary constraints might be considered to enable the full integration of mechanical stability.

Although it has been shown that asymmetric configurations are necessary in some cases, a symmetric agonist vs. antagonist behaviour was assumed in this study (Zhou *et al.* [1996]). An asymmetric antagonist law might be more adapted when considering mechanical stability.

The third main limitation of this proprioception-based approach is the lack of background data on the model parameters, particularly the physiological load thresholds. Yoganandan *et al.* [2001] found that cervical intervertebral disc failure occurs under compression forces ranging from 602N to 910N. Voo *et al.* [1998] on the other hand, reported higher compression force limits: mean 1275N (std. 292N). Moroney *et al.* [1988b] found that cervical disc segments failed both in flexion and extension at moments of around 3.40Nm. To the authors' knowledge, the shear force limits are not yet explored in literature. Only Panjabi *et al.* [1986] studied the cervical mobility under a maximal shear load of 50N, but no basis was provided for this value. The threshold values used in this study do not correspond to injury, but rather to a physiological limit, above which muscular regulation is necessary.

Nevertheless, the sensitivity analysis revealed that the intervertebral joint load threshold markedly affected the model outcome, which is consistent with its functioning, since at each iteration the outcome is weighted against the load threshold value. Decreasing the threshold value decreases postero-anterior shear, but increases compression forces. This means that the muscle activation strategy depends on the status of the intervertebral joint, which might vary in time and from one subject to the other. In situations in which clinical instability was established (i.e. a decreased spinal rigidity) the intervertebral load threshold might be lower. This can induce higher muscle forces, resulting in higher intervertebral compression forces. Furthermore, with poor muscle quality, the situation might be even more acute.

As could be confirmed by the case study, the biggest strength of this proprioception-based control model is its ability to provide physiologically relevant muscle forces and intervertebral joint load, independently from EMG recordings, by combining biplanar X-ray and MRI data. It was also shown that the model behaviour was robust to the potential uncertainty on the muscle's direction cosines, calculated from this medical image data. The random error added to the direction cosines did not yield a significantly different intra-articular load or muscle force distribution. After an extensive validation on a representative test population,

the proposed model might facilitate the biomechanical and clinical evaluation of the patient.

3.2 A Subject-specific Analysis

3.2.1 Introduction

Knowledge of the muscle force distribution and associated intra-articular joint load seems necessary, as muscular dysfunction or degeneration is shown to be an explanatory factor for spinal disorders. Moreover, given the fundamental contribution of the muscles to maintain the spinal integrity, muscle forces are a key element to be considered in surgical planning. However, due to a high inter-subject variability and the well-known muscle redundancy, obtaining this knowledge is not straightforward. The literature proposes in general three different techniques to quantify muscle forces. The optimisation-based techniques predict muscle forces by minimising muscle stresses or energy expenditure (Moroney *et al.* [1988a]; Han *et al.* [1995]; Stokes and Gardner-Morse [1995]). EMG-based methods directly link EMG-measurements to muscle forces (McGill [1992]; Cholewicki *et al.* [1995]). The so-called hybrid technique, which combines optimisation with EMG data (Cholewicki *et al.* [1995]; Gagnon *et al.* [2001]; Choi [2003]; Gagnon *et al.* [2016]; Lo Martire *et al.* [2017]). The EMG-measurements offer a first guess for the muscle force pattern, which is then further optimised.

It is difficult to integrate these techniques in a clinical context. The optimisation-based methods are based on cost functions that are more appropriate for a dynamic configuration, but less for (quasi-)static analyses and that do not guarantee a physiologically acceptable muscle activation pattern. The other two methods require EMG data which is not necessarily available in a routine clinical examination. Moreover, few studies exploited these techniques for a patient-specific analysis of cervical spine muscles forces, i.e. using patient-specific input data (Chancey *et al.* [2003]; Choi [2003]; Lo Martire *et al.* [2017]). Most studies focussed on the thoracic or lumbar spine (Stokes and Gardner-Morse [2001]; Gagnon *et al.* [2001]; Arjmand and Shirazi-Adl [2006]; Dreischarf *et al.* [2016]; Azari *et al.* [2017]). As shown before, the proprioception-based biomechanical control model (Pomero *et al.* [2004]; Van den Abbeele *et al.* [2018]) predicts physiologically relevant subject-specific muscle force distributions, entirely based on medical imaging data, thus promoting a potential use in a hospital environment.

This study aimed to exploit the proprioception-based regulation model with the analysis of a cohort of six asymptomatic subjects in the neutral and flexed configuration at the level of two intervertebral joints. The aim was to reinforce the previously performed feasibility analysis, to explore the model performance and to verify whether or not subject-specific input data is necessary.

3.2.2 Materials & Methods

Similarly to the feasibility study described in the above, MRI and biplanar X-ray data were obtained from six young asymptomatic volunteers (28 ± 4 years, 69.7 ± 9.6 kg, 2 female/4 male). The MRI data was acquired with the subject in the HSF position with a 1.5T Philips Achieva system (Philips Medical Systems, Koninklijke Philips N. V., Amsterdam, The Netherlands) and allowed a semi-automatic 3D reconstruction of the muscle geometry (Jolivet *et al.* [2008]; Li *et al.* [2014]). The external envelope was reconstructed as well with the Medical Imaging Toolkit (MITK) (German Cancer Research Center - Division of Medical Image Computing, Heidelberg, Germany). The following 21 muscles or muscle groups were considered: *sterno-cleido-mastoideus*, *trapezius*, *levator scapulae*, *scalenus* (grouping of the anterior, posterior and medial *scalenus* muscles), ventral muscles (grouping of the *longus colli* and *longus capitis*), *hyoid* (grouping of the *infra-* and *supra-* *hyoid* muscles),

longissimus (grouping of the *longissimus cervicis* and *longissimus capitis*), *transverso-spinalis* (grouping of the *semispinalis cervicis*, *multifidus*, *intertransversarii* and *interspinales* muscles), *semispinalis capitis*, *splenius* (grouping of the *splenius cervicis* and *splenius capitis* muscles) and *rhomboideus*.

The biplanar X-ray images were obtained with the subject in the erect configuration with an EOS-system (EOS Imaging SA., Paris, France). The cervical spine, as well as the external envelope were reconstructed semi-automatically (Rousseau *et al.* [2007], Essaidi *et al.* [2011] (unpublished data), Laville *et al.* [2011] (unpublished data) and Nérot *et al.* [2015]).

Based on common landmarks identified on both the MR and EOS images, a subject-specific musculoskeletal model of the cervical spine region in the erect configuration could be generated by fusing the 3D reconstruction of the spine, the envelope and the muscles, as described previously (Hauselle *et al.* [2012]; Van den Abbeele *et al.* [2018]).

From this subject-specific 3D musculoskeletal model, the muscle geometric input data, i.e. cross-sectional area (CSA), direction vector and lever arm with respect to the intervertebral joint centre, could be calculated, as shown in Figure 3.7.

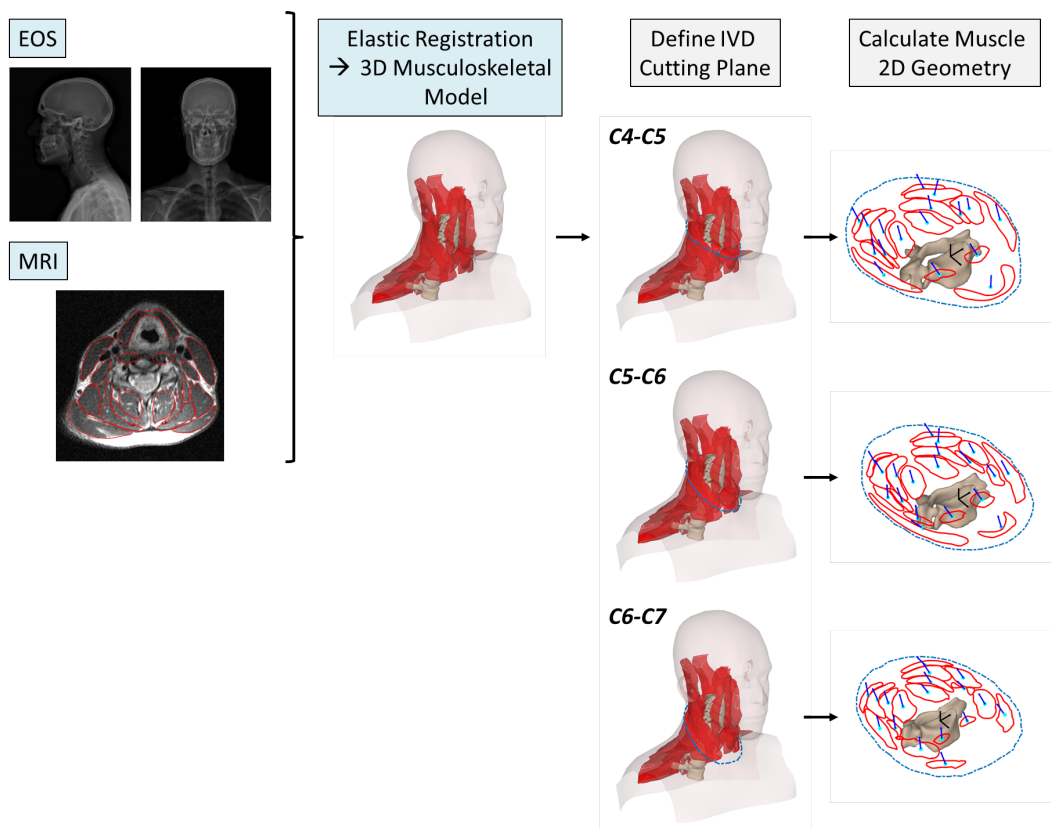


Figure 3.7: The procedure followed to calculate the muscle geometric input data at the level of the C4-C5 to C6-C7 intervertebral joints

Based on the 3D reconstruction of the external envelope and the cervical spine and with density data from the literature (Dempster [1955]), the gravity force, exerted by the head/neck segment above the intervertebral joint of interest onto the body segment below, could be calculated. To do so, a free-body diagram at the level of the intervertebral joint was calculated. The gravity force was expressed in the local joint reference frame and

decomposed into joint forces and moments. Figure 3.8 illustrates the procedure.

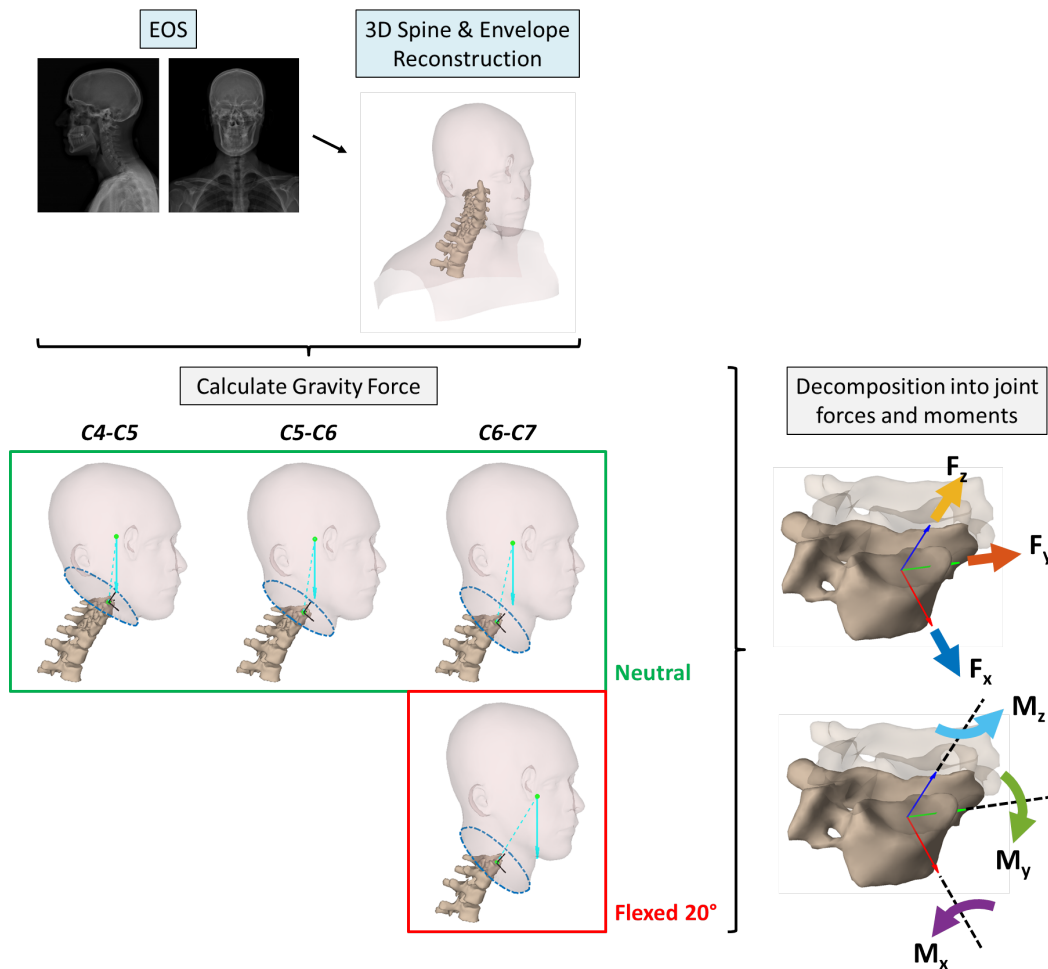


Figure 3.8: The procedure followed to calculate the external forces generated by the head/neck segment above the spinal joint of interest, i.e. C4-C5, C5-C6 and C6-C7

The muscle forces and associated intra-articular joint load at the level of the C6-C7 intervertebral joint in the neutral configuration were quantified using the proprioception-based control model. This configuration was defined as the one in which the EOS data was acquired, i.e. standing upright and maintaining a forward gaze and the eyes on a horizontal plane. To study the effect of posture, the flexed configuration was simulated by rotating the centre of mass of the head-neck segment above the C6-C7 intervertebral joint by 20° around the local y-axis. The level effect was evaluated by quantifying the joint loads and associated muscle forces at the more cranial C4-C5 and C5-C6 intervertebral joints and comparing with the predictions obtained for the C6-C7 level (see also Figures 3.7 and 3.8).

In total 24 simulations (six simulations performed on six volunteers in one configuration at one joint, six simulations performed in a different configuration at the same joint and twelve simulations in the same configuration at two different intervertebral levels) were performed.

3.2.3 Results

Inter-subject variability

The 3D musculoskeletal models, generated from the fusion of the EOS and MRI data, representing the six volunteers in the upright configuration, are shown in Figure 3.9.

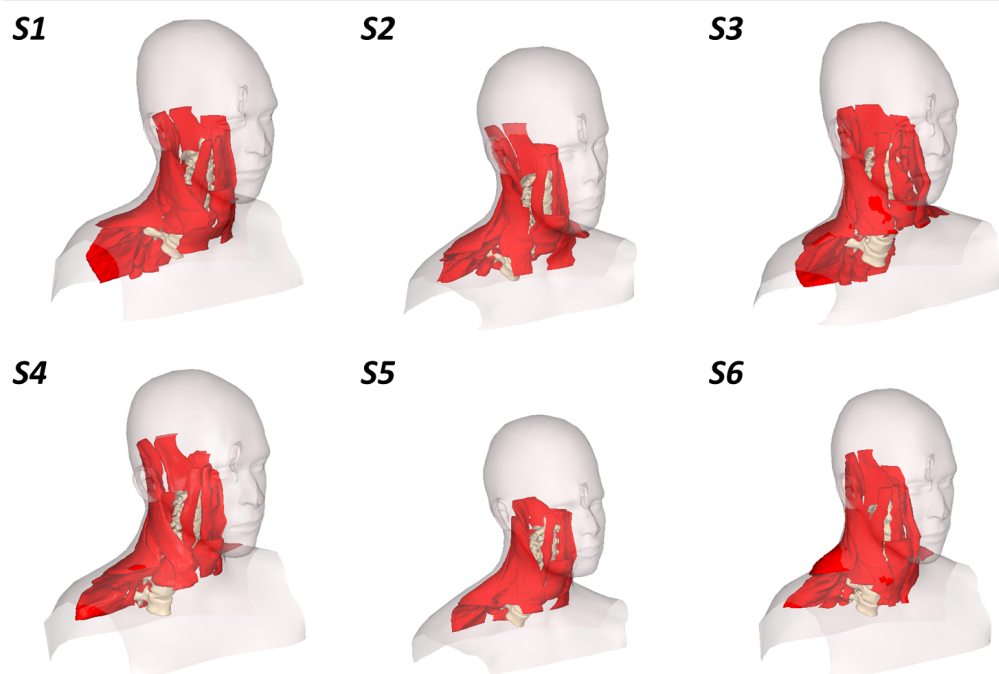


Figure 3.9: The 3D musculoskeletal models for the six volunteers, generated from the EOS data fused with the MRI data.

Figure 3.10 shows the distribution of the exertion points of the external loads, expressed in the local C6-C7 joint frame, as well as their magnitudes, among the six volunteers. The head mass was on average 4.42 kg, with a range from 3.60 kg to 5.62 kg, which was consistent with the values reported in the literature: 3.49 kg to 5.31 kg (Dempster and Gaughran [1967]; Clauser *et al.* [1969]; Reynolds *et al.* [1975]; Chandler and Young [1981]; Yoganandan *et al.* [2009]). The mass of the head/neck segment above the C6-C7 intervertebral level was on average 5.05 kg and ranged between 4.00 kg and 6.55 kg. The associated gravity force lever arm with respect to the intervertebral joint centre measured between 0.82 cm and 2.79 cm in the axial plane.

The decomposition of the external load, calculated from the head/neck mass, in three force and three moment components and expressed in the local reference frame, is shown in Figures 3.11a and 3.11b, respectively. Note that these forces and moments represent the joint load in case muscular regulation is absent.

The joint forces and moments at the C6-C7 intervertebral joint, after muscular regulation, i.e. as predicted by the muscle regulation model, are shown in Figures 3.11c and 3.11d, respectively. When comparing with Figures 3.11a and 3.11b, it becomes apparent that the muscles have efficiently decreased joint moments and shear forces to values below the physiological load limits², at the cost of an increased joint compression.

²The threshold values were the same as those used in Section 3.1, i.e. 50 N for the antero-posterior and medio-lateral shear, 1000 N for the compression and 3 Nm for the moments.

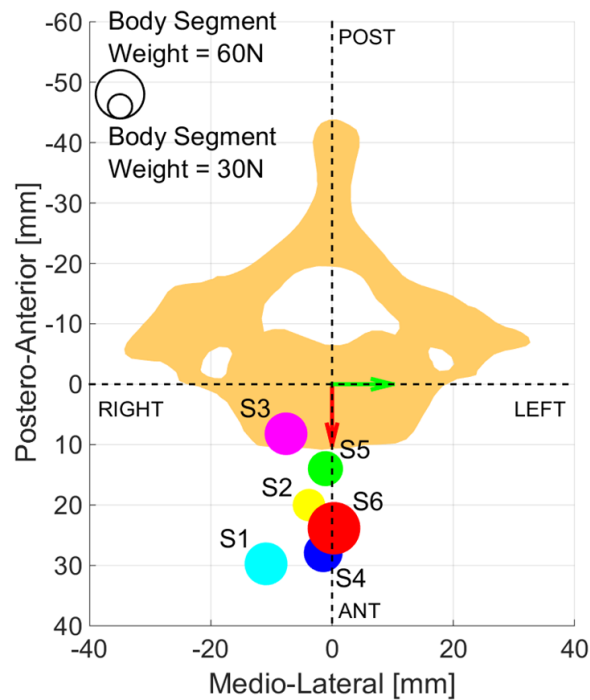


Figure 3.10: The distribution of the exertion points of the external loads, expressed in the local C6-C7 joint frame, as well as their magnitudes, among the six volunteers.

The predicted forces for seven muscles (*hyoid*, *transversospinalis*, *semispinalis* and *splenius*), corresponding to the joint load shown in Figure 3.11c and Figure 3.11d and regulating the external load visualised in Figures 3.11a and 3.11b, are presented in Figure 3.12. A 3D view of the predicted force pattern for three subjects is shown as well.

Posture Effect

Figure 3.13 presents the intervertebral joint forces and moments predicted for each subject in the simulated flexed configuration. By comparing with Figure 3.11, it becomes apparent that the joint moments, before muscular regulation, are significantly higher in the flexed than in the neutral configuration. As a matter of fact, the joint moments trespassed the physiological load limits. However, after muscular regulation, the joint moments were effectively reduced to values below these limits. Yet, the joint compression force significantly increased to values higher than after muscular regulation in the neutral configuration.

In Figure 3.14, the muscle forces predicted for the neutral configuration are compared to those predicted for the flexed configuration. Notice that the force values were increased and that supplementary muscles had to be recruited to regulate the joint load.

Level Effect

Figures 3.15 and 3.16 show the predicted intervertebral joint load before and after muscular regulation for the six subjects at the C4-C5 and C5-C6 intervertebral levels, respectively. The average head/neck mass decreased by about 0.20 kg when moving upwards along the spine: from 5.05 kg at the C6-C7 level to 4.63 kg at the C4-C5 level.

Combining with Figure 3.11, it can be appreciated that, although the head/neck mass does not markedly change, the redistribution of this load among joint forces and moments

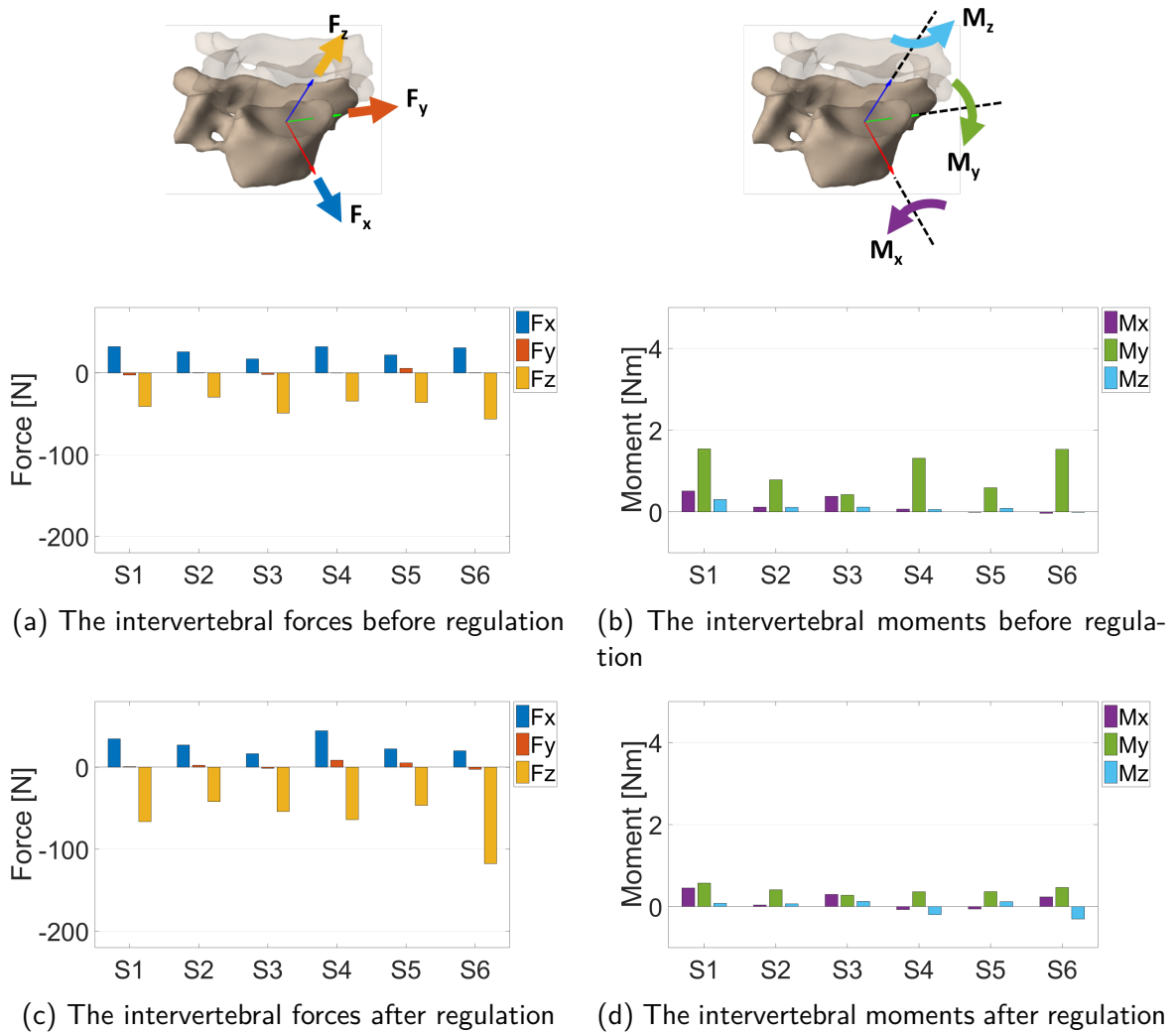
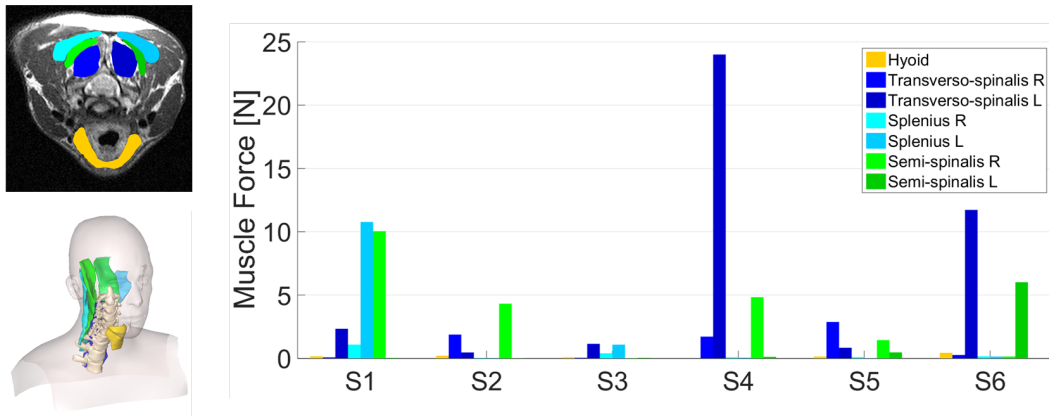
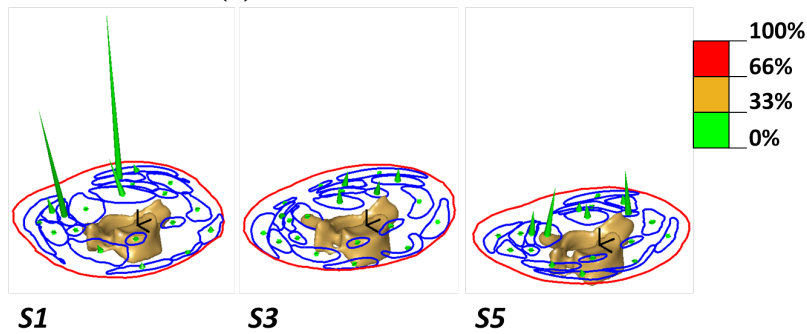


Figure 3.11: The C6-C7 joint load before (a & b) and after (c & d) muscular regulation for the six subjects in the neutral configuration. Note that the joint load before regulation is given by the external load, calculated from the mass of the body segment above the C6-C7 joint, expressed in the local joint reference frame.

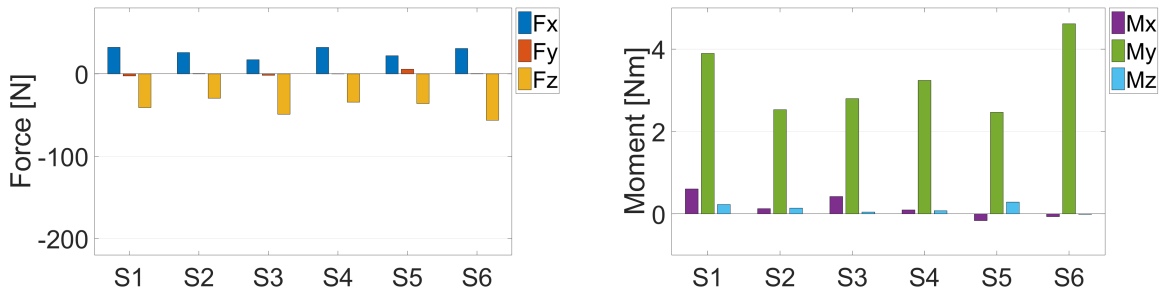


(a) The predicted muscle forces



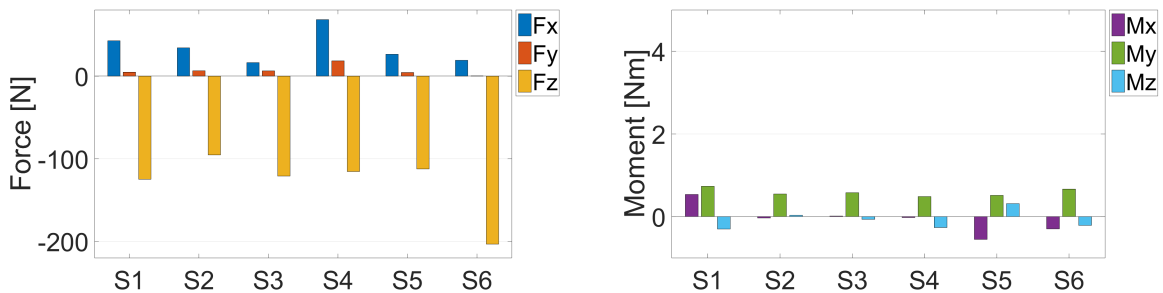
(b) 3D representation of the predicted muscle force pattern for subjects 1, 3 and 5

Figure 3.12: The estimated muscle forces regulating the C6-C7 joint load for the six subjects and a 3D representation for three subjects.



(a) The intervertebral forces before regulation

(b) The intervertebral moments before regulation



(c) The intervertebral forces after regulation

(d) The intervertebral moments after regulation

Figure 3.13: The C6-C7 joint load before (a & b) and after (c & d) muscular regulation for the six subjects in the 20° flexed configuration

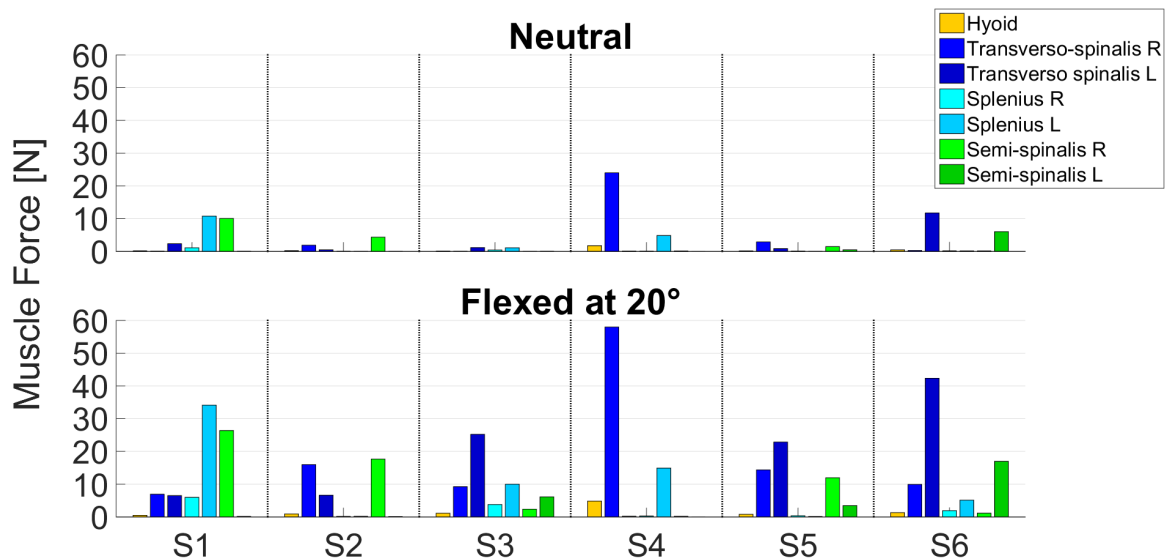
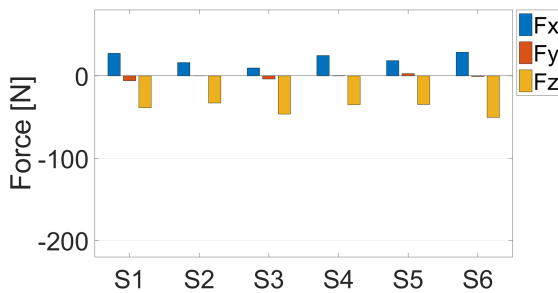
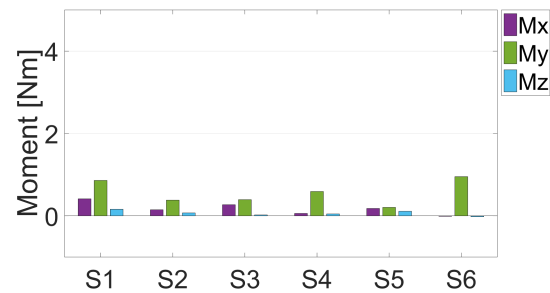


Figure 3.14: The estimated muscle forces regulating the C6-C7 joint load in the neutral and the flexed configuration

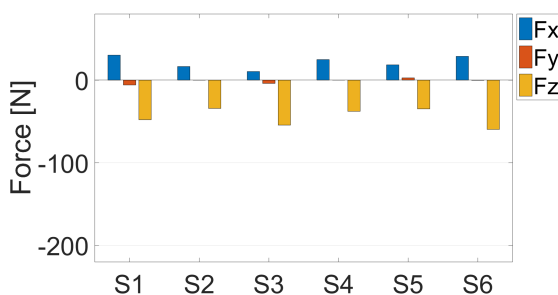
differs between the three vertebral levels, both before and after muscular regulation. Furthermore, the joint load, particularly the joint compression after muscular regulation seems to increase from the C4-C5 to the more caudal C6-C7 intervertebral joint.



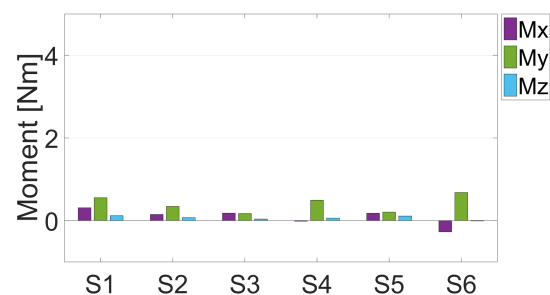
(a) The intervertebral forces before regulation



(b) The intervertebral moments before regulation



(c) The intervertebral forces after regulation



(d) The intervertebral moments after regulation

Figure 3.15: The C4-C5 joint load before (a & b) and after (c & d) muscular regulation for the six subjects in the neutral configuration

Figure 3.17 represents the muscle forces predicted at the three intervertebral levels. The inter-level differences between C4-C5 and C5-C6 are rather limited, compared to the differences noted between C4-C5 and C6-C7, even though the net difference in head/neck mass between each pair of adjacent intervertebral levels was the same.

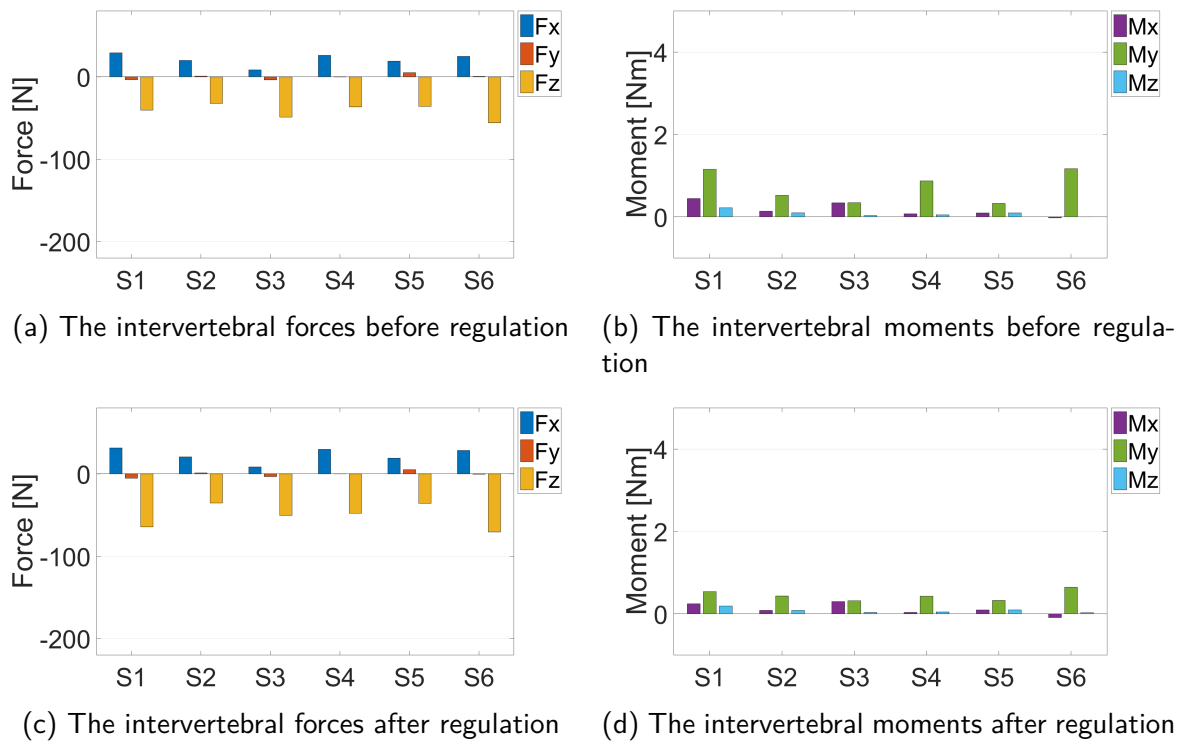


Figure 3.16: The C5-C6 joint load before (a & b) and after (c & d) muscular regulation for the six subjects in the neutral configuration

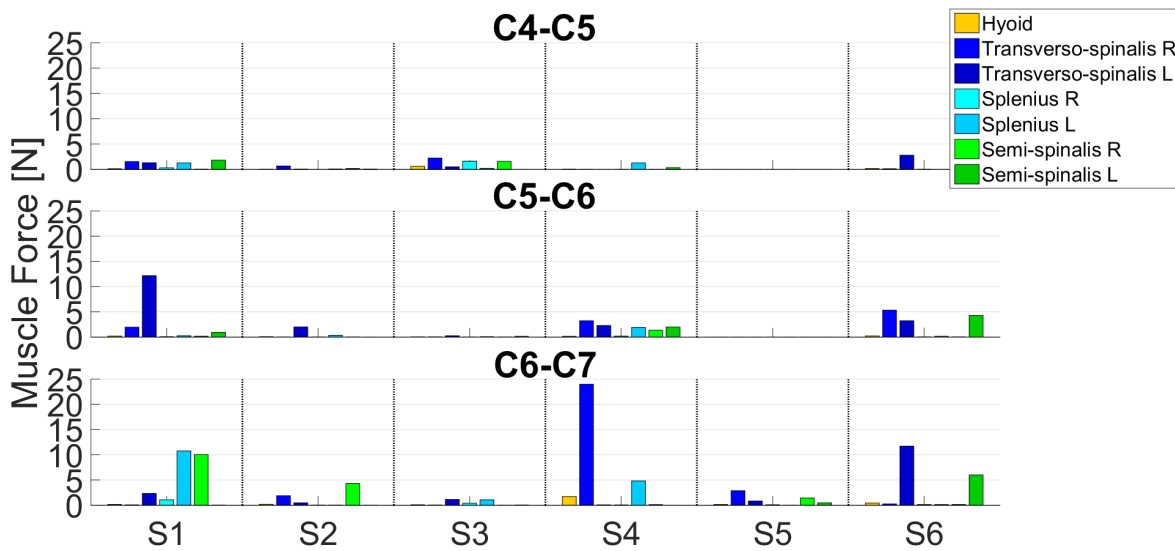


Figure 3.17: The muscle force predictions regulating the joint load at the C4-C5, C5-C6 and C6-C7 intervertebral levels in the neutral configuration

3.2.4 Discussion

It has been shown that muscle force quantification can provide insight into a variety of cervical spine pathologies (Falla *et al.* [2007]; Fernández-de-las Peñas *et al.* [2008]; Cheng *et al.* [2014]; Alpayci *et al.* [2016]). Although literature has provided several techniques to do so, they are not easily transferrable to the hospital environment. Moreover, most studies focussed on the lumbar spine and few attempted a patient-specific analysis. The proprioception-based model on the other hand predicts physiologically acceptable muscle force patterns entirely based on subject-specific medical imaging data, accessible during routine clinical examinations (Pomero *et al.* [2004]; Van den Abbeele *et al.* [2018]). This project aimed to apply this model to a cohort of asymptomatic subjects to assess its capacity to grasp the important inter- and intra-subject variability.

Generating a musculoskeletal model for each of the six volunteers, revealed a high inter-subject variability, not only in terms of geometry, as shown in Figure 3.9, but also in terms of spinal loading, as can be appreciated from Figures 3.10 and 3.11a.

Figure 3.11 shows that for all subjects, the model, as dictated by the assumption that muscles prevent intervertebral joint overloading, reduces joint moments and shear forces, at the cost of an increasing joint compression. Interestingly, the model predicted a different muscle activation pattern for each subject. The model did so, even when the external load exerted by the mass of the head/neck segment above the joint under study was the same, as was the case for subjects 1 (5.32 kg) and 3 (5.30 kg) at the C6-C7 level. Furthermore, even though the head/neck mass at the C6-C7 level of subject 6 (6.55 kg) was higher than for subject S4 (4.80 kg), higher muscle forces were predicted for subject S4. Taking into account the subject's geometry, posture and spinal loading thus seems crucial to understanding the distribution of forces and moments at the intervertebral joint.

The model indicated that flexing the head and cervical spine results in higher joint moments (compare Figures 3.11 and 3.13), which have to be counterbalanced by increasing muscle forces and the recruitment of extra muscles (see Figure 3.14). The cost, however, is a significantly higher joint compression compared to the neutral configuration. These predictions are consistent with the emergence of neck pain when persistently maintaining a flexed configuration, due to muscle fatigue (Côté *et al.* [2008]; Mousavi-Khatir *et al.* [2018]). Although in this case, the flexed configuration was simulated by rotating the head centre of mass by 20° around the local y-axis, for some subjects, e.g. patients having produced a PJK post-operatively or elder patients with postural abnormalities, this might be the permanent configuration. For the young asymptomatic subjects included in this study, the model has shown that the situation could be maintained by the spinal muscles, but for some patients this might not be case. Definitely not when the joint load limits have decreased due to degeneration. Once more, it became clear that besides the subjects morphometry, it is crucial to take into consideration posture.

Comparing Figures 3.15, 3.16 and 3.11, reveals that intra-subject variations might affect intervertebral joint forces and moments. Although the external load does not markedly change when moving cranially from the C6-C7 to the C4-C5 joint, the predicted joint forces and moments change, as do the muscle force predictions (see also Figure 3.17). These differences can be explained by the presence of a cervical lordosis: the C6 vertebra is somewhat less inclined in the sagittal plane than the subjacent C7 vertebra, which explains the increased shear forces and flexion moments in the C6-C7 intervertebral joint, giving rise to higher muscle forces to be regulated.

As mentioned before, the model has certain limitations. The passive elements, i.e. external envelope, muscle fascia and ligaments, are ignored. This might have led to an overestimation of the joint shear forces. Indeed, it is known that a contracting muscle induces axial forces, since it globulises while being contained within an inextensible external envelope and fascia. Secondly, spinal stability is only considered through the interplay between the agonist and antagonist muscles. As a third limitation, it should be noted that the muscle direction vector was based only on its centre line. Muscle fibre pennation was not considered, as it was not discernible on the MRI data. The model also does not consider the different functionalities certain muscles present depending on the activity of the surrounding muscles. The *sterno-cleido-mastoideus*, for instance, flexes the cervical spine and the head with the other muscles rigidifying the spine. If not, it induces an extension movement.

Despite these limitations, the model seems able to capture the inter- and intra-subject variability, while predicting physiologically relevant muscle forces and joint loads. This study forms a solid basis for a biomechanical and clinical study of the cervical spine, which might improve the understanding of cervical spine disorders and even reduce the prevalence of surgical complications.

Chapter 4

Finite Element Modeling of the Lower Cervical Spine

Already fully integrated in the automotive and aerospace industry, Finite Element (FE) modeling also found its way towards the biomedical industry, where it is used in the implant development process. The Food and Drug Administration (FDA) acknowledges the importance of FE modeling in healthcare and published recommendations for reporting on computational modeling studies in the context of medical device submissions for 510k clearance. As shown in Chapter 2, a large number of cervical spine FE models is described in the literature, yet few comply with all of these suggestions.

For surgery planning purposes, a model with patient-specific geometry and material properties is required. Only Laville *et al.* [2009] attempted the development of a method enabling the automatic generation of a subject-specific cervical spine FE model from medical images. However, the model geometry was simplified, as it was generated directly from the parameterisation of the imaging data. The effect of geometric accuracy on the model performance remains to be analysed.

The first section of this chapter is dedicated to the development, verification and validation of a generic morphorealistic FE model, following the FDA recommendations. This resulted in a scientific article entitled 'A Framework for the Validation of Cervical Spine FE Models' ¹. The second section treats the adaptation of the proposed procedure to enable subject-specific analyses, including a *one-to-one* comparison with *in-vitro* data. The effect of geometric accuracy was evaluated by generating a morphorealistic model from both the biplanar X-ray data and the biplanar X-ray data combined with CT data.

Contents

4.1	A Framework for the Validation of Cervical Spine FE Models	60
4.1.1	Introduction	60
4.1.2	Materials and Methods	61
4.1.3	Results	65
4.1.4	Discussion	66
4.2	A Subject-specific Analysis	71
4.2.1	Introduction	71
4.2.2	Materials and Methods	71
4.2.3	Results	72
4.2.4	Discussion	80

¹A submission to 'The European Spine Journal' is currently ongoing

4.1 A Framework for the Validation of Cervical Spine FE Models

4.1.1 Introduction

FE modeling has been recently introduced in the healthcare industry, where it is used to evaluate implant designs and to more efficiently plan *in-vitro* cadaver experiments or *in-vivo* clinical trials. Given the potential implications of wrongful decision making based on FE modeling, it is essential to verify mesh geometry, material properties and boundary conditions and to experimentally validate the model behaviour. Both the scientific literature and regulatory or advisory institutes such as the Food and Drug Administration (FDA) and the American Society of Mechanical Engineers (ASME) offer recommendations aiming to establish standardisation in FE model development (Viceconti *et al.* [2005]; American Society of Mechanical Engineers [2006]; Jones and Wilcox [2008]; Anderson *et al.* [2012]; Erdemir *et al.* [2012]; Noailly and Lacroix [2012]; US Food and Drug Administration - Center for Devices and Radiological Health [2016]). Nevertheless, particularly in terms of verification and validation, a high diversity in approaches can be found in the literature.

A non-exhaustive list of cervical spine FE models currently available in the literature is given in Tables 2.2 and 2.3. Most of the authors obtained the model geometry from CT data and used the hexahedral meshing element, also considered the golden standard in finite element modeling. However, some articles described the use of the more generic but stiffer tetrahedral element. In the few cases the meshing algorithm was detailed, the hexahedral mesh was generated through parameterisation of the medical images (Laville *et al.* [2009]) or by using other multi-block approaches (Kallemejn *et al.* [2009]).

Because of the high complexity of the FE model, few studies attempted a mesh convergence analysis to define the correct element size (Panzer and Cronin [2009]; Kallemejn *et al.* [2010]; Chen *et al.* [2018]), although it is an important step in the verification process. Hence, this explains the large variability in mesh density.

Generally, the biofidelity of the numerical behaviour was evaluated against the literature. In a few cases, direct validation was performed using dedicated experimental data (Laville *et al.* [2009]; Kallemejn *et al.* [2010]; Faizan *et al.* [2012a]). When performing *in-vitro* experiments, the boundary and loading conditions can be controlled and correctly reproduced numerically. This is not necessarily the case when using literature data. Some authors contrast stiffness and range of motion (RoM) with the corresponding experimental values (Kumaresan *et al.* [1997]; Zhang *et al.* [2005]; Hussain *et al.* [2009]; Duan *et al.* [2011]; Faizan *et al.* [2012a]). Other studies compare the numerical with the experimental load-displacement curves, reaching a more profound level of validation (Clausen *et al.* [1997]; Natarajan *et al.* [2000]; Teo and Ng [2001]; Ha [2006]; Pérez del Palomar *et al.* [2008]; Laville *et al.* [2009]; Panzer and Cronin [2009]; Toosizadeh and Haghpanahi [2011]).

A large variability in terms of assigned material properties could be observed, particularly for the soft tissue components. This complies with the important inter-subject variability, exposed in the *in-vitro* literature. Some studies resolved this uncertainty by tuning the properties of the ligaments and the intervertebral disc (IVD) to ensure a satisfactory correspondence with the experimental load-displacement curves (Maurel *et al.* [1997]; Kallemejn *et al.* [2010]). The authors experimentally removed the posterior aspect and/or sequentially removed the spinal ligaments. At each step, the load-displacement behaviour was recorded. By repeating this experiment numerically, in a reverse fashion, the fine adjustment of the soft tissue material properties became possible.

The aim of this study is to illustrate the development of a generic morphorealistic FE model of the inferior cervical spine, starting from the parametric and subject-specific FE model described by Laville *et al.* [2009] and taking into account the recommendations of the scientific literature and the FDA. An extensive validation was performed with two *in-vitro* datasets, selected from the database of our research institute (Barrey *et al.* [2015] and Coloma *et al.* [2016] (unpublished data)).

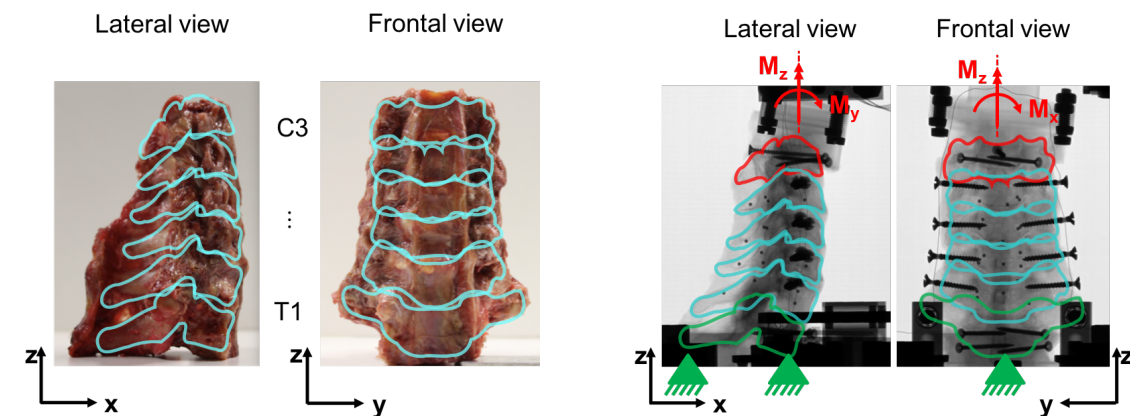
4.1.2 Materials and Methods

Experimental Study

The *in-vitro* experimental data recorded by Coloma *et al.* [2016] at our research institute was used to define the FE model geometry, to fine-tune the material properties and to evaluate the FE model behaviour. In the following, the experimental set-up is briefly described.

Six adult C3-T1 spinal segments were harvested from fresh human cadavers and immediately fresh-frozen at -20°C . The mean age was 61 ± 4 years with a distribution female/male of 2 to 4. The samples were CT-scanned in the fresh-frozen state with a Philips iCT 256 device (Philips Medical Systems, Koninklijke Philips N.V, Amsterdam, The Netherlands). The resolution and the slice thickness were set respectively to 0.47 mm and 0.8 mm. Prior to testing, the samples were gently thawed at room temperature and excessive muscular tissue was excised (see also Figure 4.1).

The samples were mounted on an in-house developed test bench, with the C3 and T1 *vertebrae* potted in polymethylmethacrylate (PMMA) (Technovit[®], Buehler, Düsseldorf, Germany). A pure moment of 2 Nm was applied to the cranial *vertebra* in six steps of 0.4 Nm, while the caudal *vertebra* was rigidly fixed to the test bench. At each load step, biplanar sagittal and frontal X-ray images were taken with an EOS-system (EOS imaging SA., Paris, France). Flexion/extension, lateral bending and axial rotation configurations were simulated. Each load cycle was preceded by three preconditioning cycles. Figure 4.1 visually explains the experimental boundary and loading conditions.



(a) One of the cadaveric samples before testing, with all muscular tissue removed

(b) Biplanar X-ray acquired at the onset of the experiments: the T1-vertebra was blocked in all DoFs, and a pure moment was applied to the C3-vertebra in three directions

Figure 4.1: Sample preparation and experimental boundary and loading conditions

From the biplanar X-ray images, acquired at the onset of the experiments, a 3D reconstruction of the spine could be obtained semi-automatically for each sample (Rousseau *et al.* [2007], Essaidi *et al.* [2011] (unpublished data) and Laville *et al.* [2011] (unpublished data)). Based on these reconstructions, a local reference frame could be assigned to each *vertebra*. The x-axis pointed in the postero-anterior direction, the z-axis in the caudo-cranial direction and the y-axis to the left. By tracking the five radio-opaque fiducial markers rigidly attached to each *vertebra* on each set of biplanar X-rays, the orientation of each *vertebra* with respect to the one below could be determined for each load step. As such, the intersegmental 3D load-displacement behaviour could be quantified.

The 3D load-displacement behaviour was decomposed in three rotational and three translational components, thus differentiating the principal from the coupled motions. The RoM and the helical axis were calculated for each functional spinal unit (FSU) in each of the three tested configurations. The helical axis was calculated from the decomposition of the transformation matrix describing the 3D motion in quaternions. As the 3D position of the helical axis, i.e. the centre of rotation, is not stable, particularly for lateral bending and axial rotation, due to the relatively small angular displacements, the focus was on its orientation.

The CT data, acquired with the sample in the fresh frozen state, was segmented and reconstructed as well, using the Medical Imaging Toolkit (MITK) (German Cancer Research Center - Division of Medical Image Computing, Heidelberg, Germany). These CT-based reconstructions were rigidly registered upon the corresponding EOS-based reconstructions, thus yielding an accurate 3D representation of the sample in the *in-vitro* configuration.

Both the EOS-based and registered CT-based reconstructions were averaged to define the mean 3D geometry, based on which the morphorealistic FE model could be generated.

FE Modeling

The FE model consisted of four *vertebrae* (C4 to C7), three IVDs, the anterior and posterior longitudinal ligaments, the interspinous ligaments, the yellow ligaments and the facet capsules. The vertebral body was modeled as an inner spongy core surrounded by a thin cortico-spongy layer. A cartilaginous endplate formed the interface between the *vertebra* and the IVD. The facet joints were modeled as layers of contacting cartilage, maintained by the capsular ligament. The IVD consisted of a quasi-incompressible *nucleus pulposus* and a fiber-reinforced *annulus fibrosus*.

Tension-only cable elements with a bilinear elastic behaviour represented the ligaments and the IVD fibres. The volumetric components (*vertebrae*, cartilage and IVD matrix) were represented by eight node hexahedral linear elastic isotropic elements. Frictionless surface-to-surface contact elements were used to model the interaction between the facet joint surfaces and the spinous processes.

The starting point for the mesh generation was a coarse and simplified FE model generated from the parameterisation of the averaged EOS-based reconstruction, following the procedure described by Laville *et al.* [2009] (see Chapter 2 for more details). The result is shown in Figure 4.2. A number of modifications were adopted to the mesh topology and the assigned material properties.

The hexahedral elements constituting the transverse processes of the C7-*vertebra* were distorted. To solve the issue, the parameterisation of the C7-*vertebra* was adjusted: instead

of using a cylinder as the geometric primitive for the articular process, a rectangular block was used.

The appropriate mesh density was defined through a preliminary mesh convergence analysis. Each hexahedral element in the coarse simplified mesh was subdivided into eight smaller elements. This was repeated twice, yielding three different mesh densities. The numerical load vs. displacement behaviour in flexion/extension and the Von Mises stresses in the IVDs were analysed. It seemed that with eight subdivisions, the results had already reached a plateau.

To better capture the morphometric particularities of the cervical spine, after mesh densification, the simplified mesh was deformed. This was achieved by iteratively evaluating the displacement field expressing the elastic transformation from the external surface of the FE mesh to the target surface, i.e. the averaged 3D CT-based reconstruction (Moshfeghi *et al.* [1994]). The position of the internal nodes was redefined by Kriging interpolation (Trochu [1993]).

The IVD geometry was obtained by extruding the vertebral endplates. After deformation and IVD mesh generation, the mesh element quality was optimised to prevent distorted elements with an in-house developed C++-based tool (Travert [2013]). Briefly, the position of the internal nodes was adjusted iteratively to bring the quality parameters for each element below the error limits. The algorithm focusses on the *Jacobian* ratio, the aspect ratio, the parallel deviation, the maximum corner angle and the warping factor. Figure 4.2 depicts the result.

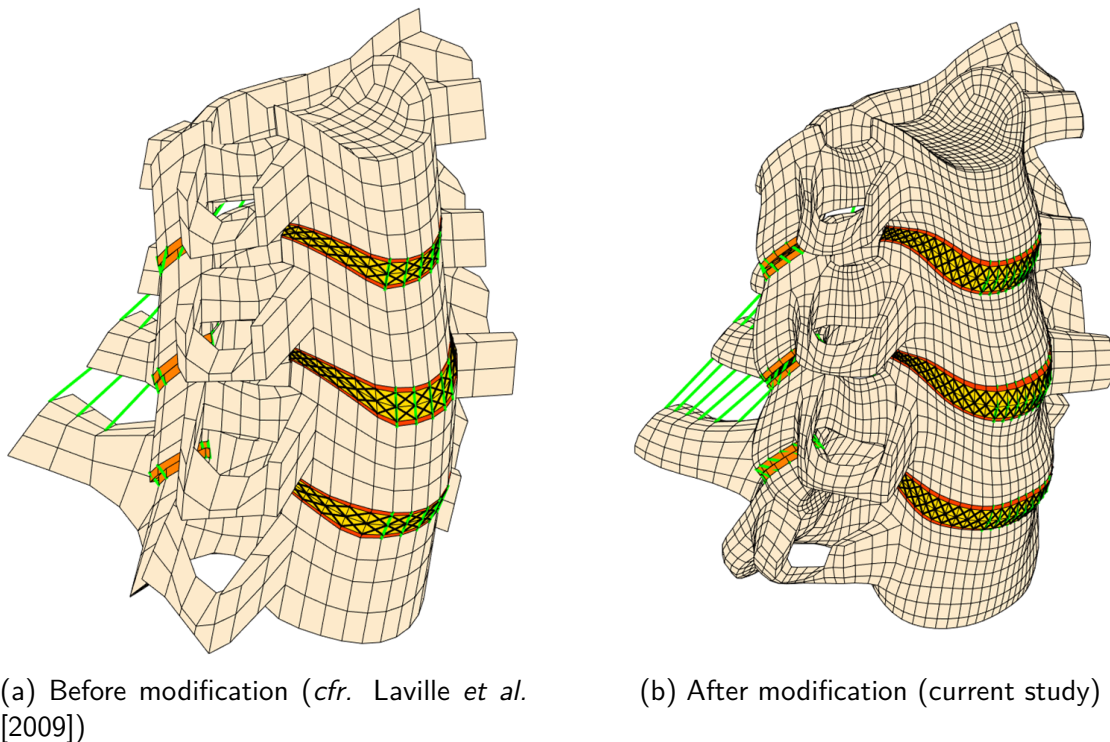


Figure 4.2: The generic FE mesh of the C4-C7 spinal segment

The mechanical properties of the different model components chosen by Laville *et al.* [2009] are given in Table 4.1. In the context of the current study, the material properties of the cortical bone, the posterior arch, the IVD and the spinal ligaments were adjusted.

The cortical bone was modeled with one layer of hexahedral elements with an approximate thickness of 0.5 mm, thus essentially describing a zone of cortico-spongious bone. Therefore, the Young's modulus was lowered from 12 GPa to 457 MPa, as prescribed by

Liebschner *et al.* [2003] and El Masri *et al.* [2012]. Because in terms of bone mineral density, calculated from the calibrated CT scans, the difference between this zone and the posterior arch was low, the same properties were assigned to the posterior arch.

A sensitivity analysis has revealed that the mechanical behaviour of the IVD and the ligaments are the primary factors determining the load-displacement behaviour of the spine. However, a high variability in terms of material properties is noted in both the *in-vitro* and *in-silico* literature. The soft tissue mechanical properties were therefore defined as follows.

In a preliminary experimental study performed at our laboratory, Tonetti *et al.* [1995] (unpublished data) has shown, by sequentially removing the spinal ligaments from cervical spine cadaveric samples, that even without the spinal ligaments, the load-displacement behaviour remained non-linear. This indicates that the assignment of a linear isotropic material behaviour to the IVD matrix, as usually described in the literature, is an oversimplification. Therefore, a multi-linear stiffening stress-strain behaviour was assigned to the IVD *annulus*, while the *nucleus* was considered incompressible. The elastic modulus characterising the *nucleus* was determined from the literature, while the parameters defining the multi-linear stress-strain behaviour of the *annulus* were defined in a non-linear optimisation procedure, as described below.

The properties of the discal fibres, the ligaments and the IVD *annulus* were adjusted in a non-linear optimisation, minimising the difference between the numerical and average experimental behaviour obtained from Coloma *et al.* [2016] (unpublished data). The starting values were those obtained from Laville *et al.* [2009]. The obtained parameters are listed in Table 4.1 and were consistent with the literature (Chazal *et al.* [1985]; Maurel *et al.* [1997]; Yoganandan *et al.* [2000]; Laville *et al.* [2009]; Mattucci *et al.* [2012]; Mattucci and Cronin [2015]).

The above described *in-vitro* experimental conditions were reproduced numerically (see Figure 4.1): the caudal *vertebra* was blocked in all degrees of freedom and a pure moment of 2 Nm was applied to the cranial *vertebra* in ten quasi-static steps. Three configurations were simulated: flexion/extension, lateral bending and axial rotation. The post-processing of the numerical and experimental data was similar: the principal and coupled motions of each *vertebra* with respect to the one below were calculated at each load step by tracing a local reference frame rigidly attached to each modeled *vertebra*². The helical axes corresponding to the principal motions were obtained as well.

The FE mesh was generated using an in-house developed Matlab-based script (Matlab R2014b, The Mathworks Inc., Natick, MA, USA), while the nonlinear FE simulations were performed using ANSYS 15.0 (ANSYS Inc., Cannonsburg, PA, USA) with the implicit formulation and using the full Newton-Raphson method.

Model Validation

In a first indirect validation step, the numerical RoM was compared with the available experimental literature in the three modeled configurations (Wen *et al.* [1993]; Richter *et al.* [2000]; Panjabi *et al.* [2001a]; Nightingale *et al.* [2007]; Barrey *et al.* [2015]). In a first direct validation step, the numerical moment load vs. angular displacement curves were compared with the corresponding experimental curves in each configuration. Differences

²Instead of five markers, four nodes of the vertebral body mesh were selected to define the local reference frame, i.e. one node in the centre of the two vertebral endplates and one node on both sides of the upper vertebral endplate.

	Element type	Young's Modulus [MPa]		Poisson's coefficient [-]		Cross section [mm ²]		Slackening [%]	
		Laville <i>et al.</i> (2009)	Current Study	Laville <i>et al.</i> (2009)	Current Study	Laville <i>et al.</i> (2009)	Current Study	Laville <i>et al.</i> (2009)	Current Study
Cortical Bone	8-node Hexa	12000	457	0.3	0.3				
Cancellous Bone	8-node Hexa	100	100	0.2	0.2				
Posterior Aspect	8-node Hexa	6000	457	0.3	0.3				
Endplate Cartilage	8-node Hexa	300	300	0.3	0.3				
Nucleus Pulposus	8-node Hexa	2.5	1	0.4	0.499				
Annulus Matrix	8-node Hexa	2.5	0.4 - 0.7 - 3.3	0.4	0.45				
AP IVD fibres	Tension-only Cable	110	110			57.6	36	0	3
ML IVD fibres	Tension-only Cable	10	10			57.6	36	0	13
ALL	Tension-only Cable	10	35.1			5	7.2	10	1
PLL	Tension-only Cable	20	34.7			5	7.2	10	0
Anterior Capsule	Tension-only Cable	60	46.5			7.2	4.8	30	45
Posterior Capsule	Tension-only Cable	60	44.9			12	8	12	29
LF	Tension-only Cable	25	24.9			2.4	8	0	49
ISL	Tension-only Cable	3	5.7			12	5.6	17	5

Table 4.1: Material and element properties of the different model aspects. [AP: antero-posterior, ML: Medio-lateral, ALL: anterior longitudinal ligament, PLL: posterior longitudinal ligament, LF: ligament *flavum*, ISL: interspinous ligament, Hexa: hexahedral].

were expressed as root mean squared error (RMSE) values. The RoM and the orientation of the helical axes of motion were compared as well. A second direct validation step was performed by comparing the numerical with the experimental behaviour recorded by Barrey *et al.* [2015] at our research institute in a similar set-up as the one described in the above.

4.1.3 Results

Experimental Study

As shown in Figure 4.3, the six samples included in the study performed by Coloma *et al.* [2016] (unpublished data) produced a non-linear moment load vs. angular displacement behaviour in each of the tested configurations. The RoM calculated from these non-linear curves corresponds well with the *in-vitro* literature data, as can be appreciated from Figure 4.4.

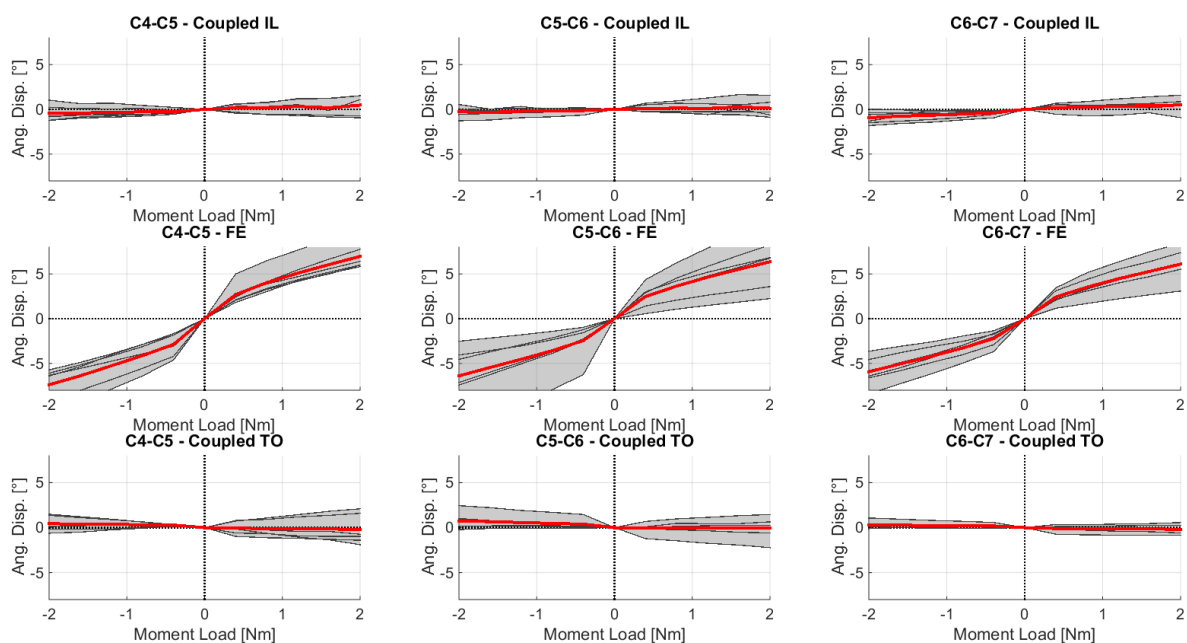


Figure 4.3: Experimental flexion/extension behaviour and associated coupled lateral bending and axial rotation. The experimental mean is indicated in red and the experimental corridor in grey.

Numerical Study

The C4-C7 FE model counts 28356 nodes and 28257 elements, with a median element size of 1.7 mm. None of the elements violated the ANSYS quality error limits and only 0.2% did not fulfil the warning criteria. The point-to-surface distance between the FE model and the corresponding averaged reconstruction reached a maximum of 3.5 mm, however differences were less than 1 mm at the level of the functional zones (e.g. facet joint surfaces and uncinat processes). The simulation of a complete cycle, i.e. a flexion/extension motion starting and ending at the neutral position, required a calculation time of about 20 min.

The FE model was able to reproduce the typical nonlinear moment load vs. angular displacement behaviour observed *in-vitro*, as can be seen in Figures 4.5 and 4.6 for flexion/extension and axial rotation, respectively. For all load configurations, the numerical curve remained within the limits of the experimental corridor and closely followed the average experimental curve. The same remark is valid for the coupled motions. Only

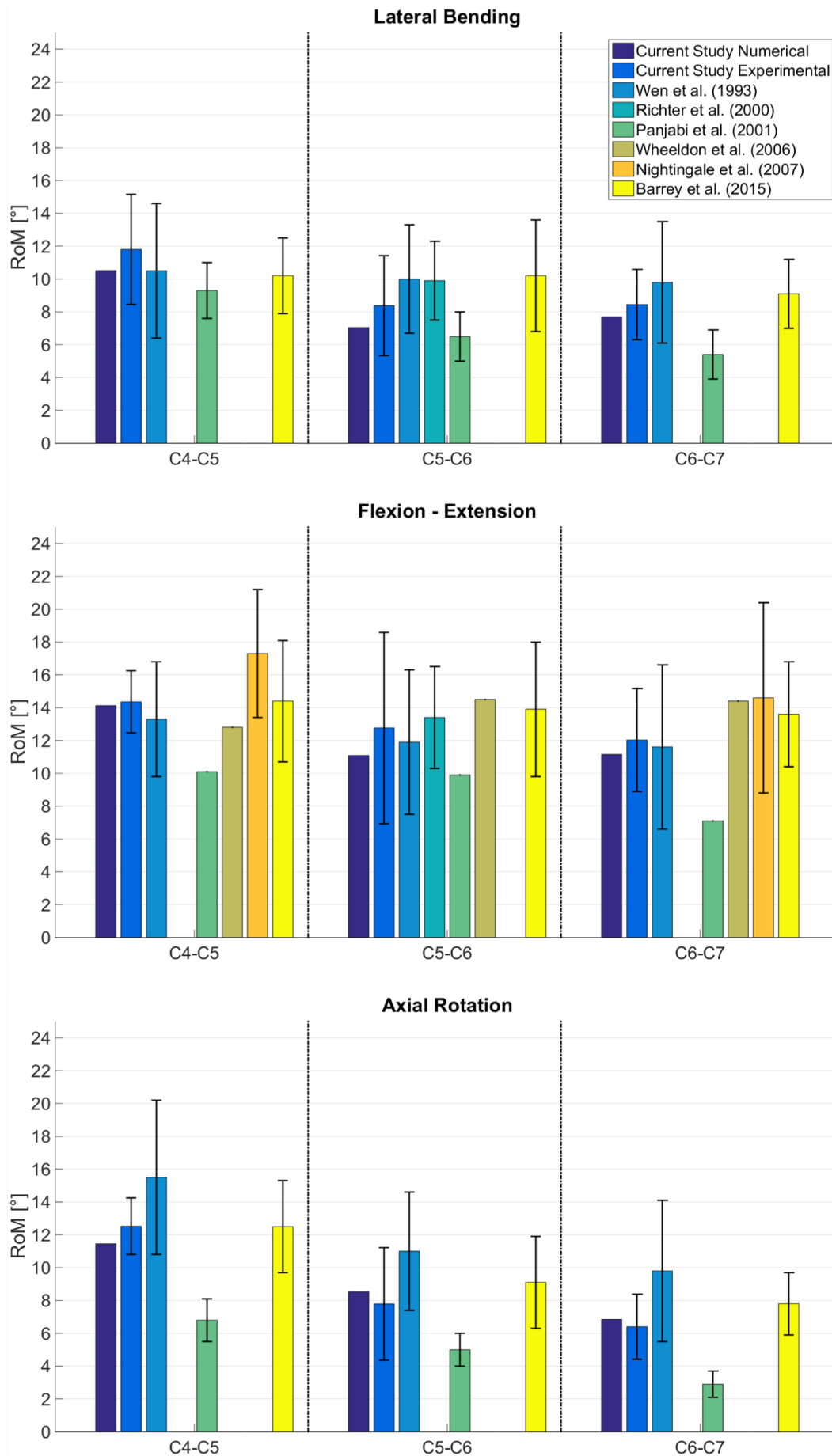


Figure 4.4: The RoM as measured in the current study for a) lateral bending, b) flexion/extension and c) axial rotation, compared to the in-vitro data available in the literature.

for the C4-C5 segment, the numerical coupled lateral bending motion under axial rotation and coupled axial rotation motion under lateral bending were less pronounced than could be observed experimentally. The RMSE between the numerical and the mean experimental curve was on average $0.70^\circ (\pm 0.29^\circ)$ for the principal and $0.71^\circ (\pm 0.60^\circ)$ for the coupled motions. RMSE values are slightly higher when comparing the predicted curves with the corresponding ex-vivo data recorded by Barrey *et al.* [2015]: $1.10^\circ (\pm 0.56^\circ)$ for the principal and $0.92^\circ (\pm 0.71^\circ)$ for the coupled motions. The RoM predicted by the morphorealistic FE model also corresponded well with the RoM reported in the literature (see Figure 4.4).

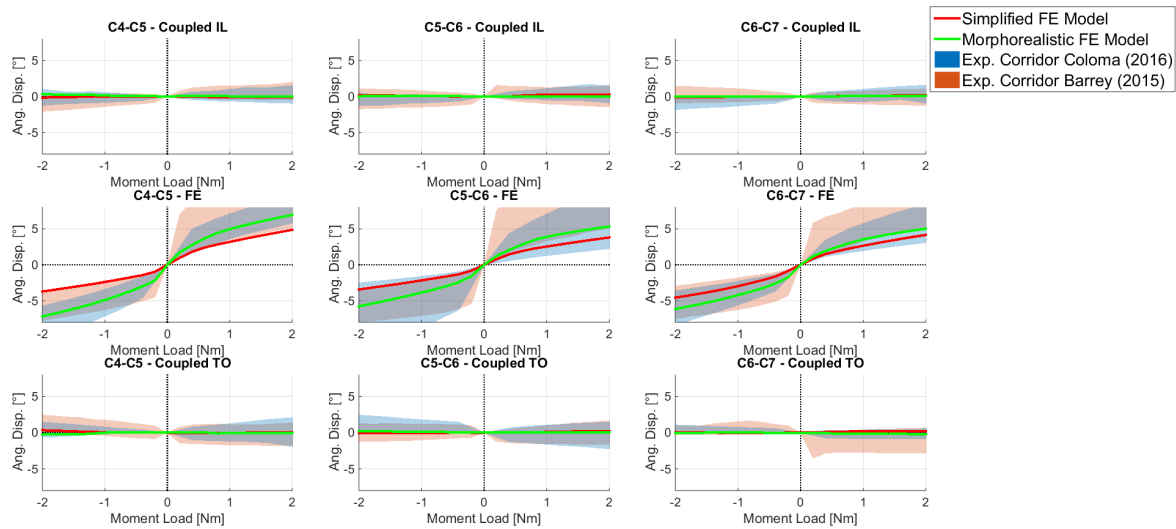


Figure 4.5: Numerical vs. experimental flexion/extension behaviour with the associated coupled motions. The numerical curves obtained with the simplified and morphorealistic FE models are depicted in red and green, respectively. The experimental corridors are rendered in blue and orange for respectively the population tested by Coloma *et al.* [2016] (unpublished data) and Barrey *et al.* [2015].

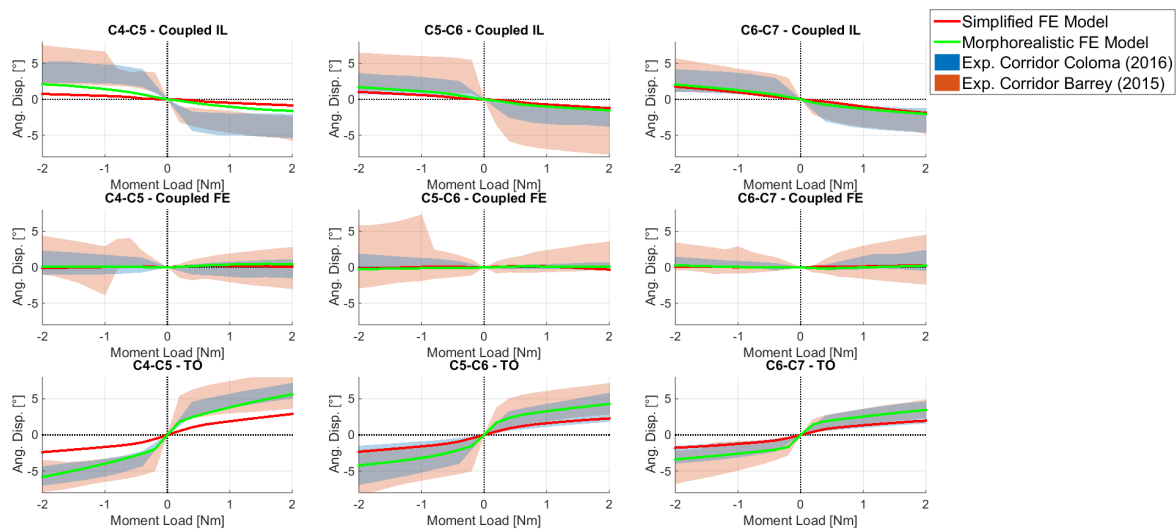


Figure 4.6: Numerical vs. experimental axial rotation behaviour with the associated coupled motions. The numerical curves obtained with the simplified and morphorealistic FE models are depicted in red and green, respectively. The experimental corridors are rendered in blue and orange for respectively the population tested by Coloma *et al.* [2016] (unpublished data) and Barrey *et al.* [2015].

Note that the numerical load-displacement behaviour obtained with the simplified FE model, although it globally remained within the limits of the experimental corridor, was

slightly stiffer than the behaviour recorded with the morphorealistic FE model.

The orientation of the predicted helical axes for each motion and at each vertebral level match closely those observed *in-vitro* by Coloma *et al.* [2016] (unpublished data), as can be seen in Figure 4.7.

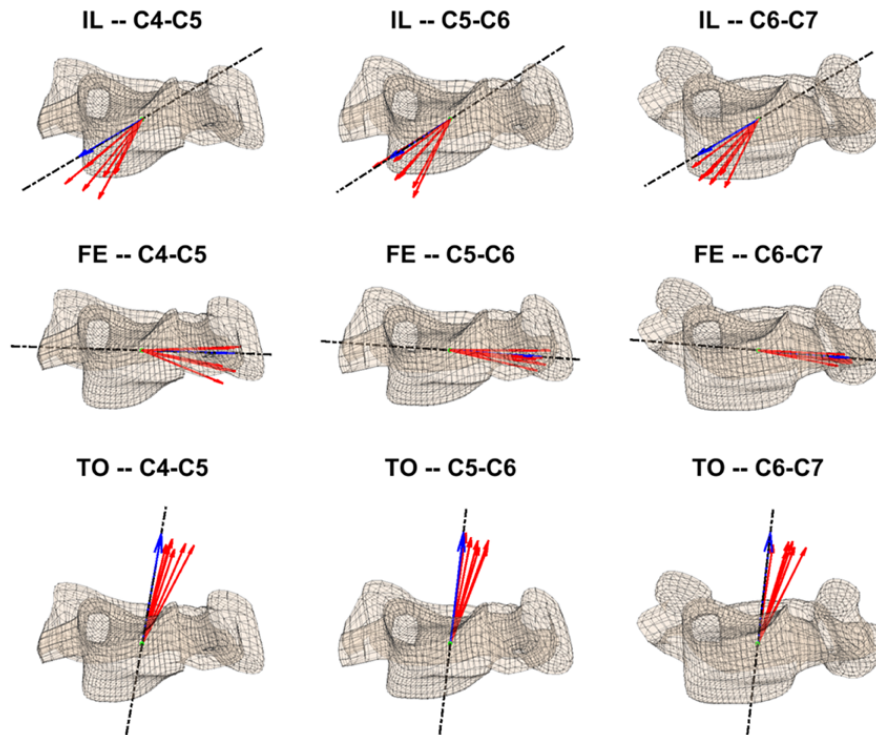


Figure 4.7: The orientation of the predicted helical axes (in blue) for each of the simulated configurations and spinal levels, compared to those observed *in-vitro* (red).

4.1.4 Discussion

The use of FE models in the healthcare industry becomes increasingly popular. It is primordial to verify and validate the model predictions before introduction in a clinical or industrial context. Regulatory agencies and the scientific literature provide a number of suggestions guiding the developer through the model development process. However, the literature contains few FE models that fully comply with these recommendations, as particularly model verification and validation remain complex issues.

The present study proposes, for the first time, a framework for cervical spine FE model validation, illustrated with the example of a morphorealistic generic C4-C7 model, taking into consideration the recommendations described in the regulatory and scientific literature.

As mentioned in the introduction, the FE model behaviour is determined by its geometry, the boundary conditions and the choice of material properties. The model geometry was obtained from the averaged CT-based 3D reconstruction. With a maximal point-to-surface distance of 3.5mm, it can be concluded that the first requirement is met.

In-vitro experimental data from two studies performed at our research institute were used to define the FE model geometry, to adjust the material properties and to evaluate the model behaviour. As such, the experimental boundary and loading conditions were well

controlled and could be accurately replicated numerically. The second requirement could thus be fulfilled as well.

As can be appreciated from Tables 2.2 and 2.3, literature seems to have reached consensus on what properties are to be assigned to the bone tissue. However, regarding the soft tissue material properties, an important variability is to be reported. To solve this uncertainty, some authors calibrated the mechanical properties by numerically reproducing the effect of the sequential removal of the ligaments *ex-vivo* on the spinal kinematics (Kallemeyn *et al.* [2010]). In this study, a similar approach was used. The mechanical properties of the soft tissue components were estimated from the literature and adjusted using input from a sensitivity analysis and a non-linear optimisation based on *in-vitro* experimental data. Although there is no guarantee that the predicted material properties are physiologically consistent, the obtained values were in good agreement with the experimental literature. The third requirement was thus also met.

The results from the indirect validation step (Figure 4.4) showed that the numerical RoM agreed with the experimental literature. Differences can be attributed to the variability in experimental set-up. Indeed, the maximum moment load varied from 1 Nm applied in three steps (Panjabi *et al.* [2001a]) to 3.5 Nm applied in seven steps (Nightingale *et al.* [2007]). Richter *et al.* [2000] let the moment load continuously increase up to 2.5 Nm, while Wen *et al.* [1993] applied a moment between 1.4 Nm and 4.5 Nm in fourteen steps of about 0.2 Nm. Wheeldon *et al.* [2006] and Barrey *et al.* [2015] limited the moment load to 2 Nm and applied it in five, respectively, ten steps. The set-up described by Barrey *et al.* [2015] closely resembles the one used by Coloma *et al.* [2016] (unpublished data). That is why both studies were used for model validation purposes. Note the close agreement between the numerically predicted RoM and the values recorded in these two studies.

The numerical load-displacement behaviour corresponded well with the behaviour recorded by Coloma *et al.* [2016] (unpublished data), at least for the principal motions, with an average RMSE of $0.70^\circ (\pm 0.29^\circ)$ (see also Figures 4.5 and 4.6). This result was expected, as the *in-vitro* data was used to fine-tune the soft tissue mechanical properties. It was thus necessary to evaluate the numerical predictions against a second data set, i.e. Barrey *et al.* [2015]. As can be appreciated from Figures 4.5 and 4.6, the model also respected this second experimental corridor.

The model predicted somewhat stiffer coupled motions than could be observed experimentally. Even though the numerical curves stayed within the limits of the experimental corridors, a significant deviation from the average experimental curves could be noted for coupled lateral bending under axial rotation and coupled axial rotation under lateral bending. This was confirmed by the analysis of the orientation of the helical axes, as visualised in Figure 4.7. Indeed, under lateral bending and axial rotation, the helical axis is less inclined for the numerical model with respect to the x-axis and z-axis, respectively. As coupled motion is primarily explained by the interplay between the uncinat processes and the facet joints (Kapandji [2002]; Ombregt [2013]), the question is raised whether or not the averaged model geometry is realistic. The model generation process based on an averaged reconstruction could have masked certain important mechanical aspects.

Regardless of these limitations, the model behaviour is consistent with the experimental recordings. The biofidelity of the model predictions for flexion/extension, lateral bending and axial rotation can thus be considered confirmed. In its current state, the model might

be used to quantitatively study the biomechanics of the cervical spine and to qualitatively study the effect of changing material properties, certain geometrical parameters or the introduction of a spinal implant.

This study also pointed out some important aspects to consider in the process of developing, verifying and validating an FE model. Firstly, as the numerical behaviour is determined by its geometry, the mechanical properties and the boundary conditions, it is fundamental to verify each of these parameters before model evaluation. Secondly, validation can merely establish the biofidelity of the model for the configuration in which it was tested. Each secondary modification necessitates re-validation. Thirdly, in case experimental data was used to tune the model behaviour, a second data set has to be used for validation purposes as the inclusion of the first data set might yield false positives. Lastly, even though comparing the numerical with the experimental RoM might seem satisfactory, the direct analysis of the load vs. displacement curves and the orientation of the helical axes might reveal more profound issues.

4.2 A Subject-specific Analysis

4.2.1 Introduction

FE models became an essential part of the development and validation of implants and surgical techniques (Ha [2006]; Duan *et al.* [2011]; Faizan *et al.* [2012b,a]; Duan *et al.* [2015]). They have also been proven useful in the study of spinal biomechanics and for injury prediction (Clausen *et al.* [1997]; Kumaresan *et al.* [2000]; Greaves *et al.* [2008]; DeWit and Cronin [2012]; Barrey *et al.* [2015]). As such, there is a clear need for verified and validated FE models.

Although the scientific literature and regulatory institutions provide guidelines standardising the development process (Viceconti *et al.* [2005]; American Society of Mechanical Engineers [2006]; Jones and Wilcox [2008]; Anderson *et al.* [2012]; Erdemir *et al.* [2012]; Noailly and Lacroix [2012]; US Food and Drug Administration - Center for Devices and Radiological Health [2016]), few validated FE models are available. Moreover, most of them are based on a unique set of CT scans and represent one particular geometry. The high inter-subject variability and the complex spinal geometry are the main difficulties to overcome when generating subject-specific hexahedral meshes (Dreischarf *et al.* [2014]). Laville *et al.* [2009] proposed a method to generate a subject-specific, yet simplified, FE model with hexahedral topology from a random set of biplanar X-ray images. In the previous section, it was described how this method was adjusted to generate a morphorealistic FE model, by integrating CT data. It was shown that after a correct assignment of material properties, the numerical behaviour was consistent with the experimental corridor determined in two *in-vitro* experimental studies. However, with the long-term aim of using this FE model in a clinical context to plan surgeries, it is important to verify to what extent the costly and highly irradiant CT scans are necessary to generate a reliable FE model. The effect of geometric accuracy is yet to be quantified.

In the present study, a morphorealistic subject-specific FE model of the intact *subaxial* cervical spine was developed and evaluated against *in-vitro* experimental data in a *one-to-one* comparison. The FE model was generated both from biplanar X-ray images and biplanar X-ray images combined with CT data. By doing so, the influence of geometric accuracy was evaluated.

4.2.2 Materials and Methods

Experimental Study

The experimental data acquired by Coloma *et al.* [2016] (unpublished data), i.e. the data used to evaluate the behaviour of the generic FE model (*cf.* Section 4.1), was used to define the model geometry and to evaluate the model behaviour (*cf.* Section 4.1).

In short, the load-displacement curves of six human cadaveric C3-T1 samples (61 ± 4 years, 4 male/ 2 female) were recorded *in-vitro*. A pure 2 Nm moment was applied in steps of 0.4 Nm to the most superior *vertebra* in three different directions, inducing flexion/extension, lateral bending and axial rotation movements. The most inferior *vertebra* was fully blocked in all DoFs. At each load step, biplanar X-ray images were acquired with an EOS-system (EOS imaging SA., Paris, France), based on which the moment load vs. angular displacement behaviour could be calculated. CT scans were obtained in the fresh-frozen state with a Philips iCT 256 device (Philips Medical Systems, Koninklijke Philips N.V, Amsterdam, The Netherlands), before sample preparation. One sample was excluded from

the study, as its resistance to the moment load was significantly lower than the resistance of the other samples.

3D reconstructions were obtained from the biplanar X-ray data acquired at the onset of the *in-vitro* experiments. The CT data was segmented and reconstructed as well. Since the reference configuration was the *in-vitro* set-up, the CT-based reconstructions were registered upon the corresponding EOS-based ones.

FE Modeling

For each of the five retained samples, a subject-specific FE model of the C4-C7 spinal segment was generated from the registered CT and alternatively from the biplanar X-ray data, following a similar procedure as the one adopted in the development of the generic FE model (*cf.* Section 4.1): from both reconstructions, a set of geometrical primitives and parameters was calculated, based on which a first coarse mesh was generated, following a methodology described previously (Lavaste *et al.* [1992]; Laville *et al.* [2009]). *Vertebrae*, *nucleus* and *annulus* matrix were meshed with hexahedral elements, while tension-only cable elements represented the ligaments and IVD fibres. The initial mesh was densified, before it was deformed to match the 3D reconstructions as close as possible. The deformation consisted of the iterative evaluation of a displacement field, determining the optimal transformation between the external surface of the FE mesh and the reconstruction data (Moshfeghi *et al.* [1994]). Mesh quality was optimised after deformation (Knupp [1999]; Traver [2013]). The isotropic and elastic material properties were the same as those chosen for the generic FE model, as were the contact parameters (see Table 4.1).

The boundary conditions mimicked the *in-vitro* experimental test set-up: the nodes of the C7 *vertebra* were blocked in all DoF, while a pure 1.4 Nm moment was applied to the C4 *vertebra*. The applied moment was intentionally reduced from 2 Nm to 1.4 Nm to prevent extensive local mesh distortion.

A *one-to-one* comparison between the numerical and experimental curves was performed, as well as between the numerical and experimental ranges of motion (RoM). Consistency was quantified using the RMSE for the load-displacement curves and the absolute difference for the RoM. The numerical and experimental location of the mean centre of rotation (MCR) in flexion/extension was also compared. The MCR was defined as the intersection of the helical axis, representing the movement from full extension to full flexion, with the sagittal plane cutting the *vertebra* in half. The experimental and numerical MCR were plotted on the same schematic representation of the FSU of interest. To do so, the MCR and the vertebral contours were retro-projected onto the corresponding lateral X-ray image. By applying the Kriging transformation, expressing the elastic transformation between the retro-projected vertebral contours and a schematic representation of the *vertebra*, the MCR could be plotted onto a schematic representation of the vertebral level of interest.

In total 30 simulations were performed (five models, generated based on two imaging modalities and simulating three configurations).

4.2.3 Results

For each sample, a regular hexahedral mesh was obtained without errors and with less than 0.2% of the elements beyond the warning limit. The meshes generated from the CT and EOS data are shown in Figure 4.8.

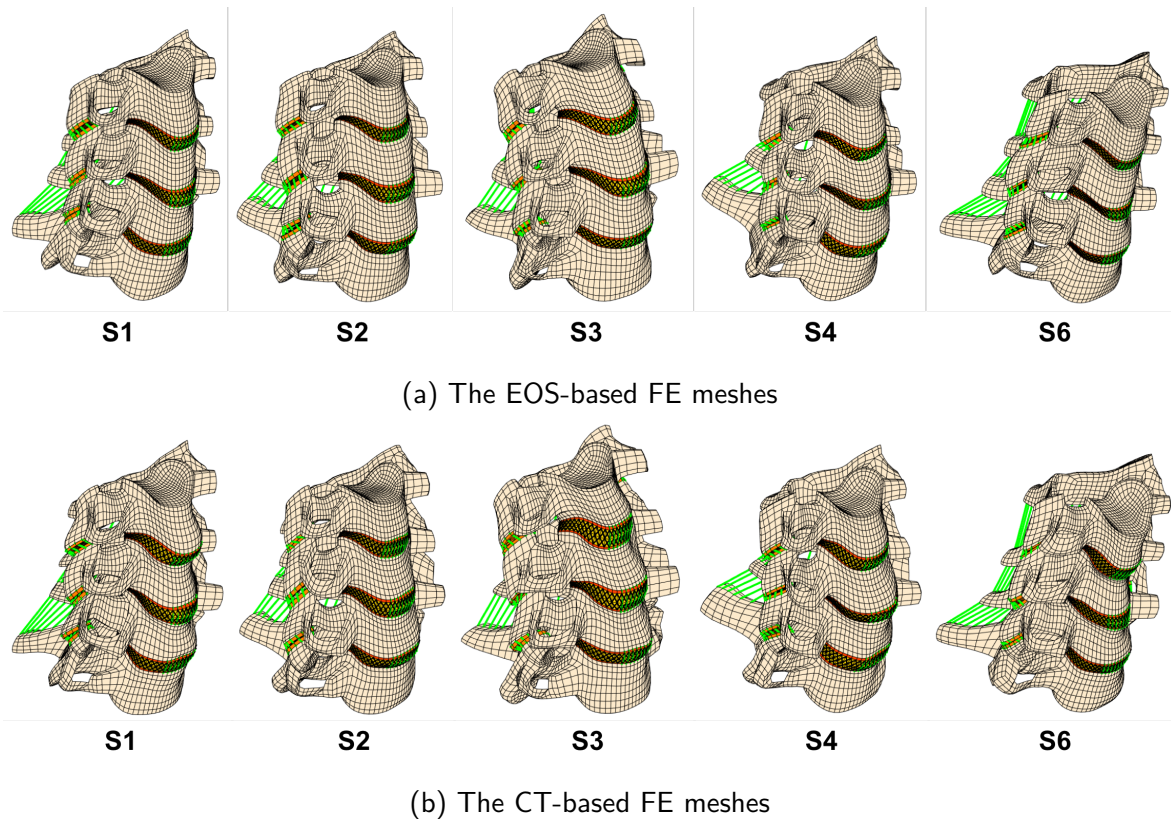
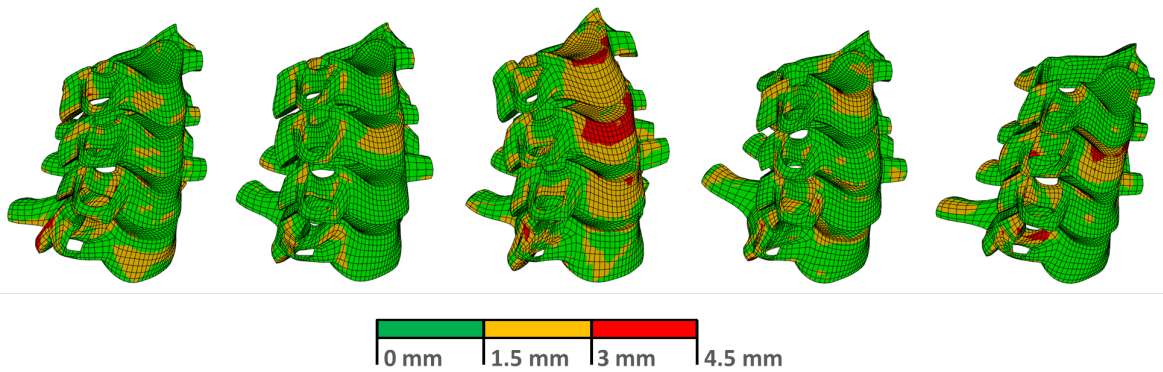


Figure 4.8: For each of the five samples, a regular FE mesh was generated from the biplanar X-ray data and from the corresponding CT data.

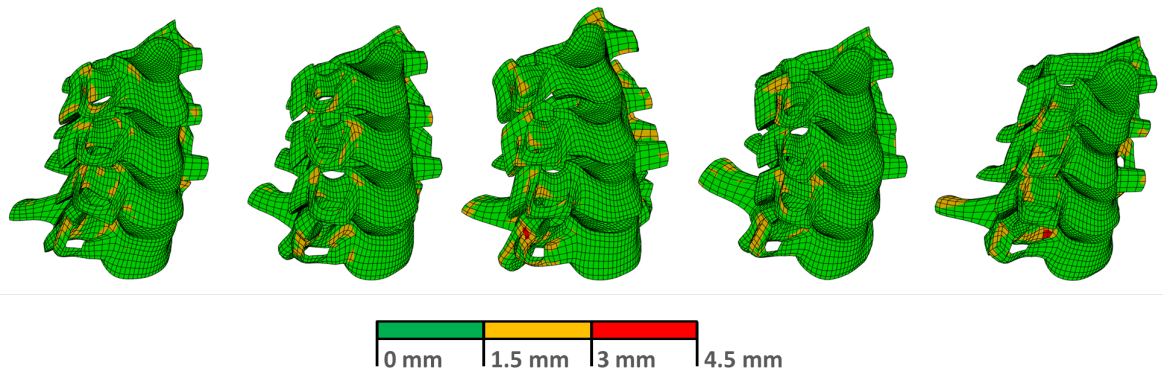
In Figure 4.9, the EOS- and CT-based meshes are compared with the corresponding CT-based reconstruction in terms of point-to-surface distances. With the EOS-based meshes, a mean point-to-surface distance of 1.18 mm (std. 0.58 mm) was observed, ranging between 0.02 mm and 4.51 mm. The CT-based meshes showed lower errors, with an average value of 0.88 mm (std. 0.39 mm), ranging between 0.02 mm and 4.08 mm. Note that globally, the errors remained below 1.5 mm for both meshes. Higher errors were only noted at the non-functional zones, such as the transverse processes.

Each of the 30 simulations converged in about 10 min. The model reproduced the typical nonlinear load-displacement behaviour and was able to differentiate between the different samples. Both the biplanar X-ray as CT-based meshes respected the experimental corridor, as shown in Figure 4.10 for flexion/extension and in Figure 4.11 for axial torsion, but with the CT-based meshes, a larger part of the corridor could be covered. Although the principal motions are relatively well predicted, both models struggle regarding the coupled motions. The numerically predicted coupled motions seemed stiffer than the experimentally observed. The results for lateral bending confirm these observations.

In Figure 4.12 the numerical moment load vs. angular displacement behaviour, recorded for flexion/extension with the EOS- and CT-based meshes, are compared with the corresponding experimental curves. A higher consistency with the experimental results was achieved with the CT-based meshes. Although for some samples the model predictions agree with the experimental observations, for other samples larger differences were found. Furthermore, the model was not always able to capture the motion asymmetry. For example, the model underestimated the angular displacement in flexion for sample S2 at each vertebral level (red curves), while the mobility in extension was overestimated.

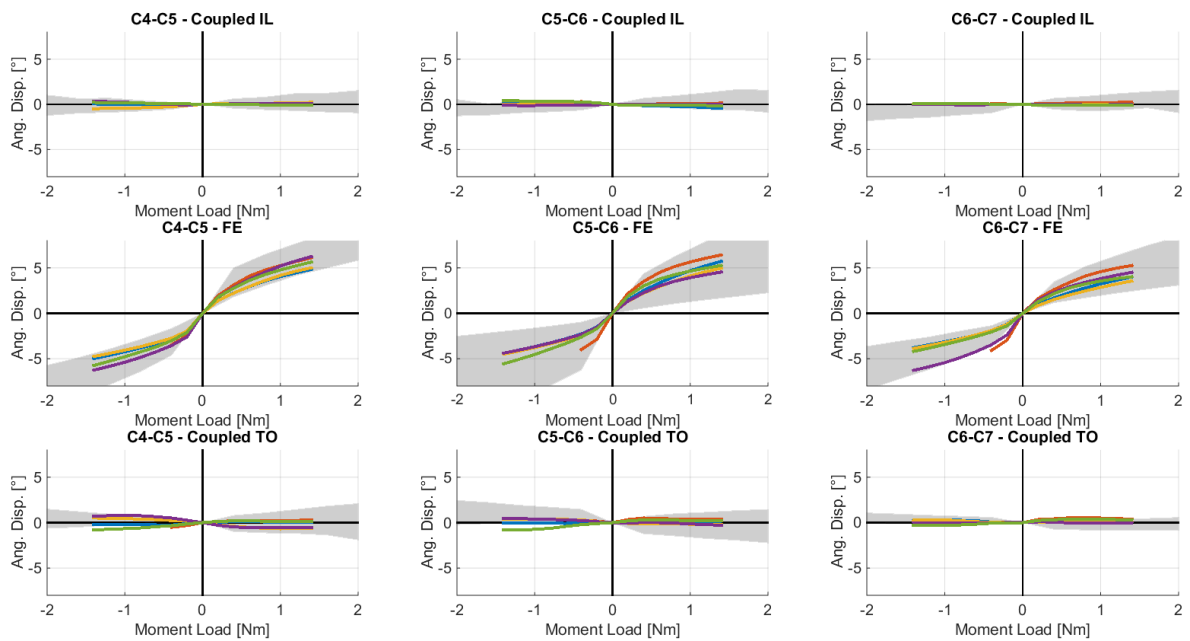


(a) The EOS-based FE meshes

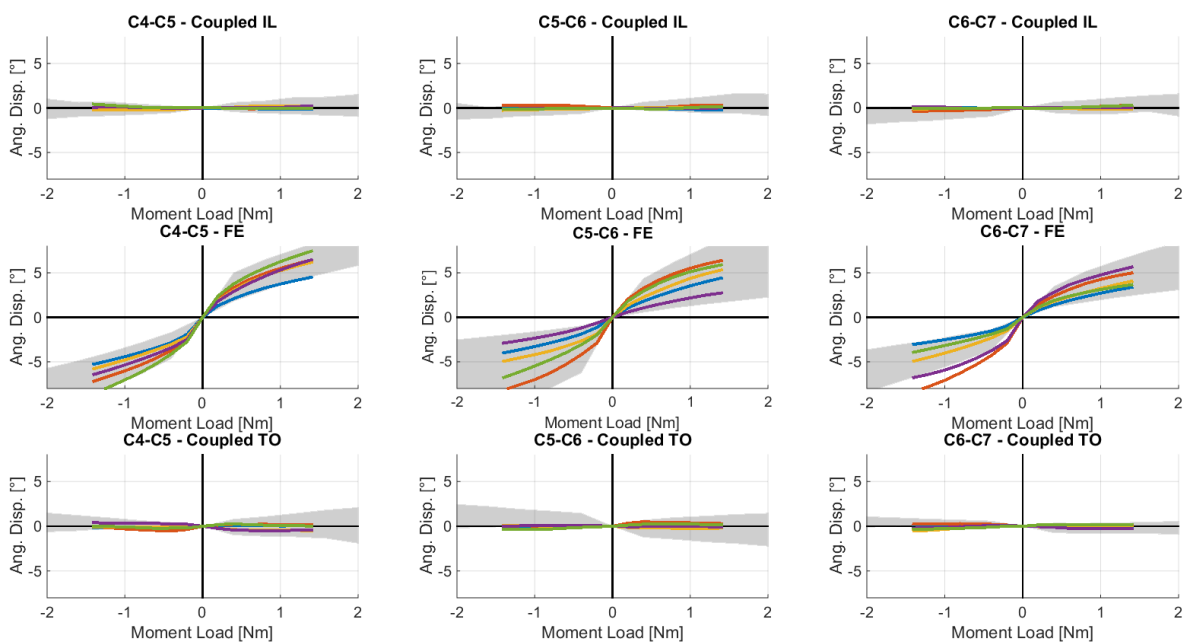


(b) The CT-based FE meshes

Figure 4.9: The point-to-surface distance between the EOS- (a) and CT-based (b) mesh and the corresponding CT-based reconstruction

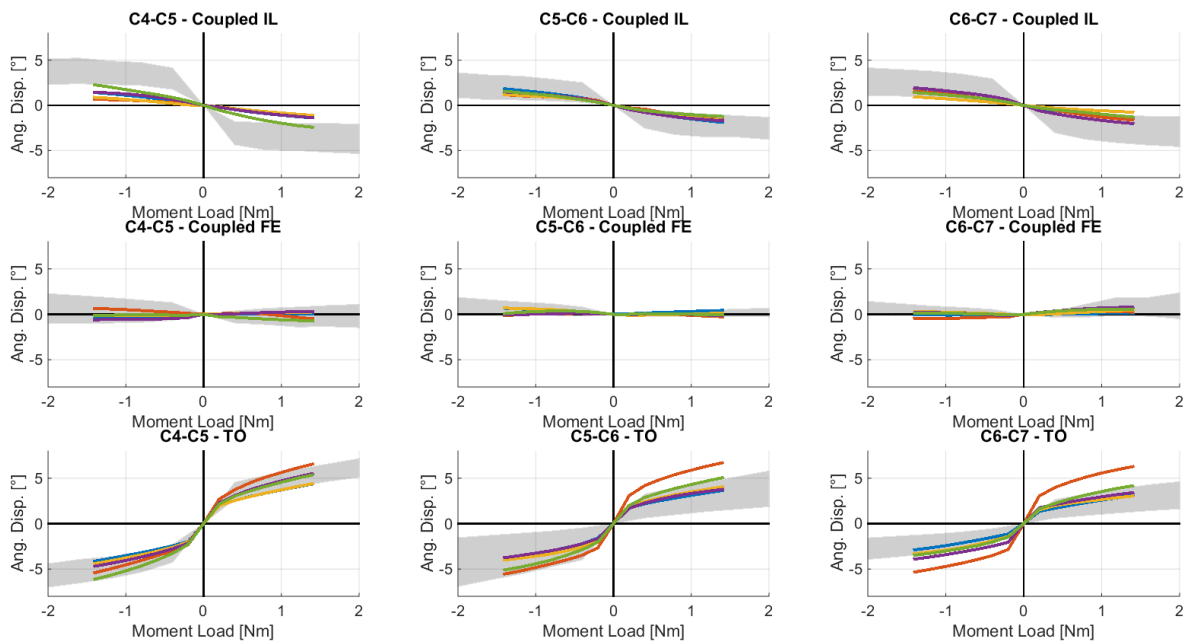


(a) EOS-based meshes

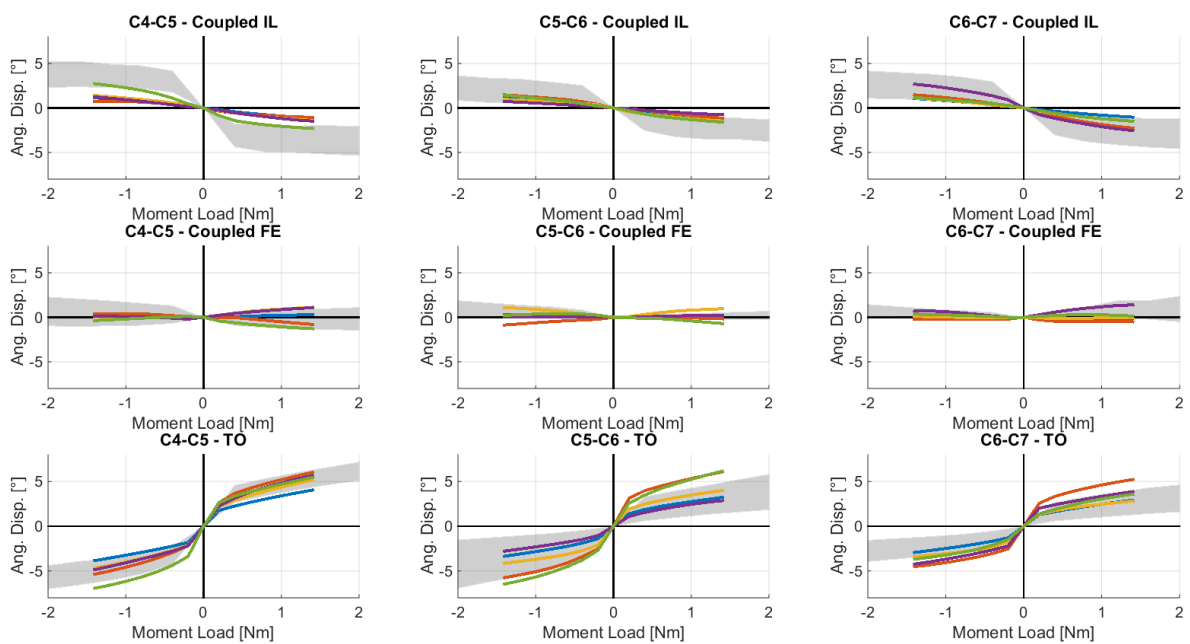


(b) CT-based meshes

Figure 4.10: The numerical moment load vs. angular displacement behaviour, as observed with the EOS- and CT-based FE models, in comparison with the experimental corridor for flexion/extension.



(a) EOS-based meshes



(b) CT-based meshes

Figure 4.11: The numerical moment load vs. angular displacement behaviour, as observed with the EOS- and CT-based FE models, in comparison with the experimental corridor for axial rotation.

The same comments could be made for lateral bending and axial torsion. The overall RMSE between the numerical and experimental curves was on average 0.9° (std. 0.5°) for the principal motions predicted by the CT-based meshes, while an average RMSE of 1.0° (std. 0.6°) was found for the EOS-based meshes. The highest differences were noted for flexion/extension. The RMSE for the coupled motions were slightly higher.

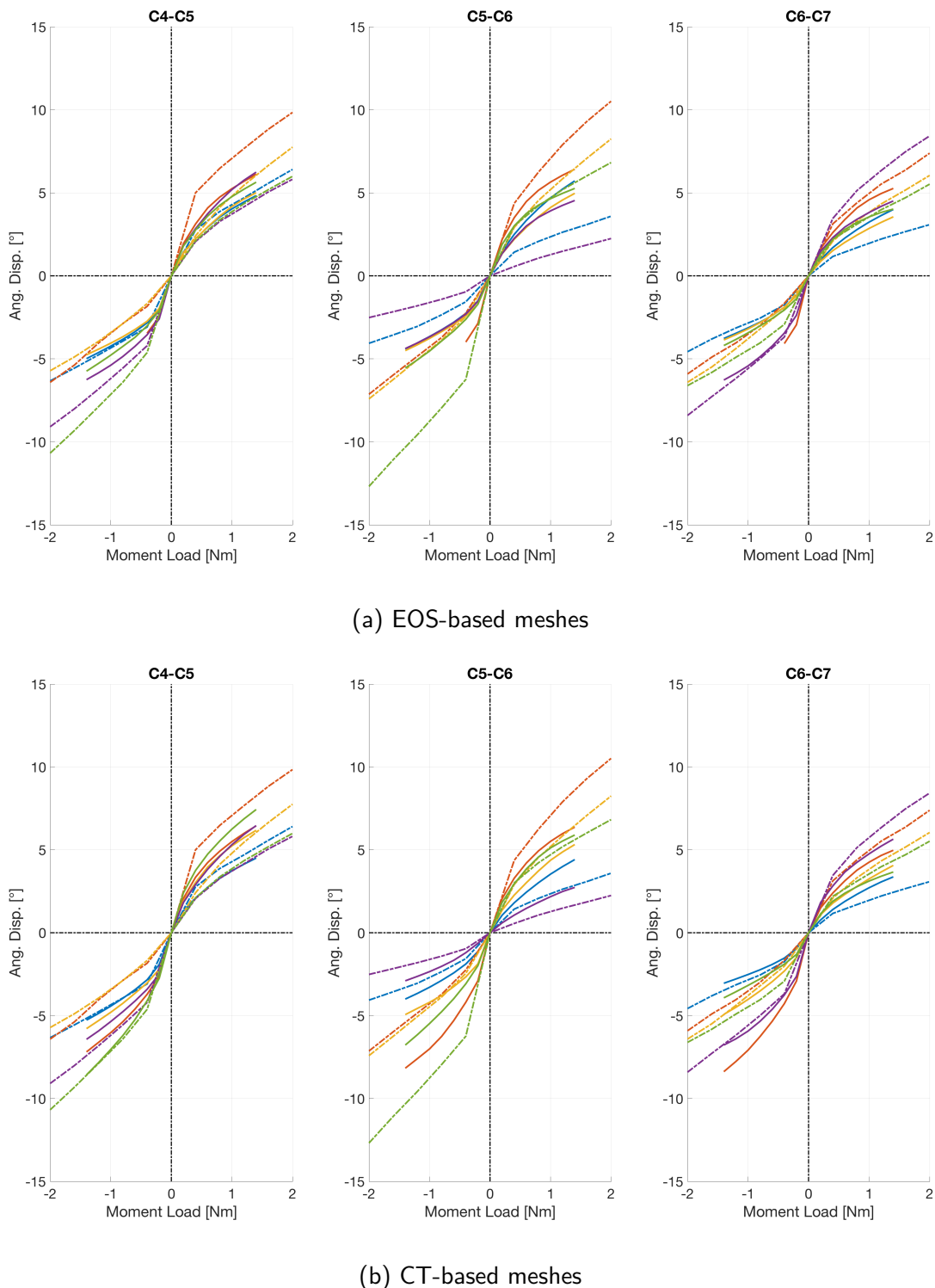
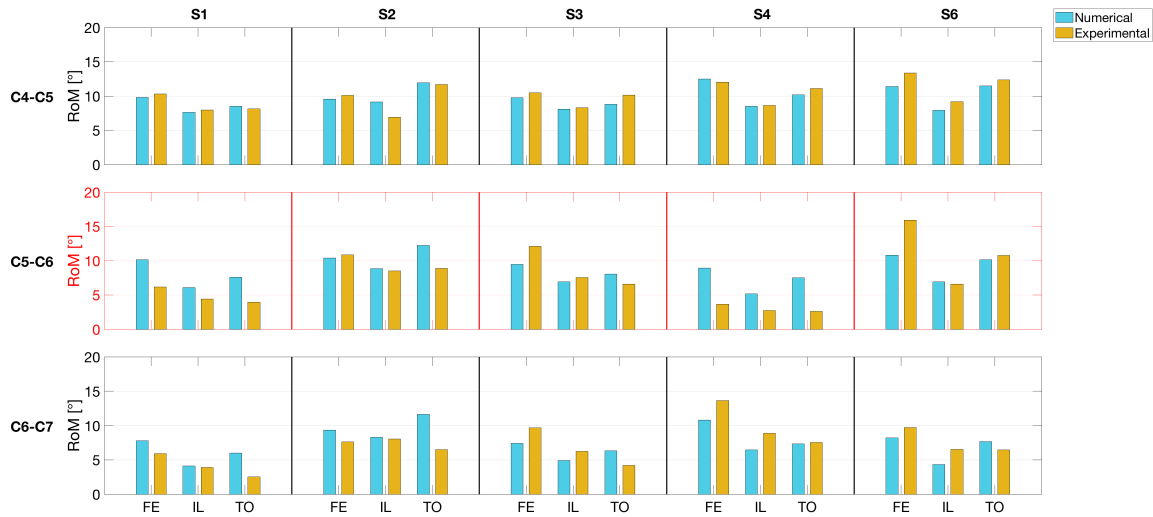
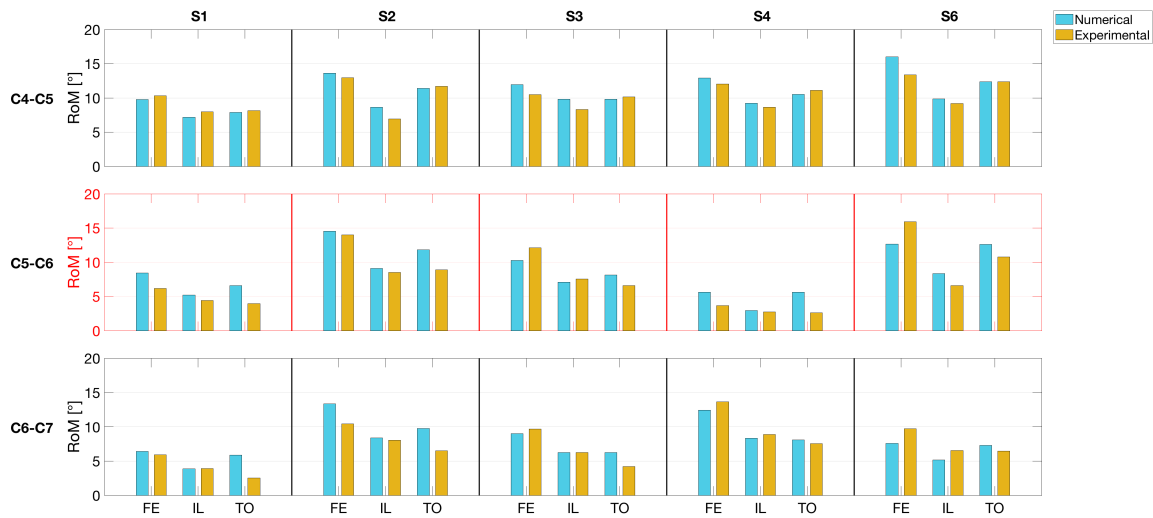


Figure 4.12: The experimental (dotted line) moment load vs. angular displacement behaviour in comparison with the corresponding numerical (full line) curves, obtained with both the EOS- (a) and CT-based (b) meshes, for flexion/extension.

Figure 4.13 compares the range of motion (RoM) calculated from the experimental curves with the one predicted by the EOS- and CT-based meshes, respectively. Although the numerical load-displacement curves differ markedly from the corresponding experimental curves, the RoM predictions seem consistent: the samples were properly ranked with an average difference of 1.3° (std. 1.0°) for the CT-based meshes and 1.7° (std. 1.5°) for the EOS-based meshes. The CT-based meshes, and to a lesser extent the EOS-based meshes, thus correctly reproduce both the inter- and intra-subject variability.



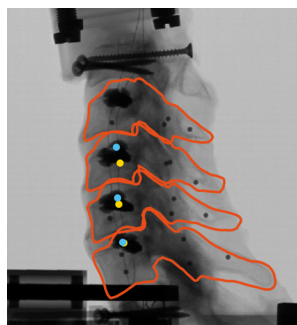
(a) EOS-based meshes



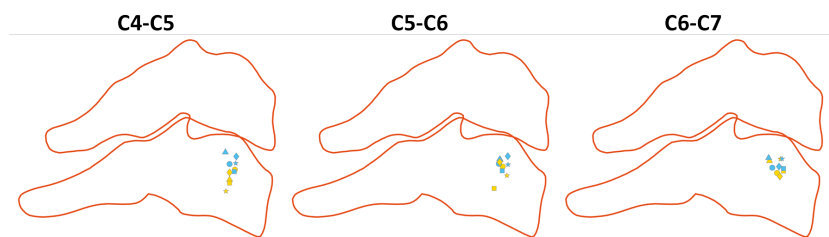
(b) CT-based meshes

Figure 4.13: The experimental vs. numerical range of motion, as predicted by both the EOS- (a) and CT-based (b) meshes, in flexion/extension (FE), lateral bending (IL) and axial torsion (TO).

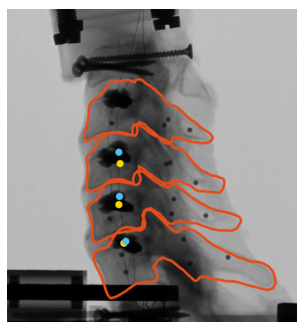
A schematic representation of the location of the MCR describing the flexion/extension movement, as predicted by the EOS- and CT-based FE models, compared to the experimental observations, is given in Figure 4.14. It can be observed that with the EOS-based FE models, the global experimental behaviour is well predicted, as the experimental corridor is respected. Yet, a slightly smaller part of the variability could be captured, compared to the CT-based FE models.



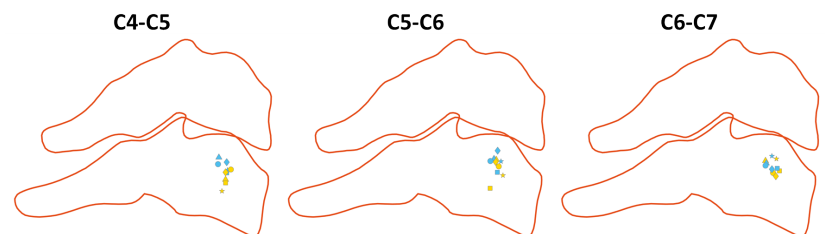
(a) EOS-based numerical (blue) vs. experimental (orange) MCR location for sample S1.



(b) A schematic representation of the MCR location as derived from the experimental data (orange) compared to the predictions made with the EOS-based FE models (blue).



(c) CT-based numerical (blue) vs. experimental (orange) MCR location for sample S1.



(d) A schematic representation of the MCR location as derived from the experimental data (orange) compared to the predictions made with the CT-based FE model (blue).

Figure 4.14: The location of the mean centre of rotation (MCR), determined from the experimental load-displacement data under flexion/extension compared to the one predicted by the EOS- (a & b) and CT-based (c & d) FE models.

4.2.4 Discussion

FE models are becoming widespread with applications in both the hospital environment and the biomedical industry. They are used to study spinal biomechanics and to evaluate implant designs. It is crucial for these models to be verified and validated, for their predictive power to be ensured. However, an extensive, yet non-exhaustive literature review has revealed that few FE models have been validated based on *in-vitro* data. Moreover, due to the high inter-subject variability and the complex morphology, few authors attempted the development of a subject-specific FE model.

This study proposes a methodology to generate a morphorealistic subject-specific FE model of the C4-C7 cervical spine segment. The *in-vitro* experimental moment load vs. angular displacement behaviour recorded for six human cadaveric samples was used to evaluate the model predictions in a direct validation step.

As shown in Figures 4.10 and 4.11, apart from the unique sample, both the EOS- and CT-based models respected the experimental corridors in all configurations. It should however be noted that with the CT-based meshes a higher consistency with the experimental recordings was achieved, with a lower RMSE. This can be explained by the less accurate EOS-based reconstruction of the spine. Although the vertebral body is clearly discernible on the biplanar X-ray images, the articular and *unciform* processes are less visible. Therefore, their reconstruction is mostly based on statistical inferences and less on information extracted directly from the images. As the orientation of the facet joint surfaces is a determinative factor for spinal kinematics, the EOS-based meshes do not show the same behaviour as the corresponding CT-based meshes. Furthermore, due to this reconstruction bias, the EOS-based meshes capture a less important part of the experimental corridor. This illustrates that the *vertebra* and associated IVD geometry are key elements determining the load-displacement behaviour, thus confirming the findings of Laville *et al.* [2009].

From the results presented in 4.13, it can be concluded that the model is able to differentiate between the samples with varying geometry. Indeed, a larger RoM value was predicted for the sample with a higher experimental mobility. However, with the CT-based meshes slightly lower differences with the experimental RoM were noted, indicating a higher predictive power.

This study has certain limitations. Firstly, the experimental data of one of the six subjects was excluded. Therefore, a one-to-one comparison was possible for only five subjects. To statistically confirm the above mentioned conclusions, a larger sample size is required. At this stage, one can merely highlight tendencies.

The mesh deformation procedure did not yield an exact match between the FE mesh and the corresponding EOS- or CT-based 3D reconstruction data. A compromise between morphorealism and mesh quality had to be found. Adjusting the meshing technique to allow closer correspondence, might improve the model predictions.

The material properties were held constant in each model. This might explain that neither with the EOS-based, nor with the CT-based meshes, an exact *one-to-one* correspondence with the experimental curves could be achieved. It is possible to estimate the Young's modulus and Poisson's ratio of spongy and cortical bone from calibrated CT images (Keyak *et al.* [1994]; Rho *et al.* [1995]; Kopperdahl *et al.* [2002]). However, the result is highly dependent from the Young's modulus vs. bone density relation, as calibration of the CT data merely gives exclusion about bone density. This discrepancy might lead to an important uncertainty on the model predictions (Helgason *et al.* [2016]). Other,

more reliable, techniques involve the destructive testing of bone samples (Hodgkinson and Currey [1992]; Keller [1994]) or destructive testing combined with inverse engineering using FE modeling (Liebschner *et al.* [2003]; El Masri *et al.* [2012]). These techniques destroy the samples and often only local mechanical properties are obtained. The mechanical properties of the soft tissue components are even more difficult to obtain. Destructive testing is the most efficient technique (Chazal *et al.* [1985]; Yoganandan *et al.* [2000]; Mattucci *et al.* [2012]; Mattucci and Cronin [2015]; Yang *et al.* [2016]). To estimate the IVD material properties, however, literature explored the possibility of using elastography based on MR or ultrasound (US) imaging (Vergari *et al.* [2014a]; Ben-Abraham *et al.* [2015]), but conclusive results are not yet available. Therefore, for the purpose of this study, mechanical properties had to be assigned based on information from the *in-vitro* and *in-silico* literature.

The facet joints were modeled as two layers of contacting cartilage, with in between frictionless surface-to-surface contact elements. In reality, however, the cartilage layers are not planar and separated by the synovial fluid contained within the capsule. This simplified representation might be one of the explanatory factors for the stiffer coupled motions predicted by the model.

Even though the experimental boundary and loading conditions were well controlled, it was proven difficult to reproduce them numerically. The most important difference was the location of the application point of the moment loading. Numerically this was defined by a node connected by undeformable beam elements to the superior plateau of the C4-vertebra. In the experimental set-up, the moment was applied to the casing surrounding the C3-vertebra, making it difficult to correctly reconstruct the C3-vertebra. With the hypothesis of a pure moment, both configurations can be considered equivalent. But, the six-degree force cell mounted underneath the most caudal vertebra *in-vitro*, revealed parasitic 3D forces. However, the norm of these forces did not go beyond 5 N. Nevertheless, this might be another element explaining the difference between the numerical and experimental behaviour.

To the author's knowledge, this is the first study proposing a method to generate, analyse and evaluate morphorealistic subject-specific cervical spine FE models and to assess the effect of geometric accuracy based on biplanar X-ray and CT data. Regardless of its limitations, the X-ray-based and CT-based models are capable of providing a reliable estimation of the RoM and an indication of the load-displacement behaviour. Although still preliminary, this model offers a promising basis for the patient-specific evaluation of spinal biomechanics and implant designs.

Chapter 5

Clinical Applications

The main objective of this PhD was the development of a subject-specific musculoskeletal model of the cervical spine for clinical analyses and implant evaluation. Chapter 3 has shown that with the proprioception-based muscle regulation model subject-specific and physiologically relevant muscle forces and intervertebral joint loads could be predicted, independently from EMG-recordings. In Chapter 4, a morphorealistic and subject-specific FE model of the intact cervical spine was proposed and the effect of geometric accuracy was assessed. An in-depth experimental validation was performed as well. However, two main issues remain to be solved.

The muscle regulation model requires both biplanar X-ray and MRI data. Contrary to a stereoradiographic scan, MRI acquisitions of the entire cervical spine are time-consuming and therefore not necessarily part of a routine clinical examination. It is however common to acquire one or two MRI slices and a set of biplanar X-ray images. The question remains whether or not it is possible to predict the internal loading based on biplanar X-ray data combined with one or two MRI slices. This is treated in the first section of this chapter.

Since FE modeling provides access to the internal forces and deformations under physiological circumstances, it became fully integrated into the implant design process. Yet, the literature contains few experimentally validated FE models of the instrumented cervical spine. In most cases, validation was performed merely for the intact configuration. Though, computational modeling of the instrumented configuration is not straightforward and necessitates additional validation. The second part of this chapter overviews the development and validation process of an FE model of the lower cervical spine in which a three-component mechanical total disc replacement was implanted.

Contents

5.1	Muscle Force Quantification based on a Reduced Set of Clinical Data	84
5.1.1	Introduction	84
5.1.2	Materials and Methods	84
5.1.3	Results	87
5.1.4	Discussion	89
5.2	Finite Element Modeling of the Cervical Spine Instrumented with a Total Disc Replacement	95
5.2.1	Introduction	95
5.2.2	Materials and Methods	96
5.2.3	Results	99
5.2.4	Discussion	103

5.1 Muscle Force Quantification based on a Reduced Set of Clinical Data

5.1.1 Introduction

Both the medical and scientific community acknowledge the importance of muscle force quantification *in-vivo*, given the essential role of the spinal muscles in maintaining stability and in locomotion. The literature proposes different techniques to do so. Widely described and evaluated are optimisation and EMG-assisted optimisation. However, these techniques often require data which is not accessible in a clinical setting, such as EMG and motion capture data.

On the other hand, the proprioception-based muscle regulation model (Pomero *et al.* [2004]; Van den Abbeele *et al.* [2018]), as shown before in Chapter 3, was found feasible for the subject-specific prediction of physiologically relevant muscle forces and intervertebral joint loads, entirely based on medical imaging data. The model input data, i.e. the muscular geometry and external loading, are calculated from a 3D musculoskeletal model, derived from the fused biplanar X-ray and MRI data. Generating a free-body diagram from the 3D reconstruction of the spine and the external envelope, obtained from the stereoradiographic images, is rather straightforward. However, the computation of the muscular geometry is a complex task and necessitates high resolution MRI scans. An MRI acquisition of the neck region is costly and time-consuming. Indeed, the patient should remain immobile during approximately 45 min, which might be particularly challenging for patients diagnosed with spinal pathology. Not only the acquisition is time-consuming: post-processing MRI data of the neck region takes about 1.5h by an experienced operator. MRI-dependency is the main limitation of this approach for a direct integration into the hospital environment. Building 3D musculoskeletal models from a reduced dataset thus seems necessary.

To the author's knowledge, only one study, performed at our research institute, attempted to tackle the issue. To speed up 3D muscle reconstruction, Dubois [2015] developed a generic lower limb model. Based on the fusion of biplanar X-ray and MRI data, a musculoskeletal model was created for four asymptomatic subjects, using a previously described elastic registration procedure (Hausselle *et al.* [2012]). The best fitting model was then deformed onto the biplanar X-ray data of the subject of interest. The first estimation of the muscle 3D geometry obtained as such, was adjusted for it to match the corresponding contours acquired from ultrasound images.

A similar approach might be a conceivable solution for the cervical spine. Moreover, the acquisition of biplanar X-ray images and possibly one or two MRI slices, is common practice in the clinic. The aim of this study was to investigate the possibility to predict the spinal muscle forces and associated joint loads with the proprioception-based muscle regulation model, merely based on biplanar X-ray data, possibly complemented with the information acquired from one or two MRI slices. Hereby looking for the minimal required information to obtain relevant muscle force predictions, i.e. identifying the compromise between simplicity and relevance.

5.1.2 Materials and Methods

Six young asymptomatic subjects (28 ± 4 years, 69.7 ± 9.6 kg, 2 female/ 4 male) were included in this study, i.e. the same subjects that were used in the subject-specific analysis

performed with the proprioception-based muscle regulation model, described in Chapter 3.

Biplanar X-ray images were acquired in the upright configuration with an EOS system (EOS Imaging SA., Paris, France), from which the 3D reconstruction of the external envelope and the C2-T3 spinal segment could be obtained semi-automatically. MRI data of the head-neck region was obtained in the head first-supine position with a 1.5T Philips Achieva system (Philips Medical Systems, Koninklijke Philips N.V, Amsterdam, The Netherlands), enabling the 3D reconstruction of the principal spinal muscles and the external envelope.

To build a 3D musculoskeletal model in the upright configuration, the EOS- and MRI-based reconstruction data were fused. The procedure was described in Chapter 3 and briefly reminded hereafter. Landmarks identifying the *vertebrae* on both the EOS and MRI scans, were indicated. Extra control points distinguishing the external envelope were defined by calculating the intersection with the axial plane through each *vertebra*. This was performed for both imaging modalities. With an elastic transformation, based on the Kriging interpolation algorithm (Trochu [1993]), both sets of control points could be matched. Applying the same transformation on the 3D muscle reconstructions yielded the musculoskeletal model in the upright configuration. In the following, this model is referenced as the *Full DataSet* (FDS) musculoskeletal model.

General Approach for the Generation of Subject-specific Musculoskeletal Models from a Reduced Dataset

The general approach consisted of the elastic deformation of a predefined *Full DataSet* (FDS) musculoskeletal model onto the 3D reconstruction of the spine and the external envelope, obtained from the stereoradiographic data of the subject under study. This elastic transformation, calculated using the Kriging interpolation algorithm, was determined from a set of control points indicated on both entities. In total 137 control points were indicated on the *vertebra* and 487 on the external envelope. Figure 5.1 provides a visual explanation of the workflow.

The resulting subject-specific musculoskeletal model, termed the *Reduced DataSet* (RDS) model in the following, was compared with the corresponding *Full DataSet* (FDS) model generated from the fused MRI and stereoradiographic data. Each model was used as an input for the proprioception-based muscle regulation model. The muscle force and joint load predictions were made for the C6-C7 intervertebral joint. The absolute differences in terms of muscle force and joint load predictions, as well as in terms of muscle volume and CSA were calculated.

Exploration of Various Templates for the RDS Model Generation

The above described procedure was carried out with various options, i.e. different template FDS musculoskeletal models were calculated. Table 5.1 provides a summary of the different templates that were used to predict the muscle forces and intervertebral joint loads for each of the six subjects.

Reduced DataSet (RDS) Musculoskeletal Models

As a first option, similarly to Dubois [2015], one of the six available FDS models was defined as the template model and deformed onto the spine and envelope reconstructions of the five remaining subjects. This analysis was repeated six times, with each of the six

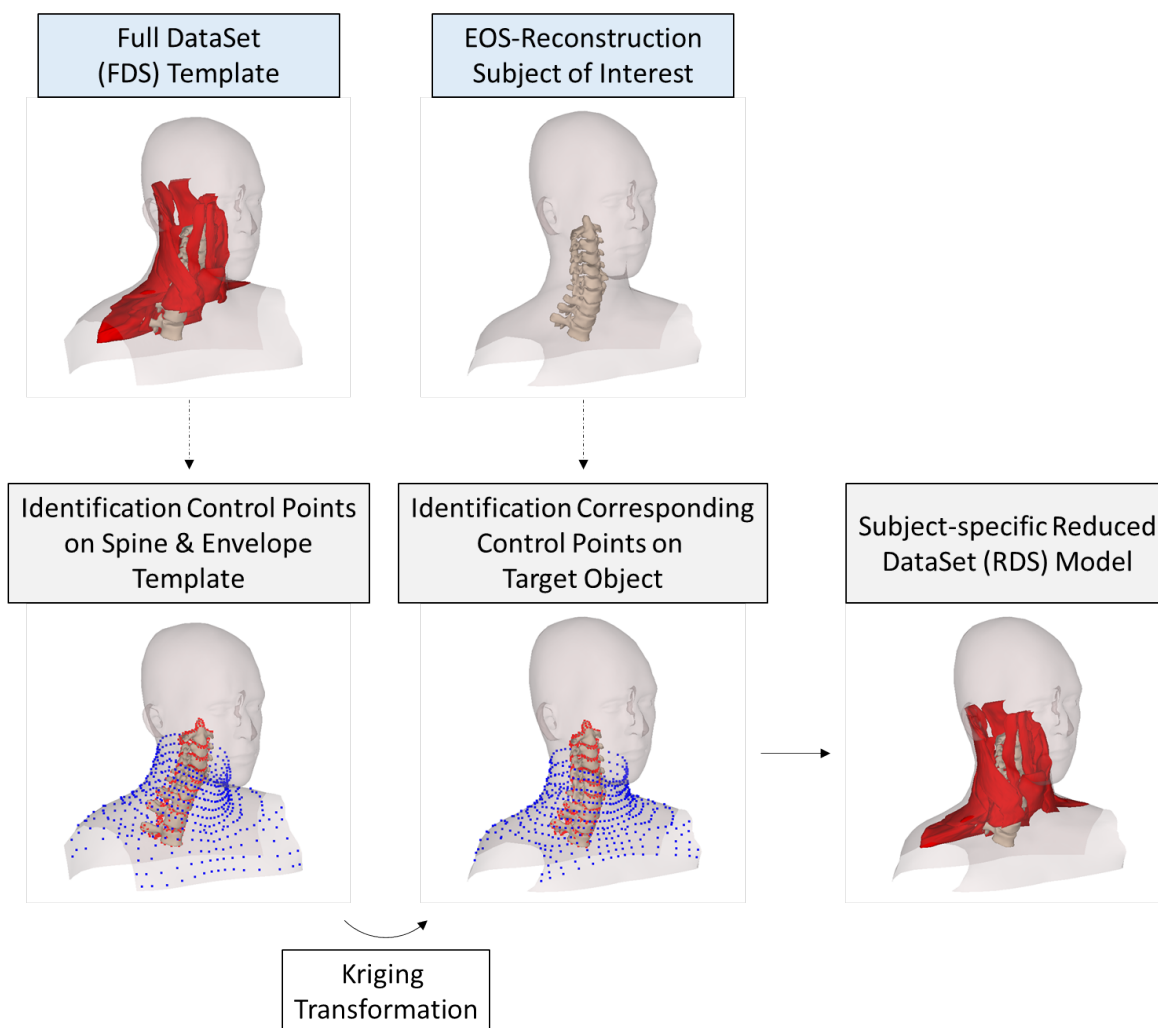


Figure 5.1: A template *Full Data Set* (FDS) musculoskeletal model was deformed onto the 3D reconstruction of the external envelope and the spine, based on a set of control points, common to both the starting and target objects, yielding a subject-specific *Reduced Data Set* (RDS) musculoskeletal model.

		Options for FDS Templates						Average Model
		S1	S2	S3	S4	S5	S6	
Subject-specific RDS Models to Evaluate	S1		•	•	•	•	•	Average of S2 to S6
	S2	•		•	•	•	•	Average of S1 and S3 to S6
	S3	•	•		•	•	•	Average of S1, S2 and S4 to S6
	S4	•	•	•		•	•	Average of S1 to S3, S5 and S6
	S5	•	•	•	•		•	Average of S1 to S4 and S6
	S6	•	•	•	•	•		Average of S1 to S5

Table 5.1: Summary of the different template musculoskeletal models used to build the subject-specific *Reduced Data Set* (RDS) models for each individual subject.

FDS models used as the template.

An alternative option involved the computation of an average musculoskeletal model from a selection of five of the six FDS models. This average model was then used as the template model to build the subject-specific RDS model for the remaining subject.

Note that mesh averaging is only possible when each input mesh has the same topology, i.e. the same number of nodes and elements and with each node having the same anatomical position. The mesh topology of the external envelope, respectively the spine, is the same for each subject, as this is inherent to the procedure followed to obtain these reconstructions from the biplanar X-rays. This was however not the case for the muscles. To deal with this issue, each individual object of one among the six FDS models, i.e. muscles, external envelope and *vertebra*, was morphed onto the corresponding object of the remaining FDS models. As such, each object in each of the six FDS models would receive the same mesh topology, while still representing the initial geometry. The six FDS models obtained as such could then be averaged. After a remeshing step, improving the mesh quality, a second morphing step was performed, this time with the averaged model.

The resulting models were used as the basis for a *leave-one-out* analysis in which six different average models and thus six different templates were calculated. In each iteration, a different FDS model was left out from the process. This template model was then deformed onto the stereographic data, i.e. the 3D reconstruction of the spine and the external envelope, of the remaining subject.

Partially Reduced DataSet (PRDS) Musculoskeletal Models

An attempt was made to improve the predictions obtained with the subject-specific RDS models generated from the average template, by including the information from one, respectively, two MRI slices. Muscle contours were manually indicated on the MRI slices and used to adjust the subject-specific RDS models, yielding the so-called *Partially Reduced DataSet* (PRDS) models. The model was termed PRDS-1 when one MRI slice was used and PRDS-2 when two were included.

The adjustments were made as follows. The muscle geometry of the subject-specific RDS model was first elastically transferred from the EOS to the MRI reference frame, based on a set of landmarks identifying the *vertebrae* and the external envelope on both the EOS and MRI data ¹. The intersection between the subject-specific RDS model, now expressed in the MRI reference frame, and the selected MRI slice(s) was calculated, thus yielding a set of estimated muscle contours. The transformation matrix elastically matching the estimated and manually indicated muscle contours was calculated and applied to the complete RDS model. A visual representation of the process is given in Figure 5.2.

5.1.3 Results

The RDS models, obtained from the deformation of a particular template chosen from the available FDS models onto the EOS-data of the subject of interest, yielded highly variable results in terms of muscle force and intervertebral joint load predictions.

The most accurate muscle force predictions were obtained when the S3 FDS model was used as the template. The mean relative difference between the predictions obtained with the subject-specific RDS models based on the S3 template and the corresponding FDS

¹The transformation matrix expressing the deformed template MS model in the MRI reference frame, is the inverse of the transformation matrix fusing the MRI and EOS data, i.e the transformation matrix that was used to generate the so-called FDS models (*cf.* Chapter 3)

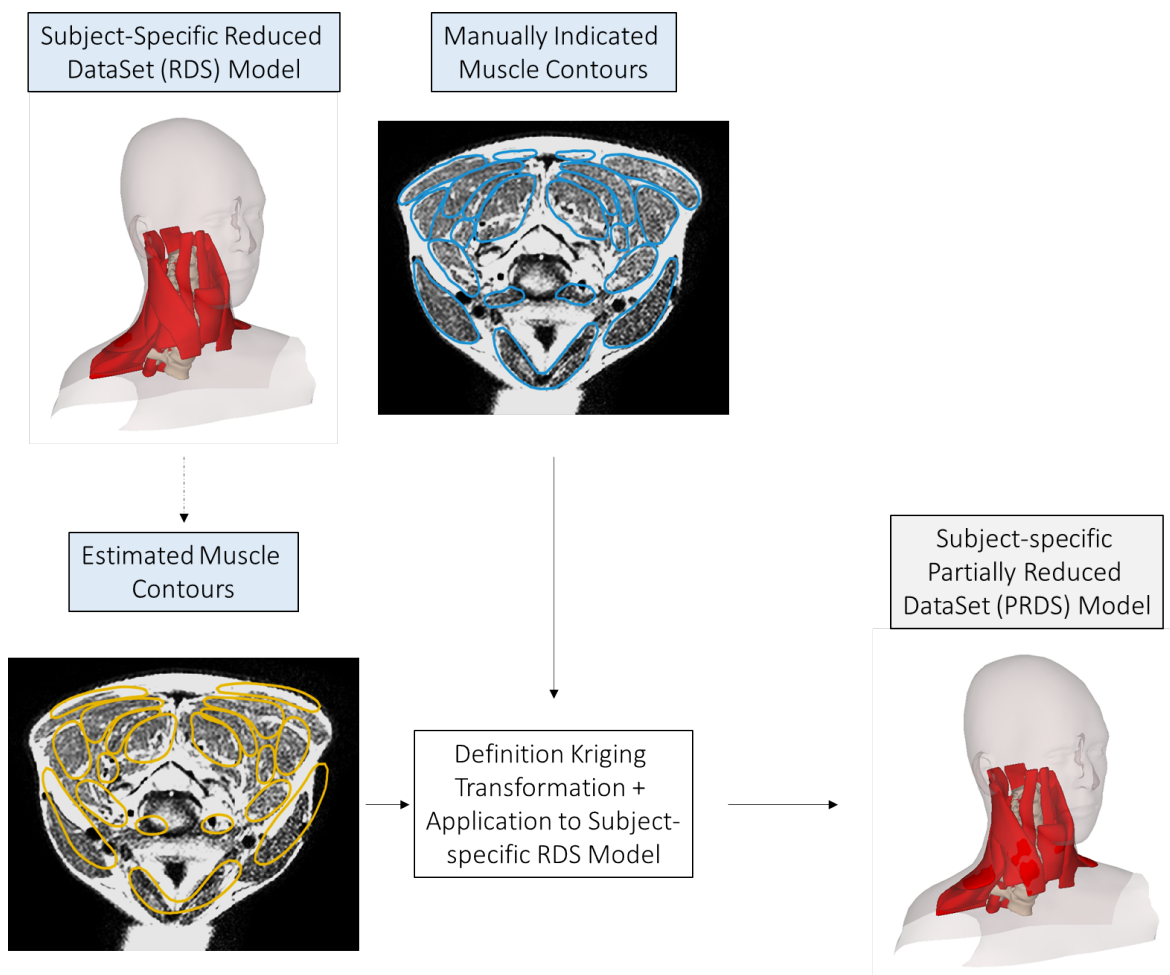


Figure 5.2: The subject-specific *Reduced DataSet* (RDS) model, built from an average musculoskeletal model, is adjusted to match the muscle contours manually indicated on one or two MRI slices, yielding the subject-specific *Partially Reduced DataSet* (PRDS-1 & PRDS-2) models. The figure presents the procedure for one MRI slice, but the same workflow is followed when considering two MRI slices. The only difference being the number of contours considered in the computation of the elastic transformation.

models was 200.8% [min.: 5.0%, max.: 972.3%]. The least accurate predictions were obtained with the S6 template. The mean relative error was 2227.4% [min.: 0.4%, max.: 35697.0%].

The most accurate joint force predictions were obtained with the S1 template, with a mean relative error of 43.6 % [min.: 0.3%, max.: 344.0%]. The largest deviation was noted with the S3 template, as the mean relative error was as high as 68.0% [min.: 2.0%, max.: 380.8%]. The joint moments were best predicted when the S4 template was used, reaching a relative error of 42% [min.: 0.1%, max.: 128.5%]. With the S2 template, the relative error was on average 171.3 % [min.: 17.5%, max.: 649.2%], the highest noted mean error.

It seemed that the closer the geometry of the template was to the target, the better the predictions were. Figure 5.3 illustrates this by presenting the joint load and muscle force predictions for subject S4, obtained with four different models, i.e. the FDS model and the subject-specific RDS models based on the S2 template, the S1 template and the average template. With the geometry of S2 completely different from S4, large prediction errors were observed. Yet, a smaller deviation was noted with the S1 model, which had a closer resemblance with the target.

Also note that when the average template was used to build the subject-specific RDS model for subject S4, the muscle force and joint load predictions were even more consistent than those obtained with the S1 template.

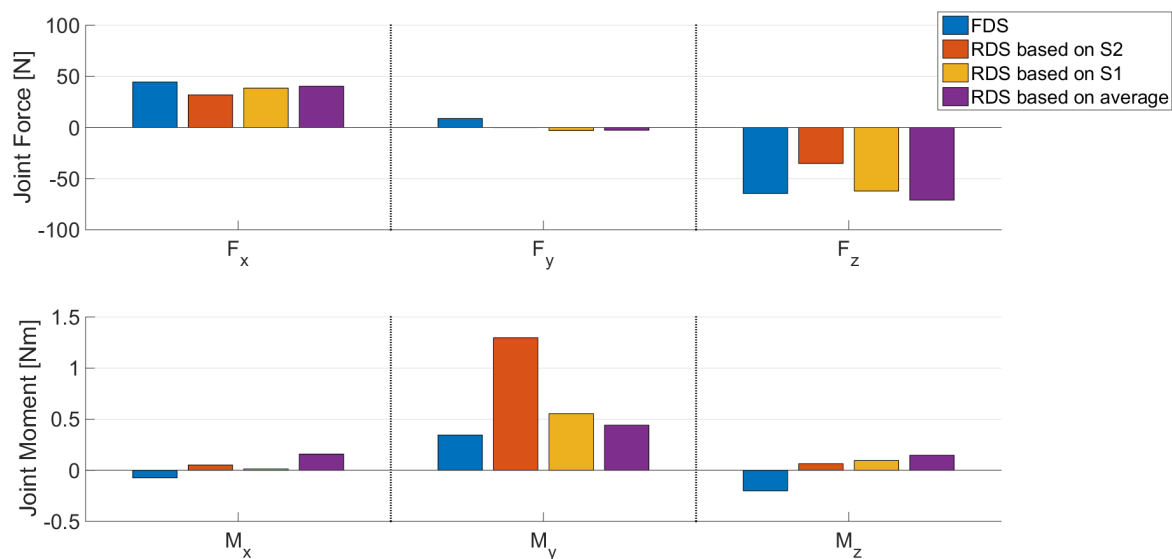
As observed in the *leave-one-out* analysis, the relative prediction errors with the average template were of the same order of magnitude as those obtained with the best-fitting template selected from the available FDS models: the mean error amounted to 1532.6% [0.5% to 53389.0%], 45.0% [0.3% to 292.6%] and 70.0% [1.2% to 305.9%] for the muscle forces, the joint forces and the joint moments, respectively.

As shown in Figure 5.4, the results could be improved slightly after adjustment based on the muscle contours manually indicated on one MRI slice. The mean relative error regarding the muscle force predictions decreased to 1087.4%. However, the mean relative error increased to 61.5% and 98.2% for the joint forces and moments, respectively. Using the information from two MRI slices did not significantly improve the results.

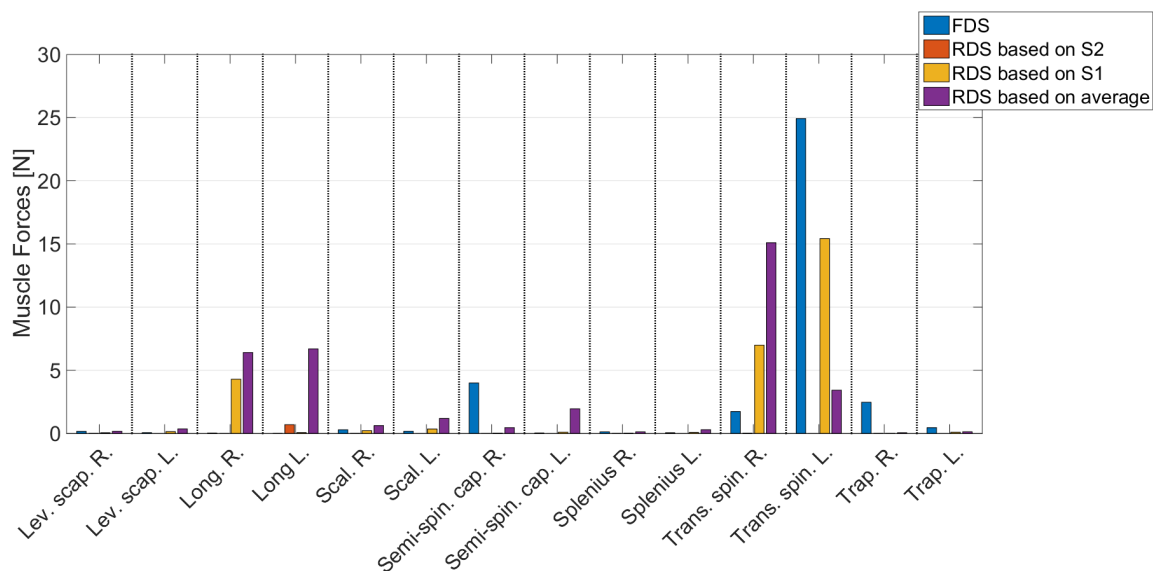
Similarly to Figure 5.3, Figure 5.5 compares the muscle force and joint load predictions for subject S4 obtained with the FDS model, the subject-specific RDS model based on the average template and the two subject-specific RDS models, also based on the average template, but adjusted using the information from one and two MRI slices, i.e. PRDS-1 and PRDS-2, respectively. With the integration of the muscle contours indicated on one MRI slice, the predicted muscle force pattern was closer to the one obtained with the FDS model. Furthermore, the muscle force directions were more consistent as well. However, the difference between the results obtained with the PRDS-1 and PRDS-2 was negligible.

5.1.4 Discussion

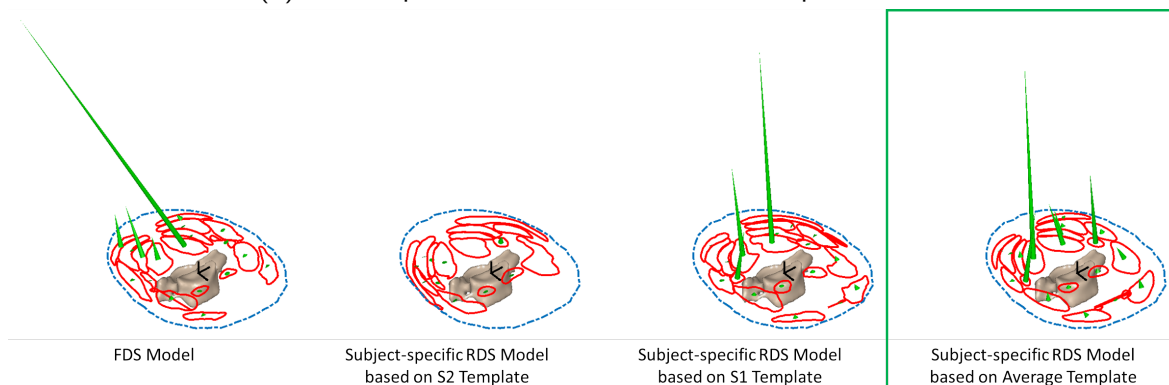
The scientific community seems to agree that, given the fundamental role of the spinal musculature in ambulation and stability, it is important to consider muscle forces when defining a strategy for spinal surgery. The literature proposes different techniques to predict the muscle forces in dynamic (ambulation) and quasi-static (maintaining posture) configurations. The most often described techniques are optimisation and EMG-assisted optimisation. However, because they require EMG data and/or motion capture data, it is



(a) Intervertebral joint load

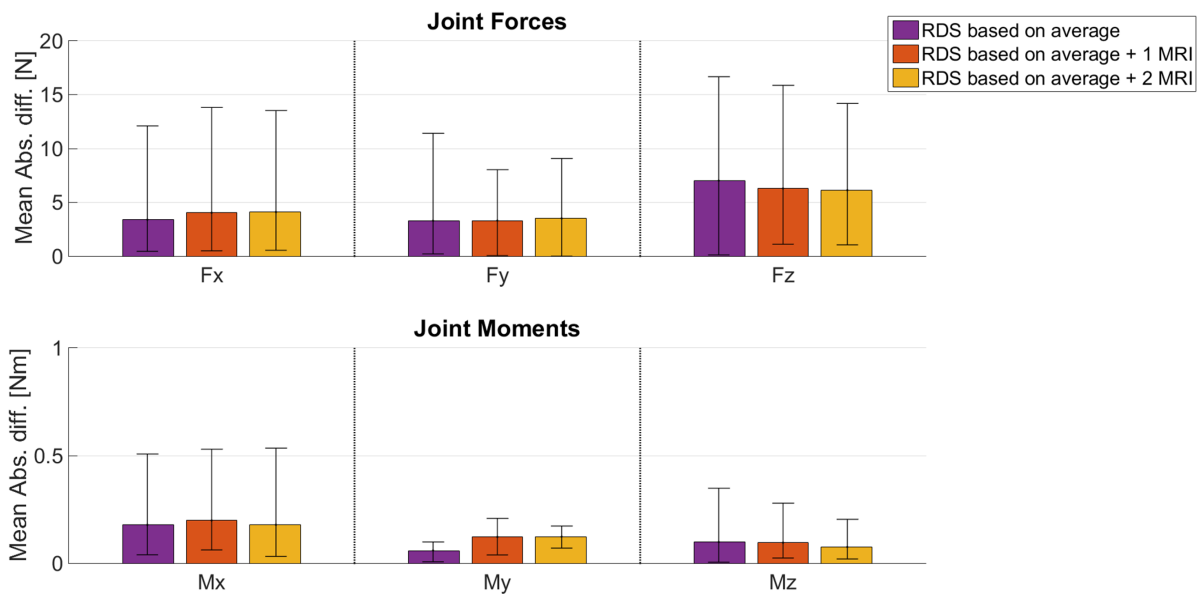


(b) A 3D representation of the muscle force predictions

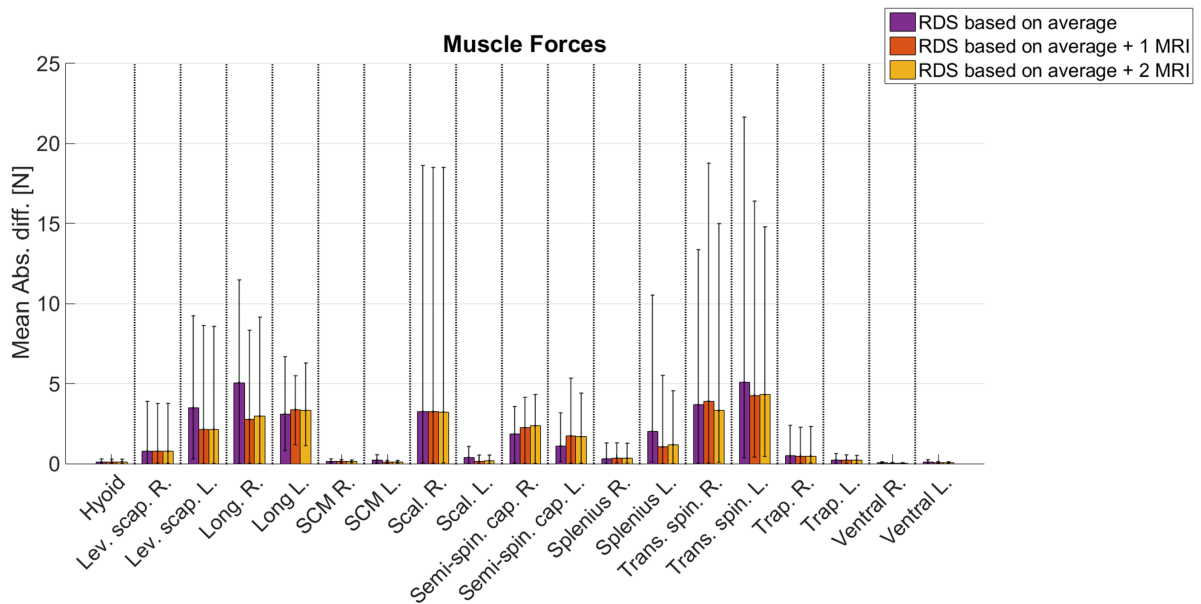


(c) A 3D representation of the muscle force predictions

Figure 5.3: Example of the joint load (a) and muscle force (b, c) predictions for subject S4, obtained with the *Full DataSet* (FDS) model and the subject-specific *Reduced DataSet* (RDS) models based on the S2 template, the S1 template and the average template

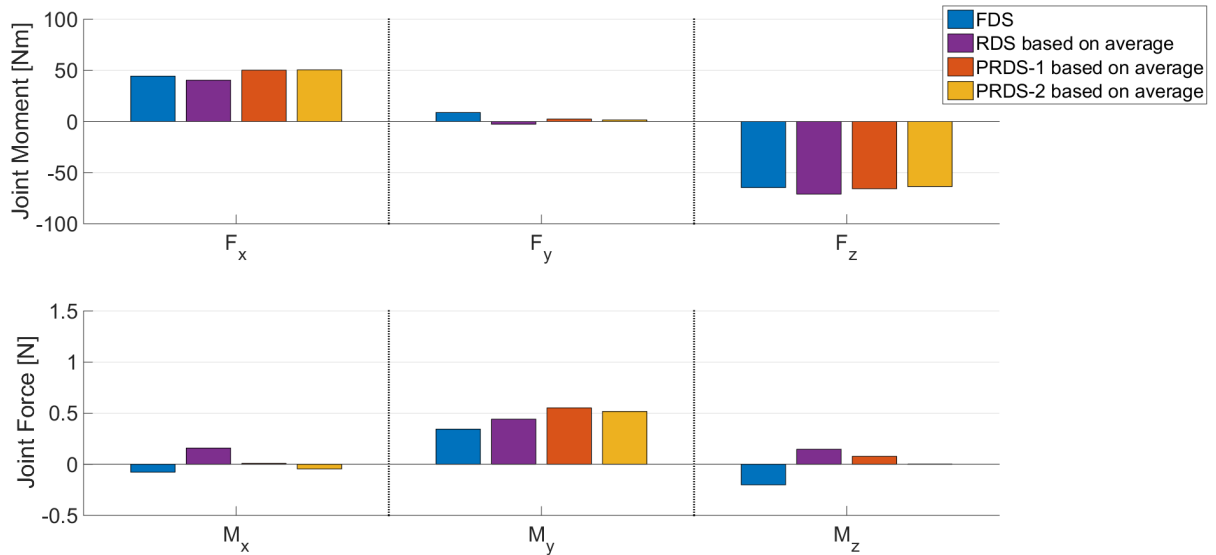


(a) Intervertebral joint load

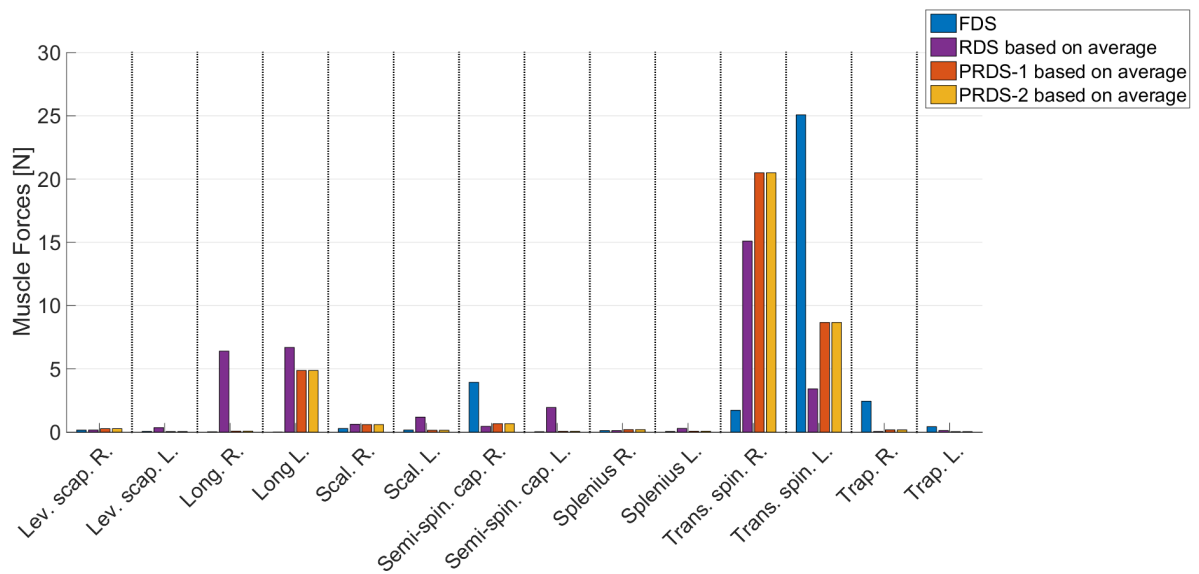


(b) Muscle forces

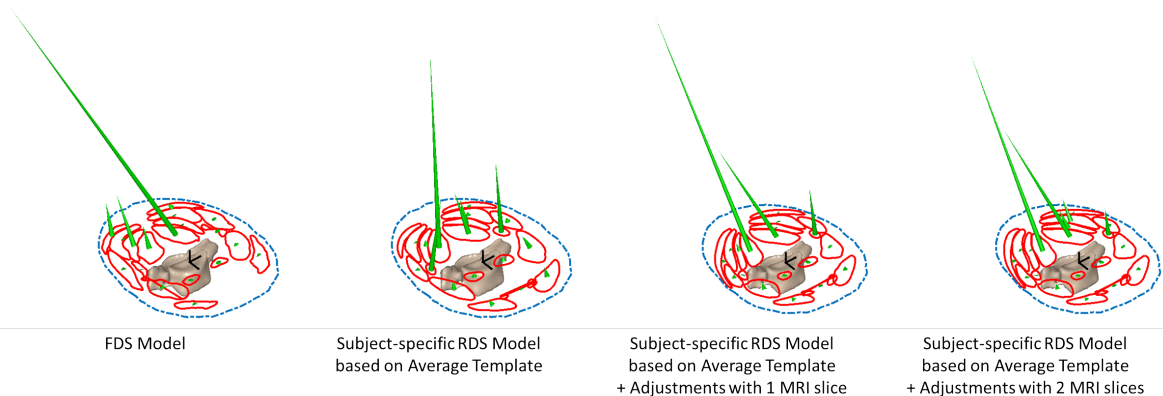
Figure 5.4: The mean absolute differences in terms of intervertebral joint loads (a) and muscle forces (b), between the predictions obtained with the RDS, PRDS-1 and PRDS-2 models and those obtained with the corresponding FDS models. The black lines indicate the range between the minimal and maximal difference.



(a) Invertebral joint load



(b) Muscle forces



(c) A 3D representation of the muscle force predictions

Figure 5.5: Example of the joint load (a) and muscle force (b, c) predictions for subject S4, obtained with *Full DataSet* (FDS) model, the subject-specific *Reduced DataSet* (RDS) model based on the average template, the subject-specific *Partially Reduced DataSet* model based on the average template and one MRI slice (PRDS-1) and the subject-specific *Partially Reduced DataSet* model based on the average template and two MRI slices (PRDS-2)

difficult to exploit these techniques in a clinical context. The proprioception-based technique predicts physiologically acceptable muscle force and joint load patterns, independently from EMG data and merely based on biplanar X-ray and MRI data (Pomero *et al.* [2004]; Van den Abbeele *et al.* [2018]). Although the model input data can be acquired in a clinical environment, MRI acquisitions are costly and time-consuming.

To avoid the acquisition of high resolution MRI scans for the estimation of the 3D muscle geometry, this study explored the feasibility of generating the subject-specific input from a reduced dataset, i.e. biplanar X-ray data, possibly complemented with one or two MRI slices. The basis was formed by six different musculoskeletal models, built from the elastic registration of the MRI-based muscle reconstructions onto the EOS-based spine and envelope reconstructions, acquired for six young volunteers. Each of these so-called *Full DataSet* (FDS) models was then deformed onto the EOS-based reconstruction of the spine and envelope of the other five subjects, as was described by Dubois [2015]. The resulting models, termed *Reduced DataSet* (RDS) models, were compared with the corresponding FDS models in terms of muscle geometry, muscle force and joint load predictions.

Instead of using one of the FDS models as the template, an average model was calculated from a selection of five FDS models and used to predict the muscle forces for the remaining subject, again by deforming this template onto the EOS data. This was repeated for each of the six subjects in a *leave-one-out* analysis.

As a third option, the analysis with the average template was repeated while considering the information acquired from one, respectively, two MRI slices. After elastic registration onto the EOS data of the subject of interest, the RDS model was adjusted for it to fit the muscle contours manually indicated on these MRI slices.

The prediction accuracy of the subject-specific RDS models based on a particular FDS model was found highly variable, as was illustrated in Figure 5.3. In terms of muscle force predictions, the relative errors could be as low as 0.4%, yet as high as 35697%. However, it seemed that the closer the geometry of the template was to the target, the more accurate the estimated muscle forces and intervertebral joint loads were. This result was expected, as the deformation of a model already close to the target is less far-reaching than when a completely different model would have been used. This also explains the comparable results obtained when instead the average musculoskeletal model was used as the template. Indeed, by definition, an average model is the best fit for all the models included in the database.

The intervertebral joint loads predicted with the subject-specific RDS models based on the average template were consistent with those obtained with the corresponding FDS models. The estimated muscle force patterns were also consistent, although the actual muscle force values could be significantly different. The prediction errors were of the same order of magnitude as those obtained when the best fitting FDS model was chosen as the template. Moreover, the performance of each of the six average templates, generated in the *leave-one-out* analysis, was comparable. I.e. the observed variability was lower than the variability noted for the six FDS models used as the template. The robustness of the proposed procedure seems confirmed.

Adjusting the subject-specific RDS models based on the average template, for them to fit the muscle contours manually indicated on one MRI slice, had a significant positive impact on the results. The muscle direction vectors were more accurately estimated, which lead to more accurate muscle force predictions. Adding information from a second MRI

slice did, however, not yield any significant improvements. This result may be somewhat counterintuitive, as it might be expected, with the two MRI slices far apart, that the muscle direction vector as well as the CSA would have been more accurate. However, the first MRI-slice was chosen close to the intervertebral joint under study. The second one thus had a smaller influence on the CSA estimation. The muscle direction vector was calculated as the first derivate of its centre line. Especially for irregularly shaped muscles, a third MRI-slice might be necessary to fully capture the changing direction of the muscle.

It has to be acknowledged that this study has certain limitations. First of all, the conclusions were based on the analysis of six asymptomatic subjects. This sample size might be too small to statistically consolidate the findings. Secondly, the average model was calculated by simply averaging five FDS models, too few to calculate statistically relevant shape variations. The results might significantly improve when the principal modes of variation, established as such, were to be considered in the model deformation process. Thirdly, muscle geometry, muscle forces and joint loads were the three parameters chosen to evaluate the performance of the subject-specific RDS models. Yet, each of these parameters has a certain level of uncertainty attached to it. Indeed, the elastic registration of the MRI onto the EOS data, yielding the FDS musculoskeletal models in the upright configuration, does not guarantee that the obtained 3D muscle geometry reflects the actual geometry in this configuration. An MRI scan acquired with the patient standing upright, might be conclusive. Secondly, although the muscle force predictions obtained with the proprioception-based muscle regulation model could be considered physiologically relevant after comparison with the literature, it was not possible to confirm the biofidelity. Only with invasive EMG-measurements and instrumented IVD implants, the force predictions can be validated. Given this uncertainty on the input and output data, the results of the current study should be treated with care.

Regardless of these limitations, this study proposes, for the first time, a fast and semi-automatic method to quantify muscle forces and associated intervertebral joint loads, merely based on biplanar X-ray data. It has been shown that by deforming an average musculoskeletal model onto the stereographic data, the intervertebral joint load predictions were in close agreement with those obtained with the corresponding FDS model, generated from the fused EOS and MRI data. Moreover, by adding the information from one MRI slice, not only the intervertebral joint load, but also the muscle force predictions were in close agreement with the estimations made with the FDS model. After fine-tuning the elastic MRI-to-EOS registration and a more complete evaluation of the muscle force predictions, the proprioception-based muscle regulation model, combined with these advancements, will be ready for use in a clinical context. For example, this approach opens the way for launching EOS-based FE simulations integrating subject-specific loading to analyse the *in-vivo* performance of spinal instrumentation, which might help preventing post-operative complications, such as PJK.

5.2 Finite Element Modeling of the Cervical Spine Instrumented with a Total Disc Replacement

5.2.1 Introduction

The most frequently applied surgical technique is anterior cervical *discectomy* and fusion (ACDF), in which the degenerated IVD is removed and replaced with bone grafts at one or multiple levels. A screw-plate system is used to stabilise the complex. Commonly reported complications are *pseudarthrosis* and adjacent segment disease (ASD). These often require revision surgery leading to the complete fixation of not only the affected spinal levels, but also the adjacent intact segments, essentially removing the patient's spinal mobility.

To prevent these complications, different techniques aiming to restore spinal mobility have been developed. A popular alternative is total disc replacement (TDR). Literature has indeed confirmed that the prevalence of ASD after TDR is significantly lower than after fusion surgery. Moreover, it has been shown that TDR might significantly reduce the risk for revision surgery (Blumenthal *et al.* [2013]; Delamarter and Zigler [2013]).

Before commercialisation, these mechanical implants undergo intensive *in-vitro* and *in-vivo* animal testing. To evaluate the implant design, to reduce the number of *in-vitro* experiments and to more efficiently plan *in-vivo* animal tests or even clinical trials, FE modeling became increasingly popular. Hence, this explains why the scientific community and regulatory agencies have published various recommendations aiming to standardise FE model development and validation.

As illustrated in the above (*cf.* Chapter 2), the literature records numerous cervical spine FE models. Although in most studies, the focus was on the intact configuration, some also evaluated the surgically restored and/or instrumented configuration. Generally, a CT-based FE model was used to analyse the effect of *facetectomy* or *laminectomy* on the spinal mobility and internal stresses (Voo *et al.* [1997]; Kumaresan *et al.* [1997]), to assess different *arthrodesis* (Hussain *et al.* [2013]; Duan *et al.* [2015]; Wu *et al.* [2017]) or TDR (Jung *et al.* [2013]; Lin *et al.* [2014]; Yu *et al.* [2016]; Chen *et al.* [2018]) techniques, to evaluate the effect of certain clinical parameters, such as *osteoporosis*, on the outcome of an *arthrodesis* (Natarajan *et al.* [2000]), to compare the performance of TDR with fusion (Faizan *et al.* [2012a]; Mo *et al.* [2014]) or to analyse the sensibility of certain implant-related geometric parameters (Rousseau *et al.* [2008a]; Faizan *et al.* [2012b]).

However, in few of these studies the FE model of the instrumented cervical spine was validated. Most authors only compared the behaviour of the FE model representing the intact configuration with the experimental or numerical literature. Usually the RoM or linearised stiffness was used to quantify the validation, only Ha [2006] also took into account the complete load-displacement curve. Two studies also attempted to evaluate the instrumented FE model. Hussain *et al.* [2009] did so by comparing the RoM with the *in-vitro* literature and Faizan *et al.* [2012a] performed dedicated *in-vitro* experiments with six cadaveric samples tested both in the intact and the instrumented configuration. However, the authors only recorded the RoM. Moreover, in none of the listed articles, a subject-specific analysis was performed. Although the generic FE model is useful for the evaluation of implant designs, a subject-specific model is necessary for a use in a clinical context.

This study proposes a subject-specific morphorealistic FE model of the cervical spine instrumented with a commercially available mechanical IVD replacement. Special attention was paid to the modeling of the instrumented configuration and to the *in-vitro* experimental

evaluation of the model behaviour. The validation was again performed in the form of a *one-to-one* comparison based on the actual moment load vs. angular displacement curves. As such, the first step towards the integration of FE models for surgery planning and implant design evaluation in a clinical and industrial environment, were made.

5.2.2 Materials and Methods

The study consisted of two parts: an *in-vitro* experimental analysis, performed earlier by Coloma *et al.* [2016] (unpublished data), and a numerical analysis. In the experimental study, the load-displacement behaviour of intact and instrumented cadaveric samples were recorded. The results obtained with the intact samples were also used for the validation of the generic and subject-specific FE models of the intact cervical spine (see Chapter 4).

From the medical imaging data and a CAD model of the implant, subject-specific FE models of the instrumented samples were generated. The numerical behaviour was then compared, in a *one-to-one* fashion, with the corresponding experimental curves.

Mechanical IVD Replacement

The IVD replacement modeled in this study, was a commercially available *ball-and-socket* implant (Lemaire and Lavaste [2008]). It consists of three moveable components: two cobalt-chromium (CoCr) parts, rigidly embedded into the adjacent vertebral endplates, and a mobile ultra high molecular weight polyethylene (UHMWPE) core. The upper metallic part has a convex surface articulating with the corresponding concave surface of the plastic core. The radii of curvature of both surfaces are equal. The inferior convex surface of the central core articulates with the corresponding concave surface of the lower metallic part. Both surfaces share the same radius of curvature, which is larger than the one characterising the superior articulating surface. With this architecture, the implant has six rotational and three translational degrees of freedom (DoF), as can be appreciated from the schematic representation shown in Figure 5.6.

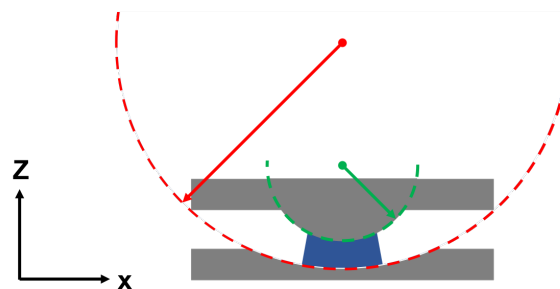


Figure 5.6: A schematic cross-sectional view of the IVD implant in the sagittal plane. Since the convex and concave surfaces of the central core have different radii of curvature, both rotation and translation are possible.

Based on the information derived from the patent (Lemaire and Lavaste [2008]) and the biplanar X-ray images acquired at the onset of the *in-vitro* experiments, a first 3D model could be designed in Fusion 360 (Autodesk Fusion 360, Autodesk Inc., San Rafael, CA, USA). This model was rigidly registered upon the biplanar X-ray data and, if necessary, adjustments were made until it matched the corresponding retro-projected contours of the X-rayed implant.

The final design was imported in the ANSYS Workbench (ANSYS 15.0, ANSYS Inc., Cannonsburg, PA, USA) to be meshed automatically with hexahedral elements. With an in-house developed Matlab-based script (Matlab2014b, The Mathworks Inc., Natick, MA, USA), the meshed model was assembled and prepared for implantation into the subject-specific FE model. The relative orientation and position of the implant parts was determined from the X-ray images. The workflow is depicted in figure 5.7.

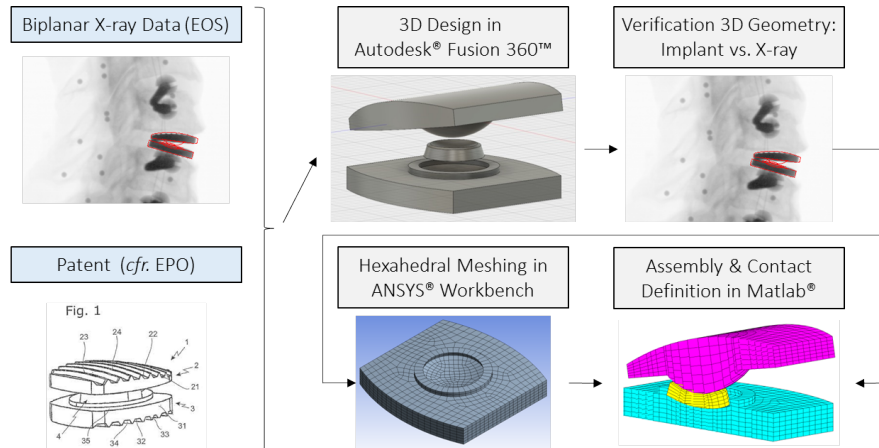


Figure 5.7: From the patent and the biplanar X-ray images, a 3D model of the implant was designed, assembled and meshed with hexahedral elements.

Frictional contact was assumed between the mobile core and the adjacent metallic parts. A CoCr vs. UHMPWE friction coefficient of 0.075 was chosen (Saikko [2006]; Crockett *et al.* [2009]; Kim *et al.* [2011]). Surface-to-surface contact elements were also defined on the inferior surface of the upper and the superior surface of the lower implant parts. Low stiffness cable elements connected the plastic core to the inferior metallic part, thus avoiding ejection during the simulations.

A Young's modulus and Poisson's coefficient of 300 GPa and 0.3, respectively, were chosen for CoCr, as defined in the literature (Baron *et al.* [2017]). For UHMWPE, values of 1.5 GPa and 0.3 were selected for respectively the elastic modulus and the Poisson's ratio (Lee *et al.* [2004]; Crockett *et al.* [2009]; Grygiel and Kaczmarek [2014]).

***In-vitro* Experimental Analysis**

The experimental analysis, performed by Coloma *et al.* [2016] (unpublished data), has been detailed before in Chapter 4. The main features are briefly reminded in the following, with a focus on the instrumented configuration.

Six human cadaveric C3-T1 samples (61 ± 4 years, 4 male/ 2 female) were included in this analysis. A pure 2 Nm moment was applied to the C3-vertebra in three different directions to simulate lateral bending, flexion/extension and axial torsion, while the T1-vertebra was blocked in all DoFs. At each load step, biplanar X-ray images were acquired. Tracking the five radio-opaque markers, embedded in each vertebra, on these images, enabled the computation of the angular displacement of each vertebra w.r.t. the subjacent one.

The protocol was repeated both for the intact and the instrumented segment. The IVD replacement was implanted at the C5-C6 vertebral level with an anterior approach. The anterior and posterior longitudinal ligaments were removed, as well as the IVD. Posterolaterally, part of the outer annulus and some ligamentous tissue might have been preserved.

The vertebral endplates were spread apart to accept the implant. The appropriate size was chosen based on the geometry of the unit to be instrumented. In this study, two different implant sizes were used, the smaller implant being a scaled version of the larger one (scaling factor = 0.85).

To prevent the central core from losing contact during the flexion/extension movement, a 50 N follower load was applied. Screws were inserted at both sides of the vertebral body, close to the theoretical centre of rotation. Two flexible and frictionless cables, attached to the casing of the motor exerting the pure moment, were passed through guide holes in the screws. A 25 N force was applied to each cable, simulating muscle co-contraction and the weight of the head. No follower load was used for lateral bending and axial torsion.

Based on the load vs. displacement data recorded for flexion/extension, the location of the mean centre of rotation (MCR) was calculated as well. First, the helical axis describing the motion from full extension to full flexion, was calculated. The intersection of this axis with the sagittal plane through the middle of the spinal segment, was defined as the MCR. This 3D point was then retro-projected onto the lateral X-ray view, as the flexion/extension motion is a more or less planar motion. To facilitate comparison with the numerical results, for each vertebral level, the MCR was expressed into a schematic representation of the FSU under study. This was based on the Kriging transformation matrix matching the retro-projected vertebral contours with those of the schematic representation.

Subject-specific FE Modeling

Using the same procedure as described in Section 4.2 of Chapter 4, a subject-specific morphorealistic FE model was generated from the combined biplanar X-ray and CT data. The following briefly reminds the procedure with a focus on the instrumented segment.

A 3D reconstruction of the C4-C7 segment was obtained semi-automatically from the biplanar X-ray data acquired for the intact sample at the onset of the experiments. The reconstructed *vertebrae* were rigidly registered manually upon the corresponding X-ray images acquired for the instrumented sample. A CT-based reconstruction was performed as well. To obtain an accurate representation of the vertebral geometry in the upright, i.e. *in-vitro*, configuration, the CT-based reconstructions were automatically registered upon the corresponding EOS-based reconstructions.

The simplified hexahedral FE model, generated from the parameterisation of the EOS reconstruction data, was densified and deformed iteratively towards the CT-based reconstruction yielding a subject-specific and morphorealistic FE model.

The C5-C6 IVD elements were removed, together with the anterior longitudinal ligaments. The posterior ligaments, part of the postero-lateral *annulus* and the cartilaginous endplates were retained. The correctly assembled implant mesh was inserted into the IVD space, guided by the information extracted from the EOS data. The rigid connection between the upper and lower part of the implant and the corresponding *vertebrae* was assured by ten rigid beam elements at each implant corner.

The follower load was modeled by temperature-activated cable elements interconnecting beam complexes, representing the screws, rigidly attached to the *vertebrae* at both sides. The location of the guiding holes through the screws were manually indicated on the X-

ray images, transferred to the FE model and used to define the attachment points of the cable elements. By tuning the CSA and the expansion coefficient of the cable elements, a follower load of 50 N could be generated at each load step. The complete mesh generation procedure is visualised in Figure 5.8.

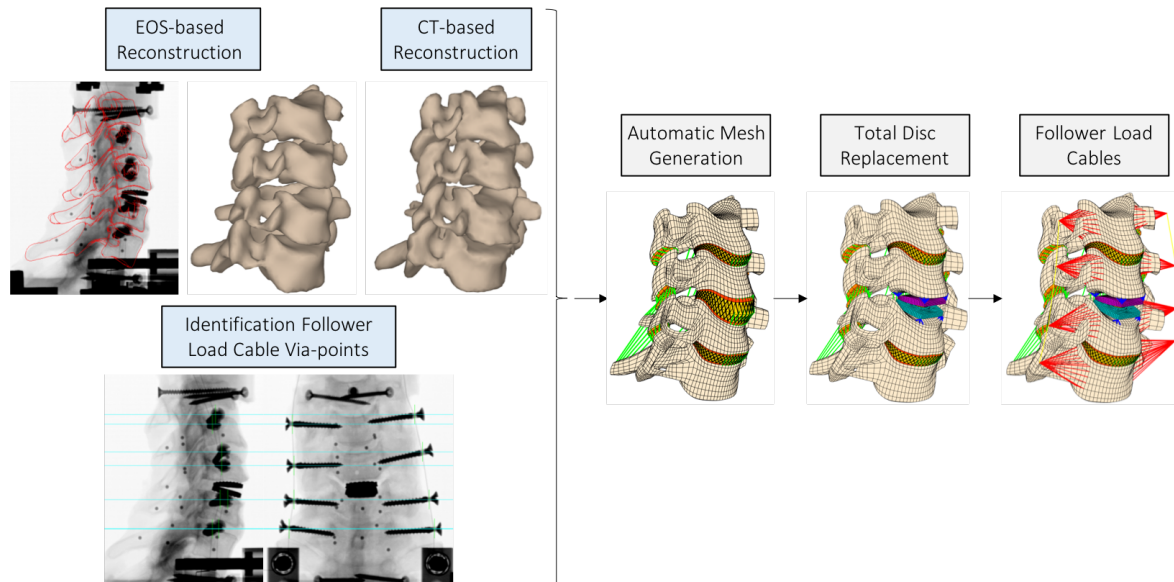


Figure 5.8: Parameterising the EOS-based reconstruction automatically results in a simplified FE mesh. After densification and iterative deformation, a morphorealistic hexahedral mesh is obtained. Based on the biplanar X-ray data, the implant could be virtually inserted.

The material properties of bone and soft tissue components were the same as those used in the intact FE model (see Table 4.1). However, to take into account the stretching of the posterior ligaments when inserting the implant, the slack length was adjusted or removed if deemed necessary. To do so, the ligament stretch was calculated by comparing its length in the intact with its length in the instrumented FE model. By evaluating its bi-linear stress-strain behaviour, the slack length could be adjusted.

To ensure numerical stability, displacement-controlled simulations were performed. A maximal angular displacement of 10° was applied to the C4 vertebra, in three different directions. Indeed, the experiments have shown that, under pure moment loading, the overall angular displacement of the sample was about 10° . The nodes on the external surface of the C7 vertebrae were fully blocked. The reaction moment at the level of the constrained nodes was evaluated at each load step, to reconstruct the moment load vs. angular displacement behaviour at each vertebral level.

As was done for the experimental data, the MCR was calculated from the intersection between the helical axis representing the flexion/extension motion and the sagittal plane. Once again, this 3D MCR was projected into a schematic representation of the vertebral level under study.

Due to meshing difficulties and because its load-displacement behaviour in the intact configuration was more flexible than for the other cadaveric samples, one sample was excluded from the analysis.

5.2.3 Results

In-vitro Experimental Analysis

Figures 5.9 and 5.10 present the load vs. displacement curves obtained with the intact and instrumented samples for flexion/extension and axial torsion, respectively. It became apparent that the vertebral levels adjacent to the instrumented one seem unaffected by the instrumentation. Generally, the implant was able to restore the mobility. However, the mobility of the intact sample could not always be reproduced. For samples S2, S3, S5 and S6, the introduction of the implant lead to a higher mobility in flexion, but a stiffer behaviour in extension, lateral bending and axial torsion, whereas for samples S1 and S4, the mobility increased in each loading configuration. The effect on flexion/extension was however more significant than for the two other configurations.

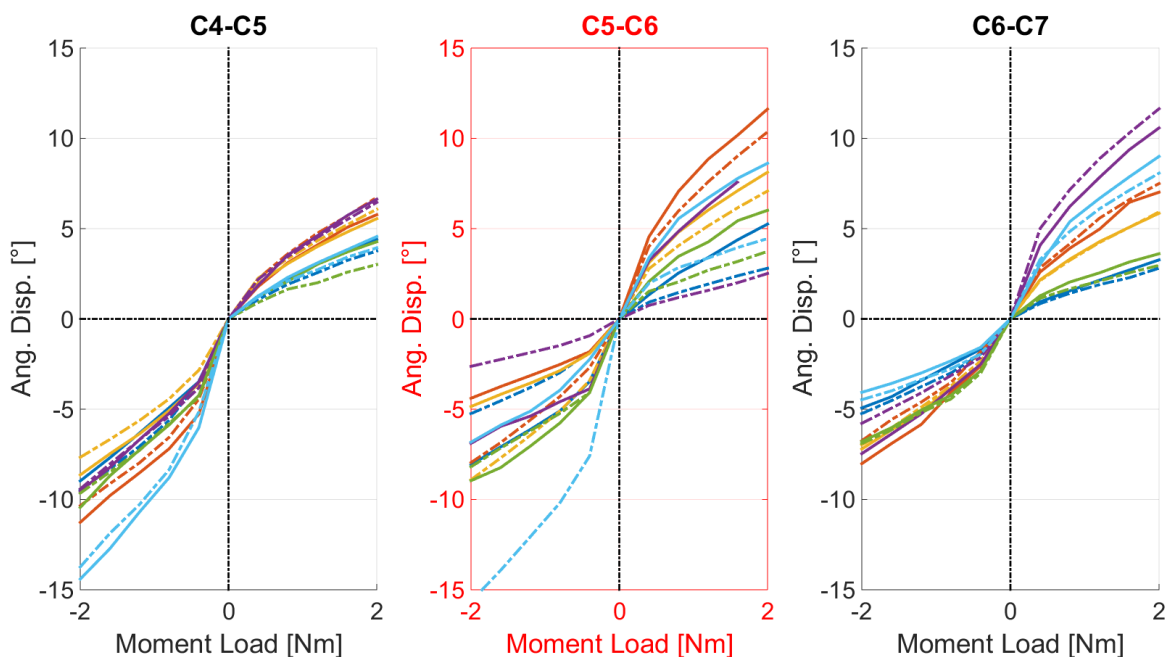


Figure 5.9: The experimental load vs. displacement curves for the intact (dotted lines) and instrumented (full lines) configuration under flexion/extension. The red box indicated the instrumented level.

Subject-specific FE Modeling

For each of the five samples, a high-quality FE mesh could be generated automatically for both the intact (see Figure 4.8) and the instrumented configuration (see Figure 5.11): none of the elements were beyond the element quality error limit and less than 0.2% were beyond the warning limit.

The retro-projected contours of the implant and spine FE models correspond well with the X-ray images, as shown in Figure 5.12. Also note that the inter-subject variability in terms of implant positioning and orientation had been taken into account as well.

Figure 5.13 presents the numerical load-displacement curves for the instrumented C5-C6 level in comparison with the corresponding experimental corridor for the principal motions in flexion/extension, lateral bending and axial rotation. It can be appreciated that, apart for axial rotation, the curves globally remained within the limits of the experimental corridor.

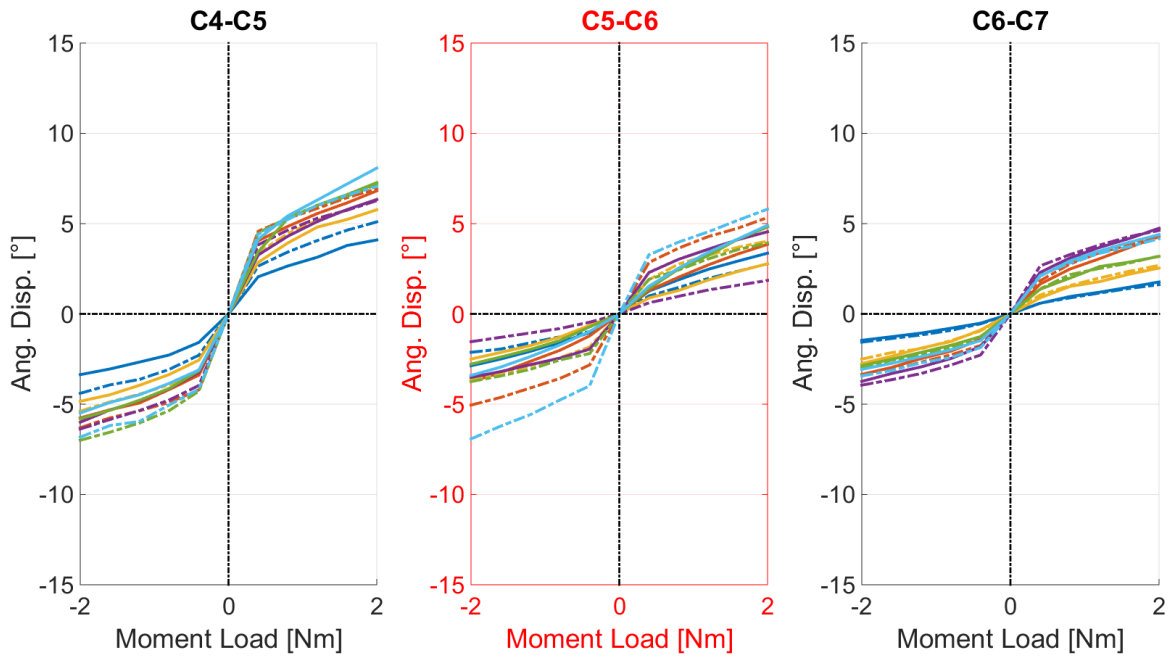


Figure 5.10: The experimental load vs. displacement curves for the intact (dotted lines) and instrumented (full lines) configuration under axial torsion. The red box indicates the instrumented level.

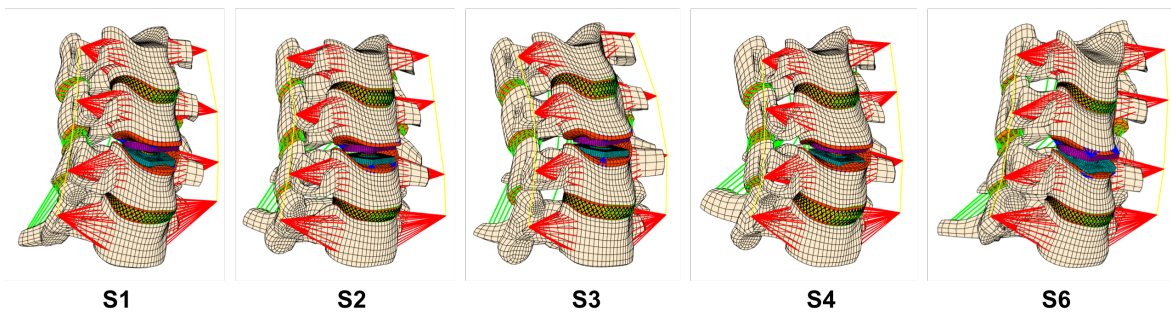


Figure 5.11: For each of the five samples, a regular FE mesh of the instrumented configuration was generated from the biplanar X-ray data and from the corresponding CT data.

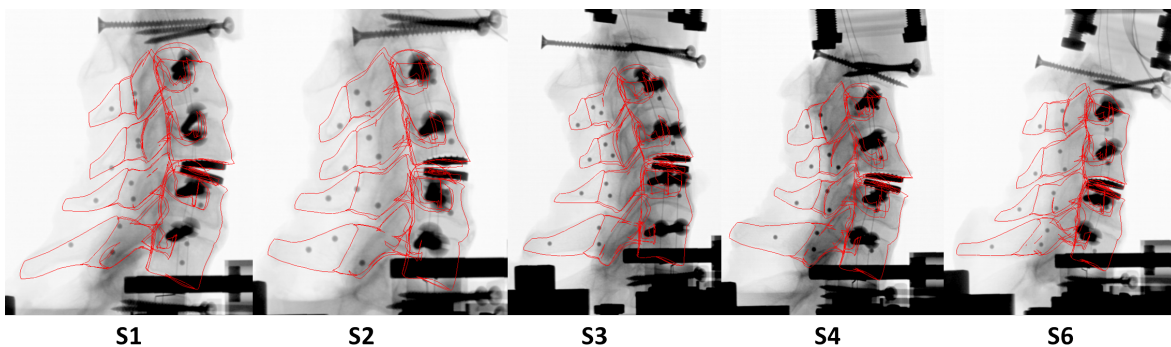


Figure 5.12: The retro-projected contours of the FE model generated for sample S1 are consistent with the EOS data.

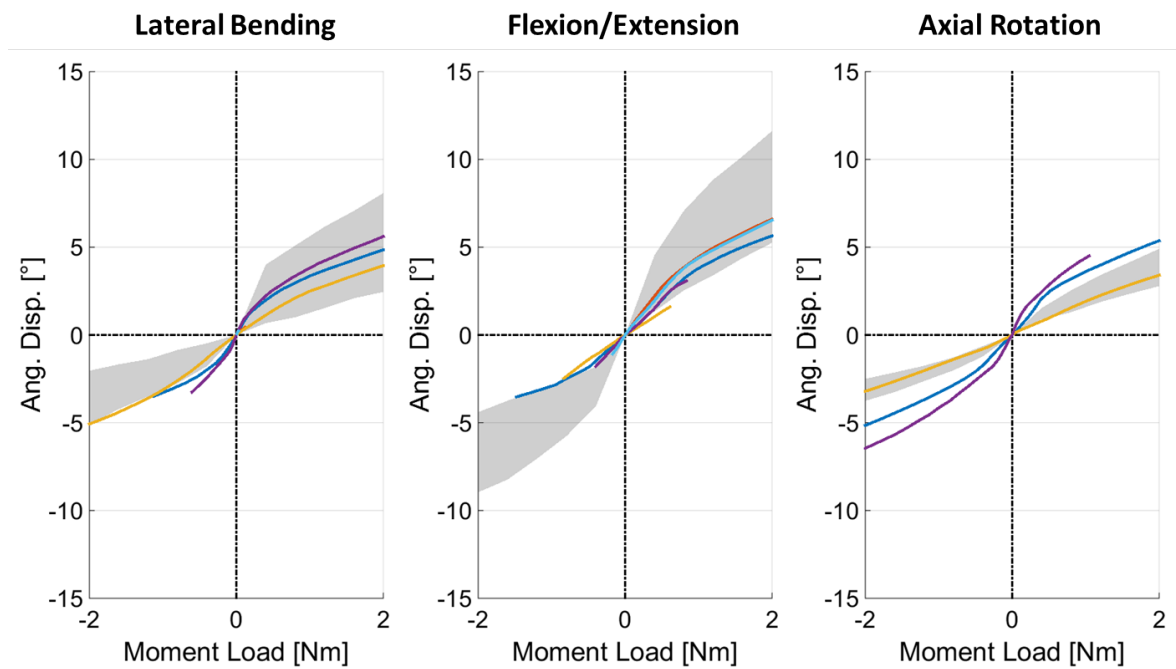


Figure 5.13: The numerical load-displacement curves vs. the experimental corridor for flexion/extension, lateral bending and axial rotation, as observed for the instrumented C5-C6 vertebral level.

Similarly, Figures 5.14 and 5.15 compare the numerical curves with the corresponding experimental corridors for both the principal and coupled motions in flexion/extension, respectively, axial torsion, for each of the evaluated vertebral levels. Overall, the numerical curves seem consistent with the experimental corridor for the principal motions. However, regarding the coupled motions, larger deviations are to be reported. The model predicted a stiffer behaviour for coupled lateral bending under axial torsion and for coupled axial torsion under lateral bending. These observations could be made for the instrumented and adjacent intact vertebral levels. However, for sample S4 (purple curve), the numerical load-displacement curves were less stiff both for the principal and coupled motions.

The FE model was able to capture a large part of the inter-subject variability at the intact levels, as could also be observed with the FE model of the intact configuration (see Chapter 4). Yet, as could also be noticed from Figure 5.13, at the instrumented level, the numerical curves lay close to each other, thus reducing the corridor. The same remark is valid for lateral bending, but for axial torsion, this was less the case.

The experimental and corresponding numerical load-displacement curves are presented in Figure 5.16 and 5.17 for flexion/extension and axial torsion, respectively. Although the FE model globally respects the experimental corridor, the numerical curves are not entirely consistent with the corresponding experimental curves at the instrumented level. The flexion behaviour for sample S1 was well predicted by the model, yet for samples S2, S3, S4 and S6, the behaviour was overestimated. A similar remark could be made for axial torsion. However, under lateral bending, almost all of the numerical curves overlap with the experimental curves.

As the numerical simulations were displacement-controlled and the experimental analysis moment-controlled, the numerical curves did not cover the entire moment range. Convergence issues due to implant vs. implant contact and contact between spinous processes

5.2. FINITE ELEMENT MODELING OF THE CERVICAL SPINE INSTRUMENTED WITH A TOTAL DISC REPLACEMENT

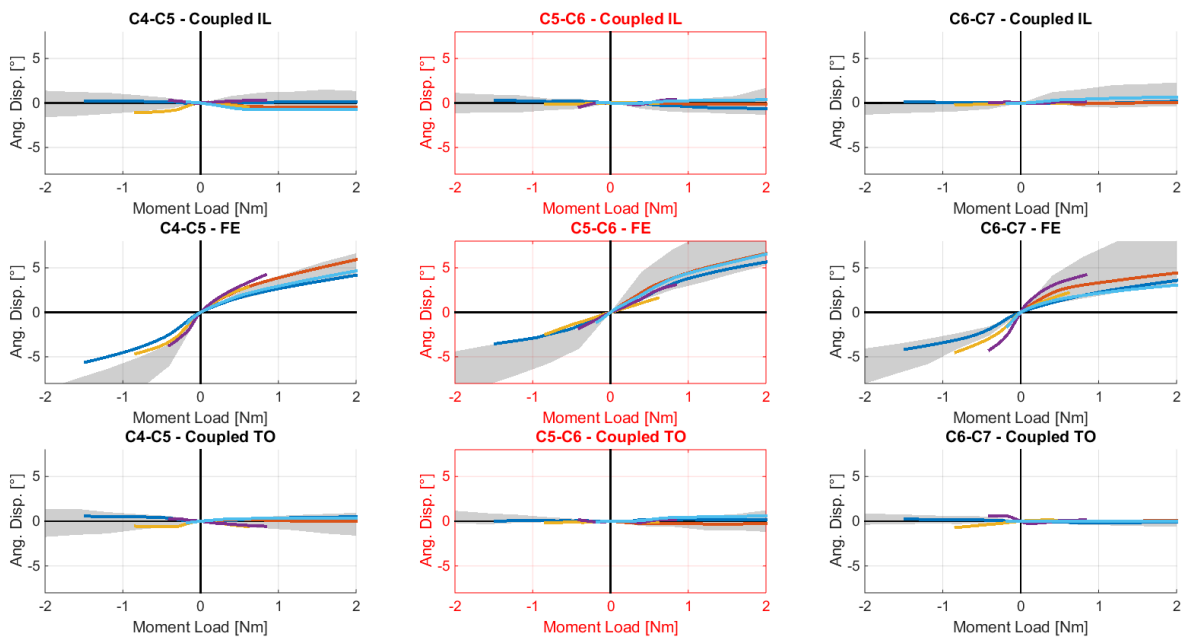


Figure 5.14: The numerical moment load vs. angular displacement behaviour in comparison with the experimental corridor for flexion/extension. The instrumented level is indicated in red.

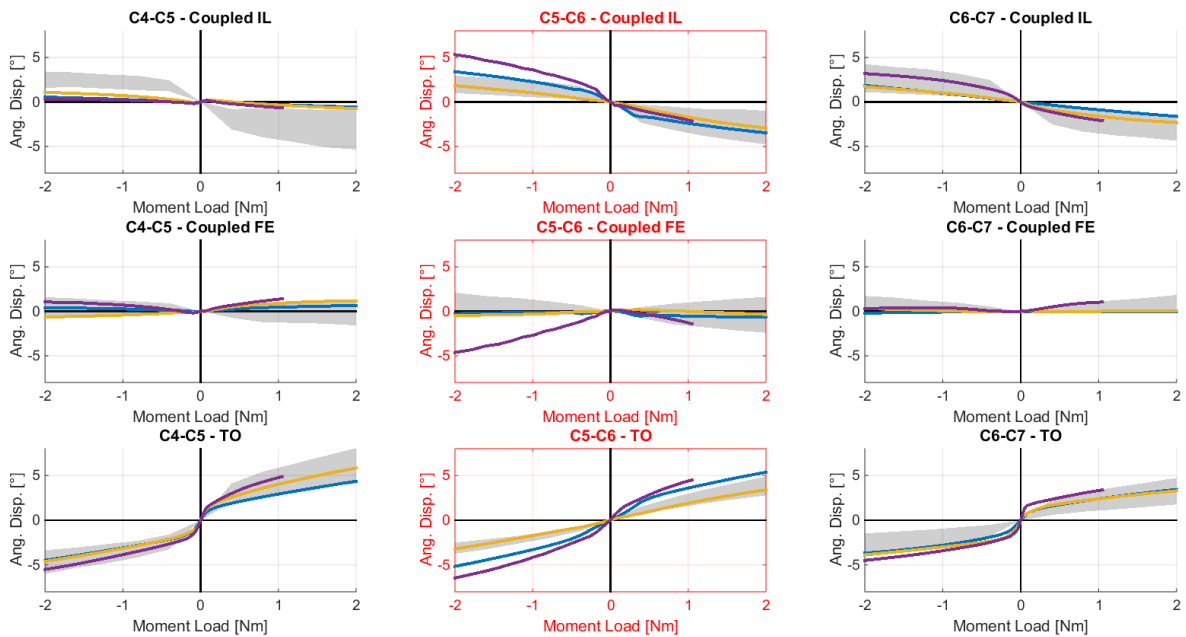


Figure 5.15: The numerical moment load vs. angular displacement behaviour in comparison with the experimental corridor for axial torsion. The instrumented level is indicated in red.

also explain why for some samples the simulations had to be ceased prematurely.

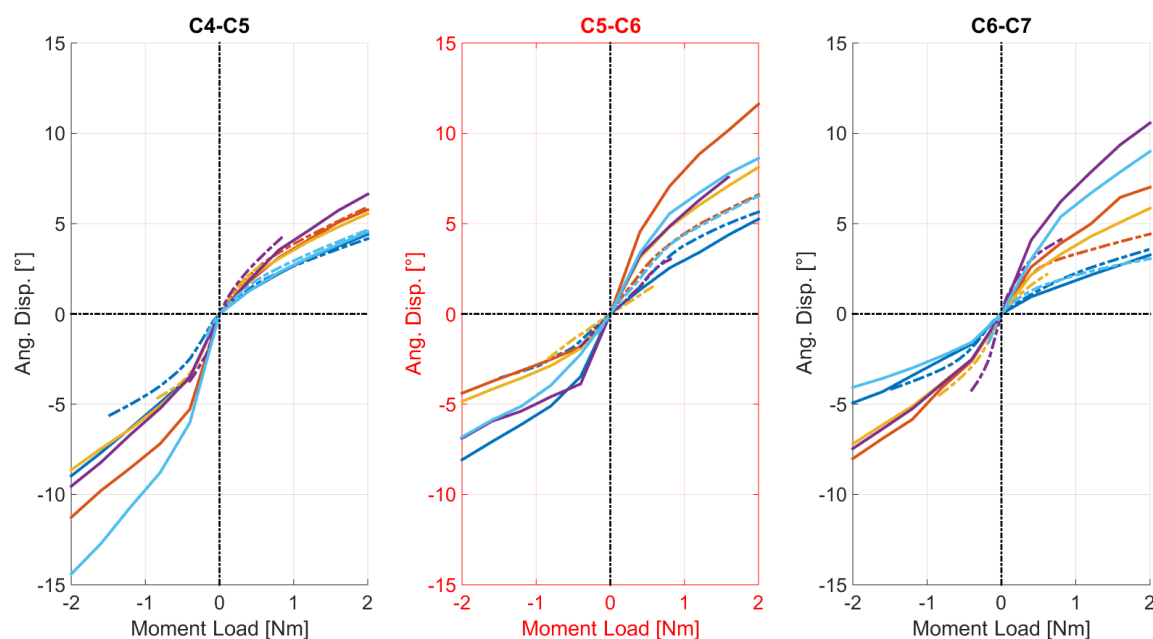


Figure 5.16: The experimental (full lines) vs. numerical (dotted lines) load-displacement curves representing the instrumented configuration under flexion/extension. The instrumented level is indicated in red.

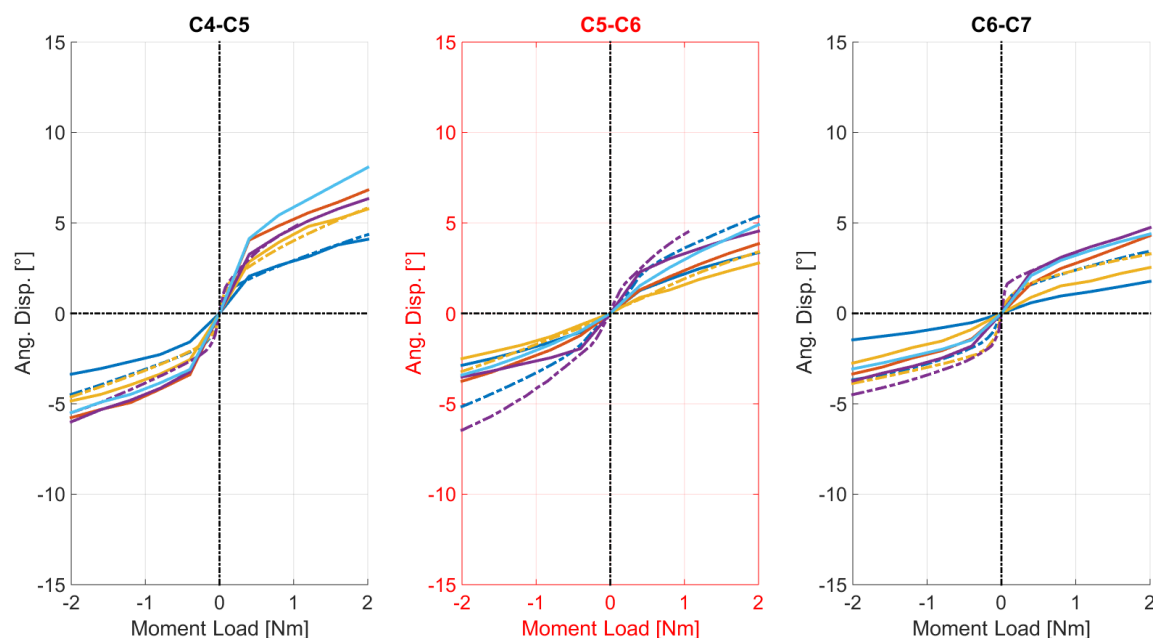


Figure 5.17: The experimental (full lines) vs. numerical (dotted lines) load-displacement curves representing the instrumented configuration under axial torsion. The instrumented level is indicated in red.

Figure 5.18 provides a schematic representation of the MCR location at each vertebral level, as recorded experimentally and predicted numerically for flexion/extension. The predicted MCR for the intact vertebral levels are consistent with the experimental recordings.

Nevertheless, at the instrumented level, the model systematically predicted a MCR located above the experimental corridor.

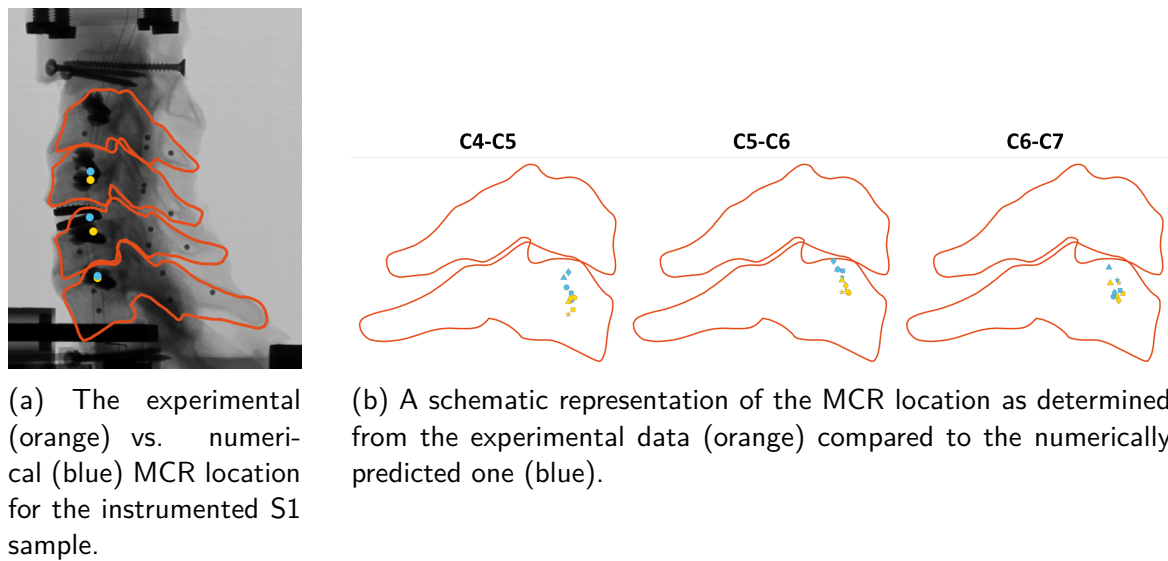


Figure 5.18: The location of the experimentally determined vs. numerically predicted mean centre of rotation (MCR).

5.2.4 Discussion

FE modeling became an essential part of the implant design process. Since it provides access to the internal stresses and deformations, it is a particularly useful tool to evaluate implant designs and to more efficiently plan *in-vitro* experiments, or even *in-vivo* clinical trials. The scientific community and regulatory agencies attempt to standardise the FE model development process by regularly reporting on best practices. However, due to, amongst other factors, the important inter-subject variability, the complex morphology of the spine and the variability in terms of implant position and orientation, computational modeling of cervical spine instrumentation remains complex.

Various cervical spine FE models focussing on implant evaluation are proposed in the literature. However, in most cases merely the FE model representing the intact configuration was evaluated against the *in-vitro* experimental literature. In only two studies, the behaviour of the instrumented FE model was compared to the literature and/or to experimental data, but only the RoM was calculated. Moreover, subject-specific analyses were not yet attempted, as most models were derived from a single set of CT scans. Such generic models are useful in the industry to evaluate implant designs, but for integration in the hospital environment, a subject-specific model is essential.

The aim of this study was therefore to overview the development of a subject-specific morphorealistic FE model of the instrumented lower cervical spine with a special attention to the *in-vitro* experimental evaluation. The model was based on a previously validated FE model of the intact lower cervical spine. Not only the load-displacement behaviour, but also the location of the mean centre of rotation was studied.

Generally, the numerical load-displacement curves obtained for the intact segment remained within the limits of the experimental corridor, both for the principal and coupled motions. This result was to be expected, with the FE model being an adjusted version of the

one developed for the healthy cervical spine of which the behaviour was extensively evaluated against *in-vitro* experimental data. Apart for axial rotation, the curves corresponding to the instrumented level respected the experimental corridor as well. The reduction of the corridor, observed both numerically and experimentally for the instrumented level could be attributed to the fact that the implant removes a large part of the geometric variability (*cfr. supra*).

The numerical and experimental curves were not necessarily similarly ordered and the model did not capture as much of the inter-subject variability as it did for the intact vertebral levels (compare Figure 4.12 with Figure 5.16). It thus appears that also for the instrumented configuration, geometry does not entirely explain the spinal mobility.

The remaining variability in load-displacement behaviour can be explained by differences in soft tissue material properties and in facet joint architecture. Numerically, the soft tissue material properties were held constant in each of the five models, meaning that merely the facet joint geometry and the initial configuration of the implant are responsible for this variability. This also explains why the numerical corridor in flexion/extension appears smaller than for lateral bending and axial torsion, as the facet surfaces play a less important role in flexion/extension.

Certain limitations have to be mentioned. The *one-to-one* comparison was performed with merely five samples, too few to establish statistical significance. The experimental analysis was also based on a small population (6 samples), just large enough to perform statistical analyses.

The actual insertion of the implant was grossly modeled. Further refinement could consider a more accurate determination of the actual ligaments stretches, the implant prestresses and the implant position and relative orientation. In this study, the TDR procedure was approximated by removing, when necessary, the ligament slack length. The initial configuration of the implant was described by measurements performed on the biplanar X-ray data.

The third limitation is the modeling of the interface between the implant and the adjacent *vertebrae*. In this study, a mechanical connection, based on beam elements, was used. A more realistic representation would be obtained with frictional surface-to-surface contact elements, to model the immediate post-operative set-up, or bonded contact elements, to model the long term post-operative configuration.

Lastly, the interaction between the metallic and plastic implant parts might not be correctly modeled. A hard frictional contact was assumed, characterised by a 0.075 friction coefficient. This coefficient was not based on experimental measurements, but estimated from literature data. Moreover, low-stiffness cable elements connected the central core to the inferior part to prevent ejection during the simulation. This might have influenced implant mechanics.

Regardless of these limitations, this is the first study proposing a subject-specific morpho-realistic FE model of the instrumented cervical spine, of which the behaviour was evaluated against experimental data. Although still preliminary, the model behaviour was already consistent with the experimental observations. The study of the effect of geometric accuracy on the model predictions is currently ongoing and in a future study a retrospective case-controlled analysis of a cohort of patients having received spinal surgery will be performed. As such, a promising basis for the biomechanical study of spinal instrumentation will be created and the way for integration in the clinic will be opened.

General Conclusion and Perspectives

The cervical spine is one of the most complex musculoskeletal structures of the human body. It has the fundamental role of ensuring the correct orientation of the head, while protecting the spinal chord, thereby compensating for any aberrant posture of the spinal structures and lower limbs below. As the head weighs on average 4.5 kg, a high risk for degeneration is to be expected. Although spinal surgery, generally considered a safe intervention, relieves the pain, clinical and mechanical complications are still frequently reported. The origin of these complications and the developmental mechanisms of spinal degeneration are still not fully understood. To better understand spinal biomechanics, to offer a more efficient diagnosis and to efficiently plan treatment and surgery, the *Institut de Biomécanique Humaine Georges Charpak* focusses on image-based subject-specific modeling, with the sponsorship of the BiomecAM program. In accordance with these objectifs, the aim of this PhD-project was to contribute to the development of a subject-specific musculoskeletal model of the cervical spine as a first step towards the design of a surgery planning tool, by combining a finite element model and a biomechanical control model enabling spine muscle force quantification.

Both the medical and the scientific community agree that a subject-specific modeling approach integrating muscle forces is essential. As highlighted in the literature study, although numerous techniques predicting physiologically acceptable spinal muscle forces are proposed, few of these techniques can be easily transferred to the clinic. Moreover, few authors tackled the issue of generating subject-specific input data. Regarding finite element modeling, a lot of common ground was found between the different FE models: most of them are based on CT data, have a hexahedral mesh architecture and are validated in terms of RoM or stiffness. However, few models were extensively validated against dedicated *in-vitro* experimental data in terms of load vs. displacement behaviour and even less models were subject-specific in the sense that they could be easily adapted to a different input. It could also be noted that none of the cervical spine FE models, intended for use in quasi-static analyses, considered the muscles and muscle forces. Three scientific needs could thus be identified: the development of an experimentally validated subject-specific and morphorealistic FE model, of a model enabling subject-specific muscle force quantification useable in a clinical environment and of a subject-specific FE model integrating a volumetric representation of the muscles and considering the active muscle forces.

During the first phase of this PhD, the focus went to the development of the biomechanical control model with proprioceptive feedback for spine muscle force quantification. The model predictions were found consistent with the literature and seemed able to capture the important inter-subject variability as different physiologically acceptable muscle force patterns were predicted for different subjects. Moreover, it has been shown that it was possible to, at least qualitatively, study the effect of postural abnormalities or degenerated intervertebral joints on the internal load distribution. An original approach was proposed to generate a 3D subject-specific musculoskeletal model, defined the Full DataSat (FDS) model, from the fused biplanar X-ray and MRI data. As MRI acquisitions are costly and time-consuming, the possibility to predict spinal muscle forces and associated joint loads from a reduced dataset containing a set of biplanar X-ray scans possibly complemented

with one or two MRI slices was evaluated. The so-called subject-specific Reduced DataSet (RDS) model, obtained from the elastic deformation of an average musculoskeletal template onto the EOS-based reconstruction data, yielded joint load predictions in agreement with the predictions obtained with the FDS model. With the integration of one MRI slice, the muscle force predictions were consistent as well.

The main contribution was to propose an innovative method to quasi-automatically quantify cervical spine muscle forces and associated intervertebral joint loads. As this approach offers in less than 30 min an accurate estimation of the internal spinal loading, it can be used in a wide range of clinical applications. It might for example help increasing our understanding of post-operative complications, such as PJK. Furthermore, it also becomes possible to perform a large scale sensibility study to assess, for instance, the effect of muscle fat infiltration on muscular regulation.

In the second phase, an morphorealistic and subject-specific FE model of the lower cervical spine was proposed. The parameterised subject-specific model developed by Laville *et al.* [2009] was refined for it to be geometrically more accurate. A thorough refinement of the material properties was performed as well. A *one-to-one* comparison was performed with five samples and the effect of using biplanar X-ray or combined biplanar X-ray and CT data as the input was assessed. It was found that both meshes provided accurate estimations for the RoM under pure moment loading and were able to capture the inter- and intra-subject variability. The numerical load-displacement curves respected the limits of the experimental corridor for the principal motions, yet a stiffer behaviour was predicted for the coupled motions. A larger part of the experimental corridor and a higher consistency with the corresponding experimental curves was observed with the CT-based FE mesh. This result is of particular interest to the clinic, as CT-scans might not be indispensable to generate an FE model with a high predictive power.

This model might be a useful tool for the study of the specific spinal biomechanics of the patients under evaluation and thus to plan surgical interventions. Combined with the subject-specific loading, as predicted by the muscle regulation model, this FE model offers a strong basis for the *in-vivo* evaluation of the instrumented spine.

To illustrate the power of the FE model and its potential use in clinical and industrial setting, a morphorealistic subject-specific FE model of the instrumented cervical spine was developed. A *one-to-one* comparison was performed based on experimental data acquired from five samples instrumented with a commercially available total disc replacement. Although still preliminary, the numerical behaviour was globally consistent with the experimental corridor. The model development procedure is thus sufficiently generic to be able to model different configurations of the cervical spine. Furthermore, because the initial stage of the model development involves the parameterisation of the medical imaging data, it remains possible to study the effect of not only the material properties but also certain geometrical and postural parameters on the spinal mobility.

The first patients have received the total disc replacement modeled in this study and were subjected to a regular follow-up. *In-vivo* case studies with the instrumented FE model and the muscle regulation model are foreseen. A larger cohort study with patients having developed degenerative changes of the cervical spine and having received spinal surgery (not limited to TDR or ACDF) and asymptomatic subjects is planned as well.

With the biomechanical control model for muscle force quantification and the morphorealistic FE model validated, both models are ready to be combined, resulting in an active musculoskeletal FE model. Indeed, some improvements might be considered, such

as the volumetric representation of the muscles. Nevertheless, as the whole process could be fully automated, providing in less than 1h an FE model with subject-specific geometry and loading, the proposed tools already enable the introduction of computational modeling in the hospital environment. This might help understanding spinal biomechanics and the outcome of spinal surgery, thus aiding surgery planning and prevention of post-operative complications.

References

- K. Abumi, Y. Shono, M. Ito, H. Taneichi, Y. Kotani, and K. Kaneda. Complications of pedicle screw fixation in reconstructive surgery of the cervical spine. *Spine*, 25(8):962–969, 2000. ISSN 0362-2436.
- H. Alosch, D. Li, L. H. Riley, and R. L. Skolasky. Health Care Burden of Anterior Cervical Spine Surgery. *Journal of Spinal Disorders and Techniques*, 28(1):5–11, 2015. ISSN 1536-0652. doi: 10.1097/BSD.0000000000000001.
- M. Alpayci, E. Senköy, V. Delen, V. Sah, L. Yazmalar, M. Erden, M. Toprak, and S. Kaplan. Decreased neck muscle strength in patients with the loss of cervical lordosis. *Clinical Biomechanics*, 33:98–102, 2016. ISSN 18791271. doi: 10.1016/j.clinbiomech.2016.02.014.
- C. Amabile. *Quantitative analysis and biomechanical modeling of the balance alteration during aging*. PhD thesis, École Nationale Supérieure d'Arts et Métiers, 2016.
- American Society of Mechanical Engineers. Guide for verification and validation in computational solid mechanics. Technical report, American Society of Mechanical Engineers, New-York, NY, USA, 2006.
- A. E. Anderson, B. J. Ellis, and J. A. Weiss. Verification, Validation and Sensitivity Studies in Computational Biomechanics. *Computer Methods in Biomechanics and Biomedical Engineering*, 10(3):1171–184, 2012. doi: 10.1080/10255840601160484.Verification.
- N. Arjmand and A. Shirazi-Adl. Model and in vivo studies on human trunk load partitioning and stability in isometric forward flexions. *Journal of Biomechanics*, 39(3):510–521, 2006. ISSN 00219290. doi: 10.1016/j.jbiomech.2004.11.030.
- N. Arjmand, D. Gagnon, A. Plamondon, A. Shirazi-Adl, and C. Larivière. Comparison of trunk muscle forces and spinal loads estimated by two biomechanical models. *Clinical Biomechanics*, 24(7):533–541, 2009. ISSN 02680033. doi: 10.1016/j.clinbiomech.2009.05.008.
- F. Azari, N. Arjmand, A. Shirazi-Adl, and T. Rahimi-Moghaddam. A combined passive and active musculoskeletal model study to estimate L4-L5 load sharing. *Journal of Biomechanics*, 2017. ISSN 00219290. doi: 10.1016/j.jbiomech.2017.04.026.
- A. A. Baaj. Number of Cervical Spine Surgeries Increased in the Last Decade, 2017. URL <https://www.spineuniverse.com/professional/news/number-cervical-spine-surgeries-increased-last-decade>.
- S. Baron, E. Ahearne, P. Connolly, S. Keaveney, and G. Byrne. An Assessment of Medical Grade Cobalt Chromium Alloy ASTM F1537 as a "Difficult-to-Cut (DTC)" Material. *Proceedings of the Machine Tool Technologies Research Foundation 2015 Annual Meeting*, 12(13):24–26, 2017.
- C. Barrey, M.-A. Rousseau, S. Persohn, S. Campana, G. Perrin, and W. Skalli. Relevance of using a compressive preload in the cervical spine: an experimental and numerical simulating investigation. *European Journal of Orthopaedic Surgery & Traumatology*, 25(S1):155–165, 2015. ISSN 1633-8065. doi: 10.1007/s00590-015-1625-2.
- J. C. Bean, D. B. Chaffin, and A. B. Schultz. Biomechanical model calculation of muscle contraction forces: a double linear programming method. *Journal of biomechanics*, 21(1):59–66, 1988. ISSN 0021-9290. doi: 0021-9290(88)90192-3[pii].
- E. J. Belin, D. E. Gelb, and E. Y. Koh. Complications in cervical spine surgeries. *Seminars in Spine Surgery*, 26(2):106–113, 2014. ISSN 15584496. doi: 10.1053/j.semss.2014.05.007.
- E. I. Ben-Abraham, J. Chen, J. P. Felmlee, P. Rossman, A. Manduca, K.-N. An, and R. L. Ehman. Feasibility of MR elastography of the intervertebral disc. *Magnetic Resonance Imaging*, 2015. ISSN 0730725X. doi: 10.1016/j.mri.2015.12.037.
- A. Bergmark. Stability of the lumbar spine. *Acta Orthopaedica Scandinavica*, 60(Suppl. 230):1–54, 1989. ISSN 0001-6470. doi: 10.3109/17453678909154177.
- P. Bernhardt, H.-J. Wilke, K. H. Wenger, B. Jungkunz, A. Böhm, and L. E. Claes. Multiple muscle force simulation in axial rotation of the cervical spine. *Clinical Biomechanics*, 14(1):32–44, 1999. ISSN 02680033. doi: 10.1016/S0268-0033(98)00031-X.

- A. H. Bernstein, D. T. Reilly, and M. Martens. Aging of Bone Tissue: Mechanical Properties. *Journal of Bone Joint Surgery*, 58(1):82–86, 1976.
- N. A. Bernstein. *The coordination and regulation of movements*. Pergamon Press, Oxford, 1967.
- Adam J. Bevevino and Alan S. Hilibrand. Adjacent segment disease: Incidence and recommended treatment. *Seminars in Spine Surgery*, 28(2):107–114, 2016. ISSN 15584496. doi: 10.1053/j.semss.2015.11.004.
- J. E. Bible and J. D. Kang. Anterior cervical discectomy and fusion: Surgical indications and outcomes. *Seminars in Spine Surgery*, 28:80–83, 2016. ISSN 10407383. doi: 10.1053/j.semss.2015.11.002.
- J. E. Bible and J. Y. Lee. Complications associated with anterior cervical surgery. *Seminars in Spine Surgery*, pages 1–5, 2015. ISSN 10407383. doi: 10.1053/j.semss.2015.11.010.
- S. L. Blumenthal, D. D. Ohnmeiss, R. D. Guyer, and J. E. Zigler. Reoperations in cervical total disc replacement compared with anterior cervical fusion. *Spine*, 38(14):1177–1182, 2013. doi: 10.1097/BRS.0b013e31828ce774.
- D. Bonneau. Conduite à tenir thérapeutique manuelle : les techniques neuromusculaires. pages 1–30.
- D. Bonneau. *Thérapeutique manuelle*. Dunod, Malakoff, 2017. ISBN 9782100754281.
- Lacey Bresnahan, Richard G Fessler, and Raghu N Natarajan. Evaluation of change in muscle activity as a result of posterior lumbar spine surgery using a dynamic modeling system. *Spine*, 35(16):E761–7, 2010. ISSN 1528-1159. doi: 10.1097/BRS.0b013e3181e45a6e.
- K. Brolin and P. Halldin. Development of a finite element model of the upper cervical spine and a parameter study of ligament characteristics. *Spine*, 29(4):376–385, 2004. ISSN 0362-2436. doi: 10.1097/01.BRS.0000090820.99182.2D.
- K. Brolin, P. Halldin, and I. Leijonhufvud. The Effect of Muscle Activation on Neck Response. *Traffic Injury Prevention*, 6(1):67–76, 2005. ISSN 1538-9588. doi: 10.1080/15389580590903203.
- M. Bydon and Z. L. Gokaslan. Surgeon Perspective on Complications after Surgery for Cervical Myelopathy. *World Neurosurgery*, 84(1):4–5, 2015. ISSN 18788769. doi: 10.1016/j.wneu.2015.04.004.
- P. G. Campbell, S. Yadla, J. Malone, B. Zussman, M. G. Maltenfort, A. D. Sharan, J. S. Harrop, and J. K. Ratliff. Early complications related to approach in cervical spine surgery: Single-center prospective study. *World Neurosurgery*, 74(2-3):363–368, 2010. ISSN 18788750. doi: 10.1016/j.wneu.2010.05.034.
- V. C. Chancey, R. W. Nightingale, C. A. Van Ee, K. E. Knaub, and B. S. Myers. Improved estimation of human neck tensile tolerance: reducing the range of reported tolerance using anthropometrically correct muscles and optimized physiologic initial conditions. *Stapp car crash journal*, 47(October):135–53, 2003. ISSN 1532-8546.
- R. F. Chandler and J. Young. Uniform Mass Distribution Properties and Body Size appropriate for the 50-percentile Male Aircrewmember during 1980-1990. Technical report, Protection and Survival Laboratory - Civil Aeromedical Insitute, Oklahoma City, 1981.
- J. Chazal, A. Tanguy, M. Bourges, G. Gaurel, G. Escande, M. Guillot, and G. Vanneuville. Biomechanical properties of spinal ligaments and a histological study of the supraspinal ligament in traction. *Journal of Biomechanics*, 18(3):167–176, 1985.
- W.-M. Chen, J. Jin, T. Park, K.-S. Ryu, and S.-J. Lee. Strain behavior of malaligned cervical spine implanted with metal-on-polyethylene, metal-on-metal, and elastomeric artificial disc prostheses - A finite element analysis. *Clinical Biomechanics*, 59(April):19–26, 2018. ISSN 02680033. doi: 10.1016/j.clinbiomech.2018.08.005.
- C.-H. Cheng, H.-Y. K. Cheng, C. P.-C. Chen, K.-H. Lin, W.-Y. Liu, S.-F. Wang, W.-L. Hsu, and Y.-F. Chuang. Altered Co-contraction of Cervical Muscles in Young Adults with Chronic Neck Pain during Voluntary Neck Motions. *Journal of physical therapy science*, 26(4):587–90, 2014. ISSN 0915-5287. doi: 10.1589/jpts.26.587.
- J. P. Y. Cheung and K. D.-K. Luk. Complications of Anterior and Posterior Cervical Spine Surgery. *Asian Spine Journal*, 10(2):385, 2016. ISSN 1976-1902. doi: 10.4184/asj.2016.10.2.385.
- H. Choi. Quantitative assessment of co-contraction in cervical musculature. *Medical Engineering & Physics*, 25: 133–140, 2003.
- H. Choi and R. Vanderby Jr. Comparison of Biomechanical Human Neck Models: Muscles Forces and Spinal Loads at C4/C5 Level. *Journal of Applied Biomechanics*, 15:120–138, 1999.

- J. Choisne, C. Travert, J.-M. Valiadis, H. Follet, and W. Skalli. A New Method to determine Volumetric Bone Mineral Density from Bi-planar Dual Energy Radiographs using a Finite Element Model: an ex-vivo Study. *Journal of Musculoskeletal Research*, 20(3):1–12, 2017. ISSN 0218-9577. doi: 10.1142/S0218957717500038.
- J. Cholewicki and S. M. McGill. Mechanical stability of the in vivo lumbar spine: Implications for injury and chronic low back pain. *Clinical Biomechanics*, 11(1):1–15, 1996. ISSN 02680033. doi: 10.1016/0268-0033(95)00035-6.
- J. Cholewicki, S. M. McGill, and R. W. Norman. Comparison of muscle forces and joint load from an optimization and EMG assisted lumbar spine model: towards development of a hybrid approach. *Journal of Biomechanics*, 28(3):321–331, 1995. ISSN 0021-9290. doi: 10.1016/0021-9290(94)00065-C.
- J. D. Clausen. *Experimental and Theoretical Investigation of Cervical Spine Biomechanics: Effects of Injury and Stabilization*. PhD thesis, University of Iowa, 1996.
- J. D. Clausen, V. K. Goel, V. C. Traynelis, and J. Scifert. Uncinate processes and Luschka joints influence the biomechanics of the cervical spine: Quantification using a finite element model of the C5-C6 segment. *Journal of Orthopaedic Research*, 15(3):342–347, 1997. ISSN 07360266. doi: 10.1002/jor.1100150305.
- C. E. Clauser, J. T. McConville, and J. W. Young. Weight, Volume, and Center of Mass of Segments of the Human Body. Technical report, Aerospace Medical Research Laboratory, Springfield, 1969.
- A. Completo, A. Nascimento, A. Ramos, and J. Simões. Failure analysis of C-5 after total disc replacement with ProDisc-C at 1 and 2 levels and in combination with a fusion cage: finite-element and biomechanical models. *Journal of Neurosurgery: Spine*, 22(6):639–646, 2015. ISSN 1547-5654. doi: 10.3171/2014.10.SPINE14217.
- P. Côté, G. van der Velde, J. D. Cassidy, L. J. Carroll, S. Hogg-Johnson, L. W. Holm, E. J. Carragee, S. Haldeman, M. Nordin, E. L. Hurwitz, J. Guzman, and P. M. Peloso. The Burden and Determinants of Neck Pain in Workers. *Spine*, 33(Suppl. 1):S60–S74, 2008. ISSN 0362-2436. doi: 10.1097/BRS.0b013e3181643ee4.
- R. Crockett, M. Roba, M. Naka, B. Gasser, D. Delfosse, V. Frauchiger, and N. D. Spencer. Friction, lubrication, and polymer transfer between UHMWPE and CoCrMo hip-implant materials: A fluorescence microscopy study. *Journal of Biomedical Materials Research - Part A*, 89(4):1011–1018, 2009. ISSN 15493296. doi: 10.1002/jbm.a.32036.
- R. B. Delamarter and J. Zigler. Five-year reoperation rates, cervical total disc replacement versus fusion, results of a prospective randomized clinical trial. *Spine*, 38(9):711–717, 2013. ISSN 03622436. doi: 10.1097/BRS.0b013e3182797592.
- W. T. Dempster. Space Requirements of the seated operator. Technical report, 1955.
- W. T. Dempster and G. R. L. Gaughran. Properties of body segments based on size and weight. *American Journal of Anatomy*, 120(1):33–54, 1967. ISSN 15530795. doi: 10.1002/aja.1001200104.
- J. A. DeWit and D. S. Cronin. Cervical spine segment finite element model for traumatic injury prediction. *Journal of the Mechanical Behavior of Biomedical Materials*, 10:138–150, 2012. ISSN 17516161. doi: 10.1016/j.jmbbm.2012.02.015.
- M. Dreischarf, T. Zander, A. Shirazi-Adl, C. M. Puttlitz, C. J. Adam, C. S. Chen, V. K. Goel, A. Kiapour, Y. H. Kim, K. M. Labus, J. P. Little, W. M. Park, Y. H. Wang, H. J. Wilke, A. Rohlmann, and H. Schmidt. Comparison of eight published static finite element models of the intact lumbar spine: Predictive power of models improves when combined together. *Journal of Biomechanics*, 47(8):1757–1766, 2014. ISSN 18732380. doi: 10.1016/j.jbiomech.2014.04.002.
- M. Dreischarf, A. Shirazi-Adl, N. Arjmand, A. Rohlman, and H. Schmidt. Estimation of loads on human lumbar spine: A review of in vivo and computational model studies. *Journal of Biomechanics*, 49(6):833–845, 2016. doi: 10.1016/j.jbiomech.2015.12.038.
- Y. Duan, H. Zhang, S.-X. Min, L. Zhang, and A.-M. Jin. Posterior cervical fixation following laminectomy: A stress analysis of three techniques. *European Spine Journal*, 20(9):1552–1559, 2011. ISSN 09406719. doi: 10.1007/s00586-011-1711-z.
- Y. Duan, H. H. Wang, A. M. Jin, L. Zhang, S. X. Min, C. L. Liu, S. J. Qiu, and X. Q. Shu. Finite element analysis of posterior cervical fixation. *Orthopaedics and Traumatology: Surgery and Research*, 101(1):23–29, 2015. ISSN 18770568. doi: 10.1016/j.otsr.2014.11.007.
- G. Dubois. *Contribution à la modélisation musculo-squelettique personnalisée du membre inférieur combinant stéréoradiographie et ultrason*. PhD thesis, Ecole Nationale Supérieure d'Arts et Métiers, 2015.

- R. Dumas, R. Aissaoui, and J. A. de Guise. A 3D generic inverse dynamic method using wrench notation and quaternion algebra. *Computer Methods in Biomechanics and Biomedical Engineering*, 7(3):159–166, 2004. ISSN 10255842. doi: 10.1080/10255840410001727805.
- F. El Masri, E. de Sapin Brosses, K. Rhissassi, W. Skalli, and D. Mitton. Apparent Young's modulus of vertebral cortico-cancellous bone specimens. *Computer Methods in Biomechanics and Biomedical Engineering*, 15(1):23–28, 2012. ISSN 10255842. doi: 10.1080/10255842.2011.565751.
- D. U. Erbulut, I. Zafarparandeh, I. Lazoglu, and A. F. Ozer. Application of an asymmetric finite element model of the C2-T1 cervical spine for evaluating the role of soft tissues in stability. *Medical Engineering and Physics*, 36(7):915–921, 2014. ISSN 18734030. doi: 10.1016/j.medengphy.2014.02.020.
- A. Erdemir, T. M. Guess, J. Halloran, S. C. Tadepalli, and T. M. Morrison. Considerations for reporting finite element analysis studies in biomechanics. *Journal of Biomechanics*, 45(4):625–633, 2012. ISSN 00219290. doi: 10.1016/j.jbiomech.2011.11.038.
- D. M. Espino, J. R. Meakin, D. W. L. Hukins, and J. E. Reid. Stochastic finite element analysis of biological systems: Comparison of a simple intervertebral disc model with experimental results. *Computer Methods in Biomechanics and Biomedical Engineering*, 6(4):243–248, 2003. ISSN 10255842. doi: 10.1080/10255840310001606071.
- F. G. Evans. *Mechanical Properties of Bone*. Charles C. Thomas, Springfield, 1973.
- F. Ezquerro, A. Simón, M. Prado, and A. Pérez. Combination of finite element modeling and optimization for the study of lumbar spine biomechanics considering the 3D thorax-pelvis orientation. *Medical Engineering and Physics*, 26(1):11–22, 2004. ISSN 13504533. doi: 10.1016/S1350-4533(03)00128-0.
- A. Faizan, V. K. Goel, A. Biyani, S. R. Garfin, and C. M. Bono. Adjacent level effects of bi level disc replacement, bi level fusion and disc replacement plus fusion in cervical spine- a finite element based study. *Clinical Biomechanics*, 27(3):226–233, 2012a. ISSN 02680033. doi: 10.1016/j.clinbiomech.2011.09.014.
- A. Faizan, V. K. Goel, S. R. Garfin, C. M. Bono, H. Serhan, A. Biyani, H. Elgafy, M. Krishna, and T. Friesem. Do design variations in the artificial disc influence cervical spine biomechanics? A finite element investigation. *European Spine Journal*, 21(SUPPL. 5):653–662, 2012b. ISSN 14320932. doi: 10.1007/s00586-009-1211-6.
- D. Falla, D. Farina, M. K. Dahl, T. Graven-Nielsen, M. Kanstrup Dahl, and T. Graven-Nielsen. Muscle pain induces task-dependent changes in cervical agonist/antagonist activity. *Journal of Applied Physiology*, 102(2):601–609, 2007. ISSN 8750-7587. doi: 10.1152/jappphysiol.00602.2006.
- R. Fejer, K. O. Kyvik, and J. Hartvigsen. The prevalence of neck pain in the world population: A systematic critical review of the literature. *European Spine Journal*, 15(6):834–848, 2006. ISSN 09406719. doi: 10.1007/s00586-004-0864-4.
- C. Fernández-de-las Peñas, D. Falla, L. Arendt-Nielsen, and D. Farina. Cervical muscle co-activation in isometric contractions is enhanced in chronic tension-type headache patients. *Cephalalgia*, 28(7):744–751, 2008. ISSN 1468-2982. doi: 10.1111/j.1468-2982.2008.01584.x.
- K. N. Fountas, E. Z. Kapsalaki, L. G. Nikolakakos, H. F. Smisson, K. W. Johnston, A. A. Grigorian, G. P. Lee, and J. S. Robinson. Anterior cervical discectomy and fusion associated complications. *Spine*, 32(21):2310–2317, 2007. ISSN 03622436. doi: 10.1097/BRS.0b013e318154c57e.
- B. Frechede, N. Bertholon, G. Saillant, F. Lavaste, and W. Skalli. Finite element model of the human neck during omni-directional impacts. Part II: relation between cervical curvature and risk of injury. *Computer methods in biomechanics and biomedical engineering*, 9(6):379–86, 2006. ISSN 1025-5842. doi: 10.1080/10255840600980940.
- D. Gagnon, C. Larivière, and P. Loisel. Comparative ability of EMG, optimization, and hybrid modelling approaches to predict trunk muscle forces and lumbar spine loading during dynamic sagittal plane lifting. *Clinical Biomechanics*, 16(5):359–372, 2001. ISSN 02680033. doi: 10.1016/S0268-0033(01)00016-X.
- D. Gagnon, N. Arjmand, A. Plamondon, A. Shirazi-Adl, and C. Larivière. An improved multi-joint EMG-assisted optimization approach to estimate joint and muscle forces in a musculoskeletal model of the lumbar spine. *Journal of biomechanics*, 44(8):1521–9, 2011. ISSN 1873-2380. doi: 10.1016/j.jbiomech.2011.03.002.
- D. Gagnon, A. Plamondon, and C. Larivière. A biomechanical comparison between expert and novice manual materials handlers using a multi-joint EMG-assisted optimization musculoskeletal model of the lumbar spine. *Journal of Biomechanics*, 2016. ISSN 00219290. doi: 10.1016/j.jbiomech.2016.07.009.

- F. Ghezelbash, A. Shirazi-Adl, N. Arjmand, Z. El-Ouaaid, and A. Plamondon. Subject-specific biomechanics of trunk: musculoskeletal scaling, internal loads and intradiscal pressure estimation. *Biomechanics and Modeling in Mechanobiology*, 15(6):1699–1712, 2016. ISSN 16177940. doi: 10.1007/s10237-016-0792-3.
- V. K. Goel and J. D. Clausen. Prediction of load sharing among spinal components of a C5-C6 motion segment using the finite element approach. *Spine*, 23(6):684–691, 1998. ISSN 0362-2436. doi: 10.1097/00007632-199803150-00008.
- V. K. Goel, W. Kong, J. S. Han, J. Weinstein, and L. G. Gilbertson. A combined finite element and optimization investigation of lumbar spine mechanics with and without muscles.pdf. *Spine*, 18(11):1531–1541, 1993.
- V. K. Goel, B. T. Monroe, L. G. Gilbertson, and P. Brinckmann. Interlaminar shear stresses and laminae separation in a disc: Finite element analysis of the L3-L4 motion segment subjected to axial compressive loads. *Spine*, 20(6):689–698, 1995. ISSN 15281159. doi: 10.1097/00007632-199503150-00010.
- V. K. Goel, A. Faizan, V. Palepu, and S. Bhattacharya. Parameters that effect spine biomechanics following cervical disc replacement. *European Spine Journal*, 21(Suppl. 5):688–699, 2012. ISSN 14320932. doi: 10.1007/s00586-011-1816-4.
- K. P. Granata and W. S. Marras. An EMG-assisted model of loads on the lumbar spine during asymmetric trunk extensions. *Journal of Biomechanics*, 26(12):1429–1438, 1993. ISSN 00219290. doi: 10.1016/0021-9290(93)90093-T.
- C. Y. Greaves, M. S. Gadala, and T. R. Oxland. A three-dimensional finite element model of the cervical spine with spinal cord: An investigation of three injury mechanisms. *Annals of Biomedical Engineering*, 36(3):396–405, 2008. ISSN 00906964. doi: 10.1007/s10439-008-9440-0.
- M. Grygiel and M. Kaczmarek. Influence of Radiation on Mechanical Properties of Ultra-High Molecular Weight Polyethylene (UHMWPE). *Information Technologies in Biomedicine*, 4:395–401, 2014. doi: 10.1007/978-3-319-06596-0.
- S. K. Ha. Finite element modeling of multi-level cervical spinal segments (C3-C6) and biomechanical analysis of an elastomer-type prosthetic disc. *Medical Engineering & Physics*, 28(6):534–541, 2006. ISSN 13504533. doi: 10.1016/j.medengphy.2005.09.006.
- M. Hajihosseinali, N. Arjmand, A. Shirazi-Adl, F. Farahmand, and M. S. Ghiasi. A novel stability and kinematics-driven trunk biomechanical model to estimate muscle and spinal forces. *Medical Engineering and Physics*, 36(10):1296–1304, 2014. ISSN 18734030. doi: 10.1016/j.medengphy.2014.07.009.
- J. S. Han, V. K. Goel, J. Y. Ahn, J. Winterbottom, D. McGowan, J. Weinstein, and T. Cook. Loads in the spinal structures during lifting: development of a three-dimensional comprehensive biomechanical model. *European Spine Journal*, 4(3):153–168, 1995. ISSN 0940-6719.
- J. Hausselle, A. Assi, A. El Helou, E. Jolivet, H. Pillet, E. Dion, D. Bonneau, and W. Skalli. Subject-specific musculoskeletal model of the lower limb in a lying and standing position. *Computer Methods in Biomechanics and Biomedical Engineering*, 17(5):480–487, 2012. ISSN 1476-8259. doi: 10.1080/10255842.2012.693173.
- B. Helgason, S. Gilchrist, O. Ariza, P. Vogt, W. Enns-Bray, R. P. Widmer, T. Fitze, H. Pálsson, Y. Pauchard, P. Guy, S. J. Ferguson, and P. A. Crompton. The influence of the modulus-density relationship and the material mapping method on the simulated mechanical response of the proximal femur in side-ways fall loading configuration. *Medical Engineering and Physics*, 38(7):679–689, 2016. ISSN 18734030. doi: 10.1016/j.medengphy.2016.03.006.
- C. Helleur, S. Gracovetsky, H. Farfan, and E. Wingrowicz. Modelling of the muscular response of the cervical spine. *Mathematical Modelling*, 6(5):443–462, 1985. ISSN 02700255. doi: 10.1016/0270-0255(85)90064-8.
- R. Hodgkinson and J. D. Currey. Young's modulus, density and material properties in cancellous bone over a large density range. *Journal of Materials Science: Materials in Medicine*, 3(5):377–381, 1992. ISSN 09574530. doi: 10.1007/BF00705371.
- A. L. Hof. EMG and muscle force: an introduction. *Human Movement Science*, 3:119–153, 1984. ISSN 1098-6596. doi: 10.1017/CBO9781107415324.004.
- A. L. Hof. The relationship between electromyogram and muscle force. *Sportverletz Sportschaden*, 11:79–86, 1997. ISSN 1098-6596. doi: 10.1017/CBO9781107415324.004.
- R. E. Hughes, D. B. Chaffin, S. A. Lavender, and G. B. Andersson. Evaluation of muscle force prediction models of the lumbar trunk using surface electromyography. *Journal of Orthopaedic Research*, 12(5):689–698, 1994. ISSN 0736-0266. doi: 10.1002/jor.1100120512.

- M. Hussain, R. N. Natarajan, A. H. Fayyazi, B. R. Braaksma, G. B. J. Andersson, and H. S. An. Screw angulation affects bone-screw stresses and bone graft load sharing in anterior cervical corpectomy fusion with a rigid screw-plate construct: a finite element model study. *Spine Journal*, 9(12):1016–1023, 2009. ISSN 15299430. doi: 10.1016/j.spinee.2009.08.461.
- M. Hussain, A. Nassr, R. N. Natarajan, H. S. An, and G. B. J. Andersson. Biomechanics of adjacent segments after a multilevel cervical corpectomy using anterior, posterior, and combined anterior-posterior instrumentation techniques: A finite element model study. *Spine Journal*, 13(6):689–696, 2013. ISSN 15299430. doi: 10.1016/j.spinee.2013.02.062.
- Institute for Health Metrics and Evaluation (IHME). GBD Compare Data Visualization, 2017. URL <https://vizhub.healthdata.org/gbd-compare/>.
- B. Jia, S. Kim, and M. A. Nussbaum. An EMG-based model to estimate lumbar muscle forces and spinal loads during complex, high-effort tasks: Development and application to residential construction using prefabricated walls. *International Journal of Industrial Ergonomics*, 41(5):437–446, 2011. ISSN 01698141. doi: 10.1016/j.ergon.2011.03.004.
- E. Jolivet, E. Daguét, V. Pomeroy, D. Bonneau, J.-D. Laredo, and W. Skalli. Volumic patient-specific reconstruction of muscular system based on a reduced dataset of medical images. *Computer Methods in Biomechanics and Biomedical Engineering*, 11(3):281–290, 2008. ISSN 1025-5842. doi: 10.1080/10255840801959479.
- A. C. Jones and R. K. Wilcox. Finite element analysis of the spine: Towards a framework of verification, validation and sensitivity analysis. *Medical Engineering and Physics*, 30(10):1287–1304, 2008. ISSN 13504533. doi: 10.1016/j.medengphy.2008.09.006.
- T. C. Jung, S. H. Woo, K. M. Park, J. W. Jang, D. W. Han, and S. J. Lee. Biomechanical behavior of two different cervical total disc replacement designs in relation of concavity of articular surfaces: ProDisc-C vs. Prestige-LP. *International Journal of Precision Engineering and Manufacturing*, 14(5):819–824, 2013. ISSN 22347593. doi: 10.1007/s12541-013-0107-x.
- N. A. Kallemeyn, S. C. Tadepalli, K. H. Shivanna, and N. M. Grosland. An interactive multiblock approach to meshing the spine. *Computer methods and programs in biomedicine*, 95(3):227–35, sep 2009. ISSN 1872-7565. doi: 10.1016/j.cmpb.2009.03.005.
- N. A. Kallemeyn, A. Gandhi, S. Kode, K. H. Shivanna, J. Smucker, and N. M. Grosland. Validation of a C2-C7 cervical spine finite element model using specimen-specific flexibility data. *Medical Engineering & Physics*, 32(5):482–489, 2010. ISSN 13504533. doi: 10.1016/j.medengphy.2010.03.001.
- P. Kamina. *Anatomy Clinique - Tome 2: Tête, Cou et Dos*. Maloine, Singapour, 4th editio edition, 2015. ISBN 9782224033569.
- I. A. Kapandji. *Physiologie articulaire, Tome 3: Tronc et Rachis*. Maloine, Paris, 5 edition, 2002.
- G. B. Kasimatis, E. Panagiotopoulos, J. Gliatis, M. Tyllianakis, P. Zouboulis, and E. Lambiris. Complications of anterior surgery in cervical spine trauma: An overview. *Clinical Neurology and Neurosurgery*, 111(1):18–27, 2009. ISSN 03038467. doi: 10.1016/j.clineuro.2008.07.009.
- T. S. Keller. Predicting the compressive mechanical behavior of bone. *Journal of Biomechanics*, 27(9):1159–1168, 1994. ISSN 00219290. doi: 10.1016/0021-9290(94)90056-6.
- A. Kettler, E. Hartwig, M. Schultheiss, L. Claes, and H.-J. Wilke. Mechanically simulated muscle forces strongly stabilize intact and injured upper cervical spine specimens. *Journal of Biomechanics*, 35(3):339–346, 2002. ISSN 0021-9290. doi: 10.1016/S0021-9290(01)00206-8.
- J. H. Keyak, I. Y. Lee, and H. B. Skinner. Correlations Between Orthogonal Mechanical Properties and Density of Trabecular Bone: Use of Different Densitometric Measures. *Journal of Biomedical Materials Research*, 28: 1329–1336, 1994.
- D. W. Kim, K. Y. Lee, Y. Jun, S. J. Lee, and C. K. Park. Friction and wear characteristics of UHMWPE against Co-Cr alloy under the wide range of contact pressures in lumbar total disc replacement. *International Journal of Precision Engineering and Manufacturing*, 12(6):1111–1118, 2011. ISSN 12298557. doi: 10.1007/s12541-011-0148-y.
- M. Kleinberger. Application of Finite Element Techniques to the Study of Cervical Spine Mechanics. *37th Stapp car crash conference*, pages 261–272, 1993. doi: 10.4271/933131.
- P. M. Knupp. Achieving Finite Element Mesh Quality via Optimization of the Jacobian Matrix Norm and Associated Quantities, Part II - A Framework for Volume Mesh Optimization and the Condition Number of the Jacobian Matrix. *International Journal for Numerical Methods in Engineering*, 48(April 1999):1165–1185, 1999.

- D. L. Kopperdahl, E. F. Morgan, and T. M. Keaveny. Quantitative computed tomography estimates of the mechanical properties of human vertebral trabecular bone. *Journal of Orthopaedic Research*, 20:801–805, 2002. ISSN 0736-0266. doi: 10.1016/S0736-0266(01)00185-1.
- M. Korinth. Treatment of Cervical Degenerative Disc Disease - Current Status and Trends. *Zentralblatt für Neurochirurgie - Central European Neurosurgery*, 69(03):113–124, 2008. ISSN 0044-4251. doi: 10.1055/s-2008-1081201.
- S. Kumaresan, N. Yoganandan, F. A. Pintar, L. M. Voo, J. F. Cusick, and S. J. Larson. Finite element modeling of cervical laminectomy with graded facetectomy. *Journal of spinal disorders*, 10(1):40–6, 1997. ISSN 0895-0385.
- S. Kumaresan, N. Yoganandan, and F. A. Pintar. Finite element modeling approaches of human cervical spine facet joint capsule. *Journal of biomechanics*, 31:371–376, 1998. ISSN 0021-9290. doi: 10.1016/S0021-9290(98)00008-6.
- S. Kumaresan, N. Yoganandan, and F. A. Pintar. Finite element analysis of the cervical spine: a material property sensitivity study. *Clinical Biomechanics*, 14(1):41–53, 1999a. ISSN 02680033. doi: 10.1016/S0268-0033(98)00036-9.
- S. Kumaresan, N. Yoganandan, F. A. Pintar, and D. J. Maiman. Finite element modeling of the cervical spine: Role of intervertebral disc under axial and eccentric loads. *Medical Engineering and Physics*, 21(10):689–700, 1999b. ISSN 13504533. doi: 10.1016/S1350-4533(00)00002-3.
- S. Kumaresan, N. Yoganandan, F. A. Pintar, D. J. Maiman, and S. Kuppa. Biomechanical study of pediatric human cervical spine: A finite element approach. *Journal of Biomechanical Engineering*, 122(February 2000): 60–71, 2000. ISSN 01480731 (ISSN). doi: 10.1115/1.429628.
- F. Lavaste, W. Skalli, S. Robin, R. Roy-Camille, and C. Mazel. Three-dimensional geometrical and mechanical modelling of the lumbar spine. *Journal of Biomechanics*, 25(10):1153–1164, 1992. ISSN 00219290. doi: 10.1016/0021-9290(92)90071-8.
- A. Laville. *Modélisation géométrique et mécanique du complexe musculo-squelettique du rachis cervical sous facteur de charge*. PhD thesis, Ecole Nationale Supérieure d'Arts et Métiers, 2011.
- A. Laville, S. Laporte, and W. Skalli. Parametric and subject-specific finite element modelling of the lower cervical spine. Influence of geometrical parameters on the motion patterns. *Journal of Biomechanics*, 42(10):1409–1415, 2009. ISSN 00219290. doi: 10.1016/j.jbiomech.2009.04.007.
- J. Lecompte, O. Maïsetti, and D. Bonneau. *Biomécanique du rachis cervical & whiplash*. Sauramps Medical.
- C. S. Lee, J. Y. Jho, K. Choi, and T.-W. Hwang. Dynamic mechanical behavior of ultra-high molecular weight polyethylene irradiated with gamma rays. *Macromolecular Research*, 12(1):141–143, 2004. ISSN 1598-5032. doi: 10.1007/BF03219007.
- J.-P. Lemaire and F. Lavaste. Patent: Self-adjusting and self-stabilizing intervertebral disc prosthesis, 2008.
- F. Li, A. Laville, D. Bonneau, S. Laporte, and W. Skalli. Study on Cervical Muscle Volume by Means of Three-Dimensional Reconstruction. *Journal of Magnetic Resonance Imaging*, 39(6):1411–1416, 2014. ISSN 10531807. doi: 10.1002/jmri.24326.
- M. A. K. Liebschner, D. L. Kopperdahl, W. S. Rosenberg, and T. M. Keaveny. Finite Element Modeling of the Human Thoracolumbar Spine. *Spine*, 28(6):559–565, 2003. ISSN 0362-2436. doi: 10.1097/01.BRS.0000049923.27694.47.
- C. Y. Lin, H. Kang, J. P. Rouleau, S. J. Hollister, and F. La Marca. Stress analysis of the interface between cervical vertebrae end plates and the Bryan, Prestige LP, and ProDisc-C cervical disc prostheses: An in vivo image-based finite element study. *Spine*, 34(15):1554–1560, 2009. ISSN 03622436. doi: 10.1097/BRS.0b013e3181aa643b.
- C. Y. Lin, S. Y. Chuang, C. J. Chiang, Y. H. Tsuang, and W. P. Chen. Finite Element Analysis of Cervical Spine With Different Constrained Types of Total Disc Replacement. *Journal of Mechanics in Medicine and Biology*, 14(3):1–13, 2014. ISSN 0219-5194. doi: 10.1142/S0219519414500389.
- C. Y. Liu, C. C. Zygourakis, S. Yoon, T. Kliot, C. Moriates, J. Ratcliff, R. Adams Dudley, R. Gonzales, P. V. Mummaneni, and C. P. Ames. Trends in Utilization and Cost of Cervical Spine Surgery Using the National Inpatient Sample Database, 2001 to 2013. *Spine*, 42(15):906–913, 2016. doi: 10.1097/BRS.0000000000002326.
- R. Lo Martire, K. Gladh, A. Westman, and B. O. Äng. Neck Muscle EMG-Force Relationship and Its Reliability During Isometric Contractions. *Sports Medicine - Open*, 3(1):16, 2017. ISSN 2199-1170. doi: 10.1186/s40798-017-0083-2.

- G. P. Malcolm. Surgical Disorders of the Cervical Spine: Presentation and Management of Common Disorders. *Journal of Neurology, Neurosurgery & Psychiatry*, 73(suppl 1):i34–i41, 2002. ISSN 0022-3050. doi: 10.1136/JNNP.73.SUPPL{ }1.I34.
- S. Marawar, F. P. Girardi, A. A. Sama, Y. Ma, L. K. Gaber-Baylis, M. C. Besculides, and S. G. Memtsoudis. National trends in anterior cervical fusion procedures. *Spine*, 35(15):1454–1459, 2010. ISSN 03622436. doi: 10.1097/BRS.0b013e3181bef3cb.
- A. Marquez-Lara, S. V. Nandyala, S. J. Fineberg, and K. Singh. Current Trends in Demographics, Practice, and In-Hospital Outcomes in Cervical Spine Surgery. *Spine*, 39(6):476–481, 2014. ISSN 0362-2436. doi: 10.1097/BRS.000000000000165.
- S. F. E. Mattucci and D. S. Cronin. A method to characterize average cervical spine ligament response based on raw data sets for implementation into injury biomechanics models. *Journal of the Mechanical Behavior of Biomedical Materials*, 41:251–260, 2015. ISSN 18780180. doi: 10.1016/j.jmbbm.2014.09.023.
- S. F. E. Mattucci, J. A. Moulton, N. Chandrashekar, and D. S. Cronin. Strain rate dependent properties of younger human cervical spine ligaments. *Journal of the Mechanical Behavior of Biomedical Materials*, 10:216–226, 2012. ISSN 17516161. doi: 10.1016/j.jmbbm.2012.02.004.
- N. Maurel, F. Lavaste, and W. Skalli. A three-dimensional parameterized finite element model of the lower cervical spine, study of the influence of the posterior articular facets. *Journal of Biomechanics*, 30(9):921–931, 1997. ISSN 00219290. doi: 10.1016/S0021-9290(97)00056-0.
- P. McClure. The degenerative cervical spine: pathogenesis and rehabilitation concepts. *Journal of hand therapy : official journal of the American Society of Hand Therapists*, 13(2):163–174, 2000. ISSN 08941130. doi: 10.1016/S0894-1130(00)80039-3.
- S. M. McGill. A myoelectrically based dynamic three-dimensional model to predict loads on lumbar spine tissues during lateral bending. *Journal of Biomechanics*, 25:395–414, 1992.
- M. L. McMulkin, J. C. Woldstad, and R. E. Hughes. Optimization model estimates of trunk muscle forces do not correlate with EMG activity of females as well as males. *Journal of Applied Biomechanics*, 19:131–138, 2003. ISSN 10658483.
- Z.-Y. Mo, Y.-B. Zhao, L.-Z. Wang, Y. Sun, M. Zhang, and Y.-B. Fan. Biomechanical effects of cervical arthroplasty with U-shaped disc implant on segmental range of motion and loading of surrounding soft tissue. *European Spine Journal*, 23(3):613–621, 2014. ISSN 14320932. doi: 10.1007/s00586-013-3070-4.
- Y. Mohammadi, N. Arjmand, and A. Shirazi-Adl. Comparison of trunk muscle forces, spinal loads and stability estimated by one stability- and three EMG-assisted optimization approaches. *Medical Engineering & Physics*, 37(8):792–800, 2015. ISSN 13504533. doi: 10.1016/j.medengphy.2015.05.018.
- S. P. Moroney, A. B. Schultz, and J. A. A. Miller. Analysis and measurement of neck loads. *Journal of Orthopaedic Research*, 6(5):713–720, 1988a. ISSN 0736-0266. doi: 10.1002/jor.1100060514.
- S. P. Moroney, A. B. Schultz, J. A. A. Miller, and G. B. J. Andersson. Load-displacement properties of lower cervical spine motion segments. *Journal of Biomechanics*, 21(9):769–779, 1988b. ISSN 00219290. doi: 10.1016/0021-9290(88)90285-0.
- M. Moshfeghi, S. Ranganath, and K. Nawyn. Three-Dimensional Elastic Matching of Volumes. *IEEE Transactions on Image Processing*, 3(2):128–138, 1994. ISSN 19410042. doi: 10.1109/83.277895.
- T. Motosuneya, T. Asazuma, T. Tsuji, H. Watanabe, Y. Nakayama, and K. Nemoto. Postoperative change of the cross-sectional area of back musculature after 5 surgical procedures as assessed by magnetic resonance imaging. *Journal of Spinal Disorders and Techniques*, 19(5):318–322, 2006. ISSN 15360652. doi: 10.1097/01.bsd.0000211205.15997.06.
- R. Mousavi-Khatir, S. Talebian, N. Toosizadeh, G. R. Olyaei, and N. Maroufi. The effect of static neck flexion on mechanical and neuromuscular behaviors of the cervical spine. *Journal of Biomechanics*, 72:152–158, 2018. ISSN 18732380. doi: 10.1016/j.jbiomech.2018.03.004.
- S. Naserkhaki, N. Arjmand, A. Shirazi-Adl, F. Farahmand, and M. El-Rich. Effects of eight different ligament property datasets on biomechanics of a lumbar L4-L5 finite element model. *Journal of Biomechanics*, 70:33–42, 2017. ISSN 18732380. doi: 10.1016/j.jbiomech.2017.05.003.

- R. Nasser, S. Yadla, M. G. Maltenfort, J. S. Harrop, D. G. Anderson, A. R. Vaccaro, A. D. Sharan, J. K. Ratliff, E. Burger, R. Nasser, S. Yadla, M. G. Maltenfort, J. S. Harrop, D. G. Anderson, A. R. Vaccaro, A. D. Sharan, and J. K. Ratliff. Complications in spine surgery. *J Neurosurg Spine*, 13(2):144–157, 2010. ISSN 1547-5646. doi: 10.3171/2010.3.spine09369.
- R. N. Natarajan, B. H. Chen, H. S. An, and G. B. Andersson. Anterior cervical fusion: a finite element model study on motion segment stability including the effect of osteoporosis. *Spine*, 25(8):955–61, 2000. ISSN 0362-2436.
- A. Nérot, J. Choisine, C. Amabile, C. Travert, H. Pillet, X. Wang, and W. Skalli. A 3D reconstruction method of the body envelope from biplanar X-rays: Evaluation of its accuracy and reliability. *Journal of Biomechanics*, 48(16):4322–4326, 2015. ISSN 18732380. doi: 10.1016/j.jbiomech.2015.10.044.
- H.-W. Ng and E.-C. Teo. Nonlinear finite-element analysis of the lower cervical spine (C4-C6) under axial loading. *Journal of Spinal Disorders & Techniques*, 14(3):201–210, 2001. ISSN 1536-0652. doi: 10.1097/00002517-200106000-00003.
- H.-W. Ng, E.-C. Teo, K.-K. Lee, and T.-X. Qiu. Finite element analysis of cervical spinal instability under physiologic loading. *Journal of spinal disorders & techniques*, 16(1):55–65, 2003. ISSN 1536-0652. doi: 10.1097/00024720-200302000-00010.
- R. W. Nightingale, V. C. Chancey, D. Ottaviano, J. F. Luck, L. Tran, M. Prange, and B. S. Myers. Flexion and extension structural properties and strengths for male cervical spine segments. *Journal of Biomechanics*, 40(3):535–542, 2007. ISSN 00219290. doi: 10.1016/j.jbiomech.2006.02.015.
- J. Noailly and D. Lacroix. Finite element modelling of the spine. *Biomaterials for Spinal Surgery*, pages 144–232, 2012. doi: 10.1016/B978-1-84569-986-4.50005-2.
- M. A. Nussbaum and D. B. Chaffin. Lumbar muscle force estimation using a subject-invariant 5-parameter EMG-based model. *Journal of Biomechanics*, 31(7):667–672, 1998. ISSN 00219290. doi: 10.1016/S0021-9290(98)00055-4.
- T. Okamoto, M. Neo, S. Fujibayashi, H. Ito, M. Takemoto, and T. Nakamura. Mechanical implant failure in posterior cervical spine fusion. *European Spine Journal*, 21(2):328–334, 2012. ISSN 09406719. doi: 10.1007/s00586-011-2043-8.
- L. Ombregt. Section 2: The cervical spine. Applied anatomy of the cervical spine. *A System of Orthopaedic Medicine*, pages 1–12, 2013. doi: 10.1016/B978-0-7020-3145-8.00060-0.
- M. M. Panjabi. The Stabilizing System of the Spine. Part I. Function, Dysfunction, Adaptation, and Enhancement. *Journal of Spinal Disorders & Techniques*, 5(4):383–389, 1992a. ISSN 0895-0385. doi: 10.1097/00002517-199212000-00001.
- M. M. Panjabi. The stabilizing system of the spine. Part II. Neutral zone and instability hypothesis. *Journal of spinal disorders*, 5(4):390–396, 1992b. ISSN 0895-0385. doi: 10.1097/00002517-199212000-00002.
- M. M. Panjabi, D. J. Summers, R. R. Pelker, T. Videman, G. E. Friedlaender, and W. O. Southwick. Three-dimensional load-displacement curves due to forces on the cervical spine. *Journal of Orthopaedic Research*, 4(2):152–161, 1986. ISSN 0736-0266. doi: 10.1002/jor.1100040203.
- M. M. Panjabi, K. Abumi, J. Duranceau, and T. Oxland. Spinal stability and intersegmental muscle forces. A biomechanical model. *Spine*, 14(2):194–200, 1989. ISSN 0362-2436. doi: 10.1097/00007632-198902000-00008.
- M. M. Panjabi, J. Cholewicki, K. Nibu, L. B. Babatl, and J. Dvorak. Critical load of the human cervical spine: an in vitro experimental study. *Clinical Biomechanics*, 13(1):11–17, 1998. ISSN 1879-1271. doi: 10.1016/S0268-0033(97)00057-0.
- M. M. Panjabi, J. J. Crisco, A. Vasavada, T. Oda, J. Cholewicki, K. Nibu, and E. Shin. Mechanical properties of the human cervical spine as shown by three-dimensional load-displacement curves. *Spine*, 26(24):2692–2700, 2001a.
- M. M. Panjabi, T. Miura, P. A. Cripton, J. L. Wang, A. S. Nain, and C. DuBois. Development of a system for in vitro neck muscle force replication in whole cervical spine experiments. *Spine*, 26(20):2214–9, 2001b. ISSN 0362-2436. doi: 10.1097/00007632-200110150-00012.
- M. B. Panzer and D. S. Cronin. C4-C5 segment finite element model development, validation, and load-sharing investigation. *Journal of Biomechanics*, 42:480–490, 2009. ISSN 00219290. doi: 10.1016/j.jbiomech.2008.11.036.

- M. B. Panzer, J. B. Fice, and D. S. Cronin. Cervical spine response in frontal crash. *Medical Engineering and Physics*, 33(9):1147–1159, 2011. ISSN 13504533. doi: 10.1016/j.medengphy.2011.05.004.
- P. G. Patil, D. Turner, and R. Pietrobon. National trends in surgical procedures for degenerative cervical spine disease: 1990–2000. *Neurosurgery*, 57(4):753–758; discussion 753–758, 2005. ISSN 0148-396X. doi: 10.1227/01.NEU.0000175729.79119.1d.
- A. Pérez del Palomar, B. Calvo, and M. Doblaré. An accurate finite element model of the cervical spine under quasi-static loading. *Journal of biomechanics*, 41(3):523–31, 2008. ISSN 0021-9290. doi: 10.1016/j.jbiomech.2007.10.012.
- W. Platzer. *Atlas van de anatomie - Bewegingsapparaat*. ThiemeMeulenhoff, Amersfoort, 2012. ISBN 9789006951981.
- V. Pomeroy, F. Lavaste, G. Imbert, and W. Skalli. A proprioception based regulation model to estimate the trunk muscle forces. *Computer Methods in Biomechanics and Biomedical Engineering*, 7(6):331–338, 2004. ISSN 1025-5842. doi: 10.1080/1025584042000327115.
- H. M. Reynolds, C. E. Clauser, J. Mcconville, R. Chandler, and J. W. Young. Mass Distribution Properties of the Male Cadaver. *SAE technical paper*, (750424):1132–1150, 1975. doi: 10.4271/750424.
- J. Y. Rho, M. C. Hobatho, and R. B. Ashman. Relations of mechanical properties to density and CT numbers in human bone. *Medical Engineering and Physics*, 17(5):347–355, 1995. ISSN 13504533. doi: 10.1016/1350-4533(95)97314-F.
- M. Richter, H.-J. Wilke, P. Kluger, L. Claes, and W. Puhl. Load-displacement properties of the normal and injured lower cervical spine in vitro. *European spine journal : official publication of the European Spine Society, the European Spinal Deformity Society, and the European Section of the Cervical Spine Research Society*, 9(2): 104–8, 2000. ISSN 0940-6719. doi: 10.1007/s005860050219.
- M.-A. Rousseau, S. Laporte, E. Chavary-Bernier, J.-Y. Lazennec, and W. Skalli. Reproducibility of measuring the shape and three-dimensional position of cervical vertebrae in upright position using the EOS stereoradiography system. *Spine*, 32(23):2569–2572, 2007. ISSN 0362-2436. doi: 10.1097/BRS.0b013e318158cba2.
- M.-A. Rousseau, X. Bonnet, and W. Skalli. Influence of the geometry of a ball-and-socket intervertebral prosthesis at the cervical spine: a finite element study. *Spine*, 33(1):E10–E14, 2008a. ISSN 0362-2436. doi: 10.1097/BRS.0b013e31815e62ea.
- M.-A. Rousseau, H. Pascal-Moussellard, Y. Catonné, and J.-Y. Lazennec. Anatomie et biomécanique du rachis cervical. *Revue du Rhumatisme*, 75(8):707–711, 2008b. ISSN 11698330. doi: 10.1016/j.rhum.2008.06.001.
- V. Saikko. Effect of contact pressure on wear and friction of ultra-high molecular weight polyethylene in multidirectional sliding. *Proceedings of the Institution of Mechanical Engineers, Part H: Journal of Engineering in Medicine*, 220(7):723–731, 2006. ISSN 09544119. doi: 10.1243/09544119JEIM146.
- T. Saito, T. Yamamuro, J. Shikita, M. Oka, and S. Tsutsumi. Analysis and prevention of spinal column deformity following cervical laminectomy. I. Pathogenetic analysis of postlaminectomy deformities. *Spine*, 16(5):494–502, 1991.
- E. Sapin de Brosses, K. Briot, S. Kolta, W. Skalli, C. Roux, and D. Mitton. Subject-specific mechanical properties of vertebral cancellous bone assessed using a low-dose X-ray device. *Irbm*, 31(3):148–153, 2010. ISSN 19590318. doi: 10.1016/j.irbm.2010.02.014.
- A. Schultz, K. Haderspeck, D. Warwick, and D. Portillo. Use of lumbar trunk muscles in isometric performance of mechanically complex standing tasks. *Journal of Orthopaedic Research*, 1(1):77–91, 1983. ISSN 1554527X. doi: 10.1002/jor.1100010111.
- A. Seth, M. Sherman, J. A. Reinbolt, and S. L. Delp. OpenSim: a musculoskeletal modeling and simulation framework for in silico investigations and exchange. *Procedia IUTAM*, 2:212–232, 2011. ISSN 1527-5418. doi: 10.1016/j.coviro.2015.09.001.Human.
- M. Sharma, N. A. Langrana, and J. Rodriguez. Role of ligaments and facets in lumbar spinal stability. *Spine*, 20(8):887–900, 1995.
- J. H. Shim. Neck Pain Causes, 2016. URL <https://www.spine-health.com/conditions/neck-pain/neck-pain-causes>.

- A. Shirazi-Adl, S. C. Shrivastava, and A. M. Ahmed. Stress Analysis of the Lumbar Disc-Body Unit in Compression A Three-Dimensional Nonlinear Finite Element Study. *Spine*, 9(2):120–134, 1984.
- I. A. F. Stokes and M. Gardner-Morse. Lumbar spine maximum efforts and muscle recruitment patterns predicted by a model with multijoint muscles and joints with stiffness. *J Biomech*, 28(2):173–186, 1995. ISSN 00219290. doi: 10.1016/0021-9290(94)E0040-A.
- I. A. F. Stokes and M. Gardner-Morse. Lumbar spinal muscle activation synergies predicted by multi-criteria cost function. *Journal of Biomechanics*, 34:733–740, 2001. ISSN 00219290. doi: 10.1016/S0021-9290(01)00034-3.
- E. E. Swartz, R. T. Floyd, and M. Cendoma. Cervical spine functional anatomy and the biomechanics of injury due to compressive loading. *Journal of Athletic Training*, 40(3):155–161, 2005. ISSN 10626050.
- A. Tasiou, T. Giannis, A. G. Brotis, I. Siasios, I. Georgiadis, H. Gatos, E. Tsianaka, K. Vagkopoulos, K. Paterakis, and K. N. Fountas. Anterior cervical spine surgery-associated complications in a retrospective case-control study. *Journal of Spine Surgery*, 3(3):444–459, 2017. ISSN 2414469X. doi: 10.21037/jss.2017.08.03.
- E.-C. Teo and H.-W. Ng. Evaluation of the role of ligaments, facets and disc nucleus in lower cervical spine under compression and sagittal moments using finite element method. *Medical Engineering and Physics*, 23:155–164, 2001. ISSN 13504533. doi: 10.1016/S1350-4533(01)00036-4.
- A. G. Todd. Cervical spine: Degenerative conditions. *Current Reviews in Musculoskeletal Medicine*, 4(4):168–174, 2011. ISSN 1935973X. doi: 10.1007/s12178-011-9099-2.
- N. Toosizadeh and M. Haghpanahi. Generating a finite element model of the cervical spine: Estimating muscle forces and internal loads. *Scientia Iranica*, 18(6):1237–1245, 2011. ISSN 10263098. doi: 10.1016/j.scient.2011.10.002.
- C. Travert. *Estimation du Risque de Fracture Ostéoporotique du Rachis Thoraco- Lombar par un Modèle en Élément Finis Personnalisé*. PhD thesis, Ecole Nationale Supérieure d'Arts et Métiers, 2013.
- C. Travert, E. Jolivet, E. Sapin-De Brosses, D. Mitton, and W. Skalli. Sensitivity of patient-specific vertebral finite element model from low dose imaging to material properties and loading conditions. *Medical and Biological Engineering and Computing*, 49(12):1355–1361, 2011. ISSN 01400118. doi: 10.1007/s11517-011-0825-0.
- F. Trochu. A Contouring Program Based on Dual Kriging Interpolation. *Engineering with Computers*, 9:160–177, 1993.
- K. Ueno and Y. K. Liu. A three-dimensional nonlinear finite element model of lumbar intervertebral joint in torsion. *Journal of biomechanical engineering*, 109(3):200–209, 1987. ISSN 0148-0731. doi: 10.1115/1.3138670.
- US Food and Drug Administration - Center for Devices and Radiological Health. Reporting of Computational Modeling Studies in Medical Device Submissions - Draft Guidance for Industry and Food and Drug Administration Staff. Technical report, US Food and Drug Administration - Center for Devices and Radiological Health, Rockville, MD, USA, 2016.
- M. Van den Abbeele, F. Li, V. Pomeroy, D. Bonneau, B. Sandoz, S. Laporte, and W. Skalli. A subject-specific biomechanical control model for the prediction of cervical spine muscle forces. *Clinical Biomechanics*, 51 (February):58–66, 2018. ISSN 18791271. doi: 10.1016/j.clinbiomech.2017.12.001.
- C. Vergari, P. Rouch, G. Dubois, D. Bonneau, J. Dubousset, M. Tanter, J.-L. Gennisson, and W. Skalli. Non-invasive biomechanical characterization of intervertebral discs by shear wave ultrasound elastography: a feasibility study. *European Radiology*, 24(12):3210–3216, 2014a. ISSN 0938-7994. doi: 10.1007/s00330-014-3382-8.
- C. Vergari, P. Rouch, G. Dubois, D. Bonneau, J. Dubousset, M. Tanter, J.-L. Gennisson, and W. Skalli. Intervertebral disc characterization by shear wave elastography : an in-vitro preliminary study. *Journal of Engineering in Medicine*, 228(6):607–615, 2014b.
- C. Vergari, G. Dubois, R. Vialle, J.-L. Gennisson, M. Tanter, J. Dubousset, P. Rouch, and W. Skalli. Lumbar annulus fibrosus biomechanical characterization in healthy children by ultrasound shear wave elastography. *European Radiology*, 26(4):1213–1217, 2015. ISSN 0938-7994. doi: 10.1007/s00330-015-3911-0.
- M. Viceconti, S. Olsen, L. P. Nolte, and K. Burton. Extracting clinically relevant data from finite element simulations. *Clinical Biomechanics*, 20(5):451–454, 2005. ISSN 02680033. doi: 10.1016/j.clinbiomech.2005.01.010.
- L. M. Voo, S. Kumaresan, N. Yoganandan, F. A. Pintar, and J. F. Cusick. Finite element analysis of cervical facetectomy. *Spine*, 22(9):964–969, 1997.

- L. M. Voo, F. A. Pintar, N. Yoganandan, and Y. K. Liu. Static and dynamic bending responses of the human cervical spine. *Journal of Biomechanical Engineering*, 120(December):693–696, 1998.
- K. Wang, H. Wang, Z. Deng, Z. Li, H. Zhan, and W. Niu. Cervical traction therapy with and without neck support: A finite element analysis. *Musculoskeletal Science and Practice*, 28:1–9, 2017. ISSN 24687812. doi: 10.1016/j.msksp.2017.01.005.
- M. C. Wang, L. Chan, D. J. Maiman, W. Kreuter, and R. A. Deyo. Complications and mortality associated with cervical spine surgery for degenerative disease in the United States. *Spine*, 32(3):342–347, 2007. ISSN 0362-2436. doi: 10.1097/01.brs.0000254120.25411.ae.
- M. C. Wang, W. Kreuter, C. E. Wolfla, D. J. Maiman, and R. A. Deyo. Trends and variations in cervical spine surgery in the United States: Medicare beneficiaries, 1992 to 2005. *Spine*, 34(9):955–61; discussion 962–3, 2009. ISSN 1528-1159. doi: 10.1097/BRS.0b013e31819e2fd5.
- N. Wen, F. Lavaste, J. J. Santin, and J. P. Lassau. Three-dimensional biomechanical properties of the human cervical spine in vitro. I. Analysis of normal motion. *European Spine Journal*, 2:2–11, 1993.
- J. A. Wheeldon, F. A. Pintar, S. Knowles, and N. Yoganandan. Experimental flexion/extension data corridors for validation of finite element models of the young, normal cervical spine. *Journal of Biomechanics*, 39(2):375–380, 2006. ISSN 00219290. doi: 10.1016/j.jbiomech.2004.11.014.
- J. A. Wheeldon, B. D. Stemper, N. Yoganandan, and F. A. Pintar. Validation of a finite element model of the young normal lower cervical spine. *Annals of Biomedical Engineering*, 36(9):1458–1469, 2008. ISSN 00906964. doi: 10.1007/s10439-008-9534-8.
- H.-J. Wilke, S. Wolf, L. E. Claes, M. Arand, and A. Wiesend. Stability Increase of the Lumbar Spine With Different Muscle Groups: A Biomechanical In Vitro Study. *Spine*, 20(2):192–197, 1995. ISSN 0362-2436. doi: 10.1097/00007632-199501150-00011.
- World Health Organisation. Health statistics and information systems - Metrics: Disability-Adjusted Life Year (DALY), 2016. URL http://www.who.int/healthinfo/global_{_}burden_{_}disease/metrics_{_}daly/en/.
- W. Wu, C. Chen, J. Ning, P. Sun, J. Zhang, C. Wu, Z. Bi, J. Fan, X. Lai, and J. Ouyang. A Novel Anterior Transpedicular Screw Artificial Vertebral Body System for Lower Cervical Spine Fixation: A Finite Element Study. *Journal of Biomechanical Engineering*, 139(6):061003, 2017. ISSN 0148-0731. doi: 10.1115/1.4036393.
- H. Yamada. *Strength of Biological Materials*. Williams & Wilkins, Baltimore, 1970.
- H. Yang, M. G. Jekir, M. W. Davis, and T. M. Keaveny. Effective modulus of the human intervertebral disc and its effect on vertebral bone stress. *Journal of Biomechanics*, 49(7):1134–1140, 2016. ISSN 00219290. doi: 10.1016/j.jbiomech.2016.02.045.
- N. Yoganandan, S. Kumaresan, V. Liming, F. A. Pintar, and S. J. Larson. Finite element modeling of the C4-C6 cervical spine unit. *Medical Engineering and Physics*, 18(7):569–574, 1996. ISSN 13504533. doi: 10.1016/1350-4533(96)00013-6.
- N. Yoganandan, S. Kumaresan, L. Voo, and F. A. Pintar. Finite element model of the human lower cervical spine: parametric analysis of the C4-C6 unit. *Journal of biomechanical engineering*, 119(1):87–92, 1997. ISSN 0148-0731. doi: 10.1115/1.2796070.
- N. Yoganandan, S. Kumaresan, and F.A. Pintar. Geometric and Mechanical Properties of Human Cervical Spine Ligaments. *Journal of Biomechanical Engineering*, 122(December):623–629, 2000.
- N. Yoganandan, S. Kumaresan, and F. A. Pintar. Biomechanics of the cervical spine Part 2: Cervical spine soft tissue responses and biomechanical modeling. *Clinical Biomechanics*, 16:1–27, 2001.
- N. Yoganandan, F. A. Pintar, J. Zhang, and J. L. Baisden. Physical properties of the human head: Mass, center of gravity and moment of inertia. *Journal of Biomechanics*, 42(9):1177–1192, 2009. ISSN 00219290. doi: 10.1016/j.jbiomech.2009.03.029.
- C.-C. Yu, P. Liu, D.-G. Huang, Y.-H. Jiang, H. Feng, and D.-J. Hao. A new cervical artificial disc prosthesis based on physiological curvature of end plate: a finite element analysis. *Spine Journal*, 16(11):1384–1391, 2016. ISSN 18781632. doi: 10.1016/j.spinee.2016.06.019.
- W. Yuan, H. Zhang, X. Zhou, W. Wu, and Y. Zhu. The Influence of Artificial Cervical Disc Prosthesis Height on the Cervical Biomechanics: A Finite Element Study. *World Neurosurgery*, 113:e490–e498, 2018. ISSN 18788769. doi: 10.1016/j.wneu.2018.02.062.

- Q.-H. Zhang, E.-C. Teo, and H.-W. Ng. Development and Validation of A C0-C7 FE Complex for Biomechanical Study. *Journal of Biomechanical Engineering*, 127(5):729, 2005. ISSN 0148-0731. doi: 10.1115/1.1992527.
- Q.-H. Zhang, E.-C. Teo, H.-W. Ng, and V.-S. Lee. Finite element analysis of moment-rotation relationships for human cervical spine. *Journal of Biomechanics*, 39(1):189–193, 2006. ISSN 00219290. doi: 10.1016/j.jbiomech.2004.10.029.
- B. H. Zhou, R. V. Baratta, M. Solomonow, L. J. Olivier, G. T. Nguyen, and R. D. D'Ambrosia. Evaluation of isometric antagonist coactivation strategies of electrically stimulated muscles. *IEEE Transactions on Biomedical Engineering*, 43(2):150–160, 1996.

Chapter A

Cervical Spine Ligamentous and Muscular Anatomy

This Appendix provides a detailed non-exhaustive overview of the cervical spine ligaments and musculature, based on the information extracted from Kapandji [2002], Platzer [2012], Kamina [2015] and Bonneau [2017].

Table A.1 provide a list of all ligaments stabilising the upper cervical intervertebral joints, while A.2 list the ligaments of the lower cervical spine.

Tables A.3 to A.6 provide list of the deep, intermediate, superficial and suboccipital muscle, respectively. For each muscle considered primordial for the understanding of cervical spine biomechanics, the insertion, termination and function are given.

Segment		Ligament		Insertion	Termination	
C0-C1	Joint capsule		Joining the edges of the cartilaginous contact faces			
	Anterior <i>atlanto-occipital</i> membrane		The anterior edge of the <i>foramen magnum</i>	The antero-superior edge of the anterior arch of the <i>atlas</i>		
	Posterior <i>atlanto-occipital</i> membrane		The posterior edge of the <i>foramen magnum</i>	The superior edge of the posterior arch of the <i>atlas</i>		
	<i>Atlanto-occipital</i> ligament		The <i>jugular</i> process of the <i>occiput</i>	The transverse processes of the <i>atlas</i>		
C1-C2	Medial joint (atlanto-odontoid joint)	Joint capsule		Joining the edges of the cartilaginous contact faces at the anterior and posterior faces of the dens axis		
		<i>Alar</i> ligament		The lateral edge of the <i>dens axis</i>	The medial face of the occipital <i>condyles</i>	
		<i>Ligamentum apicis dentis</i>		The apex of the <i>dens axis</i>	The anterior edge of the <i>foramen magnum</i>	
		<i>Cruciform</i> ligament	Transverse ligament	Inbetween the medial faces of the lateral masses of the <i>atlas</i> , contacting the <i>dens axis</i>		
			Longitudinal bundle	The posterior face of the vertebral body of the <i>axis</i>	The anterior edge of the <i>foramen magnum</i>	
		<i>Membrana tectoria</i>		The interior face of the <i>basilar</i> face of the <i>occiput</i>	The posterior face of the vertebral body of the <i>axis</i>	
	Lateral joint (facet joint)	Joint capsule		Joining the edges of the cartilaginous contact faces		
		Anterior <i>atlanto-axoidal</i> ligament		The antero-inferior edge of the anterior arch of the <i>atlas</i>	The anterior face of the vertebral body of the <i>axis</i>	
Posterior <i>atlanto-axoidal</i> ligament		The postero-inferior edge of the anterior arch of the <i>atlas</i>	The superior edge of the <i>lamina</i> of the <i>axis</i>			
Accessory <i>atlanto-axoidal</i> ligament		The posterior face of the lateral masses of the <i>atlas</i>	The posterior face of the vertebral body of the <i>axis</i>			

Table A.1: Insertion and termination of the ligaments of the upper cervical spine

Segment		Ligament	Insertion	Termination	
C2-C3 up to C7-T1	Intervertebral symphysis	Anterior longitudinal ligament	Joining the anterior faces of the vertebral body and the IVD		
		Posterior longitudinal ligament	Joining the posterior faces of the vertebral body and the IVD		
	Facet joint	Joint capsule	Joining the edges of the cartilaginous contact faces		
		Interspinous ligament	The inferior edge of the spinous process of the vertebra above	The superior edge of the spinous process of the vertebra below	
		Nuchal ligament	Joining the external protuberance of the <i>occiput</i> , the posterior tubercle of the <i>atlas</i> and the apexes of the spinous processes of the adjacent <i>vertebrae</i>		
		Supraspinous ligament	Joining the apexes of the spinous processes		
		Yellow ligament	The inferior edge of the <i>lamina</i> of the vertebra above	The superior edge of the <i>lamina</i> of the vertebra below	

Table A.2: Insertion and termination of the ligaments of the lower cervical spine

Muscle		Insertion	Termination	Direction	Function
<i>Splenius capitis</i>	Posterior	The inferior part of the <i>nuchal</i> ligament and the spinous process of C7-T3	The lateral part of the superior <i>nuchal</i> line on the <i>occiput</i>	Upwards and laterally	Head extension and ipsilateral head inclination and rotation
<i>Splenius cervicis</i>		The spinous processes of T3-T6	The posterior tubercles of the transverse processes of C1-C3	Vertically upwards	
<i>Semispinalis capitis</i>		The articular processes of C3-C6, the transverse processes of C3-T6 and the spinous processes of C7-T1	Inbetween the superior and inferior <i>nuchal</i> line on the <i>occiput</i>	Upwards and laterally	Head extension and ipsilateral head inclination and rotation
<i>Semispinalis cervicis</i>		The transverse processes of T1-T7	The spinous processes of C2-C8	Upwards and laterally	
<i>Longissimus capitis</i>		The transverse processes of T1-T5	The articular processes of C2-C6	Vertically upwards	Extension and ipsilateral inclination and rotation of the cervical spine
<i>Longissimus cervicis</i>		The transverse processes of T1-T6 and the articular processes of C4-C7	The posterior edge of the <i>mastoid</i> process	Upwards and laterally	
<i>Levator scapula</i>		The transverse processes of C1-C4	The superior angle of the <i>scapula</i>	Obliquely downwards	Flexion and ipsilateral inclination and rotation of the cervical spine
<i>Longus capitis</i>	Anterior	The transverse processes of C3-C6	The <i>basilar</i> part of the <i>occiput</i>	Vertically upwards	Flexion and ipsilateral rotation of the cervical spine
<i>Longus colli</i>		The vertebral body of C5-T3 and the transverse processes of C3-C5	The anterior tubercle of the atlas, the vertebral body of C2-C4 and the transverse processes of C5-C7	Vertically upwards	Flexion and ipsilateral inclination and rotation of the cervical spine
<i>Scalenus anterior</i>	Antero-lateral	The transverse processes of C3-C6	The anterior edge of the first rib	Downwards and externally	Ipsilateral bending and flexion of the head
<i>Scalenus medialis</i>		The transverse processes of C2-C7	The anterior edge of the first rib	Downwards and externally	
<i>Scalenus posterior</i>		The transverse processes of C4-C6	The anterior edge of the second rib	Downwards and externally	

Table A.3: Insertion, termination and function of the deep cervical spine muscles

Muscle		Insertion	Termination	Direction	Function
<i>Suprahyoideus</i>	Anterior	Inferior edge of the <i>mandible</i>	The superior edge of the <i>hyoid</i> bone	Downwards and internally	Flexion of the head and cervical spine
<i>Infrahyoideus</i>		The posterior face of the <i>manubrium</i> and the superior edge of the <i>scapula</i> (passing by the <i>clavicle</i>)	The inferior edge of the <i>hyoid</i> bone	Upwards and externally	

Table A.4: Insertion, termination and function of the intermediate cervical spine muscles

Muscle			Insertion	Termination	Direction	Function
<i>Sterno-cleido-mastoideus</i>	<i>Cleido-mastoideus</i>	Antero-lateral	The internal face of the <i>clavicle</i>	The <i>mastoid</i> process	Downwards and internally	Ipsilateral inclination, contralateral rotation, extension and flexion (only when other muscles rigidified the spine) of the head
	<i>Cleido-occipitalis</i>			The superior edge of the <i>occiput</i>		
	<i>Sterno-occipitalis</i>		The superior edge of the <i>manubrium</i>	The <i>mastoid</i> process		
	<i>Sterno-mastoideus</i>					
<i>Trapezius</i>		Posterior	The superior <i>nuchal</i> line of the <i>occiput</i> and the spinous processes of C1-T10	The <i>clavícula</i> , the <i>acromion</i> and the <i>spina scapula</i>	Obliquely and externally towards the termination	Extension, ipsilateral inclination and contralateral rotation of the cervical spine

Table A.5: Insertion, termination and function of the superficial cervical spine muscles

Muscle			Insertion	Termination	Direction	Function
<i>Rectus capitis anterior</i>	Antero-lateral		The anterior face of the lateral masses of the <i>atlas</i> and its transverse process	In front of the <i>occipital</i> condyles	Upwards and medially	Extension and ipsilateral inclination of the head
<i>Rectus capitis lateralis</i>			The transverse process of the <i>atlas</i>	The <i>jugular</i> process of the <i>occiput</i>	Upwards, externally and medially	Ipsilateral inclination of the head
<i>Rectus capitis posterior major</i>	Posterior		The spinous process of the <i>axis</i>	The inferior <i>nuchal</i> line on the <i>occiput</i>	Upwards and laterally	Extension, ipsilateral inclination and rotation of the head
<i>Rectus capitis posterior minor</i>			The posterior tubercle of the <i>atlas</i>	Underneath the inferior <i>nuchal</i> line on the <i>occiput</i>	Vertically upwards	Extension and ipsilateral inclination of the head
<i>Obliquus inferior</i>			The spinous process and <i>lamina</i> of the <i>axis</i>	The transverse process of the <i>atlas</i>	Downwards, externally and medially	Ipsilateral rotation of the head
<i>obliquus superior</i>			The transverse process of the <i>atlas</i>	Inbetween the superior and inferior <i>nuchal</i> line on the <i>occiput</i>	Upwards and medially	Extension and ipsilateral inclination of the head

Table A.6: Insertion, termination and function of the suboccipital cervical spine muscles

Chapter B

Literature Review

This Appendix contains supplementary synthesis Tables summarising the current knowledge regarding the material properties of the different cervical spine FE model aspects, i.e. the *vertebrae*, the IVD and the ligaments. These Tables were also included in the report written to complement the FDA accreditation procedure for the FE modeling method developed in the context of this PhD project.

A subsection is dedicated to each of the FE model aspects and contains at least two literature tables. The first table summarises the material properties recommended by the most commonly referenced *in-silico* studies. The starting point for this literature review is the non-exhaustive list of cervical spine FE models (Tables 2.2 and 2.3). The second table lists the material properties measured in *in-vitro* experiments. In each section, the properties selected for the FE model are also contrasted to those described in these Tables.

B.1 *Vertebrae*

Table B.1 shows that the most commonly used Young's modulus for cortical bone ranges from 10 GPa to 12 GPa, while the ranges are larger for spongy bone and the posterior arch, from 100 MPa to 511 MPa and from 1 GPa to 6 GPa, respectively. The endplates are assigned Young's moduli varying from 25 MPa to 2 GPa.

The material properties selected for the spongy bone and the endplates are consistent with these ranges. Because of its substantial thickness, the Young's modulus of the cortical outer layer was reduced, as it incorporates both cortical and spongy bone. The Young's modulus for the posterior arch was set equal to the one chosen for the cortico-spongy layer, as could be confirmed by density measurements performed on the CT-images. Tables B.2 and B.3 justify the model choices.

B.2 IVD

In the FE model, a clear distinction was made between the *nucleus*, considered quasi-incompressible with a Young's modulus of 1 MPa, and the *annulus fibrosus*, assumed quasi-incompressible but multilinear elastic with a maximal modulus of 4.3 MPa. Furthermore, the *annulus fibrosus* was interwoven with tension-only elastic fibres. These properties seem to be in agreement with the literature. Indeed, the elastic modulus range for the *nucleus* was 1 MPa to 4MPa *in-silico* and *in-vitro*, while for the *annulus fibrosus* it was 1MPa to 4 MPa *in-silico* and 1 MPa to 8.4 MPa *in-vitro* (see Tables B.4 and B.5).

Author (year)	# Citations (approx.)	Segment	Cortical Bone	Spongy Bone	Posterior Aspect	Vertebral Endplates	
Shirazi-Adl et al. (1984 1986 1993)	10	L2-L3	E = 12GPa = 0.3	E = 100MPa = 0.2	E = 3.5GPa = 0.25	-	
Saito et al. (1991)	12	C0-T2	E = 10GPa = 0.29	E = 450MPa = 0.25	-	E = 150MPa = 0.3	
Lavaste et al. (1992)	1	L1-L5	E = 12GPa = 0.3	E = 100MPa = 0.3	E = 1GPa = 0.3	E = 500MPa = 0.4	
Kleinberger (1993)	7	C5-C5	E = 208MPa = 0.2				
Goel et al. (1995a 1995b)	8	L3-L5	E = 12GPa = 0.3	E = 15 – 511MPa = 0.2	E = 3.5GPa = 0.25	-	
Sharma et al. (1995)	2	L3-L4	E = 12GPa = 0.3	E = 100MPa = 0.2	E = 3.5GPa = 0.25	E = 25MPa = 0.25	
Maurel et al. (1997)	5	C3-C7	E = 12GPa = 0.3	E = 100MPa = 0.2	E = 6GPa = 0.3	E = 300MPa = 0.3	
Yoganandan et al. (1996) Kumaresan et al. (1997 1998 1999 2000) Voo et al. (1997)	19	C4-C6	E = 10GPa = 0.29	E = 100MPa = 0.29	E = 3.5GPa = 0.29	E = 500MPa = 0.4	
Clausen et al. (1997) Goel et al. (1998)	13	C5-C6	E = 10GPa = 0.3	E = 450MPa = 0.25	E = 3.5GPa = 0.25	E = 2GPa = 0.2	

Table B.1: The vertebra mechanical properties as described in the commonly cited *in-silico* studies.

Author (year)	Origin	Sample Age	N	Test	Results
Liebschner et al. (2003)	T12-L3	68y (20-90y)	19	Compression (Reverse FEM)	E = 457 ± 934MPa (9 - 3216MPa)
El Masri et al. (2012)	T10-T12/L2	70y (57-83y)	22	Compression (Reverse FEM)	E = 374 ± 208MPa
Mirzaali et al. (2015)	Femur	46-99y	96	Tension Compression Torsion	E = 18.2 ± 1.9GPa E = 18.9 ± 1.8GPa μ = 6.1 ± 0.6GPa
Reilly et al. (1975)	Femur	/	/	Tension Compression	E _{longi} = 17.0GPa E _{trans} = 11.5GPa
Ziopoulos et al. (1998)	Femur	35-92y	10	3-point bending	E = 16.36 ± 0.75GPa

Table B.2: The *in-vitro* experimental literature on cortical and cortico-spongy bone mechanical properties.

Author (year)	Origin	Sample Age	N	Test	Results
Lambers <i>et al.</i> (2014)	L4 from 10 PMHS	47-80y	18	Compression Tension	E = 232 ± 36MPa yield = 1.2 ± 0.3MPa yield = 0.8% ± 0.04% E = 276 ± 60MPa yield = 1.5 ± 0.3MPa yield = 0.7% ± 0.03%
Liu <i>et al.</i> (2013)	C2-C7 from 5 PMHS	47-79y	40	Compression Tension	E = 286.6 ± 156.7MPa yield = 5.7MPa yield = 2.2%, ult = 6.8 ± 3.7MPa ult = 3.1 ± 0.83% E = 107.9 ± 30.6MPa yield = 2.9MPa yield = 2.9%, ult = 4.2 ± 1.9MPa ult = 6.8 ± 2.6%
Hernandez <i>et al.</i> (2014)	L2 from 21-23PMHS	64-88y	47	Compression	E = 221 ± 95MPa yield = 1.1 ± 0.5MPa yield = 0.7% ± 0.08%, ult = 1.3 ± 0.6MPa ult = 1.3% ± 0.3%
Vale <i>et al.</i> (2013)	Femur epiphysis	65-86y	31	Compression	E _{coxarthrosis} = 443.3 ± 154.3MPa E _{fracture} = 502.4 ± 224.3MPa
Zhou <i>et al.</i> (2014)	Vertebral body	56-74y	10	Compression	E = 329 ± 92MPa yield = 1.6 ± 0.4MPa yield = 0.7% ± 0.03%
	Greater troch	59-87y	21	Compression	E = 473 ± 342MPa yield = 2.3 ± 1.6MPa yield = 0.7% ± 0.07%
	Femoral neck	59-87y	21	Compression	E = 3052 ± 1458MPa yield = 18.5 ± 8.9MPa yield = 0.81% ± 0.05%
	Tibia	61-79y	22	Compression	E = 750 ± 402MPa yield = 3.9 ± 2.3MPa yield = 0.7% ± 0.08%

Table B.3: The *in-vitro* experimental literature on spongy bone mechanical properties.

Author (year)	# Citations (approx.)	Segment	Annulus	Nucleus	IVD Fibres
Shirazi-Adl et al. (1984 1986 1993)	10	L2-L3 L1-S1	E = 4.2MPa = 0.45	Incompressible fluid	Nonlinear: E 1.2GPa -> 150MPa
Ueno et al. (1987)	7	L4-L5	E = 1MPa = 0.48	Incompressible fluid	E = 500MPa
Saito et al. (1991)	12	C0-T2	E = 35/40MPa = 0.49	E = 160/200MPa = 0.49	-
Lavaste et al. (1992)	1	L1-L5	E = 2MPa = 0.45	E = 4MPa = 0.4999	E = 500MPa = 0.45
Kleinberger (1993)	7	C5-C5	E = 3.4MPa = 0.49		-
Goel et al. (1995a 1995b)	8	L3-L5	E = 4.2MPa = 0.45	E = 1MPa = 0.499	E = 450MPa = 0.3
Sharma et al. (1995)	2	L3-L4	E = 4.2MPa = 0.45	E = 0.2MPa = 0.499	E 480MPa
Yoganandan et al. (1996) Kumaresan et al. (1997 1998 1999 2000) Voo et al. (1997)	19	C4-C6	E = 3.4MPa = 0.4	E = 3.4MPa = 0.49	-
Clausen et al. (1997) Goel et al. (1998)	13	C5-C6	E = 4.2MPa = 0.45	Incompressible fluid	E = 450MPa = 0.3
Schmidt et al. (2006)	1	L4-L5	Mooney-Rivlin E 4.2MPa	Mooney-Rivlin E 1.2MPa	Nonlinear: E 1.2GPa -> 150MPa

Table B.4: The IVD mechanical properties as described in the commonly cited *in-silico* studies.

	Author (year)	Origin	Sample Age	N	Test	Results
Nucleus	Yang <i>et al.</i> (1988)	-	-	17	Compression	Bulk modulus = 1720MPa (1098 - 2114MPa)
	Cloyd <i>et al.</i> (2007)	Lumbar	19-76y	5	Unconfined compression	$E = 5.4 \pm 2.6\text{kPa}$ $\nu = 0.6 \pm 0.2$
	Johannessen <i>et al.</i> (2005)	Lumbar	58y (19-80y)	19	Confined compression	Healthy $E = 1 \pm 0.4\text{MPa}$ Degenerated $E = 0.4 \pm 0.2\text{MPa}$
Annulus	Wu <i>et al.</i> (1976)	Lumbar	20-30y	30	Uniaxial tensile	$E_1 = 4.1\text{MPa}$ $E_2 = 3.7\text{MPa}$ $\sigma_{ult} = 3.8\text{MPa}$ $\epsilon_{ult} = 0.25$
	Elliott <i>et al.</i> (2001)	L1-L2/L2-L3	53y (27-72y)	60	Uniaxial tensile	$E_{circ,outer} = 17.5 \pm 14.3\text{MPa}$ $E_{circ,inner} = 5.6 \pm 4.7\text{MPa}$ $E_{axial,outer} = 0.8 \pm 0.7\text{MPa}$ $E_{axial,inner} = 1 \pm 1.2\text{MPa}$ $E_{radial,outer} = 0.5 \pm 0.3\text{MPa}$
	Holzappel <i>et al.</i> (2005)	L1-L2	-	-	Uniaxial tensile	$E = 28 - 78\text{MPa}$
	Shan <i>et al.</i> (2015)	T11-S1	20-69y	1969	Uniaxial tensile	$E_{inner} = 4.8 \pm 2.3\text{MPa}$ $\sigma_{ult,inner} = 1.2\text{MPa}$ $\epsilon_{ult,inner} = 49.3\%$ $E_{mid} = 8.4 \pm 3.5\text{MPa}$ $\sigma_{ult,mid} = 1.8\text{MPa}$ $\epsilon_{ult,mid} = 44.9\%$ $E_{outer} = 13.0 \pm 4.2\text{MPa}$ $\sigma_{ult,outer} = 3.3\text{MPa}$ $\epsilon_{ult,outer} = 38.1\%$
	Liu <i>et al.</i> (2016)	T12-S1	31-49y	324	Indentation $\varnothing 3\text{mm}$	Central: $k = 82.6 \pm 6.6\text{N/mm}$ Inner: $k = 83.4 \pm 7.1\text{N/mm}$ Middle: $k = 90.9 \pm 6.5\text{N/mm}$ Outer: $k = 99.2 \pm 6.6\text{N/mm}$
Endplates	Yamada (1975)	-	-	-	$E = 23.8\text{MPa}$	

Table B.5: The *in-vitro* experimental literature on ligament mechanical properties.

B.3 Ligaments

Tables B.6 and B.7 show that both the numerical and the experimental literature did not yet reach consensus on the mechanical properties of the ligaments, as a high variability could be noted. The properties assigned to the ligaments in the current FE model agree with the *in-silico* and *in-vitro* literature, in terms of Young's moduli and stiffnesses. However, the generalised stiffnesses of the interspinous and capsular ligaments are lower, respectively, higher than reported in the *in-vitro* literature. The stiffness ranges for the anterior longitudinal ligament, the posterior longitudinal ligament, the yellow ligament, the interspinous ligament and the facet capsules, were $16 \frac{N}{mm}$ to $139 \frac{N}{mm}$, $23 \frac{N}{mm}$ to $215 \frac{N}{mm}$, $22 \frac{N}{mm}$ to $118 \frac{N}{mm}$, $6 \frac{N}{mm}$ to $13 \frac{N}{mm}$ and $34 \frac{N}{mm}$ to $85 \frac{N}{mm}$, respectively. The values incorporated in the model, taking into account the number of cable elements, their CSA and their elastic modulus, were $61 \frac{N}{mm}$, $97 \frac{N}{mm}$, $65 \frac{N}{mm}$, $3.1 \frac{N}{mm}$ and $247 \frac{N}{mm}$, respectively.

Author (year)	# citations (approx.)	Segment	ALL	PLL	Lig. Flavum	Interspin. Lig.	Facet Capsule
Shirazi-Adl et al. (1986 1993)	10	L2-L3 L1-S1	E ≈ 110MPa SL ≈ 20% CSA = 24mm ²	E ≈ 110MPa SL ≈ 20% CSA = 14.4mm ²	E ≈ 80MPa SL ≈ 45% CSA = 75mm ²	E ≈ 115MPa SL ≈ 15% CSA = 40mm ²	E ≈ 112MPa SL ≈ 30% CSA = 36mm ²
Kleinberger (1993)	7	C1-C7	K = 33 N/mm	K = 20.4 N/mm	K = 27.2 N/mm	-	-
Goel et al. (1995a 1995b)	8	L3-L5	E = 7.8 -> 20MPa CSA = 63.7mm ²	E = 10 -> 20MPa CSA = 20mm ²	E = 15 -> 19MPa CSA = 40mm ²	E = 10 -> 12MPa CSA = 40mm ²	E = 7.5 -> 33MPa CSA = 30mm ²
Sharma et al. (1995)	2	L3-L4	E ≈ 45.9MPa	E ≈ 18.8MPa	E ≈ 18.8MPa	E ≈ 45.9MPa	E ≈ 45.9MPa
Maurel et al. (1997)	5	L1-L5	E = 10MPa SL ≈ 10% CSA = 0.5mm ²	E = 20MPa SL ≈ 10% CSA = 0.5mm ²	E = 50MPa SL ≈ 0% CSA = 0.4mm ²	E = 3MPa SL ≈ 17% CSA = 40mm ²	E = 20MPa SL ≈ 20 -> 40% CSA = 30mm ²
Clausen et al. (1997) Goel et al. (1998)	13	C5-C6	E = 15 -> 30MPa v = 0.3 CSA = 6.1mm ²	E = 10 -> 20MPa v = 0.3 CSA = 5.4mm ²	E = 5 -> 10MPa v = 0.3 CSA = 50.1mm ²	E = 0 -> 4 -> 8MPa v = 0.3 CSA = 13.1mm ²	E = 7 -> 30MPa v = 0.3 CSA = 46.6mm ²
Yoganandan et al. (1996) Kumaresan et al. (1997 1998 1999 2000) Voo et al. (1997)	19	C4-C6	E = 11.9MPa v = 0.39	E = 12.5MPa v = 0.39	E = 2.4MPa v = 0.39	E = 3.4MPa v = 0.39	E = 7.7MPa v = 0.39

Table B.6: The ligament mechanical properties as described in the commonly cited *in-silico* studies [ALL = Anterior Longitudinal Ligament, PLL = Posterior Longitudinal Ligament, ISL = Interspinous Ligament, LF = *Ligamentum Flavum*, FC = Facet Capsule, CSA = Cross-sectional Surface Area].

Author (year)	Sample Age	FSU	ALL	PLL	Lig. Flavum	Interspin. Lig.	Facet Capsule
Chazal (1985)	53y	C2-C3 -> L4-L5	K 71N/mm E = 24.9MPa	K 145N/mm E = 61.6MPa	E = 104MPa	E = 36MPa	-
Myklebust <i>et al.</i> (1986)	67y	C2-C3 -> C7-T1	K 13 - 28N/mm	K 16 - 24N/mm	K 5 - 26N/mm	K 4 - 6N/mm	K 20 - 35N/mm
Przybylski <i>et al.</i> (1996)	80y	C2-C3 -> C6-C7	CSA = 11 - 38 mm ² K = 37 - 57N/mm E = 13 - 75MPa	CSA = 4 - 28mm ² K = 54 - 90N/mm E = 8 - 98MPa	-	-	-
Yoganandan <i>et al.</i> (2000, 2001)	68y	C2-C5 -> C5-T1	CSA = 11.1 - 12.1 mm ² K = 16 - 18N/mm E = 26.3 - 43.8MPa	CSA = 11.3 - 14.7 mm ² K = 23 - 25.4N/mm E = 22.2 - 41MPa	CSA = 46 - 49 mm ² K = 21.6 - 25N/mm E = 2.1 - 3.5MPa	CSA = 13 mm ² K = 6.4 - 7.7N/mm E = 3.1 - 5MPa	CSA = 42 - 50mm ² K = 33.6 - 37N/mm E = 4.8 - 5MPa
Stojanovic <i>et al.</i> (2012)	23 - 70y	/	K 85N/mm	K 110N/mm	K 60N/mm	-	-
Mattucci <i>et al.</i> (2012)	44y	C2-T1	K = 139N/mm E = 50MPa	K = 215N/mm E = 63MPa	K = 118N/mm E = 24.6MPa	K = 13N/mm E = 13.7MPa	K = 85N/mm E = 6.9MPa

Table B.7: The *in-vitro* experimental literature on ligament mechanical properties [ALL = Anterior Longitudinal Ligament, PLL = Posterior Longitudinal Ligament, ISL = Interspinous Ligament, LF = *Ligamentum Flavum*, FC = Facet Capsule, CSA = Cross-sectional Surface Area].

Chapter C

Muscle Regulation Model

Chapter 3 describes the functioning, performance and feasibility of a muscle regulation model. This Appendix provides more details regarding the calculation of the input data from the EOS- and MRI-data. Supplementary data regarding the model evaluation is given as well.

C.1 Input Data Calculation

The model requires a set of geometrical and mechanical input parameters:

- The direction vector, lever arm and cross-sectional surface for each muscle
- The external load, expressed in the local reference frame of the intervertebral joint
- The physiological joint load limit, considering both the IVD and the facet joints
- The maximal admissible stress for each muscle

To calculate this geometric and mechanical input data, a 3D musculoskeletal model is generated from the fusion of the MRI-based muscle reconstructions with the EOS-based spine and envelope reconstruction.

The reference configuration is the upright configuration, i.e. the configuration in which the patients is X-rayed. However, the MRI-data is acquired with the patient lying down. It is therefore necessary to elastically register the MRI-based reconstructions onto the EOS-based reconstruction.

To this purpose, landmarks defining the external envelope and the *vertebrae* common to the X-ray and MR-images are identified. Calculating the transformation, matching both sets of landmarks as close as possible, based on the Kriging interpolation algorithm (Trochu [1993]; Hausselle *et al.* [2012]), enables the elastic registration of the MRI-based muscle reconstruction onto the EOS-based spine reconstruction. The complete process is shown in Figure 3.2.

C.2 Results Model Evaluation

Figure 3.3 presented the predicted forces for a selection of four anterior and four posterior muscles in the left twisted, the left bended, the flexed and the extended configuration, in relation to those reported by Moroney *et al.* [1988a] and Choi [2003]. Figure C.2 present the predictions for all muscle that were included in the analysis.

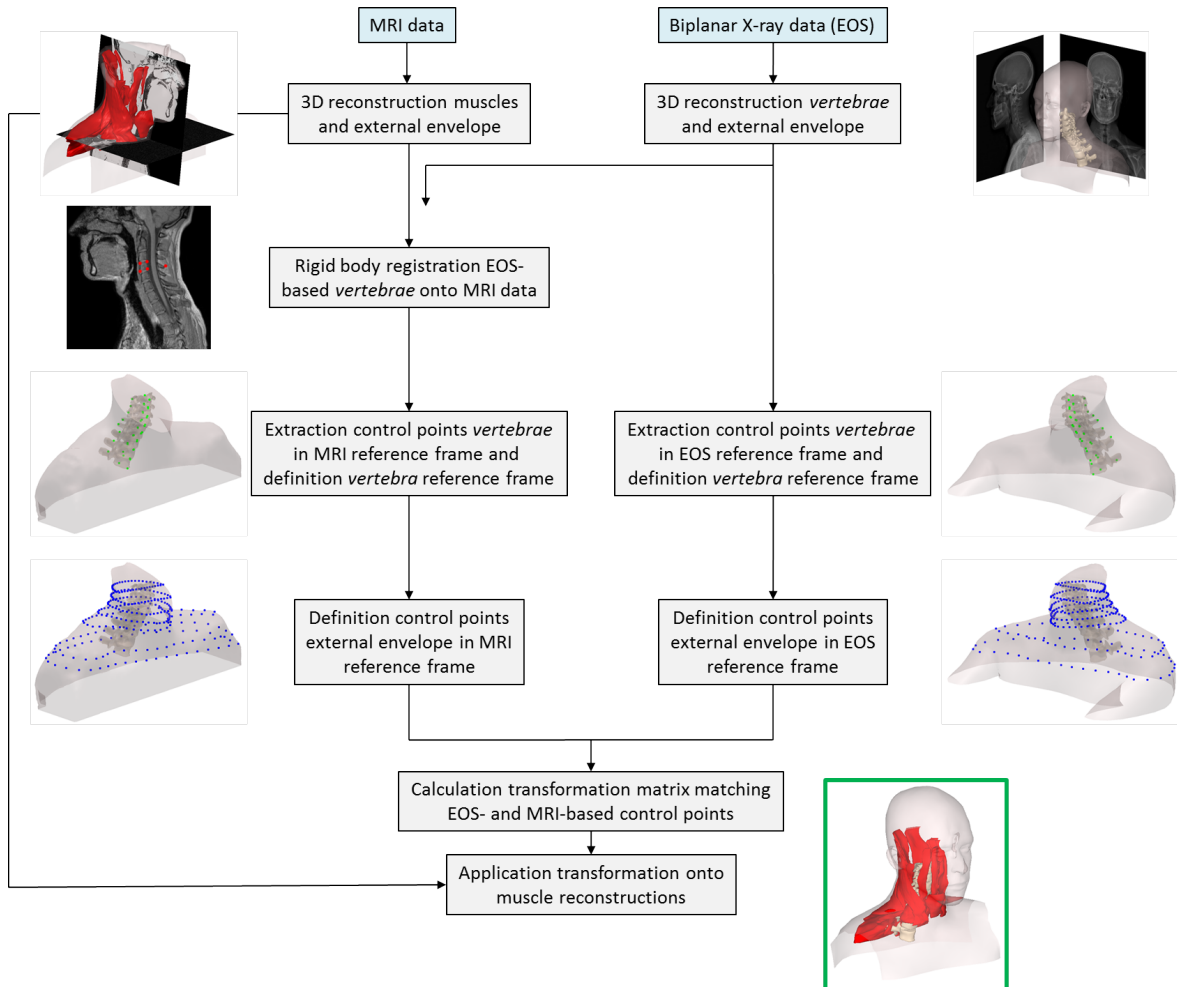
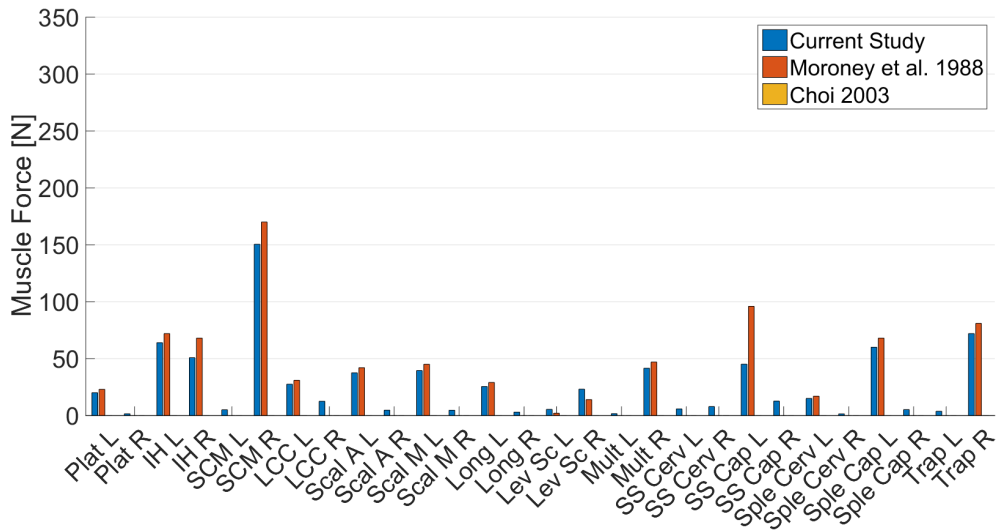
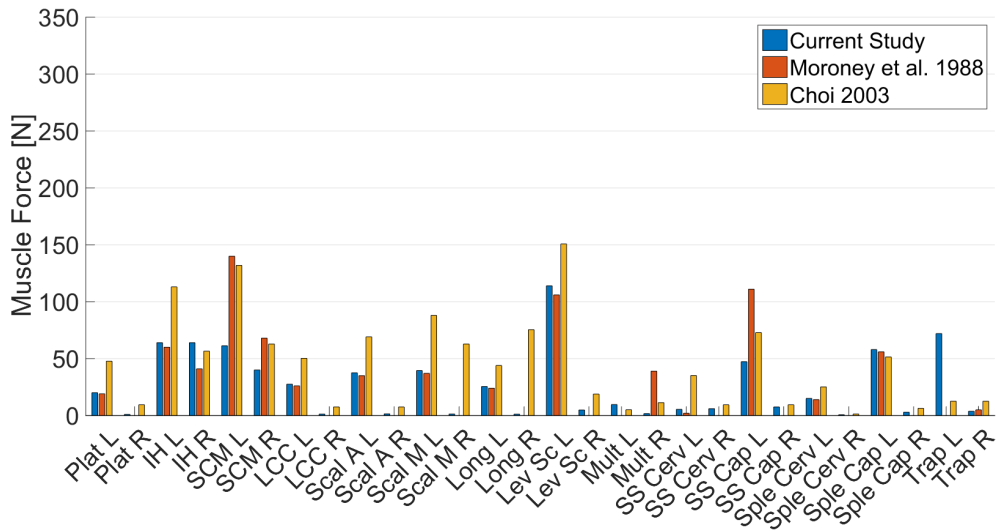


Figure C.1: The elastic registration procedure to transfer the 3D reconstruction of the muscles from the MRI to the EOS reference system.



(a) Left twist



(b) Left bending

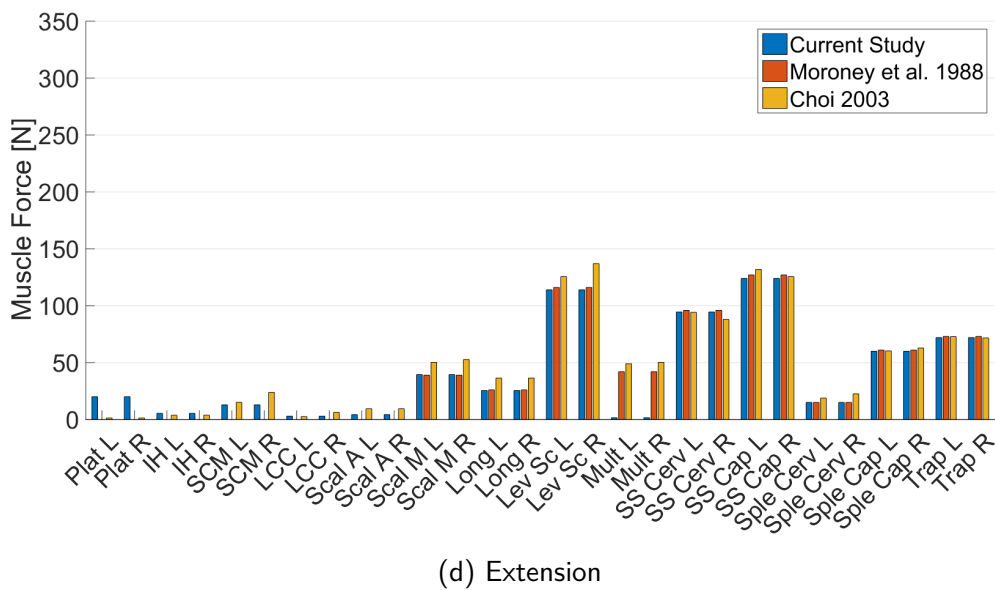
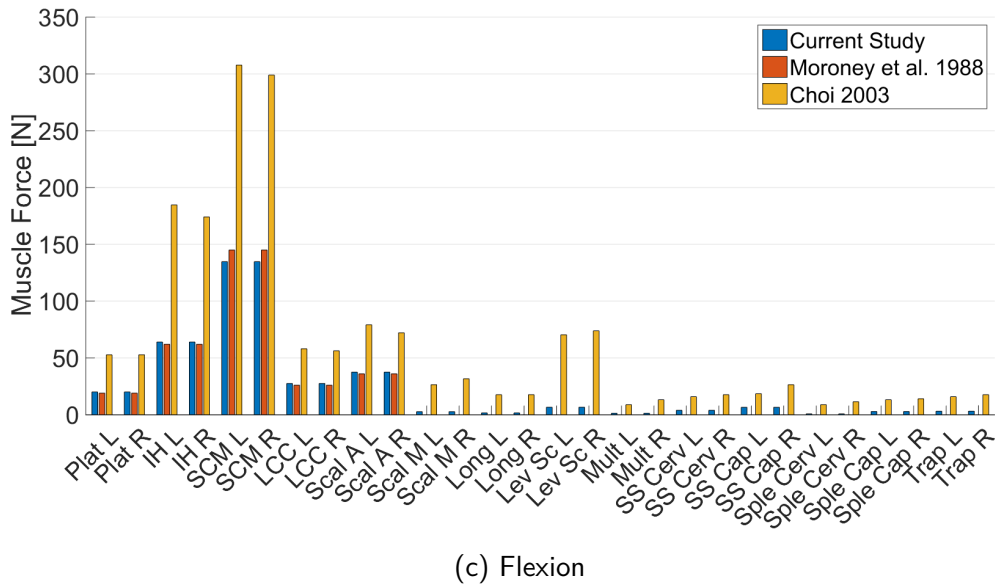


Figure C.2: Comparison of the muscle force predictions with two reference studies for all muscles/muscle groups that were considered in the analysis for the four configurations. [L: left; R: right, A: anterior, P: posterior, Plat: *Platysma*, IH: *infrahyoid*, SCM: *sternocleidomastoideus*, LCC: *longus colli & longus cervicis*, Scal: *scalenus*, Long: *longissimus*, Lev Scap: *levator scapulae*, Mult: *multifidus*, SS Cerv: *semispinalis cervicis*, SS Cap: *semispinalis capitis*, Sple Cerv: *splenius cervicis*, Sple Cap: *splenius capitis*, Trap: *trapezius*]

(Inter)national Communications

Contribution to Book Chapters

- S. Laporte, **M. Van den Abbeele**, P.Y. Rohan, C. Adam, P. Rouch and W. Skalli. *Chapter 22: Spine*, Pages 471-495. In *Biomechanics of Living Organs*, Y. Payan and J. Ohayon (editors). Academic Press, Oxford, 2017. [published]

Scientific Articles

- **M. Van den Abbeele**, J.-M. Valiadis, L. Lima, P. Khalife, P. Rouch and W. Skalli. *Contribution to FE modeling for intraoperative pedicle screw strength prediction*. *Computer Methods In Biomechanics and Biomedical Engineering*, 21(2018):13-21. [published]
- **M. Van den Abbeele**, F. Li, V. Pomeroy, D. Bonneau, B. Sandoz, S. Laporte, and W. Skalli. *A subject-specific biomechanical control model for the prediction of cervical spine muscle forces*. *Clinical Biomechanics*, 51(2018): 58-66. [published]
- A. Alzakri, C. Vergari, **M. Van den Abbeele**, O. Gille, I. Obeid and W. Skalli. *Global Sagittal Alignment and Proximal Junctional Kyphosis in Adolescent Idiopathic Scoliosis*. [accepted at Spine Deformity]

Scientific Articles In Preparation

- **M. Van den Abbeele**, P. Coloma, S. Laporte, B. Sandoz, D. Bonneau, C. Barrey and W. Skalli. *A Framework for the Validation of Cervical Spine FE Modeling*. [in preparation for submission to *The European Spine Journal*]
- **M. Van den Abbeele**, E. Ferrero, C. Maillot, B. Moal, P. Sudres, V. Pomeroy, V. Lafage, C. Marty, P. Guigui, R. Carlier and W. Skalli. *A subject-specific proprioceptive control model for spine disorder analysis*. [in preparation for resubmission, initially submitted to *Journal of Biomechanics*]

Conference Abstracts

Accepted for Poster Presentation

- **M. Van den Abbeele**, J.-M. Valiadis, L. Lima, P. Khalife, P. Rouch and W. Skalli. *Contribution to FE modeling for pedicle screw insertion*, 22nd Congress of the European Society of Biomechanics, July 10-13, 2016, Lyon, France.
- **M. Van den Abbeele**, P. Coloma, S. Laporte, B. Sandoz, D. Bonneau, C. Barrey and W. Skalli. *Patient-specific FE modeling of the inferior cervical spine*, CMBBE, March 26-29, 2018, Lisbon, Portugal.

- **M. Van den Abbeele**, P. Coloma, S. Laporte, B. Sandoz, D. Bonneau, C. Barrey and W. Skalli. *A framework for cervical spine FE model development and validation*, World Congress of Biomechanics, July 8-12, 2018, Dublin, Ireland.

Accepted for Oral Presentation

- C. Amabile, **M. Van den Abbeele**, H. Pillet, C. Maillot, P. Sudres, B. Moal, V. Pomoero, V. Lafage, C. Marty, R. Carlier and W. Skalli. *A subject-specific proprioceptive control model for spine disorder analysis*. The 2nd Workshop on Spine Loading and Deformation, May 18-20, 2017, Berlin, Germany.
- **M. Van den Abbeele**, F. Li, V. Pomoero, B. Sandoz, S. Laporte and W. Skalli. *Subject-specific prediction of cervical spine muscle forces*, 23rd Congress of the European Society of Biomechanics, July 2-5, 2017, Seville, Spain.
- **M. Van den Abbeele**, F. Li, V. Pomoero, B. Sandoz, S. Laporte and W. Skalli. *A subject-specific biomechanical control model for the prediction of cervical spine muscle forces*, 26th Congress of the International Society of Biomechanics, July 23-27, 2017, Brisbane, Australia.
- **M. Van den Abbeele**, P. Coloma, S. Laporte, B. Sandoz, D. Bonneau, C. Barrey and W. Skalli. *The subject-specific FE modeling of the inferior cervical spine*, 8th World Congress, July 8-12, 2018, Dublin, Ireland.
- C. Muth-Seng, D. Brauge, N. Soriau, B. Sandoz, **M. Van den Abbeele**, W. Skalli and S. Laporte. *Experimental analysis of the lower cervical spine in hyperflexion*, 8th World Congress, July 8-12, 2018, Dublin, Ireland.
- **M. Van den Abbeele**, P. Coloma, B. Sandoz, D. Bonneau, S. Laporte and W. Skalli. *The FE modeling of the intact and instrumented cervical spine*, NAFEMS France Conference, November 14, 2018, Paris, France.

Official Reports

- **M. Van den Abbeele**, W. Skalli, S. Laporte and B. Sandoz. *A Generic Morphorealistic Finite Element Model of the Lower Cervical Spine - A Computational Modeling and Simulation Report*. [in preparation]

LA MODELISATION MUSCULO-SQUELETTIQUE PERSONNALISEE DU RACHIS CERVICAL

RESUME : La cervicalgie, ainsi que la lombalgie, est la deuxième cause d'invalidité dans le monde développé. Pour mieux comprendre les mécanismes de dégénérescence et les complications chirurgicales, une approche patient-spécifique est indispensable. Cette thèse a pour objectif de contribuer au développement d'un modèle musculo-squelettique personnalisé du rachis cervical. Dans la première partie, un modèle éléments finis du rachis intact et instrumenté est proposé et validé *in-vitro* de manière individualisée. La géométrie du modèle est définie à partir des données radiographies biplanes et CT, ce qui révèle l'effet de la précision géométrique. Les deux modèles produisent le comportement typique non linéaire, néanmoins une correspondance plus étroite est obtenue avec le modèle basé sur CT. Le corridor expérimental est respecté dans la configuration intacte et instrumentée. La deuxième partie porte sur la quantification des forces musculaires et des charges intervertébrales associées à partir d'imagerie médicale. Les prédictions ont été jugées physiologiquement et mécaniquement admissibles. En outre, il a été démontré que l'acquisition d'une radiographie bipiane complétée par une coupe IRM suffit pour obtenir une prédiction pertinente du chargement interne.

Cette thèse pourrait nous aider à comprendre la biomécanique de la colonne vertébrale avant et après restauration chirurgicale et à nous rapprocher de la mise en œuvre de la modélisation numérique en routine clinique.

Mots clés : Modélisation personnalisée – Rachis cervical – Muscles – Éléments finis – Biomécanique

THE SUBJECT-SPECIFIC MUSCULOSKELETAL MODELING OF THE CERVICAL SPINE

ABSTRACT : Neck pain, together with lower back pain, is the second most important cause of invalidity in the developed world. To better understand spinal degeneration and surgical complications, a patient-specific approach is fundamental. This PhD aims to contribute to the development of a subject-specific musculoskeletal cervical spine model. In the first part, a finite element model of the intact and instrumented spine is proposed and validated experimentally in a *one-to-one* fashion. Biplanar X-ray and CT-data are used to define the model geometry, revealing the effect of geometry accuracy. Both models produced the typical non-linear load-displacement behavior, yet a closer correspondence was obtained with the CT-based model. The experimental corridor was respected in both the intact and instrumented configuration. The second part focuses on the quantification of muscle forces and associated intervertebral joint loads from medical image-based input data. The predictions were found physiologically and mechanically admissible. Furthermore, it has been shown that the acquisition of a biplanar X-ray scan complemented with one MRI slice suffices to obtain a relevant prediction of the internal loading configuration.

This PhD might help us understand spinal biomechanics before and after surgical restoration and brings us one step closer to implementing computational modeling in clinical routine.

Keywords : Subject-specific modeling – Cervical Spine – Muscles – Finite element modeling – Biomechanics